



The NASA Langley 16-Foot Transonic Tunnel

Historical Overview, Facility Description, Calibration, Flow Characteristics, and Test Capabilities

Francis J. Capone, Linda S. Bangert, Scott C. Asbury, Charles T. L. Mills, and E. Ann Bare
Langley Research Center • Hampton, Virginia

The use of trademarks or names of manufacturers in this report is for accurate reporting and does not constitute an official endorsement, either expressed or implied, of such products or manufacturers by the National Aeronautics and Space Administration.

Available electronically at the following URL address: <http://techreports.larc.nasa.gov/ltrs/ltrs.html>

Printed copies available from the following:

NASA Center for AeroSpace Information
800 Elkridge Landing Road
Linthicum Heights, MD 21090-2934
(301) 621-0390

National Technical Information Service (NTIS)
5285 Port Royal Road
Springfield, VA 22161-2171
(703) 487-4650

Contents

Introduction	1
Symbols	2
Wind Tunnel Description and Support Equipment	3
General Arrangement and Aerodynamic Characteristics	3
Quiescent Chamber and Entrance Cone	3
Test Section	4
General description	4
Test-section walls.	4
Transonic slots	4
Diffuser entrance vanes	4
Overview of main model support system	5
Windows and access hatches	5
Diffuser	5
Power Section and Drive Fans	5
General arrangement	5
Electric motors.	6
Drive fans.	6
Return Passage	6
Air Exchange Section	6
Screens	7
Air Removal System	7
Arrangement and function	7
Compressor	8
Electric motor.	8
Valves and controls	8
Wind Tunnel Support Areas	8
Control room	8
Model preparation area	8
Measurements and Instrumentation	9
Wind Tunnel Reference Measurements	9
Centerline Tube Static Pressures.	9
Wall Static Pressures	9
Boundary-Layer Pressures	9
Flow Field Survey Measurements.	9
Survey rake	9
Flow angle measurements	10
Fluctuating-pressure measurements.	10
Hot Wire Measurements	10
Data Acquisition System	10
Test-Section Development and Calibration Procedure	10
Slot Shape Studies.	10

Development of slot shape 18	10
Development of slot shape 26	11
Development of slot shape 29	11
Wind Tunnel Operational Principles and Procedures	11
Operational principles	11
Operational procedures	11
Calibration Procedure and Data Analysis	12
Calibration tests and data presentation	12
Basic data reduction	12
Flow-uniformity analysis for standard calibrated test-section lengths	12
Alternate calibrated test-section lengths	13
Criteria for flow uniformity	13
Wind Tunnel Aerodynamic Performance	13
Mach Number Characteristics	13
Test section	13
Test-section wall	13
Diffuser	14
Wind Tunnel Calibration	14
Test-Section Wall Divergence Angle	14
Subsonic and low supersonic Mach numbers	15
Supersonic Mach numbers	15
Divergence angles and Mach number gradients	15
Alternate calibrated test-section lengths	15
Boundary-Layer Characteristics	15
Power Requirements	16
Test-Section Flow Field Characteristics	16
Incremental Mach number	16
Upflow characteristics	16
Sideflow characteristics	16
Airstream Flow Quality	17
Turbulence intensities	17
Fluctuating-pressure characteristics	17
Transition Reynolds number	17
Test-Section Temperature Distribution	17
Air Moisture Condensation	17
Wind Tunnel Test Capabilities	18
Guidelines for Model Size and Location	18
Subsonic blockage considerations	18
Boundary-reflected-disturbance length considerations	18
Model location	18
Model volume and span	18
Main Model Support System	18
Miscellaneous Model Support Systems	19
Model attachment to main model support	19

Sting support systems	19
Sting-strut support	19
Wingtip support system	20
Air-sting supports.	20
High angle-of-attack sting-strut system	20
Semispan support system	20
Model Propulsion Systems	20
Exhaust nozzle simulation systems	21
Propulsion simulators.	21
Ejector mass flow system	22
Data Acquisition Systems	22
Steady-state data systems.	22
Dynamic data system	22
Instrumentation	22
Force and moment measurements	22
Pressure and temperature measurements	23
Weight flow rate measurements.	23
Flow-Visualization Methods	23
Oil-flow techniques	23
Pressure-sensitive paint technique	23
Laser sheet system	23
Flow Field Measurements	24
Concluding Remarks	24
References	24
Tables	26
Figures	71

Abstract

The Langley 16-Foot Transonic Tunnel is a closed-circuit single-return atmospheric wind tunnel that has a slotted octagonal test section with continuous air exchange. The wind tunnel speed can be varied continuously over a Mach number range from 0.1 to 1.3. Test-section plenum suction is used for speeds above a Mach number of 1.05. Over a period of some 40 years, the wind tunnel has undergone many modifications. During the modifications completed in 1990, a new model support system that increased blockage, new fan blades, a catcher screen for the first set of turning vanes, and process controllers for tunnel speed, model attitude, and jet flow for powered models were installed. This report presents a complete description of the Langley 16-Foot Transonic Tunnel and auxiliary equipment, the calibration procedures, and the results of the 1977 and the 1990 wind tunnel calibration with test-section air removal. Comparisons with previous calibrations showed that the modifications made to the wind tunnel had little or no effect on the aerodynamic characteristics of the tunnel. Information required for planning experimental investigations and the use of test hardware and model support systems is also provided.

Introduction

The Langley 16-Foot Transonic Tunnel is a closed-circuit single-return atmospheric wind tunnel that has a slotted transonic test section with a Mach number range from 0.1 to 1.3. Test-section plenum suction is used for speeds above a Mach number of 1.05. The facility is used primarily for internal (inlet and nozzle) and external aerodynamic studies of the propulsion airframe integration characteristics of all types of flight vehicles in the subsonic and transonic ranges. Because the configuration of the present wind tunnel is the result of several major revisions, a brief description of the revisions is presented.

The original wind tunnel was designed and built during the expansion period of the National Advisory Committee for Aeronautics (NACA) prior to World War II and was put into operation in November 1941 as the Langley 16-foot high-speed tunnel. An exterior view, taken in 1948, of the facility is shown in figure 1(a), and an artist sketch is shown in figure 1(b). This wind tunnel had a closed, circular test section that was 16 ft in diameter with a maximum test section Mach number of 0.71. Power was provided by two 8000-hp electric motors mounted in the return passage. The drive motors were directly coupled to counterrotating fans operating in tandem at the extremities of the motor nacelle. The wind tunnel was cooled by air exchange. The control room was located in the test-section plenum and was operated at test-section pressure.

The facility was designed and used primarily for aircraft engine cooling and cowling tests and for investigation of the aerodynamic characteristics of full-scale propellers, as typified by the work of references 1 and 2. No description and calibration report was prepared for the original wind tunnel.

The need for increased air speed capability led to a major redesign of the original tunnel over a period of several years prior to 1950. During this time, the NACA developed the slotted-wall transonic test section (refs. 3 and 4), which was selected for the revised tunnel. Major revisions in the modification consisted of an octagonal slotted transonic test section, a 60 000-hp drive system with two counterrotating fans, a new control room, air filters in the air exchange system, and acoustical treatments. The repowered facility, designated the Langley 16-Foot Transonic Tunnel, was placed in operation on December 6, 1950 and is shown in figure 2.

A description of the wind tunnel and its calibration to a maximum Mach number of 1.08 is presented in reference 5. The modified tunnel was redesigned to study propeller aerodynamics at supersonic speeds (ref. 6) and jet effects on aircraft performance. A propulsion simulation system that used a hydrogen peroxide monopropellant system (ref. 7) was developed and utilized extensively until about 1965. This system was then replaced with one that uses high-pressure air.

After repowering of the tunnel in 1950, the need for a further increase in maximum speed became apparent. For the Mach number range from 1.03 to 1.10, shock waves were generated at the nose of a model and reflected from the test-section walls back to the model and frequently resulted in force measurements, especially drag, which were not representative of free-flight conditions. In addition, the rapid development of aircraft and missiles with supersonic speed capability and the necessity for aircraft, reentry vehicles, and spacecraft to negotiate the transonic speed regime emphasized the importance of experimental aerodynamic research at transonic speeds. Design studies, such as that reported in reference 8, indicated that test-section air removal was

the most economical method for extending the test-section air speed to a low supersonic value.

A revision of the Langley 16-Foot Transonic Tunnel added a compressor driven by a 36 000 hp motor. This compressor is capable of removing about 4.5 percent of the tunnel mass flow from the test section and surrounding plenum and exhausting it to the atmosphere. The wind tunnel with this test-section air removal system was placed in operation on March 9, 1961 and a maximum test-section Mach number slightly greater than 1.30 was achieved. The calibration of the facility with air removal was initially conducted from March to June of 1961. During this time, slot shape 26 was developed from slot shape 18. Further refinements to slot shape 26 were made in 1963 and 1965 that resulted in slot shape 29, which is the current slot configuration. The results of these three calibrations are in reference 9.

A major rehabilitation of the facility occurred in 1977 in which new fan blades, tunnel controls, and associated control room equipment were installed. In addition, an on-site data acquisition and a computer system were installed. Following this rehabilitation, a calibration of the wind tunnel was performed in October of 1977, which essentially repeated the results of the 1965 calibration.

From mid-1989 to 1990, several significant modifications that could affect the test-section flow characteristics were made to the 16-Foot Transonic Tunnel. These modifications included installation of a new model support system with increased blockage, new fan blades, and a catcher screen installed on the first set of turning vanes. In addition, a new data acquisition system, a computer system, and process controllers to control tunnel speed, model attitude, and jet flow for powered models were added. Following this addition, the wind tunnel was again calibrated in the fall of 1990.

This report presents a complete description of the Langley 16-Foot Transonic Tunnel (from ref. 9), its auxiliary equipment, a description of the calibration procedures, and the results of the 1977 and 1990 wind tunnel calibrations with test-section air removal. Comparisons are made with the previous calibrations to provide a sense of continuity with respect to the aerodynamic performance of the wind tunnel. In addition, information required for planning experimental investigations and the use of test hardware and model support systems is provided.

Symbols

d_{eq} equivalent diameter, ft
 dM/dx Mach number gradient, per foot

dpr/dx pressure ratio gradient, per foot
 H equivalent pressure altitude, ft
 M Mach number
 M_l test-section Mach number from least-squares fit of centerline Mach number data from left side of centerline tube
 M_r test-section Mach number from least-squares fit of centerline Mach number data from right side of centerline tube
 N motor rotational speed, rpm
 P motor power, MW
 P_{sh} motor shaft power, hp
 p static pressure, psi
 \tilde{p} rms value of fluctuating component of static pressure, psi
 p_a ambient pressure, psi
 p_t stagnation pressure, psi
 q dynamic pressure, psi
 R gas constant; for air, 1716 (ft²/sec²)/°R
 R_e Reynolds number, per foot
 $R_{e,t}$ transition Reynolds number
 r/R fraction of radial distance from tunnel centerline to slot centerline
 s_w slot half-width, in.
 T_a ambient temperature, °F
 T_{dp} dew point, °F
 T_t stagnation temperature, °F
 U_∞ free-stream velocity, ft/sec
 \tilde{u} rms longitudinal velocity component of local flow, ft/sec
 v_p 10-ft valve position, percent open
 x axial distance, ft
 y_{probe} survey probe distance from centerline in vertical direction, ft
 y_{wall} distance measured from tunnel wall, in.
 z_{probe} survey probe distance from centerline in lateral direction, ft
 α_u upflow angle, deg
 β_s sideflow angle, deg
 ΔC_p fluctuating-pressure coefficient, $(\sqrt{\tilde{p}})/q_\infty$, percent
 γ ratio of specific heats; 1.4 for air
 δ_{flat} test-section wall divergence angle with respect to tunnel centerline, min

ϕ	survey rake roll angle, deg
2σ	standard deviation of Mach number
σ_{\max}	maximum deviation of Mach number
Subscripts:	
ave	average of Mach numbers measured at right and left sides of centerline tube
<i>bl</i>	boundary layer
<i>c</i>	corrected
cal	calculated
comp	compressor motor
<i>l</i>	parameters measured on left side of centerline tube
<i>lo</i>	local
<i>m1</i>	main drive motor 1
<i>m2</i>	main drive motor 2
probe	flow-angularity probe
<i>r</i>	parameters measured on right side of centerline tube
tank	measured in test-section plenum
tot	total
<i>wt</i>	power input from two main drive motors
∞	free stream

Abbreviations:

AMES	Ames Research Center
AEDC	Arnold Engineering and Development Center
CTSL	calibrated test-section length
ESP	electronically scanned pressure system
FM	frequency modulation
LaRC	Langley Research Center
MPA	model preparation area
NACA	National Advisory Committee for Aeronautics
NASA	National Aeronautics and Space Administration
rms	root mean square
SRB	shock reflection body
TS	tunnel station, ft
4T	4-foot transonic tunnel at AEDC
8-ft TPT	The Langley 8-Foot Transonic Pressure Tunnel
11TWT	11-foot transonic tunnel at AMES
16-ft TT	The Langley 16-Foot Transonic Tunnel

Wind Tunnel Description and Support Equipment

General Arrangement and Aerodynamic Characteristics

The Langley 16-Foot Transonic Tunnel is a single-return atmospheric wind tunnel with a slotted transonic test section. An exterior view of the facility is shown in figure 2(a) and a phantom view (without air removal equipment) in figure 2(b). The major components of the wind tunnel are presented in the schematic diagram in figure 3. Starting at TS 0, these components are the quiescent chamber, entrance cone, test section, diffuser, power section, return passage, and air exchange section. The maximum inside diameter of the quiescent chamber of the tunnel is 58.0 ft and the length of the tunnel circuit along the centerline is 930 ft. (Note that TS 0 = TS 930.00.) The test section is a regular octagonal cylinder with a cross-sectional area slightly less than that of a 16-ft circle. The top half of the entire test section is removable. Four sets of turning vanes are located at the 90° elbows in the tube. The tunnel has three screens; one is in the air exchange section, another is in the quiescent chamber, and one is on the first set of turning vanes. The test-section air removal equipment is located outside the tunnel between the diffuser and the return passage. The axial locations and the dimensions of the major components of the wind tunnel are given in table 1.

The variation of test-section airstream aerodynamic parameters, which include Reynolds number per unit length, air stagnation temperature, static pressure, dynamic pressure, and equivalent pressure altitude with Mach number is presented in figure 4.

Quiescent Chamber and Entrance Cone

A photograph of the quiescent chamber from the end of the entrance cone is shown in figure 5. The dimensions of these two components provide a contraction ratio of 13.3:1 from the large end of the wind tunnel to the test section. At test-section Mach numbers above 1.0, the average air speed in the quiescent chamber is 54 ft/sec. This low velocity region downstream of the antiturbulence screen permits further decay of residual turbulence prior to acceleration of the airstream through the entrance cone and into the test section. The entrance cone incorporates a transition from circular to octagonal cross sections and includes a slowly converging entrance liner that terminates at the upstream end of the test section.

Test Section

General description. A schematic arrangement of the test section with the centerline calibration tube installed is presented in figure 6. Views of the test section with research models are shown in the photographs of figure 7. Figure 7(a) is a view looking forward to the quiescent chamber, while figure 7(b) is a view looking aft toward the diffuser. A view looking down with the top half of the test section removed is shown in figure 7(c). The geometric throat of the test section is located at TS 107.00. The cross section of the throat is a closed regular octagon with an area of 199.15 ft². The test section and diffuser entrance, which are the portions of the wind tunnel that have variable geometry, extend from TS 107.00 to TS 154.00, as indicated in figure 6. These sections, which are also octagonal but opened at the corners (slots), have cross-sectional areas that vary with test-section wall divergence. The feature that gives the wind tunnel transonic capability is the venting of the test section to the plenum. In this tunnel, the vents are eight longitudinal slots that are located at the intersections of the wall flats and provide a 3.9-percent open periphery. The plenum is a sealed tank 32 ft in diameter, which encloses the test section and the diffuser entrance.

Test-section walls. The test-section wall is made up of eight longitudinal flats symmetrically located about the tunnel centerline. For convenience, the flats are numbered in clockwise order for a viewer looking upstream with number 1 on the lower left as shown in figure 6. The surface of each flat is a continuous machined steel plate that is located from TS 107.00 to TS 154.00 with a width of 66.50 in. As seen in figure 8(a), long metal strips are attached to the sides of each of the flats to form the longitudinal slots. The steel plates that form the walls are attached rigidly to the tunnel structure between TS 107.00 and TS 110.00. Each flat is rigidly supported by a main truss and strongback between TS 114.00 and TS 138.00 and by a second truss and strongback between TS 140.00 and TS 154.00. (See figs. 7(c) and 8.) The combination of the machined steel plates and truss and strongback structural system was chosen to keep the tunnel walls as flat as possible. The trusses are attached to the tunnel structure by flexure plates at TS 112.00 and TS 154.00 and are jointly supported at TS 138.00 by an actuator that provides radial motion with respect to the tunnel centerline. These plates have flexural regions centered at TS 112.00 and TS 139.00 and a sliding joint at TS 154.00, where a sealed transverse gap varies with wall divergence. The eight wall divergence actuators are interconnected and are driven by a single electric motor. When the test-section walls are diverged, bending takes place between TS 110.00 and TS 114.00 and between TS 138.00 and TS 140.00. Wall divergence angle is mea-

sured as the angle between the tunnel centerline and the rigid portion of the wall from TS 114.00 to TS 138.00. The bending that occurs between TS 138.00 and TS 140.00 and the upstream portion of the diffuser starts at an angle of 2.75° to the tunnel centerline. As divergence increases, the wall bending between TS 138.00 and TS 140.00 decreases and the divergence angle of the diffuser entrance decreases. Actuation is provided for a maximum angular divergence of 0°45'.

Transonic slots. The test-section transonic slots, which are located at the intersections of the wall flats, are eight longitudinal openings that are generally parallel to the tunnel centerline. These slots provide vents between the test-section airstream and the plenum that surrounds the test section. The slot width or opening is nominally zero between TS 107.00 and TS 107.50. Each slot starts at TS 107.50 and extends to TS 154.00, but is closed by the diffuser entrance vanes between TS 141.40 and TS 154.00. Some structural details of the wall flats and the slots are shown by the sectional views of figures 6 and 8(a). The slots are shown in the photographs in figure 7. The planform of slot shape 29 is given in figure 8(b). A discussion of slot shape development is presented in the section entitled "Slot Shape Studies."

Longitudinally, the major portion of each wall is made of a single steel plate that extends from TS 107.00 to TS 154.00. In cross section, however, the construction is composite. Each edge of a flat is trimmed with a strip that carries a skirt that is 24 in. wide normal to the plane of the flat (fig. 8(a)). The adjacent skirts form a channel with walls mutually inclined at 45° that is completely open to the plenum. At the test-section wall, the edges of these skirts form a basic rectangular slot with a half width of 5.207 in. The actual slot shape is determined by the contour of the slot edge strip, which is effectively an extension of the flat in width, as shown in figure 8(a). The slot half widths (table 2) are measured in the plane of the flat surface from the edge of the flat to a line normal to the intersection of two adjacent flats when the wall divergence angle is zero.

Diffuser entrance vanes. The purpose of the diffuser entrance vanes and lips is to reintroduce the low energy axial flow that exists in the plenum adjacent to and at the downstream end of the slots into the tunnel airstream. The diffuser entrance vanes and lips shown in figure 9 are integral. They are adjustable as a unit to form a part of the tunnel wall that closes the openings between the plenum and the airstream in the region where the downstream end of the slots would otherwise extend into the diffuser. The slot width increases abruptly just ahead of the diffuser near TS 140.00, so that in plan view, the leading edge of the diffuser entrance lip at TS 141.40 is

16 in. wide. The vane width increases linearly with distance downstream to a value of 21 in. at TS 154.00. In the longitudinal section, the vanes are flat between TS 143.00 and TS 154.00, and the lips are deflected 20° away from the tunnel centerline between TS 141.40 and TS 143.00 to form scoops that extend into the plenum. The diffuser entrance with vanes and lips installed is shown in figure 7(c) and figure 9. The vanes are hinged at TS 153.33 to permit angular motion in a radial plane with respect to the tunnel centerline. Each vane is individually supported by an adjustable strut that connects the underside of the vane to the plenum wall near TS 144.00. When the flats are diverged, the approximately parallel walls of the channel in which the diffuser entrance vanes are installed separate laterally and thereby create a channel of greater width. The sealing of the vane edges is maintained by spring loaded blocks that take up the change in width as the flats are diverged. Vane setting is specified as depth of the entrance lip leading edge into the plenum and is measured from and normal to the plane of the flat surface at TS 141.40. (See fig. 9.) Sealing the vane edges and rear at TS 154.00 was found to reduce tunnel power (ref. 9).

Overview of main model support system. The main model support system that is used in the wind tunnel is shown in figure 10. The part of the support strut exposed to the airstream is a cast steel circular-arc segment surmounted by a short straight swept strut. At its upper end is the strut head, which is a cylindrical body 113.52 in. long, 21.0 in. in diameter, and it is terminated downstream by a hemispherical tail cone. At angle of attack of 0°, the strut-head centerline is coincident with the tunnel centerline. The support strut penetrates the tunnel floor (flat 8) in the diffuser entrance region through an unsealed opening and moves on a circular-arc track within a pressure box that is in the plenum. The support system moves in a vertical plane containing the tunnel centerline with the center of rotation at TS 134.00. The support system provides an angle-of-attack range from -9° to 24°. Lateral aerodynamic force tests can be done by remotely rolling the model from -90° to 90° and traversing the main tunnel support in the vertical plane. Depending on the nature of the investigation, various methods are available for mounting models to the model support system in the test section. Further details on the model support system are presented in the section entitled "Wind Tunnel Test Capabilities."

Windows and access hatches. Two windows 6 ft long and 3 ft high are centered at TS 134.00 in wall flats 2 and 6. (See fig. 6.) In line with these windows are others of equal size in the walls of the plenum. The windows are used primarily for model observation and flow visualization. A laser velocimeter system is located in the

test-section plenum behind a window made of BK-7 (borosilicate crown glass) in flat 2. However, when the laser velocimeter is not in use, this window is replaced by a steel plate. A window 1.5 ft long and 1 ft wide is located in the ceiling (flat 4) at TS 136.00 and is used for observation and recording of flow patterns on a model that are defined by tufts, oil, dyes, or pressure-sensitive paint.

The model installation hatch for this wind tunnel was made unusually large to permit free use of the hoist required for handling heavy models. The upper 3/8 of the plenum together with the upper three flats (flats 3, 4, and 5) can be raised as a unit and stowed overhead to permit free movement of a 15 ton traveling hoist over the entire control room and test-section area. The open hatch is 15.5 ft wide and 52 ft long and extends from TS 106.00 to TS 158.00. The length upstream avoids transverse cuts in the test-section wall in the region of supersonic flow. A view of the test section with the upper hatch open is shown in figure 7(c). Quick access walk-through hatches are located as follows: one in the floor of the tunnel wall downstream of the plenum at TS 163.00, which leads to the test section and one on each side of the plenum, which leads to the region surrounding the test section.

Diffuser

The diffuser extends from the downstream end of the test section to the power section and is shown in figure 11. Because the diffuser entrance, which begins at TS 138.00, includes the diffuser entrance vanes, the cross section of the tunnel in this region has 16 sides and variable geometry. Downstream of TS 154.00, the diffuser geometry is fixed except for expansion joints. The diffuser half angle is 6°. The diffuser decelerates the airstream after it passes through the test section, and thereby, converts as much kinetic energy as possible into pressure energy.

Power Section and Drive Fans

General arrangement. The drive end of the wind tunnel has a constant diameter of 34 ft, and the power section includes two 90° elbows, which incorporate the first and the second sets of turning vanes. The major components of the tunnel drive end are indicated in figure 3. The two main drive motors, which are housed outside the tunnel, are each connected directly to one of the drive fans by a 60-ft-long shaft. The drive shafts are enclosed in a streamlined fairing between the tunnel wall and the fan-hub enclosure. Quick access to the shafts and the hubs is provided by rail cart through these fairings. The fan-hub enclosure, which also houses the bearing pedestals for both units, has a streamlined shape with a

maximum diameter of 20 ft near the fan stations. The leading edge of this enclosure is just downstream of the first set of turning vanes at TS 354.00. Downstream of the fans, however, gradual tapering of the afterbody is required which results in a conical fairing that extends downstream of the second set of turning vanes. This conical fairing, shown in figure 12, has a 90° elbow at the turning vanes to maintain its alignment with the airstream and terminates at TS 500.30.

Electric motors. The two main drive electric motors have wound rotors. Each is rated for continuous operation at 23 000 hp (17.16 MW) at a rotational speed of 340 rpm, for 2 hr of operation at 30 000 hp (22.38 MW) at 366 rpm, and for 1/2 hr of operation at 34 000 hp (25.36 MW) at 372 rpm. The rotational speed of the motors is controlled by a modified Kramer system, which permits continuous variation of speed from 60 rpm to 372 rpm. A photograph showing one of the motors is presented in figure 13.

Drive fans. The drive fans constitute a two-stage axial-flow compressor with two sets of counterrotating blades and no stator blades. A photograph of the drive fans and the tunnel interior in this region is shown in figure 14. The fans are 34.0 ft in diameter less 0.2 in. radial clearance between blade tip and tunnel wall. The fan blades are made of laminated sitka spruce with frangible foam tips. The upstream fan has 25 blades and the downstream fan has 26 blades. The blades have Clark Y airfoil sections and the average solidity of each fan is about 0.8. The adiabatic efficiency of the fan system is 96 percent. The aerodynamic design of the fan blades is based on the procedures outlined in reference 10. The axial space between the two fan hubs is occupied by a floating spinner 8.0-ft long and 20 ft in diameter, which represents a continuation of the shaft enclosure contour. This spinner is supported on bearings housed in the ends of the fan drive shafts and is restrained from rotating by four small rods.

Return Passage

The return passage upstream of the air exchange section is a large conical diffuser and downstream, a cylinder (fig. 3). Dimensions of these components are given in table 1. The return passage primarily ducts reenergized air from the power section through the air exchange section back to the quiescent chamber. Air velocities throughout the return passage are too low to yield much pressure recovery in the diffuser portion of the return passage. The cylindrical portion has two 90° elbows, which incorporate the third and fourth sets of turning vanes.

Air Exchange Section

The air exchange section cools the wind tunnel airstream and scavenges exhaust gases when operating engines are under investigation in the test section. All energy expended through the main drive fans is eventually converted into heat, which elevates the airstream temperature. With no cooling of the wind tunnel during operation at high power, the airstream temperature would increase rapidly to levels that would exceed 175°F, which is the temperature limit imposed by the wooden fan blades.

In most high-speed wind tunnels, the airstream is cooled by a water-cooled heat exchanger. An important advantage of this method of cooling is that the wind tunnel may be a closed circuit and charged with dry air to avoid condensation. However, the original Langley 16-foot high-speed tunnel was designed primarily for investigation of propulsion system effects on airframe aerodynamic characteristics. Investigations of propulsion system effects (refs. 2 and 11) frequently entail the operation in the test section of real engines emitting hot and toxic exhaust gases that must be scavenged continuously from the wind tunnel airstream. The process of cooling by air exchange allows exhausting a part of the wind tunnel airstream that has become heated and may contain exhaust gases. The heated air is replaced with cool ambient air.

The air exchange section that performs this function is shown in figures 1(b) and 2(b). A photograph looking downstream from inside the return passage (fig. 15) shows the air exchange exhaust openings in the foreground, which duct the heated boundary-layer air out of the wind tunnel circuit and into the exchange tower. Farther downstream, the inner surfaces of the intake louvers may be seen, and in the far background are the third set of turning vanes. The air exchange section is basically a constriction in the return passage with exhaust and intake openings located, respectively, upstream and downstream of the constricted cross section. Both exhaust and intake openings are essentially annular and have 36 segments equipped with adjustable louvers. The interconnected intake louvers are manually adjustable and are generally left in an open position. The interconnected exhaust louvers are mechanically actuated, and heated air exhaust is quickly adjusted during a test for partial control of airstream stagnation temperature. Air exchange can be varied between 5 and 20 percent of the tunnel mass flow. When test-section air is removed, the air exchange intake mass flow exceeds the exhaust by the amount being removed from the test-section plenum. The air exchange section is housed in a rectangular tower with baffles that duct the heated exhaust out of the top of the tower while cool air is taken in at the sides near the

top. Dust is removed from the intake air by filters. In both intake and exhaust, acoustic baffles are used to attenuate noise.

Screens

The circuit of the 16-Foot Transonic Tunnel has three screens. Two antiturbulence screens each composed of a single layer of square mesh woven wire, are installed in the tunnel. One screen is installed in the air exchange section at TS 747.20 and the other is in the quiescent chamber at TS 2.30 (fig. 3). In addition to reducing turbulence, the screen in the air exchange section also increases the effectiveness of the air exchange by creating a slight pressure drop between exhaust and intake. A catcher screen was installed at the first set of turning vanes in 1990 and is shown in figure 16. The purpose of this screen is to stop most of the debris that may occur due to failures and prevent it from striking the fan blades. The dimensions and characteristics of the screens are shown in the following table.

Screen characteristic	Quiescent chamber	Air exchange section	Catcher screen
Axial station, ft	2.3	747.2	349.1
Diameter, ft	58.0	56.0	34.0
Wire diameter, in.	0.054	0.080	0.105
Wire centerline spacing, in.	0.167	0.444	1.000
Solidity, in.	0.560	0.325	0.190
Pressure loss, p/q units	2.500	0.650	0.370

Air Removal System

Arrangement and function. The general arrangement of the test-section air removal equipment with respect to the wind tunnel is shown in figures 2, 3, and 17. The air removal system consists of a large motor-driven axial-flow compressor that removes low energy air (up to 4.5 percent of test-section mass flow) from the plenum surrounding the test section and discharges this air to the atmosphere.

Test-section air removal is used to obtain low supersonic speeds in a transonic wind tunnel. As indicated in reference 3, properly sized longitudinal slots in a test-section wall and the plenum around the test section serve to reduce or eliminate solid blockage of a model, and thereby, permit tests of the model at sonic speed without choking the airstream at the station of model maximum cross-sectional area. By application of sufficient tunnel drive power and by providing a sufficiently low static pressure at the diffuser entrance in relation to the local

supersonic flow on the curved wall between test section and diffuser, it was found that low supersonic speeds could be established in the test section. The low static pressure in the vicinity of the diffuser entrance is transmitted through the slots at their downstream end and into the plenum. Thus, a low static pressure corresponding to a supersonic speed is established in the plenum. Because air in the plenum is relatively stagnant, the low pressure in the plenum is exerted directly through the slots and the test-section boundary layer to the test-section airstream along the full length of the slots. The result is an expansion of a portion of the test-section airstream through the slots into the plenum and, when airstream velocity is sonic at the upstream end of the test section, supersonic speeds are established throughout the length of the test section. The air that flows from the test section into the plenum loses most of its kinetic energy in the process. With no test-section air removal, this low energy air is reintroduced into the tunnel airstream at the diffuser entrance and causes further energy loss by reducing the effectiveness of the diffuser. In this case, the tunnel main drive is required to overcome the energy losses in the test section because of slot mixing and a terminal shock, as well as increased diffuser losses, friction, and turbulence losses in the remainder of the wind tunnel. Thus, without test-section air removal, the maximum supersonic speed in a slotted or vented test section is limited by the power of the tunnel main drive. Without air removal, the maximum Mach number in the 16-Foot Transonic Tunnel was 1.08.

For test-section air removal, the compressor is sized to pump stagnant air from the plenum and exhaust it to the atmosphere. The pressure difference and compressor mass flow are determined by the test-section Mach number and air state. The compressor pumping redirects the slot mixing losses and some of the tunnel skin-friction loss because boundary-layer air is removed. The tunnel main drive, which is aided by this quasi-boundary-layer control is only required to overcome the normal friction and turbulence losses of the wind tunnel and the test-section terminal shock. Therefore, in a slotted wind tunnel test section, less total power is required to achieve a specified low supersonic speed when power is applied partly in the main drive and partly in the test-section air removal system than when all the power is applied through the main drive. For example, to achieve a Mach number of 1.3 without an air removal system, the installation of two new 60 000 hp drive motors would be required for the compressor. The current air removal system only needs a 35 000 hp drive motor for the compressor. Therefore, a Mach number of 1.3 is achieved in the wind tunnel with an expenditure of 113 000 hp rather than 120 000 hp.

Compressor. The air removal compressor is a nine-stage axial-flow compressor rated as follows:

Total-pressure ratio	3.33
Inlet volume flow	956 000 ft ³ /min
Rotational speed.....	2290 rpm
Inlet pressure.....	4.7 psia
Inlet temperature	120°F
Power	36 000 hp (27 MW)
Mass flow	11.65 slug/sec
Throat area	36.6 ft ²

The compressor is shown in figure 18(a) and the compressor blades are shown in figure 18(b). The normal operating range is between 80 and 100 percent of rated speed.

Electric motor. The compressor is driven by a wound rotor induction motor through a gear box. The drive and pinion gears have 328 and 79 teeth, respectively. These gears have a ratio of compressor to motor speed of approximately 4.15. The motor rating is 36 000 hp (27 MW) at 552 rpm. Speed is controlled by a slip regulator that incorporates a brine tank rheostat.

Valves and controls. The compressor inlet consists of a dual-passage manifold with protective screens and bell mouth. The manifold air passages consist of a central pipe with a 12-ft diameter that leads from the test-section plenum and is surrounded by the wall of the manifold, which has an 18-ft diameter that forms an annular passage as indicated in figure 17. The annular passage also receives the air taken in through the surge control valve and distributes this air to the compressor. The dual-passage manifold was arranged to minimize the generation of turbulence when flows from separate sources mix ahead of the compressor inlet.

The surge control valve, which is located on top of the compressor inlet manifold, is a hydraulically actuated butterfly valve with a 4-ft diameter. Because surge pressure ratio varies with rotational speed, the electronic component of the control accepts feedback signals from a compressor drive tachometer and a pressure transducer in the inlet manifold. These signals are combined through a servo that maintains the surge control valve position. The valve position is maintained at compressor rotational speeds from 80 to 100 percent of rated speed to ensure a safe margin between maximum operating and surge pressure ratios. To prevent surging at speeds below 80 percent of rated speed, an overriding or surge limit control causes the valve to move to the full open posi-

tion. During operation of the wind tunnel at near maximum air speed, the surge control valve remains closed. An additional remotely operated 4-ft-diameter relief valve is provided for emergency control.

The flow of air from the test section to the compressor is controlled by a 10-ft-diameter hydraulically actuated butterfly valve located in the air removal duct just outside the test-section plenum, as indicated in figure 17. This valve can be controlled either automatically to maintain preselected values of compressor pressure ratio as a function of rotational speed, or manually to maintain compressor inlet suction pressure at any value less than that established by the surge control.

Wind Tunnel Support Areas

Control room. The control room is located on the second floor of the wind tunnel building in an area that is behind and below flat 6 of the test section. All functions associated with a test, such as tunnel air speed, model attitude, and compressed air for propulsion tests are controlled from this room. A schematic of the control room floor plan is presented in figure 19(a) and a photograph of the current control room is shown in figure 19(b). Depending on the test, three or four operators are required for operation. All the computer systems necessary for tunnel operation, data acquisition, and off-line data processing are also located within this room.

Model preparation area. The model preparation area (MPA) allows pretest buildup and complete calibration of propulsion models. The MPA consists of two rooms, which comprise a calibration bay area with a 10.75-ft-high ceiling (fig. 20(b)) and a control room (fig. 20(a)). The area is completely enclosed, and thus, provides physical security for most test requirements. The MPA is located within the wind tunnel building underneath the wind tunnel at about TS 80.00.

A model support system, which can be seen in figure 20(b), has an attachment station that is identical to that of the wind tunnel at TS 141.94 and accepts standard model mounting systems. (See "Main Model Support System" section.) A pitch drive system allows for $\pm 5^\circ$ of movement. Roll angle is provided by a manual system. Dual 1800 psi air supply systems can provide two independently controlled 15 lb/sec flows to the model. The jet exhausts to atmosphere through a vent aft of the test apparatus. Duplicate instrumentation, data acquisition, and data reduction provide the same capabilities for the model preparation area as provided for the 16-Foot Transonic Tunnel. The MPA computer and the data acquisition system are located in the control room of the tunnel as indicated in figure 19(a).

Measurements and Instrumentation

Wind Tunnel Reference Measurements

The two wind tunnel reference pressures are the airstream stagnation pressure and the plenum static pressure. Airstream stagnation pressure is measured by four shielded total-pressure probes mounted on a cruciform support as shown in figure 21. Also visible in this photograph is the antiturbulence screen in the quiescent chamber. The probes are located 2.0 ft downstream of the antiturbulence screen at TS 4.30 and each is 1.5 ft from the tunnel centerline. The plenum static-pressure (referred to as tank pressure) orifices located at TS 110.50 in the plenum wall behind flats 2, 6, and 8, are completely open to the plenum interior, but are protected from air gusts by adjacent tunnel structure. Both stagnation and tank (plenum) pressures are measured with Ruska model 6010 digital pressure gages, which have a fused-quartz bourdon tube transducer with a digital readout. Another set of Ruska model 6010 pressure gages are used as a backup system. The accuracy quoted by the manufacturer for the gages is given in table 3.

Airstream stagnation temperature is measured with platinum resistance temperature probes located on the fourth set of turning vanes at four points near the tunnel centerline. Dew point is measured with a condensation mirror dew point indicator that continuously samples air from the quiescent chamber of the wind tunnel. The indicator is located on the fourth set of turning vanes near the centerline of the tunnel. The mirror temperature (dew point) is measured with a platinum resistance thermometer. The accuracy quoted by the manufacturer for the platinum resistance thermometers is given in table 3.

Centerline Tube Static Pressures

Test-section steady state conditions during the calibration of the wind tunnel are primarily determined by a centerline survey tube shown in figures 3, 6, and 22. This tube has a 4-in. diameter and extends from TS 74.50 in the entrance cone to TS 141.50 at the downstream end of the test section where it is fastened into the strut head shown in figures 6 and 22(a). The upstream end of the centerline survey tube is supported by eight cables that are anchored to the tunnel shell and exert both tension and bending on the tube (fig. 22(b)). In the vicinity of the supporting cables, airstream Mach number never exceeds about 0.35. Deflection of the tube under its own weight results in an angle between the tube axis and the tunnel centerline that does not exceed 1° . Maximum deflection of the tube occurs at about TS 112.00. Between TS 127.00 and TS 138.00, the tube incidence angle is less than 0.1° .

The survey tube was originally instrumented with 54 static-pressure orifices that had 0.020-in. diameters. The orifices are located from TS 100.25 to TS 140.00 and spaced 9.0 in. apart. These orifices lie on the left side of the tube surface (looking upstream) 90° from the vertical plane that contains the tube axis. This location minimizes the effects of tube curvature on the tube surface pressures. Prior to the 1977 calibration, an additional 37 static-pressure orifices were installed on the right side of the centerline tube. These orifices are located from TS 129.00 to TS 140.00 and have 6.00 in. spacing from TS 129.00 to TS 131.00 and TS 138.00 to TS 140.00. The spacing between orifices is 3.00 in. from TS 131.00 to TS 138.00. The axial locations of the orifices on both the right and the left sides of the survey tube are given in table 4. All static pressures on both sides of the centerline tube are measured with electronically scanning pressure devices, which acquire data in less than 0.1 sec (accuracy given in table 3). In addition, static pressures from TS 129.00 to TS 140.00 on the right side and pressures from TS 129.50 to TS 137.50 on the left side are also measured with individual pressure transducers (accuracy given in table 3).

Wall Static Pressures

Static-pressure orifices are also provided on the test-section wall flat 1, as shown in figure 6. The orifices lie 6 in. above the centerline of flat 1. The orifices have 0.020-in. diameters with centers spaced 6 in. apart axially from TS 95.50 to TS 153.50. This row of static orifices extends into the diffuser to TS 320.00 and has axial spacings of 2 ft, 6 ft, and 12 ft. The axial locations of the orifices on the test-section wall and diffuser are given in table 4(b). All the wall and the diffuser static pressures are measured with electronically scanning pressure devices.

Boundary-Layer Pressures

Boundary-layer pressures are determined with a 14-probe total-pressure rake as shown in figure 23. This rake was located on flat 7 at TS 133.00. These pressures are measured with individual pressure transducers.

Flow Field Survey Measurements

Survey rake. Flow field survey measurements were made with either flow-angularity or fluctuating-pressure probes located along the leading edge of a survey rake as shown in figure 24(a). The survey rake was mounted on an offset sting, which allowed the rake to be positioned at selected tunnel stations. The sting was mounted on the main tunnel strut head, which provided the capability to roll the rake assembly with the strut-head roll mechanism. A photograph of the survey rake with

flow-angularity probes installed in the 16-Foot Transonic Tunnel is shown in figure 24(b). The tests to determine test-section flow angularity and pressure fluctuation characteristics were conducted during 1991.

Flow angle measurements. Flow angle measurements were made with five-hole pyramid-head flow-angularity probes. The five probes were equally spaced at 14-in. intervals on the survey rake, which provides a maximum survey radius of 28 in. about the tunnel centerline. A sketch of an individual probe is shown in figure 24(c). Each probe was instrumented with four static orifices, one on each face of the pyramidal tip, and a total-pressure orifice at the probe apex. Individual pressure transducers were used to measure the probe static pressures, the pressure difference between opposing pressure orifices, and the probe stagnation pressure. Two orthogonal flow angles were measured with each probe; the flow angles were proportional to the pressure difference between the opposing pressure taps. The probes were calibrated in the wind tunnel. Further details concerning these measurements and probe calibration techniques are found in reference 12.

Fluctuating-pressure measurements. Fluctuating-pressure measurements were made with either static or total fluctuating-pressure (acoustic) probes. Two acoustic static-pressure probes were equally spaced at 28-in. intervals on the survey rake about the tunnel centerline and provided a maximum survey radius of 28 in. about the tunnel centerline. A third acoustic probe was located on the centerline. A sketch of an individual probe is shown in figure 26(d). A total-pressure probe was located 21 in. below the centerline of the tunnel. Each probe was instrumented with a 5-psid fluctuating-pressure probe and was calibrated both in place and outside the wind tunnel test section.

Hot Wire Measurements

Turbulence measurements with hot wires were made in two locations in the quiescent chamber of the wind tunnel during 1992. These measurements were made near the tunnel centerline and wall just downstream of the turbulence screen at about TS 10.00. A hot wire holder was mounted on a 10-ft-long piece of pipe that had a 3-in. diameter. This pipe was suspended by wire ropes and was located 3 ft below the wind tunnel centerline so it did not interfere with the probes that were used to measure total pressure. This installation is shown in figure 25(a). A hot wire was also attached to a 6-ft-long steel pipe that was mounted to the floor of the wind tunnel as shown in figure 25(b). The two channels of the hot wire data were amplified and recorded on FM tape. A

block diagram of the hot wire data acquisition system is presented in figure 25(c).

Data Acquisition System

All data were digitized and then recorded simultaneously on magnetic tape. Approximately 50 frames of data at a rate of 10 frames per sec were taken for each data point; average values were used in data reduction computations. In addition to the aforementioned pressure and temperature measurements, flat divergence angle, all motor rotational speeds and powers, and valve positions were also recorded.

Test-Section Development and Calibration Procedure

Slot Shape Studies

The test-section wall and slot configuration have primary control of the flow conditions for the test model. Because of this well recognized fact, considerable study and effort has been expended in the development of the slot configuration after both the installation of the first slotted test section in 1950 and the installation of the air removal system in 1961. After the slot shape was chosen in 1961, the test-section flow conditions were examined with respect to the effects of test-section wall divergence angle, tunnel drive power, moisture content in the tunnel airstream, model blockage, shock reflection, and several other smaller related effects.

Development of slot shape 18. When the Langley 16-foot high-speed tunnel was repowered and converted from a high-speed wind tunnel to a transonic wind tunnel in 1950, the objective of the slot shape development at that time was to minimize test-section wall interference that was related to model solid blockage near sonic speeds. The results of slotted-tunnel flow-uniformity investigations presented in references 4 and 13 indicated that the slot-entrance planform design was particularly important to the development of uniform supersonic flows. Reference 13 also indicated that large wall divergence angles apparently exerted a predominate influence on the development of low supersonic flows and resulted in flow unsuitable for model tests. Slot shape planform and wall divergence angle, which were conveniently made variable in the redesigned wind tunnel, were studied in some detail in reference 5.

Six slot shape planforms were investigated during the initial operation of the tunnel. Slot shapes 1, 9, and 11 that correspond to and are numbered the same as the most promising slot shapes tested in reference 13 were investigated. Three additional shapes, arbitrarily numbered 16, 17, and 18 were also tested. Planforms of the

slot shapes that were tried during this calibration are shown in figure 26(a). Studies by Wright and Ward (ref. 3) indicated that an open porosity of about 12 percent of the test-section periphery would be near optimum for an eight-slot octagonal test section. The theory of Goethert (ref. 14) showed, however that for $M = 1.0$, the slot width should be about half that indicated by Wright and Ward. Slot shape 18 with a 13.5-percent open periphery was developed from the initial calibration of the wind tunnel (ref. 5). Slot shape 18 had a maximum test-section Mach number with uniform flow of 1.08 and was in continuous use until the wind tunnel was provided with the test-section air removal system in 1961.

Development of slot shape 26. After the air removal system was available, the maximum Mach number was found to have increased to about 1.3; however, it was observed that slot shape 18 did not provide a uniform flow in the test section at the higher supersonic speeds (ref. 9). As a consequence, a program was initiated to develop a slot shape that would yield the highest feasible test-section Mach number with the largest possible test region over the complete Mach number range.

Before proceeding with the study to develop an acceptable slot shape for the test-section Mach number distribution and tunnel power, investigations were required to determine the factors essential to the procedures for operating the wind tunnel with test-section air removal. At this stage, no test-section calibration existed; consequently, Mach number was determined directly from airstream stagnation pressure and test-section wall static pressure at TS 134.00 without regard to Mach number gradient in the test section. These exploratory investigations included determining the effects of air removal on the power balance between the main drive motors, on diffuser entrance vane settings, and on diffuser entrance leakage. (See ref. 9.) In addition, tests were also conducted to determine the effects of air removal on test-section wall divergence.

After completion of these exploratory tests, an experimental program was initiated to determine an acceptable slot shape and resulted in the development of slot shape 26. Planforms of the slot shapes tested in this time period are presented in figures 26(b) to 26(e). Details of this program are found in reference 9. The wind tunnel incorporating slot shape 26 was operated over a wide range of test-section wall divergence angles at several nominal values of Mach number. For each value of Mach number, test-section wall divergence angle was selected to yield static-pressure gradient of 0 psi. The wind tunnel calibration of 1961 was established from these data and continued in use until 1963.

Development of slot shape 29. The wind tunnel calibration of 1963 included an abbreviated verification of the performance of slot shape 26, an investigation of slot shape 27, and a complete calibration of the wind tunnel incorporating slot shape 28. Slot shapes 27 and 28 are the same as slot shape 26 except at a short region downstream from TS 132.00. Slot shape 28 was fabricated primarily with wooden edge strips and, although regarded as temporary, was used until the wind tunnel was calibrated in 1965 with slot shape 29. The coordinates of slot shapes 28 and 29 are identical; however, the slot edge strips for shape 29 are almost entirely of steel. The new designation 29 was given primarily for physical differentiation of these slot edge strips. Planforms of slot shapes 26 to 29 are presented in figure 26(f). Under all operating conditions, the most uniform flow in the test section was achieved with slot shape 29. This slot shape is defined over the upstream third of the slot length by an approximately triangular starting section that faired into a relatively narrow slot with a constant width (3.9-percent open periphery) over the downstream two-thirds of its length. Slot shape 29 has been in use since.

Wind Tunnel Operational Principles and Procedures

Operational principles. Experience acquired prior to 1965 in operation of the wind tunnel with test-section air removal had established the techniques for obtaining any preselected value of Mach number up to 1.30. Speed of the main drive fans, compressor speed, plenum valve and surge control valve positions, and approximate values of test-section wall divergence angle were known. This experience had shown also that moisture content of the airstream did not have a large effect on aerodynamic data (ref. 15), but did have some effect on the axial static-pressure gradient in the test section, especially at supersonic speeds. Although the gradient does not affect the mean value of Mach number in the test section, a static-pressure gradient can exert horizontal buoyancy on a model, and thereby, may cause an error in drag measurement. In the wind tunnel calibration of 1965, some empirical determination was made of the effect of air humidity on static-pressure gradient in the test section and on selection of the proper angle of wall divergence to eliminate the gradient. With the advent of an on-site computer and data acquisition system in 1977, it was possible to determine the proper wall divergence angle by taking data for several angle settings and observing where a Mach number gradient of zero occurred.

Operational procedures. With the addition of test-section air removal, two modes of operation of the wind tunnel exist.

For $M < 1.05$, the mode of operation is as follows:

1. Set δ_{flat} for desired M .
2. Set fan rpm to obtain desired M .

For $M \geq 1.05$, the mode of operation is as follows:

1. Set $M = 0.3$.
2. For $M = 1.05$ to 1.15 , set compressor motor to 475 rpm, or for $M > 1.15$ set compressor motor to 552 rpm.
3. Increase fan rpm to 42 MW total power on main drive motors.
4. Set δ_{flat} for desired M and dew point.
5. Open 10-ft valve to set $M \approx 1.23$. (Valve will be 100-percent open at $M \approx 1.23$.)
6. For $M > 1.23$ with 10-ft valve open 100 percent, increase fan rpm to achieve desired M .

Calibration Procedure and Data Analysis

Calibration tests and data presentation. Up through 1965, all calibration tests of the 16-Foot Transonic Tunnel had a test number of 100. The calibrations of 1977 and 1990 had test numbers of 321 and 432, respectively. Designation of test, run, and test point number identifies a unique set of test conditions. A typical calibration run includes all tests performed between the start and the stop of the main drive motors. A single run may have many values of Mach number and appropriate variation of operating parameters at each Mach number. Data were typically acquired by holding Mach number constant and varying test-section wall divergence over a preselected range of values. For each test point, all pertinent data, such as wind tunnel operating conditions, test-section pressures and temperatures, and wind tunnel air state and humidity were recorded simultaneously. Critical runs were repeated to verify repeatability of measurements.

The results of the 1990 wind tunnel calibration are presented in tables 5 to 18. Operational characteristics such as flat divergence angle, dew point, free-stream stagnation temperature, motor and compressor rotational speeds, and 10-ft valve position for selected test points are presented in table 5. Also presented in table 5 are the estimated values of corrected power. These values were derived from measured values minus estimated losses in the Kramer drive system (ref. 9) and corrected to standard atmospheric pressure and airstream average stagnation temperature.

Basic data reduction. Static pressures measured on both the right and the left sides of the centerline survey

tube and on the test-section wall and diffuser are expressed as Mach number with the following equation:

$$M = \sqrt{\frac{2}{\gamma - 1} \left[\left(\frac{P_{t\infty}}{P_{\infty}} \right)^{\frac{\gamma - 1}{\gamma}} - 1 \right]}$$

Local Mach numbers measured on the left side of the centerline survey probe are given in table 6. Local Mach number and pressure ratios determined on the right side of the centerline survey probe for selected test points are listed in tables 7 and 8, respectively. Local Mach numbers measured on the test-section wall and diffuser are given in table 9.

Flow-uniformity analysis for standard calibrated test-section lengths. The data reduction procedure also includes an analysis section to determine the flow-uniformity parameters for calibrated test-section lengths (CTSL). These parameters are test-section Mach number, Mach number gradient, and standard and maximum deviations in Mach number. These parameters are determined for 6-ft and 8-ft CTSL, which represent the majority of model lengths tested in the 16-Foot Transonic Tunnel. This data reduction procedure is a least-squares fit of a straight line to values of local Mach number in the test section. The least-squares analysis is performed for both the right and the left sides of the centerline tube from measurements made from the individual pressure transducers and the electronic scanning units. The tunnel station and number of pressure orifices used in analysis for test-section length is as follows:

Centerline side	Nominal test section length, ft	Tunnel stations, ft	Number of static-pressure orifices used in analysis
Right	6.00	131.00 to 137.00	24
Right	8.00	129.00 to 137.00	30
Left	6.00	131.00 to 137.00	9
Left	7.50	129.00 to 137.00	11

Results of this least-squares analysis for the right side of the centerline tube from measurements made with the individual pressure transducers for all the data points selected for the wind tunnel calibration are listed in table 12. In this table, the test-section Mach number is the value M_r of a least-squares straight-line fit to the Mach number data over the chosen length of test section at TS 134.00 (midpoint of test section). The slope dM/dx defines the Mach number gradient. The standard deviation of Mach number 2σ from the straight line of best fit is a measure of average discrepancy. The maximum deviation σ_{max} represents the worst departure from the line of best fit of a single value of Mach number on the

centerline within the selected length of test section. Similar results from the measurements of static-pressure ratios are given in table 13. In general, the agreement of the parameters listed in tables 12 and 13 for 6-ft and 8-ft CTSL is excellent. Mach number gradients for the 6-ft CTSL for the right side and the left side of the centerline tube that were determined from measurements made with individual transducers and electronic scanning units are presented in table 14. Here again, very good agreement of the Mach number parameters occurred for the two measurements made on the right side of the centerline tube and for the right and left sides of the centerline tube.

Alternate calibrated test-section lengths. The least-squares analysis was also performed for a number of alternate test-section lengths for very long models that are tested at subsonic speeds. This analysis was made with only the measurements from the left side of the centerline tube with the electronic scanning units. The tunnel station and number of pressure orifices used in analysis for test-section length is as follows:

Centerline side	Nominal test section length, ft	Tunnel stations, ft	Number of static-pressure orifices used in analysis
Left	9.0	128.00 to 137.00	13
Left	10.5	126.50 to 137.00	15
Left	12.0	125.00 to 137.00	17
Left	15.0	122.00 to 137.00	20
Left	18.0	119.50 to 137.00	24
Left	21.0	116.50 to 137.00	27

Results of this least-squares analysis for selected data points on the left side of the centerline tube that were measured with electronic scanning units are listed in table 15.

Criteria for flow uniformity. The general criteria of acceptability that was applied to Mach number distribution for the wind tunnel calibration was that the average Mach number gradient be less than about 0.0006 per foot and that the standard and the maximum deviations of Mach number from a least-squares straight-line fit be less than 0.005 and 0.010, respectively, for the 6-ft CTSL. Generally, the differences in Mach number between those determined for the 6-ft and the 8-ft CTSL were less than 0.0005 (table 12). However, a maximum difference of 0.0069 was noted to occurred at $M_r = 0.905$ (run 9, point 5). Generally, the criterion used to select the test points to establish the wind tunnel calibration, which are listed in table 12, was a Mach number gradient of zero or minimum value. Test points obtained over a wide variation in wall divergence angle at each Mach number were

screened to select those falling closest to a Mach number gradient of zero. Fifty-six test points were selected from a group of about 160 points. This procedure also established the wall-divergence-angle settings for subsequent wind tunnel operation.

Wind Tunnel Aerodynamic Performance

Mach Number Characteristics

Test section. Mach number distributions measured on the left side of the centerline tube along the tunnel centerline for the entire test section between TS 100.25 and TS 140.00 are shown in figure 27 and the values of local Mach number are given in table 6. These distributions indicate uniform flow within ± 0.005 for Mach number at speeds up to $M_l = 1.0$ from about TS 112.00 to TS 137.50. At supersonic speeds, the length of uniform flow that fixes usable test-section length is a function of Mach number. This length of uniform flow decreases as Mach number increases. Mach number distributions measured along the right side of the centerline tube are presented in figure 28. The values of local Mach number and pressure ratios are tabulated in tables 7 and 8, respectively. Mach numbers for the right and the left sides of the centerline tube are shown in figure 29. These data show that the local Mach number on the right side of the centerline tube is always slightly higher than that of the left side. This result will be discussed in the "Wind Tunnel Calibration" section.

An inspection of the Mach number distributions for the test-section centerline (figs. 27 and 28) shows that at supersonic speeds the distributions are uniform to TS 140.00, but that at high subsonic speeds the individual values of local Mach number decrease progressively downstream of TS 137.00. This phenomenon was also present in previous calibrations and was attributed to interference from the strut head of the model support system (ref. 9). This interference, which does not extend upstream of TS 137.00, is always considered in choosing the axial position of a model in the test section. With the installation of the new model support system in 1990, an additional concern arose because the new strut head represented a 60-percent increase in blockage. To investigate these effects, a comparison of Mach number distributions for the 1990 and the 1965 calibrations is presented in figure 30. The apparent effect of the new, larger strut head is a further decrease in Mach number at tunnel stations greater than 137.50 ft. With this exception, this comparison shows excellent repeatability between the two calibrations.

Test-section wall. Mach number distributions along the test-section wall for selected calibration points are

presented in figure 31. There is generally good agreement between the centerline and wall Mach number distributions. Although not shown (because of loss of pressure orifices), curvature of the wall between test section and diffuser in the vicinity of station TS 139.00 causes local Mach number on the wall to exceed that at the centerline. The curvature in the wall occurs at one of the flexure points and results from variable wall divergence.

Diffuser. Mach number distributions along the test-section wall diffuser are presented in figure 32. Mach number is computed in the same manner as for the test section with airstream total pressure assumed to be the same as that measured in the quiescent chamber. There is some loss of total pressure in the diffuser caused by skin friction and air turbulence at all speeds, and at supersonic speeds, by shock losses at the downstream end of the test section. Most pressure recovery in the diffuser appears to have been obtained within a length of about 4 test-section diameters (64 ft) from the downstream end of the test section.

Wind Tunnel Calibration

The basic calibration technique for the 16-Foot Transonic Tunnel is a correlation of the average airstream static pressure measured in the test section with the centerline tube and the reference static pressure measured in the plenum. This calibration may also be regarded as a comparison of test-section airstream Mach number with the equivalent plenum Mach number, where the plenum Mach number is computed from the reference pressure measurements. This calibration is essential to the normal operation of the wind tunnel, because, while M_{tank} can be computed whether a model is installed or not, M_{ave} can only be obtained from pressure measurements made with the centerline tube installed. Any pressure probe installed in the test section to measure free-stream static pressure would most likely cause interference for the model also installed in the test section. Note, a model installed near the centerline in the calibrated region of the test section is assumed to be subjected to the Mach numbers measured by the centerline tube in that same region.

As previously noted, an examination of the Mach number distributions in the test section (fig. 29) indicates that small differences exist between those measured on the right and the left sides of the centerline tube. The Mach number is always higher on the right side and the difference between the two Mach numbers is less than about 0.6 percent. These differences are believed to be caused by a combination of centerline probe asymmetry and the effects of a cross flow in the wind tunnel and are noted in table 11 for all the calibration test points. For the

calibration of 1990, these two test-section static pressures were averaged and this average value was subsequently used for correlation with the plenum static pressure. These average static-pressure ratios and Mach numbers are also presented in table 14. The values of test-section airstream static pressures and Mach number selected for the calibration and the corresponding values of plenum pressure and Mach number are compiled in table 16 and presented graphically in figure 33. For computational purposes, a ninth-order polynomial curve was used for the correlation of test-section static pressure to plenum pressure. The ninth-order curve was necessary for a good fit of the data between Mach numbers of 0.90 to 1.10. This single calibration defines test-section airstream Mach number. Deviations of less than 0.005 exist between the average Mach number M_{ave} and the Mach number calculated from the calibration M_{cal} for 75 percent of the calibration points. (See table 16.)

The wind tunnel calibration of 1990, the calibration of 1977, and the previously published calibrations of 1965 (ref. 9) and 1951 (ref. 5) are presented in figure 34. The agreement between these calibrations is excellent and indicates that the basic calibration was essentially not effected by changes in the test section such as the slot shape or the new model support strut. The differences noted are believed to be mainly a result of the accuracy of the various instrumentation used in each calibration. For example, for the 1965 calibration, the wind tunnel reference pressures were measured with absolute mercury manometers with the column height determined by an electromechanical follower. Similarly, centerline pressures in 1965 were acquired by using electromechanical stepping valves each attached to an electronic pressure gage. Approximately 1 min was needed to acquire data with these instruments, and during this time, tunnel conditions can vary slightly.

Test-Section Wall Divergence Angle

Remotely controlled test-section wall divergence had been incorporated in the design of 1950 as a means to control the effect of boundary-layer growth on the longitudinal distribution of Mach number. However, test-section wall divergence was not required prior to the use of test-section air removal for tests at the maximum Mach number of 1.08. In addition, the original wind tunnel calibration indicated Mach number gradients were insignificant. However, exploratory tests conducted during the calibration of 1961 showed that Mach number gradient could be varied greatly by varying wall divergence, especially at supersonic Mach numbers. Thus, test-section divergence would be a critical parameter in the operation of the wind tunnel. The large effect of wall divergence was believed to result partly from the decrease in slot porosity from 13.5 percent for slot 18 to

about 4 percent for slot 26. Although the Mach number gradient does not affect the mean value of Mach number in the test section, a static-pressure gradient can exert horizontal buoyancy on a model and thereby may cause an error in drag measurement. Therefore, the calibrations conducted during 1977 and 1990 were intended to refine this existing schedule of wall divergence angles that had been developed empirically in some cases in the calibration of 1965.

Subsonic and low supersonic Mach numbers.

Mach number gradients for free-stream Mach numbers from 0.502 to 1.134 that were obtained from the 1990 calibration are presented in figure 35. At Mach numbers less than 0.825, a negative Mach number gradient always exists in the test section with a maximum value of -0.00076 occurring at $M = 0.60$. At Mach numbers greater than 0.825, it is possible to select a wall divergence where $(dM/dx)_r = 0$. For this range of Mach numbers, airstream dew point has no discernible effect on the gradient. The data in figure 35 also suggests that setting negative wall divergence angles (walls move into test section) would eliminate the gradient; however, this is not mechanically possible. For a transport model with a span and length of 80 in. and a volume of about 3 ft^3 , the Mach number gradient at $M = 0.6$ is calculated to 0.00001 in drag coefficient. Typically, most models tested in the 16-Foot Transonic Tunnel have less than 3 ft^3 of volume.

Supersonic Mach numbers. Because at supersonic Mach numbers the Mach number gradient is a function of dew point, it is desirable to obtain calibration data over the widest range of dew points. This range of dew points may not always be possible because the 16-Foot Transonic Tunnel is an atmospheric wind tunnel. During the 1977 calibration, data were obtained at dew points from 21° to 60° . The resulting Mach number gradients obtained in 1977 are presented in figure 36 as a function of divergence angle for various values of dew point. Note that the variation of test-section wall divergence angle with dew point at Mach numbers 1.15 and 1.178 does not follow the systematic trend of the data at both the lower and the higher values of Mach number. As was the case in 1965, no technical explanation can be offered for this lack of consistency with the other data. Although the 1977 results exhibit the same trends as those obtained in 1965, differences of up to 4 min in divergence angles existed between the two calibrations. The 1977 set of data were chosen for selecting a new wall divergence angle schedule because with the addition of the on-site data acquisition system, it was possible to determine almost instantly where gradients of zero would occur for a particular Mach number. This determination was not the case for the 1965 calibration. In 1990, calibration

data were obtained at dew points from 51° to 65° and these results were used to check the 1977 calibrations. The Mach number gradients of the calibrations from 1977 and 1990 are shown in figure 37, and except for $M = 1.25$, show excellent agreement.

Divergence angles and Mach number gradients.

The schedule of wall divergence angles for the 16-Foot Transonic Tunnel is shown in figure 38 and tabulated in table 17. The schedule of divergence angles for Mach numbers less than 1.1 was determined from the 1990 calibration; whereas the schedule for Mach numbers greater than 1.1 is from the 1977 calibration. The 1977 data were used because of the wide variation in dew point. The average Mach number gradients and the standard and the maximum deviations in Mach number for this schedule for both the 6-ft and 8-ft CTSL are shown in figure 39. A comparison of Mach number gradients and divergence angles between the 1965, the 1977, and the 1990 calibrations is presented in figure 40. Mach number gradients are greater for the 1990 calibration than for the other two calibrations and may be associated with the new support system (installed prior to 1990 calibration), which has more blockage than the old support system. The new support system induces a more positive static-pressure gradient which results in a negative Mach number gradient.

Alternate calibrated test-section lengths. The centerline Mach number distributions shown in figure 27 indicate that models in excess of 20 ft can be tested in the 16-Foot Transonic Tunnel at subsonic Mach numbers. However, no attempts were made previously to determine flow-uniformity characteristics for the models installed in that portion of the test section outside of the calibrated test section. Accordingly, Mach number gradients for a series of alternate CTSL from 9 ft to 21 ft have been determined and are shown in figure 41 for selected Mach numbers. They show trends similar to the trends of 6-ft and 8-ft CTSL, which are also shown in figure 41. The average Mach number gradients and the standard and the maximum deviations in Mach number are presented in figure 42. In general, there is a decrease in the Mach number gradient as test-section length increases.

Boundary-Layer Characteristics

Boundary-layer characteristics measured with a 14-probe total-pressure rake on flat 7 at TS 133.00 are presented in figure 43. No corrections were made for total-pressure losses through the bow shock ahead of the total-pressure tubes at supersonic speeds. These data indicate a turbulent boundary-layer profile and that no losses in the total pressure in the free stream are evident until a point about 8 in. from the flat. The air removal

system has no effect on boundary-layer depth at the specific probe location examined.

Power Requirements

The total power requirements for the Langley 16-Foot Transonic Tunnel for two dew points are shown in figure 44. Also shown is the average total power from several runs from the 1990 calibration. The steep rise in power between $M = 1.04$ and $M = 1.05$ results from the additional power from the motor of the air removal system. In general, this motor requires about 28 MW for operation. Operation of the wind tunnel at supersonic speeds with the air removal system requires a total input to the main tunnel drive of at least 42 MW. This power input is necessary to keep the test-section shockwave well aft of the model support system strut head. As a result, power requirements from $M = 1.05$ to about $M = 1.22$ are constant, and in this range, Mach number is set by throttling the 10-ft valve. As expected, for the narrow range of dew points tested, dew point did not significantly effect the total power requirements. Reference 9 indicated an approximate 3-percent decrease in power with about a 20° decrease in dew point.

A comparison of total corrected power from the 1990, the 1977, and the 1965 calibrations is presented in figure 45. The estimated values of corrected power, which were derived from measured values minus estimated losses in the Kramer drive system (ref. 9), have been corrected to standard atmospheric pressure and to the airstream average stagnation temperature. This comparison indicates that installation of both the new support system (with increased blockage) and the catcher screen had no effect on power consumption except at Mach numbers greater than 1.25, where it was estimated that the catcher screen would require 3 to 5 MW of additional power.

Test-Section Flow Field Characteristics

A flow field survey was made over a circular cross section of the wind tunnel test section by rotating a survey rake containing five flow-angularity probes at TS 130.60, TS 133.60, and TS 136.00. Local Mach number and flow angles were measured parallel and perpendicular to the rake and then resolved to the tunnel wind axis coordinate system. The region of the test section over which these surveys were made is representative of the maximum distance from the centerline that a model is generally tested. The survey at TS 136.00 was limited to a maximum roll angle of 142° because of interference between the retracted sting and the main tunnel support system. Further details of these flow surveys are given in reference 12.

Incremental Mach number. Incremental Mach number distributions in both a vertical and a lateral plane are presented in figures 46 and 47, respectively. Incremental Mach number is simply the difference between the local Mach number, which is measured by an individual probe on the rotating rig, and free-stream Mach number. In general, these data indicate that the flow is uniform about that region of the test section in which the surveys were made. Incremental Mach numbers of about 0.002 to 0.004 were found for most Mach numbers below 0.80.

Upflow characteristics. The variation of test-section upflow angles with Mach number at TS 130.60, TS 134.60, and TS 136.00 are shown in figure 48. The upflow data are those measured along the vertical centerline with the rake positioned at roll angles of $\phi = 0^\circ$ and 180° . Along the centerline, the local upflow angle is typically about 0.10° , which increases to about 0.40° at 1.2 ft above the centerline and decreases to -0.20° at 1.2 ft below the centerline. At all tunnel stations, the local upflow angles at a distance of 2.3 ft from the centerline exhibit an increase in the flow divergence away from the test-section centerline at Mach numbers above 0.80. Upflow angles that were determined from tests with a force balance in the model generally average about 0.10° .

The variation of upflow angle with tunnel station is shown in figure 49 for Mach numbers of 0.60, 0.80, and 0.90. These data show little variation in upflow angle in the tunnel streamwise (longitudinal) direction.

Sideflow characteristics. The sideflow characteristics at TS 130.60, TS 133.60, and TS 136.00 are shown in figure 50. These data show that the sideflow angle is about 0.10° at the center of the test section, with the flow diverging from the center at locations off the test-section centerline. At the outermost probe location (2.3 ft off centerline) the local sideflow angles are as large as 0.90° . Supersonic sideflow angles are also shown in figure 50. In general, the supersonic sideflow angles tend to diverge from the centerline at the downstream station. The largest supersonic sideflow angles are observed on the left side of the test section closest to the point where the test-section air removal takeoff duct is located (fig. 3).

A plot of the subsonic sideflow angles at each tunnel station and at Mach numbers of 0.60, 0.80, and 0.90 is presented in figure 51. The data show that the variation in sideflow across the horizontal centerline is nearly linear with a gradient of about 0.3° per foot. Along the tunnel centerline, the sideflow is about 0.10° . Toward the inside of the tunnel circuit (z_{probe}), the sideflow angle increases to an average of about 0.80° at a location 2.3 ft from the centerline. Toward the outside of the tunnel

circuit ($-z_{\text{probe}}$), the sideflow decreases to an average of about -0.70° , which is directed away from the centerline at each station. The variation in sideflow angles with tunnel station is small.

Airstream Flow Quality

Turbulence intensities. The turbulence intensities that were determined from hot wire measurements in the quiescent chamber of the wind tunnel are presented in figure 52. The data presented were obtained at Mach numbers in the test section from 0.2 to 1.25 with and without a single-engine propulsion simulation system operating. The longitudinal turbulence intensity varies from approximately 0.4 to 2.6 percent along the center of the quiescent chamber. Turbulence levels measured near the centerline in the quiescent chamber are in good agreement with those measured previously (unpublished results) in the test section and indicate that essentially the entrance had no effect on turbulence levels. In addition, jet operation had little or no effect on the turbulence levels. This result is important because the vast majority of investigations carried out in the 16-Foot Transonic Tunnel involve some means of jet simulation.

Fluctuating-pressure characteristics. A flow field survey was made over a circular cross section of the wind tunnel test section by rotating a survey rake containing three static-pressure and one total-pressure acoustic probes at TS 130.60, TS 133.60, and TS 136.00. Pressure fluctuation characteristics were determined at rake roll angles from -90° to 90° . The region of the test section over which these surveys were made is representative of the maximum distance from the centerline that a model is generally tested. Static- and total-pressure fluctuation characteristics for the 16-Foot Transonic Tunnel are presented in figure 53. Static-pressure fluctuation varies from approximately 0.002 to 0.016 percent at a radius of 2.3 ft about the tunnel centerline (fig. 53(a)). However, along the centerline of the test section, some unknown disturbances cause the pressure fluctuations to increase to values as high as 0.052 percent at $M_\infty = 1.25$. These disturbances are apparently attenuated through the test section because the pressure fluctuation characteristics on the centerline at TS 136.00 are similar to those off the test-section centerline. The flow quality in the 16-Foot Transonic Tunnel is very good relative to similar facilities (refs. 16 to 18). As seen in figure 53(b), total-pressure fluctuation varies from approximately 0.002 to 0.007 percent throughout the region in the test section where measurements were made.

Transition Reynolds number. Transition Reynolds number and noise characteristics for the 16-Foot Transonic Tunnel, which previously were reported in refer-

ence 19, are presented in figure 54. Also presented in figure 54 are similar results for several other transonic wind tunnels. All measurements were made by the same investigators who used the same techniques and equipment for all wind tunnels. The analysis of the flow transition data presented in reference 19 indicates that the Langley 16-Foot Transonic Tunnel had the lowest disturbance level through the transonic Mach number range of all tunnels considered, and accordingly, the highest transition Reynolds number.

Test-Section Temperature Distribution

A radial temperature gradient in the test-section airstream is almost inherent because the wind tunnel is cooled by continuous air exchange. After passing through the drive fans, the airstream in the return passage is uniform in temperature. On the downstream (inlet) side of the air exchange, the difference in temperature between the cool incoming air and the recirculated airstream is equal to the difference between stagnation and outside air temperatures. By the time that the airstream has traversed the third and the fourth sets of turning vanes, an antiturbulence screen, the quiescent chamber, and the entrance cone, the radial region of temperature gradient extends inwardly from the test-section wall for about half of the test-section radius. Radial distributions of stagnation temperature in the test section for several values of Mach number are shown in figure 55. The temperature of the airstream core is very uniform and is identical to stagnation temperature, which is measured by probes located in the quiescent chamber.

The temperature gradient in the test-section airstream is not a desirable feature, but in general, it has no adverse effect on most investigations conducted in the wind tunnel. The temperature gradient has no effect on Mach number distribution, but does result in a velocity gradient directly related to the temperature gradient. Models with a wing span of 9 ft to 10 ft would probably be located in an area with essentially no gradient. Except in special cases, the temperature gradient effectively eliminates from consideration the investigation of wall-mounted models.

Air Moisture Condensation

During tests made with high dew points, condensation of water vapor in the test-section airstream occurs in varying degrees. The tendency toward the formation of fog in the test-section airstream increases with absolute humidity and with increasing air speed. This moisture condensation decreases as air stagnation temperature is raised. Because of the radial temperature gradient, condensation occurs first in the annular layer of air adjacent to the test-section wall as shown in figure 56(a), which is

a view of the test section from the downstream end of the diffuser. At supersonic speeds when air moisture content is very high, condensation will occur throughout the entire test section as illustrated in figure 56(b). Under such conditions, the condensation cannot be completely eliminated by increasing the airstream stagnation temperature.

The extent to which moisture condensation in the test-section airstream may invalidate aerodynamic data is controversial. For the 16-Foot Transonic Tunnel, the effects of air moisture content on the wind tunnel test-section static-pressure gradient are accounted for in the calibration procedure through test-section wall divergence. There remains, however, the effects of local condensation adjacent to model curved surfaces. The investigation reported in reference 15 shows little difference in data obtained with the same model tested first in moist air and subsequently in relatively dry air. Unpublished data of a transport model also indicated no effects of dew point on pressures measured on the wing surfaces. Another facet of this problem of moisture effects is the validity of the procedure of applying wind tunnel data obtained in desiccated air to aircraft performance estimation when the aircraft must operate in air having a natural moisture content that is frequently sufficient to cause visible local condensation on curved surfaces of the aircraft.

Wind Tunnel Test Capabilities

Guidelines for Model Size and Location

Subsonic blockage considerations. Generally, model size is dictated by wind tunnel blockage effects at subsonic speeds and boundary-reflected disturbances at supersonic speeds. The maximum cross-sectional area of the model can limit the transonic Mach number at which interference-free data can be obtained. Experimental blockage studies, which have been made in the 16-Foot Transonic Tunnel (ref. 20) with slot shape 29 (width of 3.9 percent open periphery), indicated that no serious wall interference occurred at subsonic Mach numbers up to $M = 0.98$ for models with blockage ratios of 0.0004. These results are presented in figure 57 and can be used to size a model. For example, to obtain interference-free data at a Mach number of 0.97, the model can have a maximum blockage ratio of 0.0008. With a 0.0008 blockage ratio, the model would have a maximum cross-sectional area with an equivalent diameter of 5.4 in. Similarly, interference-free data could be obtained up to a Mach number of 0.95 for a model with a blockage ratio of 0.0024 and an equivalent diameter of 9.4 in. In general, no tests are permitted in the 16-Foot Transonic Tunnel between Mach numbers of 0.98 to 1.05 because of the

possibility of both subsonic and supersonic blockage effects (refs. 20 and 21).

Boundary-reflected-disturbance length considerations. At low supersonic Mach numbers, boundary-reflected disturbances tend to limit the useful test-section length. Tests have been conducted to determine the location of the reflected bow shock on the model, which then determines the extent of the interference-free region. Boundary-reflected-disturbance lengths for several models are presented in figure 58. Results for models 1, 2, 3, and 5 were taken directly from reference 21 and the remainder are from unpublished sources. The disturbance length depends on the strength of the bow shock as affected by the body nose half angle and the change in nose shape from conical to ogive. At Mach numbers greater than 1.15, aircraft models with a length of 71 in. or less are generally free of boundary-reflected disturbances.

Model location. For subsonic Mach numbers, the model nose can be located as far forward as TS 116.50, which places the model within a 21-ft CTSL. At supersonic speeds, the model longitudinal position in the tunnel must be considered because the length of the usable test section with a uniform centerline Mach number distribution is limited (fig. 28). In addition, the model base should always be kept forward of TS 137.00 to avoid the drop in Mach number that occurs aft of this tunnel station (fig. 28).

Model volume and span. Model volume should not exceed 3.5 ft^3 for tests up to a Mach number of 0.7. This limit is necessary to minimize the buoyancy effect due to the Mach number gradient on the measured drag of a model. For a transport model with a span and length of 80 in. and a volume of about 3 ft^3 , the Mach number gradient at $M = 0.6$ would cause a buoyancy effect equivalent to 0.00001 in drag coefficient. Typically, most models tested in the 16-Foot Transonic Tunnel have less than 3 ft^3 of volume. At Mach numbers greater than 0.7, no buoyancy corrections are needed because wall divergence is varied to eliminate the Mach number gradient.

The wing span of a model should not exceed 9 to 10 ft to avoid the effect of the temperature gradient that exists in the test section (fig. 55). The temperature gradient has no effect on Mach number distribution, but does result in a velocity gradient directly related to the temperature gradient.

Main Model Support System

The main model support system used in the wind tunnel is shown in figure 59. The support system consists of a cast steel circular-arc segment surmounted by a short

straight swept strut that has at its upper end the strut head, which is a cylindrical body 102.0 in. long and 21.0 in. in diameter. At an angle of attack of 0° , the strut-head centerline is coincident with the tunnel centerline. The support strut penetrates the tunnel floor (flat 8) in the diffuser entrance region through an unsealed opening and moves on a circular-arc track located within a pressure box that is in the plenum. The support system moves in a vertical plane that contains the tunnel centerline with the center of rotation at TS 134.00 and is actuated through an angle-of-attack range from -9° to 24° . Lateral aerodynamic force tests can be done by remotely rolling the model from -90° to 90° and traversing the main tunnel support in the vertical plane. The load capacity of the main support system is 10 000 lb of normal force and 10 000 lb of side force that acts at TS 134.00.

The 16-Foot Transonic Tunnel support system also can conduct a variety of propulsion tests. Two separate, independently controlled air supplies are provided within the model support system. Flexible high-pressure air lines with swivel joints at one end are used as a connection between the fixed air supply in the strut head and the model. Each line can provide air to a model at a rate of 15 lb/sec at 1000 psi at temperatures from 70°F to 130°F . Thus, the entire model, model support hardware, and each air line can be rolled remotely as a unit from -90° to 90° through the angle-of-attack range from -9° to 24° .

Miscellaneous Model Support Systems

A significant amount of model support hardware exists that is appropriate for both aerodynamic and propulsion tests. This hardware has accumulated over the years and has generally emerged from either specific test programs or was acquired for a particular type of test, such as propulsion tests. Therefore, there is a wide variation in the versatility and usefulness of these components. Some of this hardware will be discussed herein. A more complete description of this hardware can be found in reference 22.

Model attachment to main model support. Various methods are available for mounting models to the main model support system in the test section. For most tests, a model is attached to the main support system of the strut head with a combination sting-knuckle-butt assembly shown in figure 60(a). This assembly is attached to the upstream end of the strut head at TS 141.94. A sketch of standard and air butts is presented in figure 60(b). An offset butt (fig. 60(c)), which displaces the model centerline either 22 in. below or above the tunnel centerline, is generally used with sting-strut mounting arrangements. This butt also provides ducts for two high-pressure air flows for propulsion tests. Several other adapter butts are also available and are described in detail in reference 22.

Attachment of a model sting to a standard or air butt is made with a split coupling or knuckle as shown in figure 60(d). A cross section of a typical knuckle and a list of available knuckles are also presented in this figure. Tapers at both ends of the knuckles are seated with split nuts, as shown in figure 60(a). The knuckles are split in half longitudinally so that they can be changed manually between wind tunnel runs without disconnecting the instrumentation leads passing through them; however, this process can be time consuming if the model is large or complex. In addition, many adapters that would replace or be used in conjunction with a knuckle are available (ref. 22). These adapters allow hardware designed for other wind tunnels to be used.

Sting support systems. A variety of model stings for nonpropulsion tests are available for tests at the 16-Foot Transonic Tunnel (ref. 22). These stings were built at various times for specific model installations and load requirements. Several force balances with varying load capabilities are also available for tests. Some typical stings are shown in figure 61. A photograph showing a typical sting mounted model in the 16-Foot Transonic Tunnel is presented in figure 62.

Model mounts are not limited to those available at the wind tunnel, because adapters make it possible to install stings built for other wind tunnels. However, tandem installation of a series of knuckles and adapters increases the length of the assembled support and can, in some cases, put the model too far forward in the test section. The model longitudinal position in the tunnel must be considered because the length of the usable test section with a uniform centerline Mach number distribution is limited, especially at supersonic Mach numbers. In addition, the model base should be kept forward of TS 137.00 to avoid the effects of the diffuser Mach number gradient. All sting and model hardware designs must satisfy the requirements reported in reference 23.

Sting-strut support. One model support for propulsion tests is the sting and strut arrangement shown in figure 63. This sting and strut is used with either an air or offset butt. High-pressure air for exhaust simulation is routed from the air supply in the strut head through a 1.5-in-diameter hole in the sting and six 0.625-in-diameter holes in the strut. The maximum airflow capability through the sting and strut is 15 lb/sec at a pressure of about 1000 psi at the top of the strut. Instrumentation leads are routed through upper and lower passages in the sting and through passages in the strut leading and trailing edges. Model hardware is attached to the top of the strut by a high-pressure plenum, which then directs the air aft through the model for either single- or twin-engine simulation. There are currently two sting-and-strut

supports, one fixes the model at 0° yaw and the other fixes the model at either 0° or 5° yaw (with respect to the strut). Typical models supported by the sting and strut are shown in figure 64.

Wingtip support system. The wingtip model support system, shown in figure 65, was designed for afterbody and nozzle integration research on twin-engine fighter aircraft at high angles of attack. The wingtip support system attaches to the tunnel support system through two pairs of V struts. The forward pair of struts attaches through a bullet nose fairing to the strut head at TS 141.94. Air lines are routed through the forward struts; instrumentation lines are routed through the aft struts. Electric flow control valves located in the bullet fairing allow remote balancing of the left and right engine flows. The maximum airflow capability of the wingtip support is 15 lb/sec. Twin booms attach to the top of the V struts and carry air and instrumentation lines forward to the model. As shown in figure 62, the model longitudinal position in the tunnel test section can be varied 6 or 12 in. by sliding the booms forward or aft on the V struts. An integral wing and centerbody is supported between the booms and all other model hardware attaches to the wing and centerbody. Air and instrumentation lines are routed from the booms to the model through the wing and centerbody. The uncambered wing planform was designed to be typical of fighter aircraft. The planform can be rotated with respect to the booms at incidence angles of 0°, 8°, 16°, 32°, and 45°, thereby providing an angle-of-attack range from -9° to 64°. Photographs showing several model installations with the wingtip support system are shown in figures 66(a) to 66(c). The fighter wing can be replaced with other wings to do other propulsion tests. Figures 66(d) and 66(e) show both a straight and a swept wing, respectively, that were used for nacelle and pylon integration studies. Further details on the wingtip support system can be found in reference 22.

Air-sting supports. Sketches of the two air-sting supports that are available for tests in the 16-Foot Transonic Tunnel are presented in figure 67. The first air-sting support that used the flow-through balance and bellows assembly was designed for research on subsonic transport configurations. This air sting attaches directly to the tunnel support (TS 141.94) and does not use a knuckle or a sting butt. Two 1.75-in-diameter holes in the sting route the exhaust simulation air (upper passage) and instrumentation leads (lower passage) into the model. Two 0.75-in-diameter holes near the sting and model attachment are also available for routing instrumentation leads. Additional information on this balance configuration can be found in the "Instrumentation" section and in reference 22.

The second air-sting support (fig. 67(b)) attaches to the tunnel support system sting butt, and is generally mounted with the sting on the tunnel centerline. Exhaust simulation air is routed to the model through a 2.0-in-diameter hole in the sting. All instrumentation leads are routed on the exterior of the sting and secured in place.

High angle-of-attack sting-strut system. A sketch of a sting-strut model support system for powered models at high angles of attack is presented in figure 68(a) and a photograph of a model installation is shown in figure 68(b). This support system uses a strut in conjunction with the sting shown in figure 61(c) and attaches to the offset butt, which places the model on the tunnel centerline. The strut, and consequently, the model centerline can be set at incidence angles of 0°, 30°, and 60°, which allows models to be tested up to an angle of attack of 84°. Higher model angles of attack are possible with the use of nonzero degree knuckles. This system utilizes the dual high-pressure air supply of the wind tunnel by routing high-pressure air for exhaust simulation through two 0.5-in-diameter air lines. Each air line is capable of an airflow rate of up to 5 lb/sec. Instrumentation leads are routed through a passage in the strut trailing edge.

Semispan support system. A sketch of the semispan support system is shown in figure 69. This system consists of a 11- by 6-ft reflection plane located 5.1 ft from the lower test-section wall (2.65 ft from the tunnel centerline). The model axis of rotation is located at TS 134.00. High-pressure air is routed to the model by a flexible air line at airflow rates up to 15 lb/sec. Aerodynamic forces and moments are measured with the 1637S Langley force balance. The semispan support was designed for models with a wing semispan up to 6.5 ft and weighing up to 500 lb with the following aerodynamic loads:

Normal force	5700 lb
Axial force	500 lb
Pitching moment	15 000 in-lb
Yawing moment	15 000 in-lb
Rolling moment	215 000 in-lb

Model Propulsion Systems

The 16-Foot Transonic Tunnel is used primarily for internal (inlet and nozzle) and external aerodynamic studies of the propulsion and airframe integration characteristics of transport aircraft, high performance military aircraft, and spacecraft. Engine exhaust flow is simulated with flow-through nacelles, cold high-pressure air, or turbine powered simulators. Several high-pressure air systems are available for exhaust flow simulation. The two

primary high-pressure air systems can each deliver to a model, a separate individually controlled air supply with each providing an airflow of up to 15 lb/sec at temperatures from 70° to 130°F. The high-pressure air, which is continuously supplied from a central 5000 psi system, is held in an 1800 psi reservoir outside the building and regulated inside the building as required for a particular test condition. In addition, 3 lb/sec at 1800 psi and 1 lb/sec at 350 psi air systems are also available. All models that use the high-pressure air systems must have high-pressure components designed and tested in accordance with references 23 and 24. Design details not included in the subsequent brief descriptions of these systems may be found in reference 22.

Exhaust nozzle simulation systems. Several single- and twin-engine exhaust simulation systems that are used primarily for research of installed nozzle performance and nozzle/afterbody/empennage integration are available. Maximum flexibility was designed into these systems with respect to balance selection and hardware variations. The primary component of each exhaust simulation system is a flow transfer device that is designed to eliminate the transfer of axial momentum as air is passed from the nonmetric (not mounted on the force balance) to metric portions of the model. Either two flexible metal bellows (ref. 22) or nonmetallic diaphragms (ref. 25), which connect the nonmetric and the metric portions of the system, are used as seals and serve to compensate for the axial forces caused by pressurization.

The single-engine exhaust simulation systems were designed to be installed on the sting-strut model support. All sting struts have similar systems that duct high-pressure air through the sting strut into a high-pressure plenum and then into a single flow transfer bellows arrangement. The bellows arrangement is housed in a low-pressure plenum. This bellows arrangement directs the flow through either a choke plate or flow straightener, and into an instrumentation section that contains total-pressure and temperature probes. Hardware aft of the instrumentation section is chosen to meet test requirements and objectives.

One axisymmetric and three nonaxisymmetric external body shapes can be used. A sketch of one of the single-engine systems is presented in figure 70. Figures 64(a) and 64(b) show photographs of the single-engine system with the axisymmetric and the nonaxisymmetric bodies mounted on the sting-strut support system. Typical experimental investigations conducted with this hardware are reported in references 26 and 27.

Two separate twin-engine propulsion simulation systems are available for research at the 16-Foot Transonic Tunnel. One system is the sting-strut twin-jet system and

the other system is the wingtip-mounted twin-jet system. As was the case with the single-engine simulators, the designs allow maximum flexibility for balance selection and hardware arrangements. Further design details can be found in reference 22.

For the sting-strut twin-jet system, high-pressure air is ducted through the sting-strut support system and into a high-pressure plenum. At this point, the air is split into two flows and ducted into two separate bellows assemblies, which then exhaust into two tailpipes and exhaust nozzles. The two airflows can be balanced by manually operated flow control valves that are located in each air supply pipe. A photograph of the twin-jet system installed on the sting strut is presented in figure 64(c). Typical research conducted with this simulation system is reported in references 28 and 29.

The wingtip-mounted twin-jet system has high-pressure air ducted through the wingtip support centerbody into two high-pressure plenums, which are located on either side of the fuselage. These plenums direct the air into two separate bellows assemblies, which in turn supply the twin nozzles. Electrically operated flow control valves in each supply pipe serve to balance the flow into each bellows assembly. Two separate force balances with different load capacities and each with their own bellows assembly can be installed in the wingtip support system. One bellows assembly is also used in the twin-engine system previously described in this section. A sketch of a powered F-18 model that used the wingtip support system and bellows assemblies from the strut-mounted twin-jet simulation system is shown in figure 71(a). The bellows assembly used in this model is presented in figure 71(b). Photographs of other models that have utilized the wingtip support system are shown in figure 66. Typical experimental investigations conducted with this hardware are reported in references 30 to 33.

Propulsion simulators. Research on subsonic transport wing/pylon/nacelle(s) integration can be conducted with high-pressure air-driven turbofan or turboprop engine simulators. These simulation systems can be used in conventional sting-mounted models or with a model on the semispan support. Two air-driven simulators are available.

One turbofan simulator, shown in figure 72, has an air-driven, single-stage turbine that powers a single-stage compressor with a 4.1-in-diameter tip. At the design condition of 80 000 rpm, the turbine operates with a drive pressure of 350 psi and a fan pressure ratio of 1.6. Turbine drive gas requirements at design are (nominally) 1.3 lb/sec at 350 psi total pressure and 160°F total temperature. This pressure ratio and the ratio of fan diameter

to turbine diameter are representative of medium-bypass-ratio turbofan engines installed on transport aircraft.

Another turbofan simulator is used with the semi-span support system. A sketch of this simulator is presented in figure 73. This simulator has a four-stage turbine motor that is capable of powering fans from 6.6 in. to about 10 in. in diameter, which represents fan bypass ratios from 6 to about 12. The turbine air motor has a turbine diameter of 2.75 in. and produces up to 348 hp. Turbine drive gas requirements at design are (nominally) 4 lb/sec at 860 psi total pressure and 135°F total temperature. For a configuration with a bypass ratio of 9, the 22-blade fan has a 8.697-in. diameter.

Ejector mass flow system. An ejector mass flow measurement system, shown in figure 74, is available for use in the 16-Foot Transonic Tunnel to conduct inlet research. The ejector attaches to a model at an aerodynamic interface plane. Several high-pressure air attachment points are available to tailor a particular inlet installation. Maximum available ejector pressure is 1200 psi. Variation in mass flow is provided for by remotely actuating a conical plug to change duct exit area. Mass flow is computed from the ratio of the average flow plug exit static pressure to the average total pressure measured at the aerodynamic interface plane. A combination of 40 steady-state and fluctuating total-pressure probes that are arrayed in 5 rings with 8 probes each are used to measure duct flow characteristics. In addition, eight single fluctuating-pressure probes are available to be placed at various points at the aerodynamic interface plane. If complete fluctuating-pressure measurements are not needed, an array with 40 steady-state total-pressure probes with 8 static-pressure probes can be used. This array can be used with or without the eight single dynamic probes. Multiple combinations of the steady-state and fluctuating-pressure measurements can also be made because the measurement array is formed by using eight individual rakes that can be mixed in any combination.

Data Acquisition Systems

Steady-state data systems. The 16-Foot Transonic Tunnel steady-state data acquisition system is composed of ModComp REAL/Star 2000 computer running a real-time Unix operating system and interfaced with a Neff system 620 analog amplifier conditioning unit (analog-to-digital converters). A block diagram of this steady-state system is presented in figure 75. This system monitors and acquires data from the model and generates various alphanumeric displays. The system then calculates engineering units for all test measurements, free-

stream conditions, model attitude, jet parameters, and aerodynamic and pressure coefficients. The reduced data are then available for real-time graphic display or near-real-time tabular display on a line printer. The ModComp computer also interfaces with microprocessors to control wind tunnel free-stream conditions, model attitude, and jet parameter settings. The data acquisition system can acquire data from 128 analog (measured in microvolts) pressure, force, and temperature measurements, 52 digital measurements, and 1024 electronically scanned pressure (ESP) channels. A duplicate ModComp REAL/Star 2000 computer system is used in the model preparation area.

Data in a binary format are transferred from the Modcomp disk to a Sun Sparc-10 workstation on which postrun processing of the data are performed. A discussion of the data reduction procedures and formulas can be found in reference 34. A data analysis system, which is an integrated system of programs, is available that can plot data in several formats, tabulate data, and generate formatted data files.

Dynamic data system. The dynamic data acquisition system has two Metrum model 101e 28-track wide-band FM tape recorders for recording unsteady signals. A block diagram of this dynamic data system is presented in figure 76. Also available is a 28-track FM tape playback unit. Data analysis is performed with a 14-channel spectrum analyzer that has a frequency capability of 100 kHz with simultaneous 14-channel acquisition. A personal computer operates a windows-based system that controls the analyzer. Support hardware includes 40 channels of computer compatible amplifier filters and 21 two-channel oscilloscopes. Data are acquired through the personal computer that automatically starts the tape recorders at a specified time. The computer also records time codes, amplifier settings, and filter settings and stores them for later use in data reduction. This system also interfaces with the tunnel data acquisition system to obtain test parameters for data reduction.

Instrumentation

Force and moment measurements. Model force and moment measurements in the Langley 16-Foot Transonic Tunnel are made with internal, six-component, strain-gage balances. Langley Research Center maintains a very extensive inventory of balances that have a wide variation in both physical size and load capacity. The quoted accuracy of the balances is better than 0.5 percent of full scale (statistically determined). Although most of these balances could be used in the 16-Foot Transonic Tunnel, generally, balances such as those shown in

figure 77 are utilized. The 1613 and 1621 balances (figs. 77(a) and 77(b)) are typically used in powered model tests. The 1617 and 1629 balances (fig. 77(c)) are generally used in large models. In addition, a sketch of the six-component, flow-through 1627 balance is presented in figure 77(d) as it is used with the air-sting model support system (described in the "Air-sting supports" section). This balance is unique because it is a flow-through balance with its own internal bellows systems.

Pressure and temperature measurements. Individual measurements of model static and total pressures are made with either differential or absolute pressure transducers, which range in capacity from 0.5 psi to 2000 psi. Multiple pressure measurements utilize the electronically scanned pressure (ESP) system. The ESP system consists of a data acquisition and calibration unit, a pressure control unit, and pressure-measuring modules with 32, 48, or 64 ports or transducers each. The ESP system is designed to permit simultaneous measurement of up to 1024 model pressures. The ESP modules are usually mounted inside the model, with the 32-port modules that measure 1.0 in. by 2.2 in. by 1.8 in. (not including pressure tubing). A rack-mounted system (external to the model) with four modules that have 32-pressure ports each is also available. Transducer capacities range from 5 psi to 100 psi for the internal modules and either 100 psi or 250 psi modules are available for the rack-mounted system. The preferred individual thermocouples for measuring model temperatures are Chromel-Alumel, Iron-Constantan, or Copper-Constantan.

Weight flow rate measurements. Weight flow rate of the high-pressure air used for jet exhaust simulation in the 16-Foot Transonic Tunnel is measured by a multiple critical venturi system in each of the two air systems. The six critical-flow venturies (in each multiple critical venturi system) vary in size, so that 47 increments of flow area are available to meet test requirements. This system provides high accuracy of flow measurement, an extremely wide range of weight flow, small pressure losses, and a very low level of noise in the airstream and pipe structures. More information on this system may be found in references 22 and 35.

Flow-Visualization Methods

Oil-flow techniques. The 16-Foot Transonic Tunnel can diagnose model flow with various oil-flow techniques such as fluorescent oil flow and "permanent-record" oil flow. In the fluorescent oil-flow technique, an oil that fluoresces under ultraviolet light is applied to the

model prior to the tunnel run. The model is illuminated with ultraviolet light during the run, and the flow patterns shown by the fluorescing oil are photographed. An example of this technique is shown in figure 78. In the permanent-record oil-flow technique, a mixture of linseed-oil-based paint, tempura paint, and vacuum pump oil is applied to the model surface. Then the tunnel is run at the test condition until the mixture has dried on the model surface. This provides a permanent record of the surface flow that can be photographed in detail at a later time. Two examples of the permanent-record flow-visualization technique are presented in figure 79. Figure 79(a) shows the flow over a nozzle afterbody that was tested on the single-engine propulsion simulation system similar to that shown in figure 70. The flow at the aft portion of the juncture of the wing and body of a transport model is shown in figure 79(b).

Pressure-sensitive paint technique. The pressure-sensitive paint (PSP) technique is based on the measured luminescence of an excited, coated aerodynamic surface. The coating or PSP luminesces at levels that are inversely proportional to the surface static pressure in the oxygen environment when excited with a specified light source. A video luminescent imaging system is used to record PSP images at specified test conditions. The PSP technique is a relatively nonintrusive test because the PSP is applied to the area of interest in a thickness of 1 to 3 mil. The PSP can operate under static conditions of 0 to 1 atm and at temperatures ranging from about 50° to 130°F. The PSP is temperature sensitive, and therefore, is most applicable in environments where the surface thermal gradients can be kept to a minimum (maximum about 50°F). An example of PSP technique is presented in figure 80.

Laser sheet system. The laser sheet system consists of a 6-W argon-ion laser, a fiber-optic cable for transmitting the laser beam to the test section, and an optical head for converting the laser beam to a sheet of laser light. The laser is mounted on a table outside the plenum chamber. The fiber-optic cable transmits the laser beam from the laser into the plenum to the optical head, which is mounted behind the window in the top flat (flat 4). The laser sheet is transmitted perpendicular to the longitudinal axis of the test section and is capable of scanning fore and aft along the longitudinal axis of the model. In addition, the width of the laser sheet is variable. Tunnel flow is seeded with water vapor from the laser seeding system located in the quiescent chamber of the wind tunnel. The flow can be observed from a variety of viewpoints, such as a camera mounted on the strut head, a sidewall camera window, and various slots and portholes in the test section.

Flow Field Measurements

Flow field measurements can be made in the 16-Foot Transonic Tunnel with a laser velocimeter system, which is a nonintrusive flow measurement device that allows the determination of two components of the flow velocity (streamwise and vertical) at a point in the tunnel test section. A 6-W argon-ion laser provides the light source. The laser and associated optics are mounted on a movable scanning rig located in the test-section plenum behind the window in flat 2. This position allows the laser to survey a volume of the test section. The surveyed volume is limited by the size of the window in the test-section wall and the transmitting lens size. The volume that can be surveyed with the scan rig encompasses 21.5 in. forward of TS 134.25 and is 14.5 in. above and below the tunnel centerline. The spanwise movement of the sample volume is obtained by use of a zoom lens, which allows a movement of 39.0 in. about the tunnel centerline. The spatial resolution of the sample volume is a cylinder with a diameter of 0.012 in. and length of 0.24 in. Data are acquired and recorded on magnetic or optical disk by a computer dedicated to the laser velocimeter, which also reduces the data so that the velocities displayed are obtained almost in real time. The seeding system consists of an array of particle generators mounted on the fourth set of turning vanes in the quiescent chamber upstream of the antiturbulence screen. The seeding particles are polystyrene microspheres with a diameter of 0.8 μm that are suspended in alcohol. Figure 81 shows a flow field being measured with the laser velocimeter.

Concluding Remarks

The Langley 16-Foot Transonic Tunnel is a closed-circuit single-return atmospheric wind tunnel that has a slotted octagonal test section with continuous air exchange. The wind tunnel speed can be varied continuously over a Mach number range from 0.1 to 1.3. Test-section plenum suction is used for speeds above a Mach number of 1.05. Over a period of some 40 years, the wind tunnel has undergone many modifications. In the modifications completed in 1990, a new model support system with increased blockage, new fan blades, a catcher screen for the first set of turning vanes, process controllers for tunnel speed, model attitude, and jet flow for powered models were installed. This report presents a complete description of the Langley 16-Foot Transonic Tunnel, calibration procedures, and the results of the 1977 and the 1990 wind tunnel calibrations with test-section air removal. Comparisons with previous calibrations showed that the modifications made to the wind tunnel

had little or no effect on the aerodynamic characteristics of the tunnel.

NASA Langley Research Center
Hampton, VA 23681-0001
May 15, 1995

References

1. Corson, Blake W., Jr.; and Maynard, Julian D.: *The Langley 2,000-Horsepower Propeller Dynamometer and Tests at High Speed of an NACA 10-(3) (08)-03 Two-Blade Propeller*. NACA TN 2859, 1952. (Supersedes NACA RM L7L29.)
2. Runckel, Jack F.; and Hieser, Gerald: *Pressure-Rise and Leakage-Loss Characteristics of a Rotating Cowling*. NACA RM L50D07, 1950.
3. Wright, Ray H.; and Ward, Vernon G.: *NACA Transonic Wind-Tunnel Test Sections*. NACA Rep. 1231, 1955. (Supersedes NACA RM L8J06.)
4. Ward, Vernon G.; Whitcomb, Charles F.; and Pearson, Merwin D.: *An NACA Transonic Test Section With Tapered Slots Tested at Mach Numbers to 1.26*. NACA RM L50B14, 1950.
5. Ward, Vernon G.; Whitcomb, Charles F.; and Pearson, Merwin D.: *Air-Flow and Power Characteristics of the Langley 16-Foot Transonic Tunnel With Slotted Test Section*. NACA RM L52E01, 1952.
6. Maynard, Julian D.; Swihart, John M.; and Norton, Harry T., Jr.: *Effect of Blade-Section Camber on Aerodynamic Characteristics of Full-Scale Supersonic Type Propellers at Mach Numbers to 1.04*. NACA RM L56E10, 1956.
7. Runckel, Jack F.; and Swihart, John M.: *A Hydrogen Peroxide Hot-Jet Simulator for Wind-Tunnel Tests of Turbojet-Exit Models*. NASA MEMO 1-10-59L, 1959.
8. Little, B. H., Jr.; and Cabbage, James M., Jr.: *Effects of Combining Auxiliary Bleed With Ejector Pumping on the Power Requirements and Test-Section Flow of an 8-Inch by 8-Inch Slotted Tunnel*. NACA RM L55E25, 1955.
9. Corson, Blake W., Jr.; Runckel, Jack F.; and Igoe, William B.: *Calibration of the Langley 16-Foot Transonic Tunnel With Test Section Air Removal*. NASA TR R-423, 1974.
10. Corson, Blake W., Jr.: *The Aerodynamics of a Wind-Tunnel Fan*. NACA TN 820, 1941.
11. Capone, Francis J.; and Norton, Harry T., Jr.: *Subsonic Performance Characteristics of a Large-Scale 1.075-Pressure-Ratio Tip-Turbine Cruise-Fan Propulsion System*. NASA TN D-5314, 1969.
12. Yetter, J. A.; and Abeyounis, W. K.: *16-Foot Transonic Tunnel Test Section Flowfield Survey*. NASA TM-109157, 1994.
13. Wright, Ray H.; Ritchie, Virgil S.; and Pearson, Albin O.: *Characteristics of the Langley 8-Foot Transonic Tunnel With Slotted Test Section*. NACA Rep. 1389, 1958. (Supersedes

- NACA RM L51H10 by Wright and Ritchie and NACA RM L51K14 by Ritchie and Pearson.)
14. Goethert, Bernhard H.: *Transonic Wind Tunnel Testing*. AGARDograph No. 49, Pergamon Press, 1961.
 15. Norton, Harry T., Jr.; Runckel, Jack F.; and Pendergraft, Odis C., Jr.: *Transonic Performance of Two Convergent-Divergent Ejector Nozzles Designed for Corrected Secondary Flows of 3 and 9.4 Percent*. NASA TM X-909, 1964.
 16. Harvey, William D.: *Influence of Free-Stream Disturbances on Boundary-Layer Transition*. NASA TM-78635, 1978.
 17. Harvey, William D.; Stainback, P. Calvin; and Owen, F. Kevin: *Evaluation of Flow Quality in Two Large NASA Wind Tunnels at Transonic Speeds*. NASA TP-1737, 1980.
 18. Brooks, Joseph D.; Stainback, P. Calvin; and Brooks, Cuyler W., Jr.: Additional Flow Quality Measurements in the Langley Research Center 8-Foot Transonic Pressure Tunnel. *A Collection of Technical Papers—AIAA 11th Aerodynamic Testing Conference*, Mar. 1980, pp. 138–145. (Available as AIAA-80-0434.)
 19. Dougherty, N. S., Jr.; and Steinle, Frank W., Jr.: Transition Reynolds Number Comparisons in Several Major Transonic Tunnels. AIAA-74-627, July 1974.
 20. Couch, Lana M.; and Brooks, Cuyler W., Jr.: *Effect of Blockage Ratio on Drag and Pressure Distributions for Bodies of Revolution at Transonic Speeds*. NASA TN D-7331, 1973.
 21. Capone, Francis J.; and Coates, Edward M., Jr.: *Determination of Boundary-Reflected-Disturbance Lengths in the Langley 16-Foot Transonic Tunnel*. NASA TN D-4153, 1967.
 22. Staff of the Propulsion Aerodynamics Branch: *A User's Guide to the Langley 16-Foot Transonic Tunnel Complex, Revision 1*. NASA TM-102750, 1990. (Supersedes NASA TM-83186, Kathryn H. Peddrew, compiler.)
 23. *Wind-Tunnel Model Systems Criteria*. LHB 1710.15, NASA Langley Research Center, Aug. 1986.
 24. *Safety Regulations Covering Pressurized Systems*. LHB 1710.40, NASA Langley Research Center, Nov. 1988.
 25. Capone, Francis J.; and Price, Barry L.: A Flow-Transfer Device With Nonmetallic Diaphragms for Propulsion Wind Tunnel Models. AIAA-88-2048, May 1988.
 26. Wing, David J.; and Capone, Francis J.: *Performance Characteristics of Two Multiaxis Thrust-Vectoring Nozzles at Mach Numbers Up to 1.28*. NASA TP-3313, 1993.
 27. Carlson, John R.; and Asbury, Scott C.: *Two-Dimensional Converging-Diverging Rippled Nozzles at Transonic Speeds*. NASA TP-3440, 1994.
 28. Capone, Francis J.; Mason, Mary L.; and Carson, George T., Jr.: *Aeropropulsive Characteristics of Canted Twin Pitch-Vectoring Nozzles at Mach 0.20 to 1.20*. NASA TP-3060, 1991.
 29. Bangert, Linda S.; and Carson, George T., Jr.: *Effect of Afterbody Geometry on Aerodynamic Characteristics of Isolated Nonaxisymmetric Afterbodies at Transonic Mach Numbers*. NASA TP-3236, 1992.
 30. Leavitt, Laurence D.: *Effect of Empennage Location on Twin-Engine Afterbody/Nozzle Aerodynamic Characteristics at Mach Numbers From 0.6 to 1.2*. NASA TP-2116, 1983.
 31. Bangert, Linda S.; Leavitt, Laurence D.; and Reubush, David E.: *Effects of Afterbody Boattail Design and Empennage Arrangement on Aeropropulsive Characteristics of a Twin-Engine Fighter Model at Transonic Speeds*. NASA TP-2704, 1987.
 32. Capone, Francis J.; Mason, Mary L.; and Leavitt, Laurence D.: *An Experimental Investigation of Thrust Vectoring Two-Dimensional Convergent-Divergent Nozzles Installed in a Twin-Engine Fighter Model at High Angles of Attack*. NASA TM-4155, 1990.
 33. Asbury, Scott C.; and Capone, Francis J.: Multiaxis Thrust-Vectoring Characteristics of a Model Representative of the F/A-18 High-Alpha Research Vehicle at Angles of Attack from 0° to 70°. NASA TP-3531, 1995.
 34. Mercer, Charles E.; Berrier, Bobby L.; Capone, Francis J.; and Grayston, Alan M.: *Data Reduction Formulas for the 16-Foot Transonic Tunnel—NASA Langley Research Center, Revision 2*. NASA TM-107646, 1992. (Supersedes NASA TM-86319, Rev. 1.)
 35. Berrier, Bobby L.; Leavitt, Laurence D.; and Bangert, Linda S.: *Operating Characteristics of the Multiple Critical Venturi System and Secondary Calibration Nozzles Used for Weight-Flow Measurements in the Langley 16-Foot Transonic Tunnel*. NASA TM-86405, 1985.

Table 1. Major Dimensions of Langley 16-Foot Transonic Tunnel

Component	TS, ft	d_{eq} , ft	Shape	Component	TS, ft	d_{eq} , ft	Shape
Quiescent chamber begins	0	58.0	Circular	Power section begins	326.1	34.0	Circular
Antiturbulence screen	2.3	58.0	Circular	First set turning vanes ^b	349.1	34.0	Elliptical
Quiescent chamber ends	40.0	58.0	Circular	Catcher screen	349.1	34.0	Elliptical
Converging fillet begins	40.0	58.0	Circular	Drive fan 1 ^c	386.6	34.0	Circular
Converging transition begins	45.0	55.3	Octagonal	Drive fan 2 ^c	396.6	34.0	Circular
Converging octagon begins	70.0	27.1	Octagonal	Second set turning vanes ^{b,c}	434.1	34.0	Elliptical
Entrance liner begins	95.5	16.1	Octagonal	Power section ends	457.1	34.0	Circular
Entrance cone ends	107.0	15.9	Octagonal	Return passage begins	457.1	34.0	1.67° half angle
Test section begins	107.0	15.9	Octagonal	Return passage continues	500.3	36.7	3° half angle
Test section ends	138.0	15.9	Octagonal	Return passage ends	703.0	58.0	Circular
Diffuser entrance begins ^a	138.0	15.9	Octagonal	Lips of air exit vanes ^d	703.0	54.0	36-sided polygon
Diffuser entrance ends	154.0	17.3	16-sided polygon	Pressure drop screen	747.2	56.0	36-sided polygon
Diverging transition begins	154.0	17.3	16-sided polygon	Lips of air inlet vanes	773.0	54.0	36-sided polygon
Diverging transition ends	179.0	20.5	Circular	Cylindrical return begins	773.0	58.0	Circular
Conical diffuser begins	179.0	20.5	3° half angle	Third set turning vanes ^b	814.2	58.0	Elliptical
Diffuser continues	285.9	31.7	1.64° half angle	Fourth set turning vanes ^b	899.2	58.0	Elliptical
Diffuser ends	326.1	34.0	Circular	Cylindrical return ends	930.0	58.0	Circular

^aTest-section wall divergence, 0°.^bMinor axis on centerline.^cInclude nacelle cross-sectional area.^dAir exchange full open.

Table 2. Half-Width Dimensions for Test-Section Longitudinal Slot Shape 29

TS, ft	s_w , in.	TS, ft	s_w , in.	TS, ft	s_w , in.
107.5	0.000	120.0	1.500	134.5	1.500
108.0	0.155	121.0	1.500	135.0	1.500
108.5	0.290	122.0	1.500	135.5	1.500
109.0	0.420	123.0	1.500	136.0	1.500
109.5	0.545	124.0	1.500	136.083	1.597
110.0	0.670	125.0	1.500	136.167	1.727
110.5	0.780	125.5	1.500	136.250	1.857
111.0	0.890	126.0	1.500	136.333	1.997
111.5	0.990	126.5	1.500	136.417	2.177
112.0	1.095	127.0	1.500	136.500	2.507
112.5	1.165	127.5	1.500	136.583	2.627
113.0	1.245	128.0	1.500	136.667	2.827
113.5	1.320	128.5	1.500	136.750	3.037
114.0	1.380	129.0	1.500	136.833	3.227
114.5	1.440	129.5	1.500	136.917	3.407
115.0	1.480	130.0	1.500	137.0	3.567
115.5	1.500	130.5	1.500	137.5	4.457
116.0	1.500	131.0	1.500	138.0	5.207
116.5	1.500	131.5	1.500	138.5	5.221
117.0	1.500	132.0	1.500	139.0	5.265
117.5	1.500	132.5	1.500	139.5	5.337
118.0	1.500	133.0	1.500	140.0	5.439
118.5	1.500	133.5	1.500	140.27	5.506
119.0	1.500	134.0	1.500		

Table 3. Instrument Accuracies

Instrument	Range	Manufacturers quoted accuracy, percent full-scale	Accuracy
Ruska digital pressure gages	20 psi	0.012	0.002 psi
Pressure transducers	2.5 psi	0.250	0.006 psi
ESP transducer	15 psi	0.060	0.009 psi
Platinum resistance thermometer for T_{dp}	0° to 100°	0.25	0.25°
Platinum resistance thermometer for $T_{t,\infty}$	0° to 200°	0.25	0.50°

Table 4. Satic-Pressure Orifice Locations

(a) Centerline tube

TS, ft	Location	TS, ft	Location	TS, ft	Location
100.25	Left side	119.75	Left side	133.00	Right side
101.00	Left side	120.50	Left side	133.25	Left and right side
101.75	Left side	121.25	Left side	133.50	Right side
102.50	Left side	122.00	Left side	133.75	Right side
103.25	Left side	122.75	Left side	134.00	Left and right side
104.00	Left side	123.50	Left side	134.25	Right side
104.75	Left side	124.25	Left side	134.50	Right side
105.50	Left side	125.00	Left side	134.75	Left and right side
106.25	Left side	125.75	Left side	135.00	Right side
107.00	Left side	126.50	Left side	135.25	Right side
107.75	Left side	127.25	Left side	135.50	Left and right side
108.50	Left side	128.00	Left side	135.75	Right side
109.25	Left side	128.75	Left side	136.00	Right side
110.00	Left side	129.00	Right side	136.25	Left and right side
110.75	Left side	129.50	Left and right side	136.50	Right side
111.50	Left side	130.00	Right side	136.75	Right side
112.25	Left side	130.25	Left side	137.00	Left side
113.00	Left side	130.50	Right side	137.50	Right side
113.75	Left side	131.00	Left and right side	137.75	Left and right side
114.50	Left side	131.25	Right side	138.00	Right side
115.25	Left side	131.50	Right side	138.50	Left and right side
116.00	Left side	131.75	Left and right side	139.90	Right side
116.75	Left side	132.00	Right side	139.25	Left side
117.50	Left side	132.25	Right side	139.50	Right side
118.25	Left side	132.50	Left and right side	140.00	Left and right side
119.00	Left side	132.75	Right side		

Table 4. Concluded

(b) Test-section wall and diffuser

TS, ft	Location	TS, ft	Location	TS, ft	Location
108.0	Test section	129.5	Test section	152.0	Start diffuser and transition
108.5	Test section	130.0	Test section	152.5	Start diffuser and transition
110.0	Test section	130.5	Test section	153.0	Start diffuser and transition
111.0	Test section	131.5	Test section	153.5	Start diffuser and transition
111.5	Test section	133.5	Test section	168.0	Start diffuser and transition
113.0	Test section	134.0	Test section	174.0	Start diffuser and transition
113.5	Test section	134.5	Test section	180.0	Conical diffuser
114.5	Test section	135.5	Test section	186.0	Conical diffuser
115.0	Test section	137.0	Test section	192.0	Conical diffuser
115.5	Test section	137.5	Test section	198.0	Conical diffuser
116.0	Test section	138.0	Test section	206.0	Conical diffuser
117.0	Test section	143.5	Start diffuser and transition	216.0	Conical diffuser
119.5	Test section	144.0	Start diffuser and transition	218.0	Conical diffuser
121.0	Test section	144.5	Start diffuser and transition	224.0	Conical diffuser
123.5	Test section	145.0	Start diffuser and transition	236.0	Conical diffuser
124.0	Test section	145.5	Start diffuser and transition	248.0	Conical diffuser
125.5	Test section	146.0	Start diffuser and transition	260.0	Conical diffuser
126.0	Test section	146.5	Start diffuser and transition	272.0	Conical diffuser
126.5	Test section	148.5	Start diffuser and transition	284.0	Conical diffuser
127.0	Test section	149.0	Start diffuser and transition	296.0	Conical diffuser
127.5	Test section	150.0	Start diffuser and transition	308.0	Conical diffuser
128.0	Test section	150.5	Start diffuser and transition	320.0	Conical diffuser
129.0	Test section	151.0	Start diffuser and transition		

Table 5. Wind Tunnel Operational Characteristics

(a) Motor rotational characteristics

Run	Point	M_r	δ_{flat} , min	T_{dp} , °F	$T_{t,\infty}$, °F	N_{m1} , rpm	N_{m2} , rpm	N_{comp} , rpm	v_p , percent open
14	93	0.1000	0	57.0	92.1	48.5	52.6	0	0
12	43	0.2021	0	47.6	92.2	96.9	100.6	0	0
12	42	0.3015	0	48.9	97.5	142.2	145.5	0	0
12	41	0.4044	0	49.6	103.2	185.9	188.8	0	0
14	87	0.5028	0	60.5	114.2	224.7	227.5	0	0
14	84	0.6036	0	60.7	121.8	258.6	260.9	0	0
14	81	0.6535	0	60.5	126.6	273.9	275.9	0	0
12	38	0.7030	0	50.2	118.4	284.2	286.0	0	0
14	75	0.7285	0	60.5	133.3	294.1	295.7	0	0
11	21	0.7538	0	49.3	128.8	298.4	300.2	0	0
14	69	0.7795	0	60.1	138.8	306.6	308.1	0	0
16	23	0.8058	0	56.0	142.0	313.2	314.9	0	0
14	61	0.8284	0	59.8	145.5	318.0	319.6	0	0
14	57	0.8555	1	59.6	149.1	323.6	325.1	0	0
14	53	0.8809	3	59.5	151.9	328.2	329.8	0	0
11	3	0.9038	4	50.5	119.3	323.1	324.9	0	0
14	44	0.9304	7	58.6	157.7	336.4	338.3	0	0
12	27	0.9579	10	50.0	145.1	336.2	338.1	0	0
14	36	0.9816	12	64.2	164.2	344.1	346.1	0	0
11	20	1.0086	14	50.5	148.3	343.2	345.0	0	0
14	25	1.0595	7	64.0	167.4	350.1	351.7	481.1	15.1
12	14	1.1106	5	50.4	152.7	345.6	347.4	476.8	30.6
14	23	1.1351	10	63.8	168.7	348.3	350.0	480.7	38.1
10	8	1.1595	17.9	50.4	157.9	345.4	343.2	464.5	44.6
10	14	1.1796	26.5	58.2	163.7	347.6	345.4	540.3	35.9
11	44	1.2054	10	59.8	160.0	341.9	343.6	554.4	46.9
13	21	1.2262	14	62.7	166.0	343.1	344.7	534.1	55.4
11	38	1.2483	14.5	61.6	161.9	342.3	344.0	553.1	100.0
14	6	1.2714	21	60.1	168.1	355.6	356.5	551.9	100.0
13	7	1.2947	23	58.3	136.0	366.7	367.5	535.9	100.0

Table 5. Continued

(b) Power characteristics

Run	Point	M_r	δ_{flat} , min	T_{dp} , °F	P_{m1} , MW	P_{m2} , MW	P_{comp} , MW	P_{wt} , MW	P_{tot} , MW	$(P_{wt})_c$, MW	$(P_{\text{tot}})_c$, MW
14	93	0.1000	0	57.0	0.5	0.5	0	1.0	1.0	1.0	1.0
12	43	0.2021	0	47.6	1.0	1.0	0	2.0	2.0	1.9	1.9
12	42	0.3015	0	48.9	3.0	2.0	0	5.0	5.0	3.8	3.8
12	41	0.4044	0	49.6	6.0	4.0	0	10.0	10.0	6.5	6.5
14	87	0.5028	0	60.5	9.0	6.0	0	15.0	15.0	11.3	10.5
14	84	0.6036	0	60.7	11.5	8.5	0	20.0	20.0	15.4	15.4
14	81	0.6535	0	60.5	13.0	10.0	0	23.0	23.0	18.0	18.0
12	38	0.7030	0	50.2	15.0	12.0	0	27.0	27.0	21.7	21.0
14	75	0.7285	0	60.5	15.5	12.0	0	27.5	27.5	22.0	22.0
11	21	0.7538	0	49.3	16.0	12.0	0	28.0	28.0	22.3	22.9
14	69	0.7795	0	60.1	17.0	13.5	0	30.5	30.5	24.6	24.6
16	23	0.8058	0	56.0	17.0	14.0	0	31.0	31.0	24.8	26.0
14	61	0.8284	0	59.8	18.5	15.0	0	33.5	33.5	27.1	27.1
14	57	0.8555	1	59.6	19.0	16.5	0	35.5	35.5	28.8	28.8
14	53	0.8809	3	59.5	20.0	17.0	0	37.0	37.0	30.1	30.1
11	3	0.9038	4	50.5	21.0	18.0	0	39.0	39.0	32.6	32.6
14	44	0.9304	7	58.6	21.0	19.0	0	40.0	40.0	32.8	32.2
12	27	0.9579	10	50.0	22.0	20.0	0	42.0	42.0	34.6	34.6
14	36	0.9816	12	64.2	22.0	21.0	0	43.0	43.0	35.0	35.0
11	20	1.0086	14	50.5	23.0	21.0	0	44.0	44.0	36.1	36.1
14	25	1.0595	7	64.0	23.0	22.0	27.0	45.0	72.0	36.7	65.6
12	14	1.1106	5	50.4	23.0	23.0	27.0	46.0	73.0	37.8	66.6
14	23	1.1351	10	63.8	23.0	23.0	27.0	46.0	73.0	37.6	66.6
10	8	1.1595	17.9	50.4	24.0	23.0	27.0	47.0	74.0	38.4	67.2
10	14	1.1796	26.5	58.2	24.0	24.0	28.0	48.0	76.0	39.2	67.4
11	44	1.2054	10	59.8	23.0	23.0	29.0	46.0	75.0	37.6	67.6
13	21	1.2262	14	62.7	23.0	23.0	28.5	46.0	74.5	37.8	68.0
11	38	1.2483	14.5	61.6	23.0	23.0	29.0	46.0	75.0	37.4	68.3
14	6	1.2714	21	60.1	27.0	29.0	28.0	56.0	84.0	46.8	76.5
13	7	1.2947	23	58.3	29.0	30.0	28.0	59.0	87.0	49.3	78.7

Table 5. Concluded

(c) Horsepower characteristics

Run	Point	M_r	$P_{sh,m1}$, hp	$P_{sh,m2}$, hp	$P_{sh,comp}$, hp	$P_{sh,wt}$, hp	$P_{sh,tot}$, hp	$(P_{sh,wt})_c$, hp	$(P_{sh,tot})_c$, hp
14	93	0.1000	65	71	0	136	136	3 972	3 972
12	43	0.2021	286	297	0	583	583	4 481	4 481
12	42	0.3015	1 345	900	0	2 244	2 244	6 152	6 152
12	41	0.4044	3 572	2 394	0	5 966	5 966	9 891	9 891
14	87	0.5028	6 513	4 362	0	10 875	10 875	14 733	14 733
14	84	0.6036	9 599	7 125	0	16 724	16 724	20 188	20 188
14	81	0.6535	11 503	8 880	0	20 383	20 383	23 962	23 962
12	38	0.7030	13 791	11 074	0	24 865	24 865	28 324	28 324
14	75	0.7285	14 748	11 445	0	26 193	26 193	29 530	29 530
11	21	0.7538	15 450	11 616	0	27 065	27 065	27 776	27 776
14	69	0.7795	16 876	13 431	0	30 307	30 307	33 365	33 365
16	23	0.8058	17 237	14 236	0	31 474	31 474	34 330	34 330
14	61	0.8284	19 059	15 492	0	34 551	34 551	37 280	37 280
14	57	0.8555	19 919	17 345	0	37 273	37 273	37 084	37 084
14	53	0.8809	21 270	18 142	0	39 412	39 412	41 740	41 740
11	3	0.9038	22 004	18 934	0	40 938	40 938	43 806	43 806
14	44	0.9304	22 901	20 817	0	43 717	43 717	45 651	45 651
12	27	0.9579	23 984	21 908	0	45 892	45 892	47 778	47 778
14	36	0.9816	24 565	23 555	0	48 120	48 120	49 607	49 607
11	20	1.0086	25 607	23 482	0	49 089	49 089	50 684	50 684
14	25	1.0595	26 112	25 083	27 878	51 195	79 072	52 336	77 730
12	14	1.1106	25 782	25 912	27 628	51 693	79 322	52 963	78 166
14	23	1.1351	25 980	26 109	27 850	52 089	79 940	53 081	78 424
10	8	1.1595	26 894	25 604	26 911	52 498	79 409	53 327	77 751
10	14	1.1796	27 067	26 898	32 467	53 966	86 433	54 429	83 757
11	44	1.2054	25 509	25 635	34 500	51 144	85 644	52 138	83 475
13	21	1.2262	25 597	25 715	32 666	51 313	83 979	52 504	82 312
11	38	1.2483	25 539	25 664	34 421	51 203	85 625	52 122	83 340
14	6	1.2714	31 173	33 586	33 162	64 759	97 921	64 870	95 068
13	7	1.2947	34 537	35 813	32 200	70 350	102 550	69 843	99 044

Table 6. Test-Section Mach Number Distributions From Left Side of Centerline Tube

(a) TS 100.25 to 106.25

Run	Point	M_r	$M_{lo,l}$ at TS of—								
			100.25	101.00	101.75	102.50	103.25	104.00	104.75	105.50	106.25
14	93	0.1000	0.0940	0.0942	0.0957	0.0965	0.0953	0.0967	0.0948	0.0971	0.0950
12	43	0.2021	0.1938	0.2012	0.2022	0.1893	0.1886	0.2070	0.1956	0.1956	0.1967
12	42	0.3015	0.2927	0.2981	0.2989	0.2909	0.2913	0.3028	0.2961	0.2971	0.2978
12	41	0.4044	0.3941	0.3985	0.3993	0.3938	0.3939	0.4046	0.3993	0.4005	0.4018
14	87	0.5028	0.4909	0.4928	0.4940	0.4953	0.4949	0.4999	0.4981	0.5004	0.5019
14	84	0.6036	0.5868	0.5892	0.5912	0.5932	0.5924	0.5995	0.5970	0.5993	0.6020
14	81	0.6535	0.6337	0.6363	0.6384	0.6409	0.6408	0.6487	0.6456	0.6484	0.6513
12	38	0.7030	0.6789	0.6834	0.6862	0.6851	0.6859	0.6992	0.6930	0.6958	0.6991
14	75	0.7285	0.7026	0.7058	0.7089	0.7116	0.7119	0.7221	0.7181	0.7209	0.7241
11	21	0.7538	0.7253	0.7294	0.7321	0.7353	0.7357	0.7460	0.7424	0.7457	0.7493
14	69	0.7795	0.7477	0.7522	0.7555	0.7597	0.7597	0.7721	0.7671	0.7703	0.7745
16	23	0.8058	0.7708	0.7754	0.7786	0.7830	0.7853	0.7963	0.7924	0.7962	0.8003
14	61	0.8284	0.7885	0.7939	0.7984	0.8030	0.8042	0.8144	0.8126	0.8165	0.8209
14	57	0.8555	0.8108	0.8163	0.8218	0.8272	0.8284	0.8444	0.8379	0.8418	0.8467
14	53	0.8809	0.8305	0.8381	0.8439	0.8499	0.8522	0.8697	0.8625	0.8670	0.8726
11	3	0.9038	0.8466	0.8539	0.8609	0.8686	0.8716	0.8851	0.8830	0.8880	0.8937
14	44	0.9304	0.8629	0.8727	0.8808	0.8886	0.8924	0.9144	0.9063	0.9118	0.9185
12	27	0.9579	0.8766	0.8873	0.8967	0.9067	0.9126	0.9365	0.9290	0.9359	0.9436
14	36	0.9816	0.8836	0.8957	0.9507	0.9170	0.9237	0.9494	0.9425	0.9499	0.9591
11	20	1.0086	0.8891	0.9003	0.9110	0.9253	0.9336	0.9589	0.9541	0.9634	0.9747
14	25	1.0595	0.8917	0.9047	0.9168	0.9297	0.9380	0.9673	0.9610	0.9710	0.9825
12	14	1.1106	0.8925	0.9049	0.9170	0.9310	0.9399	0.9695	0.9638	0.9736	0.9853
14	23	1.1351	0.8932	0.9060	0.9178	0.9314	0.9402	0.9701	0.9639	0.9741	0.9854
10	8	1.1595	0.8941	0.8050	0.9172	0.9335	0.9430	0.9686	0.9649	0.9759	0.9875
10	14	1.1796	0.8932	0.9053	0.9176	0.9317	0.9412	0.9692	0.9650	0.9746	0.9870
11	44	1.2054	0.8934	0.9058	0.9181	0.9314	0.9407	0.9706	0.9651	0.9750	0.9867
13	21	1.2262	0.8932	0.9056	0.9174	0.9315	0.9415	0.9691	0.9644	0.9753	0.9870
11	38	1.2483	0.8932	0.9056	0.9178	0.9318	0.9409	0.9700	0.9648	0.9752	0.9867
14	6	1.2714	0.8927	0.9053	0.9173	0.9319	0.9409	0.9703	0.9646	0.9750	0.9847
13	7	1.2947	0.8933	0.9040	0.9152	0.9346	0.9443	0.9676	0.9649	0.9761	0.9865

Table 6. Continued

(b) TS 107.00 to 113.00

Run	Point	M_r	$M_{lo,l}$ at TS of—								
			107.00	107.75	108.50	109.25	110.00	110.75	111.50	112.25	113.00
14	93	0.1000	0.0948	0.0936	0.0985	0.0971	0.0976	0.0961	0.0995	0.0965	0.0973
12	43	0.2021	0.2019	0.1814	0.1995	0.2022	0.2010	0.1890	0.2017	0.1889	0.1938
12	42	0.3015	0.3006	0.2860	0.2989	0.3006	0.2999	0.2916	0.3004	0.2925	0.2958
12	41	0.4044	0.4032	0.3908	0.4016	0.4032	0.4023	0.3969	0.4036	0.3976	0.4004
14	87	0.5028	0.4994	0.4947	0.5006	0.5008	0.5007	0.5000	0.5017	0.5000	0.5008
14	84	0.6036	0.5990	0.5932	0.5999	0.6002	0.6001	0.5992	0.6011	0.5992	0.6005
14	81	0.6535	0.6477	0.6412	0.6492	0.6496	0.6491	0.6486	0.6502	0.6487	0.6500
12	38	0.7030	0.6965	0.6848	0.6966	0.6986	0.6977	0.6947	0.6988	0.6947	0.6971
14	75	0.7285	0.7201	0.7131	0.7221	0.7229	0.7222	0.7219	0.7236	0.7219	0.7201
11	21	0.7538	0.7447	0.7375	0.7462	0.7474	0.7467	0.7464	0.7479	0.7464	0.7480
14	69	0.7795	0.7701	0.7628	0.7723	0.7730	0.7730	0.7718	0.7736	0.7721	0.7738
16	23	0.8058	0.7948	0.7883	0.7975	0.7985	0.7976	0.7988	0.7991	0.7986	0.8001
14	61	0.8284	0.8162	0.8075	0.8188	0.8199	0.8196	0.8186	0.8206	0.8188	0.8210
14	57	0.8555	0.8419	0.8334	0.8446	0.8458	0.8458	0.8447	0.8473	0.8450	0.8469
14	53	0.8809	0.8679	0.8586	0.8713	0.8727	0.8723	0.8717	0.8738	0.8719	0.8741
11	3	0.9038	0.8886	0.8804	0.8915	0.8941	0.8948	0.8944	0.8960	0.8944	0.8965
14	44	0.9304	0.9136	0.9049	0.9182	0.9206	0.9208	0.9206	0.9235	0.9213	0.9240
12	27	0.9579	0.9388	0.9308	0.9443	0.9482	0.9490	0.9500	0.9523	0.9504	0.9525
14	36	0.9816	0.9555	0.9484	0.9643	0.9684	0.9707	0.9718	0.9743	0.9723	0.9749
11	20	1.0086	0.9709	0.9675	0.9840	0.9913	0.9969	1.0049	1.0096	1.0073	0.9962
14	25	1.0595	0.9819	0.9788	0.9993	1.0090	1.0185	1.0276	1.0409	1.0469	1.0561
12	14	1.1106	0.9846	0.9826	1.0041	1.0164	1.0272	1.0398	1.0507	1.0633	1.0757
14	23	1.1351	0.9852	0.9842	1.0061	1.0181	1.0300	1.0424	1.0552	1.0684	1.0832
10	8	1.1595	0.9867	0.9888	1.0077	1.0209	1.0334	1.0493	1.0608	1.0773	1.0940
10	14	1.1796	0.9867	0.9869	1.0084	1.0219	1.0346	1.0488	1.0634	1.0787	1.0977
11	44	1.2054	0.9867	0.9869	1.0094	1.0222	1.0353	1.0480	1.0622	1.0760	1.0938
13	21	1.2262	0.9862	0.9875	1.0092	1.0223	1.0354	1.0511	1.0645	1.0802	1.0978
11	38	1.2483	0.9868	0.9865	1.0093	1.0232	1.0371	1.0511	1.0660	1.0809	1.0992
14	6	1.2714	0.9850	0.9848	1.0066	1.0214	1.0367	1.0485	1.0644	1.0798	1.0997
13	7	1.2947	0.9857	0.9895	1.0085	1.0228	1.0385	1.0565	1.0688	1.0878	1.1066

Table 6. Continued

(c) TS 113.75 to 119.75

Run	Point	M_r	$M_{lo,l}$ at TS of—								
			113.75	114.50	115.25	116.00	116.75	117.50	118.25	119.00	119.75
14	93	0.1000	0.0959	0.0986	0.1130	0.0982	0.0955	0.0979	0.0952	0.0998	0.0946
12	43	0.2021	0.1991	0.2060	0.1952	0.1998	0.1883	0.1875	0.2028	0.1961	0.1971
12	42	0.3015	0.2988	0.3034	0.2964	0.2991	0.2921	0.2926	0.3013	0.2975	0.2971
12	41	0.4044	0.4024	0.4061	0.4003	0.4027	0.3971	0.3976	0.4041	0.4011	0.4012
14	87	0.5028	0.5004	0.5019	0.5018	0.5006	0.5003	0.5014	0.5010	0.5014	0.5003
14	84	0.6036	0.6005	0.6014	0.5993	0.6003	0.6000	0.6012	0.6005	0.6013	0.5998
14	81	0.6535	0.6493	0.6505	0.6475	0.6492	0.6493	0.6506	0.6497	0.6500	0.6490
12	38	0.7030	0.6975	0.7006	0.6972	0.6980	0.6957	0.6970	0.6991	0.6981	0.6969
14	75	0.7285	0.7230	0.7243	0.7226	0.7231	0.7229	0.7245	0.7233	0.7241	0.7224
11	21	0.7538	0.7467	0.7488	0.7444	0.7472	0.7477	0.7495	0.7477	0.7484	0.7470
14	69	0.7795	0.7731	0.7741	0.7730	0.7731	0.7730	0.7746	0.7737	0.7742	0.7728
16	23	0.8058	0.7982	0.7995	0.7984	0.7988	0.7999	0.8017	0.7984	0.7998	0.7980
14	61	0.8284	0.8199	0.8217	0.8196	0.8202	0.8196	0.8209	0.8203	0.8208	0.8196
14	57	0.8555	0.8456	0.8482	0.8464	0.8466	0.8464	0.8482	0.8469	0.8477	0.8460
14	53	0.8809	0.8731	0.8758	0.8733	0.8734	0.8736	0.8752	0.8741	0.8748	0.8733
11	3	0.9038	0.8952	0.8967	0.8957	0.8952	0.8959	0.8981	0.8957	0.8968	0.8950
14	44	0.9304	0.9226	0.9254	0.9233	0.9237	0.9232	0.9251	0.9240	0.9250	0.9229
12	27	0.9579	0.9511	0.9534	0.9518	0.9519	0.9522	0.9543	0.9525	0.9534	0.9518
14	36	0.9816	0.9731	0.9756	0.9737	0.9733	0.9733	0.9756	0.9736	0.9748	0.9730
11	20	1.0086	1.0004	1.0048	1.0005	0.9966	1.0039	1.0079	0.9987	1.0001	1.0018
14	25	1.0595	1.0578	1.0588	1.0579	1.0578	1.0633	1.0626	1.0541	1.0538	1.0498
12	14	1.1106	1.0806	1.0877	1.0867	1.0911	1.0960	1.1090	1.1105	1.1121	1.1095
14	23	1.1351	1.0921	1.1014	1.0986	1.1096	1.1158	1.1261	1.1351	1.1391	1.1361
10	8	1.1595	1.1049	1.1152	1.1166	1.1276	1.1390	1.1492	1.1572	1.1664	1.1673
10	14	1.1796	1.1112	1.1258	1.1273	1.1412	1.1548	1.1670	1.1770	1.1900	1.1987
11	44	1.2054	1.1049	1.1166	1.1116	1.1270	1.1357	1.1456	1.1580	1.1681	1.1702
13	21	1.2262	1.1098	1.1224	1.1260	1.1342	1.1469	1.1569	1.1671	1.1815	1.1817
11	38	1.2483	1.1125	1.1268	1.1249	1.1387	1.1509	1.1619	1.1734	1.1877	1.1902
14	6	1.2714	1.1154	1.1313	1.1373	1.1459	1.1584	1.1709	1.1830	1.2012	1.2034
13	7	1.2947	1.1212	1.1363	1.1491	1.1534	1.1703	1.1825	1.1876	1.2095	1.2154

Table 6. Continued

(d) TS 120.50 to 126.50

Run	Point	M_r	$M_{lo,l}$ at TS of—								
			120.50	121.25	122.00	122.75	123.50	124.25	125.00	125.75	126.50
14	93	0.1000	0.1007	0.0964	0.0953	0.0979	0.0989	0.0966	0.0979	0.0958	0.0963
12	43	0.2021	0.2003	0.1850	0.1867	0.1973	0.2033	0.1960	0.2016	0.1977	0.2013
12	42	0.3015	0.3000	0.2895	0.2911	0.2980	0.3014	0.2972	0.3003	0.2977	0.2996
12	41	0.4044	0.4032	0.3958	0.3966	0.4019	0.4043	0.4015	0.4034	0.4020	0.4020
14	87	0.5028	0.5016	0.5003	0.5004	0.5016	0.5025	0.5019	0.5020	0.5019	0.4989
14	84	0.6036	0.6009	0.6003	0.5999	0.6016	0.6023	0.6016	0.6014	0.6022	0.5986
14	81	0.6535	0.6503	0.6494	0.6493	0.6510	0.6518	0.6509	0.6505	0.6517	0.6480
12	38	0.7030	0.6988	0.6945	0.6952	0.6987	0.7006	0.6988	0.6990	0.6993	0.6960
14	75	0.7285	0.7239	0.7234	0.7229	0.7244	0.7255	0.7249	0.7240	0.7257	0.7213
11	21	0.7538	0.7482	0.7482	0.7481	0.7493	0.7502	0.7499	0.7487	0.7503	0.7458
14	69	0.7795	0.7741	0.7733	0.7731	0.7750	0.7760	0.7751	0.7744	0.7759	0.7709
16	23	0.8058	0.7996	0.8003	0.7999	0.8004	0.8010	0.8018	0.8002	0.8021	0.7965
14	61	0.8284	0.8209	0.8198	0.8193	0.8216	0.8229	0.8219	0.8211	0.8230	0.8178
14	57	0.8555	0.8475	0.8463	0.8460	0.8485	0.8494	0.8484	0.8478	0.8491	0.8438
14	53	0.8809	0.8749	0.8737	0.8732	0.8754	0.8769	0.8756	0.8750	0.8766	0.8711
11	3	0.9038	0.8960	0.8964	0.8955	0.8978	0.8985	0.8982	0.8963	0.8984	0.8920
14	44	0.9304	0.9248	0.9234	0.9234	0.9254	0.9267	0.9253	0.9248	0.9264	0.9205
12	27	0.9579	0.9531	0.9531	0.9526	0.9543	0.9556	0.9546	0.9534	0.9551	0.9487
14	36	0.9816	0.9752	0.9746	0.9741	0.9762	0.9773	0.9766	0.9755	0.9771	0.9708
11	20	1.0086	1.0043	1.0037	1.0021	1.0060	1.0071	1.0041	1.0019	1.0081	0.9997
14	25	1.0595	1.0492	1.0497	1.0481	1.0481	1.0528	1.0543	1.0527	1.0559	1.0480
12	14	1.1106	1.1101	1.1087	1.1047	1.1087	1.1108	1.1109	1.1078	1.1046	1.0929
14	23	1.1351	1.1409	1.1393	1.1360	1.1368	1.1407	1.1410	1.1383	1.1418	1.1308
10	8	1.1595	1.1703	1.1791	1.1787	1.1748	1.1756	1.1770	1.1767	1.1795	1.1683
10	14	1.1796	1.1961	1.2014	1.2028	1.2084	1.2078	1.2075	1.2077	1.2104	1.2005
11	44	1.2054	1.1749	1.1802	1.1809	1.1823	1.1868	1.1873	1.1902	1.1962	1.1902
13	21	1.2262	1.1898	1.1954	1.1981	1.2005	1.2036	1.2050	1.2074	1.2146	1.2083
11	38	1.2483	1.1983	1.2037	1.2065	1.2136	1.2146	1.2185	1.2202	1.2269	1.2213
14	6	1.2714	1.2098	1.2163	1.2194	1.2267	1.2315	1.2329	1.2358	1.2451	1.2363
13	7	1.2947	1.2212	1.2345	1.2390	1.2398	1.2445	1.2525	1.2518	1.2624	1.2519

Table 6. Continued

(e) TS 127.25 to 133.25

Run	Point	M_r	$M_{lo,l}$ at TS of—								
			127.25	128.00	128.75	129.50	130.25	131.00	131.75	132.50	133.25
14	93	0.1000	0.0984	0.0973	0.0999	0.1011	0.1002	0.1000	0.0996	0.0992	0.0993
12	43	0.2021	0.1933	0.1947	0.2017	0.2029	0.2015	0.2018	0.2019	0.2016	0.2020
12	42	0.3015	0.2954	0.2970	0.3006	0.3025	0.3004	0.3010	0.3011	0.3003	0.3013
12	41	0.4044	0.4003	0.4020	0.4031	0.4054	0.4023	0.4033	0.4037	0.4018	0.4038
14	87	0.5028	0.5022	0.5034	0.5017	0.5038	0.4998	0.5011	0.5017	0.4987	0.5018
14	84	0.6036	0.6026	0.6036	0.6015	0.6044	0.5994	0.6011	0.6019	0.5980	0.6023
14	81	0.6535	0.6523	0.6539	0.6514	0.6540	0.6484	0.6504	0.6513	0.6471	0.6519
12	38	0.7030	0.6990	0.7009	0.6997	0.7032	0.6968	0.6992	0.7003	0.6956	0.7013
14	75	0.7285	0.7263	0.7277	0.7250	0.7283	0.7219	0.7244	0.7256	0.7208	0.7265
11	21	0.7538	0.7514	0.7530	0.7497	0.7535	0.7468	0.7494	0.7507	0.7456	0.7517
14	69	0.7795	0.7766	0.7784	0.7754	0.7788	0.7718	0.7745	0.7749	0.7708	0.7771
16	23	0.8058	0.8037	0.8054	0.8010	0.8045	0.7973	0.8001	0.8018	0.7967	0.8033
14	61	0.8284	0.8241	0.8258	0.8224	0.8266	0.8194	0.8223	0.8239	0.8187	0.8256
14	57	0.8555	0.8503	0.8522	0.8486	0.8536	0.8459	0.8490	0.8507	0.8453	0.8524
14	53	0.8809	0.8748	0.8766	0.8743	0.8776	0.8693	0.8725	0.8742	0.8689	0.8761
11	3	0.9038	0.8998	0.9010	0.8969	0.9023	0.8931	0.8966	0.8983	0.8919	0.9000
14	44	0.9304	0.9280	0.9290	0.9253	0.9297	0.9207	0.9239	0.9255	0.9197	0.9268
12	27	0.9579	0.9569	0.9544	0.9533	0.9574	0.9480	0.9514	0.9529	0.9468	0.9542
14	36	0.9816	0.9790	0.9796	0.9756	0.9811	0.9713	0.9747	0.9762	0.9702	0.9773
11	20	1.0086	1.0095	1.0090	1.0036	1.0081	0.9980	1.0029	1.0033	0.9956	1.0045
14	25	1.0595	1.0620	1.0625	1.0560	1.0601	1.0485	1.0514	1.0547	1.0471	1.0552
12	14	1.1106	1.1052	1.1033	1.1019	1.1104	1.0977	1.1005	1.0972	1.0942	1.1030
14	23	1.1351	1.1364	1.1329	1.1263	1.1317	1.1210	1.1275	1.1306	1.1223	1.1285
10	8	1.1595	1.1846	1.1741	1.1624	1.1635	1.1498	1.1509	1.1492	1.1465	1.1554
10	14	1.1796	1.2139	1.2125	1.2007	1.1932	1.1770	1.1774	1.1740	1.1648	1.1708
11	44	1.2054	1.2077	1.2030	1.1990	1.2071	1.1920	1.1979	1.1974	1.1916	1.1978
13	21	1.2262	1.2249	1.2313	1.2243	1.2268	1.2134	1.2172	1.2205	1.2125	1.2173
11	38	1.2483	1.2391	1.2453	1.2411	1.2505	1.2330	1.2395	1.2416	1.2354	1.2415
14	6	1.2714	1.2546	1.2618	1.2597	1.2715	1.2601	1.2606	1.2639	1.2599	1.2659
13	7	1.2947	1.2742	1.2819	1.2775	1.2902	1.2796	1.2839	1.2860	1.2826	1.2874

Table 6. Concluded

(f) TS 134.00 to 140.00

Run	Point	M_r	$M_{lo,l}$ at TS of—								
			134.00	134.75	135.50	136.25	137.00	137.75	138.50	139.25	140.00
14	93	0.1000	0.0998	0.1000	0.0988	0.0986	0.0986	0.0979	0.0951	0.0931	0.0956
12	43	0.2021	0.2014	0.2015	0.2011	0.2005	0.2001	0.1986	0.1935	0.1820	0.1843
12	42	0.3015	0.3004	0.3004	0.3000	0.2989	0.2984	0.2961	0.2906	0.2817	0.2781
12	41	0.4044	0.4024	0.4024	0.4021	0.4004	0.3998	0.3968	0.3914	0.3820	0.3755
14	87	0.5028	0.5002	0.5001	0.4999	0.4976	0.4969	0.4931	0.4882	0.4814	0.4690
14	84	0.6036	0.6003	0.6003	0.6002	0.5973	0.5966	0.5919	0.5862	0.5768	0.5614
14	81	0.6535	0.6498	0.6499	0.6499	0.6467	0.6461	0.6409	0.6342	0.6243	0.6063
12	38	0.7030	0.6989	0.6991	0.6994	0.6957	0.6954	0.6896	0.6814	0.6689	0.6489
14	75	0.7285	0.7251	0.7244	0.7248	0.7213	0.7206	0.7147	0.7070	0.6950	0.6734
11	21	0.7538	0.7493	0.7496	0.7501	0.7463	0.7461	0.7396	0.7315	0.7190	0.6953
14	69	0.7795	0.7747	0.7753	0.7759	0.7722	0.7718	0.7653	0.7575	0.7441	0.7186
16	23	0.8058	0.8007	0.8015	0.8024	0.7988	0.7986	0.7917	0.7837	0.7702	0.7419
14	61	0.8284	0.8231	0.8240	0.8252	0.8216	0.8212	0.8144	0.8049	0.7893	0.7597
14	57	0.8555	0.8498	0.8509	0.8522	0.8485	0.8484	0.8411	0.8306	0.8131	0.7808
14	53	0.8809	0.8748	0.8760	0.8773	0.8735	0.8735	0.8652	0.8546	0.8352	0.7994
11	3	0.9038	0.8970	0.8983	0.9001	0.8961	0.8974	0.8880	0.8763	0.8549	0.8164
14	44	0.9304	0.9235	0.9249	0.9264	0.9225	0.9223	0.9129	0.8995	0.8744	0.8315
12	27	0.9579	0.9506	0.9520	0.9537	0.9498	0.9499	0.9398	0.9243	0.8954	0.8474
14	36	0.9816	0.9735	0.9751	0.9772	0.9740	0.9756	0.9656	0.9443	0.9108	0.8583
11	20	1.0086	1.0013	1.0018	1.0029	1.0010	1.0041	1.0010	0.9884	0.9340	0.8723
14	25	1.0595	1.0491	1.0518	1.0555	1.0530	1.0539	1.0509	1.0533	1.0521	0.9605
12	14	1.1106	1.1049	1.1070	1.1096	1.1031	1.1043	1.0953	1.0986	1.1038	1.0936
14	23	1.1351	1.1229	1.1267	1.1297	1.1289	1.1333	1.1309	1.1277	1.1246	1.1153
10	8	1.1595	1.1481	1.1543	1.1570	1.1462	1.1538	1.1533	1.1563	1.1562	1.1464
10	14	1.1796	1.1668	1.1699	1.1786	1.1726	1.1758	1.1695	1.1685	1.1783	1.1013
11	44	1.2054	1.1931	1.1947	1.2034	1.1985	1.1981	1.1892	1.1834	1.1790	1.1889
13	21	1.2262	1.2147	1.2162	1.2204	1.2181	1.2183	1.2146	1.2086	1.2062	1.2039
11	38	1.2483	1.2340	1.2387	1.2382	1.2462	1.2448	1.2360	1.2337	1.2324	1.2331
14	6	1.2714	1.2595	1.2613	1.2627	1.2400	1.2410	1.2338	1.2298	1.2275	1.2310
13	7	1.2947	1.2825	1.2851	1.2860	1.2864	1.2934	1.2846	1.2793	1.2873	1.2913

Table 7. Test-Section Mach Number Distributions From Right Side of Centerline Tube

(a) TS 129.00 to 132.75

Run	Point	M_r	$M_{lo,r}$ at TS of—											
			129.00	129.50	130.00	130.50	131.00	131.25	131.50	131.75	132.00	132.25	132.50	132.75
14	93	0.1000	0.1002	0.0997	0.1002	0.0996	0.0998	0.1004	0.993	0.1000	0.0902	0.1010	0.1006	0.1028
12	43	0.2021	0.2027	0.2024	0.2027	0.2027	0.2027	0.2027	0.2023	0.3023	0.2970	0.2030	0.2028	0.2024
12	42	0.3015	0.3023	0.3020	0.3024	0.3025	0.3026	0.3024	0.3021	0.3019	0.2994	0.3027	0.3025	0.3020
12	41	0.4044	0.4054	0.4051	0.4056	0.4057	0.4059	0.4055	0.4052	0.4050	0.4024	0.4058	0.4057	0.4050
14	87	0.5028	0.5037	0.5033	0.5040	0.5043	0.5045	0.5040	0.5036	0.5035	0.5017	0.5045	0.5043	0.5043
14	84	0.6036	0.6043	0.6038	0.6047	0.6051	0.6055	0.6048	0.6043	0.6042	0.6028	0.6054	0.6052	0.6046
14	81	0.6535	0.6538	0.6534	0.6543	0.6548	0.6553	0.6545	0.6540	0.6539	0.6526	0.6552	0.6551	0.6541
12	38	0.7030	0.7029	0.7025	0.7035	0.7041	0.7048	0.7038	0.7034	0.7031	0.7018	0.7046	0.7046	0.7034
14	75	0.7285	0.7282	0.7278	0.7289	0.7295	0.7301	0.7291	0.7287	0.7286	0.7274	0.7300	0.7300	0.7278
11	21	0.7538	0.7531	0.7528	0.7539	0.7546	0.7554	0.7542	0.7539	0.7538	0.7563	0.7552	0.7552	0.7531
14	69	0.7795	0.7784	0.7780	0.7792	0.7800	0.7807	0.7796	0.7792	0.7791	0.7781	0.7808	0.7808	0.7788
16	23	0.8058	0.8040	0.8037	0.8049	0.8058	0.8066	0.8055	0.8053	0.8052	0.8061	0.8068	0.8069	0.8035
14	61	0.8284	0.8263	0.8260	0.8273	0.8281	0.8291	0.8279	0.8275	0.8274	0.8265	0.8292	0.8293	0.8267
14	57	0.8555	0.8532	0.8529	0.8542	0.8551	0.8561	0.8549	0.8544	0.8543	0.8534	0.8562	0.8563	0.8532
14	53	0.8809	0.8792	0.8788	0.8801	0.8809	0.8819	0.8805	0.8800	0.8799	0.8790	0.8819	0.8818	0.8787
11	3	0.9038	0.9018	0.9014	0.9027	0.9037	0.9048	0.9031	0.9028	0.9025	0.9009	0.9024	0.9044	0.9029
14	44	0.9304	0.9292	0.9288	0.9300	0.9309	0.9319	0.9303	0.9298	0.9296	0.9286	0.9315	0.9315	0.9283
12	27	0.9579	0.9571	0.9565	0.9578	0.9588	0.9597	0.9580	0.9574	0.9571	0.9559	0.9589	0.9590	0.9571
14	36	0.9816	0.9807	0.9801	0.9814	0.9824	0.9833	0.9816	0.9810	0.9807	0.9796	0.9826	0.9825	0.9793
11	20	1.0086	1.0074	1.0076	1.0084	1.0102	1.0119	1.0099	1.0091	1.0080	1.0023	1.0084	1.0085	1.0066
14	25	1.0595	1.0615	1.0595	1.0605	1.0602	1.0606	1.0592	1.0597	1.0596	1.0572	1.0609	1.0604	1.0581
12	14	1.1106	1.1092	1.1092	1.1116	1.1105	1.1111	1.1082	1.1043	1.1017	1.1014	1.1078	1.1091	1.1051
14	23	1.1351	1.1306	1.1299	1.1324	1.1251	1.1386	1.1381	1.1377	1.1367	1.1337	1.1344	1.1354	1.1329
10	8	1.1595	1.1618	1.1519	1.1616	1.1576	1.1538	1.1650	1.1629	1.1610	1.1639	1.1614	1.1641	1.1621
10	14	1.1796	1.1750	1.1724	1.1758	1.1782	1.1742	1.1784	1.1777	1.1787	1.1790	1.1772	1.1863	1.1828
11	44	1.2054	1.2064	1.2062	1.2052	1.2081	1.2099	1.2069	1.2049	1.2039	1.2017	1.2057	1.2059	1.2029
13	21	1.2262	1.2307	1.2259	1.2282	1.2281	1.2302	1.2278	1.2275	1.2263	1.2256	1.2277	1.2264	1.2259
11	38	1.2483	1.2491	1.2493	1.2481	1.2489	1.2432	1.2505	1.2475	1.2483	1.2453	1.2516	1.2496	1.2462
14	6	1.2714	1.2680	1.2704	1.2750	1.2736	1.2727	1.2725	1.2728	1.2711	1.2705	1.2729	1.2745	1.2682
13	7	1.2947	1.2866	1.2891	1.2941	1.2981	1.2988	1.2932	1.2927	1.2937	1.2921	1.2966	1.2967	12940

Table 7. Continued

(b) TS 133.00 to 135.75

Run	Point	M_r	$M_{lo,r}$ at TS of—											
			133.00	133.25	133.50	133.75	134.00	134.25	134.50	134.75	135.00	135.25	135.50	135.75
14	93	0.1000	0.1001	0.1002	0.0997	0.1009	0.1005	0.0999	0.1002	0.0994	0.0977	0.999	0.0999	0.0995
12	43	0.2021	0.2029	0.2023	0.2024	0.2024	0.2020	0.2026	0.2023	0.2018	0.2022	0.2016	0.2019	0.2015
12	42	0.3015	0.3025	0.3018	0.3020	0.3019	0.3013	0.3024	0.3019	0.3012	0.3016	0.3007	0.3014	0.3007
12	41	0.4044	0.4056	0.4045	0.4051	0.4049	0.4041	0.4057	0.4049	0.4040	0.4045	0.4033	0.4043	0.4034
14	87	0.5028	0.5043	0.5031	0.5037	0.5035	0.5023	0.5045	0.5034	0.5023	0.5025	0.5015	0.5027	0.5016
14	84	0.6036	0.6052	0.6039	0.6047	0.6044	0.6030	0.6057	0.6045	0.6030	0.6035	0.6021	0.6037	0.6024
14	81	0.6535	0.6551	0.6536	0.6545	0.6543	0.6527	0.6558	0.6544	0.6528	0.6534	0.6519	0.6537	0.6523
12	38	0.7030	0.7072	0.7054	0.7065	0.7061	0.7046	0.7081	0.7065	0.7049	0.7060	0.7039	0.7060	0.7020
14	75	0.7285	0.7302	0.7284	0.7296	0.7293	0.7275	0.7313	0.7297	0.7297	0.7288	0.7270	0.7292	0.7276
11	21	0.7538	0.7543	0.7536	0.7548	0.7545	0.7528	0.7567	0.7550	0.7534	0.7543	0.7522	0.7546	0.7530
14	69	0.7795	0.7811	0.7792	0.7805	0.7803	0.7784	0.7825	0.7809	0.7790	0.7800	0.7781	0.7806	0.7790
16	23	0.8058	0.8074	0.8053	0.8069	0.8046	0.8091	0.8074	0.8074	0.8053	0.8071	0.8046	0.8073	0.8057
14	61	0.8284	0.8297	0.8277	0.8293	0.8290	0.8270	0.8317	0.8300	0.8281	0.8293	0.8273	0.8302	0.8258
14	57	0.8555	0.8567	0.8546	0.8562	0.8561	0.8540	0.8589	0.8571	0.8551	0.8564	0.8544	0.8575	0.8557
14	53	0.8809	0.8823	0.8800	0.8817	0.8816	0.8793	0.8844	0.8825	0.8803	0.8817	0.8796	0.8829	0.8810
11	3	0.9038	0.9038	0.9025	0.9045	0.9041	0.9019	0.9073	0.9052	0.9037	0.9044	0.9025	0.9061	0.9042
14	44	0.9304	0.9319	0.9293	0.9311	0.9308	0.9283	0.9338	0.9318	0.9296	0.9310	0.9288	0.9322	0.9303
12	27	0.9579	0.9595	0.9565	0.9586	0.9580	0.9553	0.9613	0.9591	0.9569	0.9589	0.9560	0.9597	0.9578
14	36	0.9816	0.9829	0.9799	0.9819	0.9816	0.9787	0.9847	0.9825	0.9802	0.9818	0.9795	0.9835	0.9817
11	20	1.0086	1.0083	1.0071	1.0098	1.0098	1.0065	1.0128	1.0101	1.0048	1.0075	1.0051	1.0092	1.0078
14	25	1.0595	1.0625	1.0583	1.0584	1.0579	1.0550	1.0615	1.0594	1.0573	1.0592	1.0577	1.0629	1.0609
12	14	1.1106	1.1071	1.1069	1.1130	1.1129	1.1109	1.1176	1.1132	1.1122	1.1143	1.1108	1.1175	1.1155
14	23	1.1351	1.1367	1.1307	1.1315	1.1326	1.1296	1.1348	1.1343	1.1356	1.1354	1.1305	1.0369	1.1368
10	8	1.1595	1.1618	1.1591	1.1616	1.1576	1.1538	1.1650	1.1629	1.1610	1.1639	1.1614	1.1641	1.1621
10	14	1.1796	1.1750	1.1725	1.1758	1.1782	1.1742	1.1784	1.1777	1.1787	1.1790	1.1772	1.1863	1.1828
11	44	1.2054	1.2069	1.1994	1.2034	1.2056	1.2046	1.2104	1.2034	1.2010	1.2066	1.2033	1.2108	1.2090
13	21	1.2262	1.2278	1.2230	1.2227	1.2250	1.2226	1.2297	1.2270	1.2209	1.2228	1.2232	1.2282	1.2264
11	38	1.2483	1.2484	1.2460	1.2489	1.2449	1.2436	1.2526	1.2517	1.2459	1.2427	1.2394	1.2505	1.2495
14	6	1.2714	1.2740	1.2687	1.2726	1.2705	1.2665	1.2752	1.2727	1.2715	1.2718	1.2670	1.2680	1.2674
13	7	1.2947	1.2977	1.2918	1.2962	1.2951	1.2937	1.2980	1.2930	1.2927	1.2972	1.2925	1.2969	1.2890

Table 7. Concluded
(c) TS 136.00 to 140.00

Run	Point	M_r	$M_{lo,r}$ at TS of—										
			136.00	136.25	136.50	136.75	137.50	137.75	138.00	138.50	139.00	139.50	140.00
14	93	0.1000	0.1003	0.0995	0.0993	0.0990	0.0995	0.0989	0.0991	0.980	0.0969	0.0963	0.0936
12	43	0.2021	0.2018	0.2010	0.2009	0.2008	0.1998	0.1996	0.1995	0.1982	0.1968	0.1947	0.1904
12	42	0.3015	0.3010	0.2999	0.2998	0.2996	0.2981	0.2978	0.2976	0.2956	0.2936	0.2902	0.2839
12	41	0.4044	0.4038	0.4022	0.4022	0.4018	0.3998	0.3993	0.3990	0.3964	0.3934	0.3888	0.3799
14	87	0.5028	0.5021	0.5001	0.5001	0.4996	0.4970	0.4963	0.4960	0.4925	0.4886	0.4826	0.4710
14	84	0.6036	0.6031	0.6006	0.6006	0.6001	0.5968	0.5959	0.5955	0.5911	0.5862	0.5784	0.5636
14	81	0.6535	0.6531	0.6504	0.6504	0.6498	0.6463	0.6453	0.6448	0.6399	0.6343	0.6256	0.6088
12	38	0.7030	0.7029	0.6998	0.7000	0.6994	0.6955	0.6944	0.6938	0.6885	0.6823	0.6724	0.6536
14	75	0.7285	0.7285	0.7255	0.7256	0.7250	0.7208	0.7198	0.7191	0.7135	0.7069	0.6963	0.6762
11	21	0.7538	0.7540	0.7508	0.7509	0.7503	0.7461	0.7449	0.7442	0.7381	0.7311	0.7197	0.6983
14	69	0.7795	0.7801	0.7768	0.7770	0.7764	0.7721	0.7709	0.7701	0.7637	0.7561	0.7440	0.7204
16	23	0.8058	0.8068	0.8035	0.8037	0.8032	0.7987	0.7975	0.7967	0.7899	0.7818	0.7687	0.7439
14	61	0.8284	0.8300	0.8265	0.8267	0.8263	0.8217	0.8205	0.8196	0.8125	0.8037	0.7896	0.7632
14	57	0.8555	0.8573	0.8537	0.8540	0.8536	0.8489	0.8474	0.8465	0.8386	0.8290	0.8133	0.7846
14	53	0.8809	0.8826	0.8788	0.8791	0.8786	0.8736	0.8719	0.8706	0.8618	0.8509	0.8336	0.8026
11	3	0.9038	0.9058	0.9022	0.9025	0.9022	0.8970	0.8950	0.8940	0.8843	0.8725	0.8536	0.8203
14	44	0.9304	0.9322	0.9282	0.9284	0.9281	0.9221	0.9200	0.9181	0.9070	0.8928	0.8712	0.8346
12	27	0.9579	0.9597	0.9556	0.9559	0.9558	0.9496	0.9471	0.9446	0.9314	0.9145	0.8897	0.8497
14	36	0.9816	0.9839	0.9803	0.9807	0.9811	0.9762	0.9734	0.9703	0.9541	0.9336	0.9051	0.8616
11	20	1.0086	1.0107	1.0075	1.0083	1.0096	1.0085	1.0095	1.0117	0.9952	0.9583	0.9216	0.8739
14	25	1.0595	1.0634	1.0594	1.0583	1.0591	1.0582	1.0598	1.0616	1.0643	1.0658	1.0617	0.9658
12	14	1.1106	1.1149	1.1096	1.1085	1.1092	1.1070	1.1057	1.1064	1.1103	1.1149	1.1196	1.0951
14	23	1.1351	1.1409	1.1365	1.1339	1.1377	1.1387	1.1411	1.1436	1.1401	1.1422	1.1413	1.1087
10	8	1.1595	1.1633	1.1547	1.1525	1.1538	1.1620	1.1644	1.1674	1.1697	1.1697	1.1731	1.1420
10	14	1.1796	1.1830	1.1803	1.1802	1.1818	1.2170	1.1837	1.1707	1.1868	1.1915	1.1929	1.0814
11	44	1.2054	1.2099	1.2051	1.2017	1.2034	1.1992	1.1993	1.2008	1.1957	1.2006	1.1970	1.1971
13	21	1.2262	1.2304	1.2293	1.2263	1.2255	1.2239	1.2235	1.2216	1.2223	1.2225	1.2174	1.2055
11	38	1.2483	1.2516	1.2500	1.2498	1.2487	1.2472	1.2507	1.2502	1.2476	1.2489	1.2488	1.2409
14	6	1.2714	1.2731	1.2708	1.2722	1.2764	1.2687	1.2717	1.2719	1.2695	1.2759	1.2727	1.2704
13	7	1.2947	1.2974	1.2967	1.2914	1.2955	1.2942	1.2968	1.2938	1.2947	1.2949	1.2990	1.2977

Table 8. Test-Section Pressure Distributions From Right Side of Centerline Tube

(a) TS 129.00 to 132.75

Run	Point	M_r	$p_{lo,r}/p_{t,\infty}$ at TS of—											
			129.00	129.50	130.00	130.50	131.00	131.25	131.50	131.75	132.00	132.25	132.50	132.75
14	93	0.1000	.99300	.99307	.99300	.99309	.99306	.99297	.99312	.99304	.99432	.99289	.99295	.99263
12	43	0.2021	.97176	.97184	.97177	.97176	.97177	.97176	.97186	.97189	.97330	.97169	.97172	.97184
12	42	0.3015	.93856	.93868	.93853	.93849	.93847	.93853	.93867	.93873	.93972	.93842	.93848	.93870
12	41	0.4044	.89300	.89315	.89290	.89282	.89274	.89292	.89310	.89319	.89443	.89276	.89284	.89318
14	87	0.5028	.84091	.84114	.84075	.84059	.84047	.84077	.84099	.84105	.84205	.84049	.84060	.84058
14	84	0.6036	.78140	.78164	.78111	.78085	.78064	.78108	.78134	.78140	.78231	.78066	.78078	.78116
14	81	0.6535	.75042	.75067	.75010	.74976	.74949	.75001	.75030	.75036	.75119	.74951	.74963	.75022
12	38	0.7030	.71907	.71929	.71864	.71828	.71784	.71849	.71875	.71890	.71979	.71796	.71800	.71875
14	75	0.7285	.70274	.70301	.70229	.70188	.70148	.70211	.70238	.70248	.70322	.70153	.70158	.70297
11	21	0.7538	.68653	.68674	.68602	.68557	.68506	.68582	.68605	.68613	.68448	.68520	.68521	.68599
14	69	0.7795	.67011	.67034	.66958	.66908	.66858	.66929	.66955	.66961	.67029	.66854	.66856	.66985
16	23	0.8058	.65341	.65363	.65282	.65226	.65170	.65243	.65258	.65264	.65204	.65159	.65154	.65373
14	61	0.8284	.63891	.63912	.63826	.63772	.63711	.63786	.63810	.63820	.63880	.63703	.63697	.63862
14	57	0.8555	.62143	.62163	.62076	.62024	.61955	.62036	.62066	.62073	.62132	.61945	.61945	.62142
14	53	0.8809	.60463	.60492	.60406	.60353	.60287	.60377	.60409	.60418	.60476	.60292	.60298	.60496
11	3	0.9038	.59014	.59038	.58955	.58889	.58815	.58927	.58947	.58965	.59070	.58856	.58842	.58938
14	44	0.9304	.57259	.57291	.57209	.57152	.57091	.57189	.57223	.57237	.57303	.57118	.57118	.57322
12	27	0.9579	.55498	.55536	.55454	.55395	.55334	.55441	.55478	.55499	.55575	.55383	.55377	.55497
14	36	0.9816	.54021	.54058	.53979	.53916	.53860	.53970	.54008	.54025	.54094	.53906	.53911	.54111
11	20	1.0086	.52374	.52362	.52314	.52204	.52098	.52219	.52268	.52339	.52688	.52312	.52305	.52421
14	25	1.0595	.49100	.49221	.49162	.49180	.49153	.49239	.49209	.49215	.49358	.49135	.49168	.49304
12	14	1.1106	.46302	.46302	.46162	.46226	.46196	.46359	.46588	.46735	.46755	.46383	.46311	.46539
14	23	1.1351	.45078	.45118	.44976	.44823	.44625	.44652	.44675	.44729	.44902	.44860	.44803	.44948
10	8	1.1595	.42991	.43308	.43164	.43268	.43311	.43475	.43662	.43673	.43759	.43494	.43425	.43526
10	14	1.1796	.40984	.41649	.41729	.41744	.41886	.42033	.42179	.42280	.42577	.42346	.42365	.42559
11	44	1.2054	.40895	.40905	.40960	.40805	.40707	.40868	.40974	.41028	.41144	.40934	.40923	.41081
13	21	1.2262	.39606	.39862	.39740	.39744	.39635	.39759	.39775	.39840	.39876	.39766	.39834	.39862
11	38	1.2483	.38651	.38644	.38706	.38661	.38442	.38582	.38733	.38695	.38849	.38524	.38624	.38800
14	6	1.2714	.37685	.37568	.37331	.37406	.37451	.37461	.37446	.37530	.37563	.37440	.37359	.37676
13	7	1.2947	.36754	.36628	.36381	.36184	.36153	.36428	.36453	.36400	.36481	.36260	.36256	.36385

Table 8. Continued

(b) TS 133.00 to 135.75

Run	Point	M_r	$p_{lo,r}/p_{t,\infty}$ at TS of—											
			133.00	133.25	133.50	133.75	134.00	134.25	134.50	134.75	135.00	135.25	135.50	135.75
14	93	0.1000	.99302	.99301	.99307	.99290	.99296	.99304	.99300	.99312	.99334	.99305	.99304	.99310
12	43	0.2021	.97172	.97186	.97185	.97185	.97195	.97178	.97187	.97200	.97191	.97207	.97197	.97209
12	42	0.3015	.93850	.93877	.93869	.93874	.93896	.93853	.93872	.93901	.93884	.93919	.93894	.93920
12	41	0.4044	.89286	.89330	.89311	.89322	.89362	.89284	.89323	.89366	.89341	.89400	.89353	.89396
14	87	0.5028	.84062	.84126	.84095	.84107	.84173	.84051	.84108	.84175	.84162	.84219	.84149	.84211
14	84	0.6036	.78078	.78162	.78113	.78129	.78217	.78049	.78126	.78217	.78187	.78271	.78171	.78253
14	81	0.6535	.74958	.75054	.74996	.75012	.75112	.74915	.75003	.75107	.75069	.75162	.75047	.75137
12	38	0.7030	.71787	.71902	.71828	.71856	.72955	.71728	.71831	.71935	.71862	.72002	.71863	.72965
14	75	0.7285	.70143	.70257	.70179	.70201	.70318	.70070	.70177	.70292	.70236	.70353	.70208	.70312
11	21	0.7538	.68577	.68624	.68543	.68567	.68678	.68422	.68532	.68635	.68578	.68711	.68558	.68664
14	69	0.7795	.66835	.66958	.66870	.66885	.67011	.66740	.66848	.66971	.66905	.67029	.66864	.66973
16	23	0.8058	.65121	.65254	.65151	.65179	.65302	.65007	.65121	.65255	.65143	.65302	.65126	.65234
14	61	0.8284	.63667	.63799	.63697	.63714	.63848	.63537	.63651	.63771	.63695	.63822	.63639	.63746
14	57	0.8555	.61915	.62052	.61948	.61958	.62094	.61775	.61892	.62020	.61939	.62065	.61867	.61981
14	53	0.8809	.60261	.60409	.60300	.60310	.60455	.60129	.60253	.60390	.60304	.60438	.60227	.60350
11	3	0.9038	.58880	.58967	.58835	.58861	.59004	.58658	.58791	.58886	.58847	.58969	.58738	.58856
14	44	0.9304	.57091	.57257	.57142	.57159	.57320	.56968	.57099	.57236	.57145	.57290	.57069	.57190
12	27	0.9579	.55348	.55535	.55408	.55444	.55611	.55234	.55374	.55512	.55386	.55571	.55339	.55457
14	36	0.9816	.53887	.54072	.53948	.53965	.54148	.53774	.53912	.54057	.53953	.54097	.53850	.53963
11	20	1.0086	.52318	.52394	.52223	.52223	.52429	.52043	.52208	.52534	.52368	.52511	.52261	.52351
14	25	1.0595	.49040	.49292	.49284	.49317	.49489	.49101	.49224	.49351	.49240	.49328	.49019	.49137
12	14	1.1106	.46422	.46434	.46085	.46087	.46202	.45817	.46071	.46132	.46007	.46208	.45827	.45942
14	23	1.1351	.44734	.45071	.45028	.44966	.45135	.44837	.44867	.44795	.44803	.45084	.44719	.44727
10	8	1.1595	.43326	.43473	.43337	.43557	.43770	.43149	.43262	.43371	.43209	.43345	.43196	.43306
10	14	1.1796	.42599	.42741	.42554	.42419	.42643	.42411	.42449	.42395	.42380	.42474	.41980	.42168
11	44	1.2054	.40867	.41268	.41054	.40935	.40993	.40680	.41058	.41183	.40882	.41062	.40658	.40753
13	21	1.2262	.39758	.40012	.40027	.39906	.40035	.39663	.39803	.40124	.40024	.40001	.39737	.39832
11	38	1.2483	.38686	.38812	.38661	.38871	.38934	.38470	.38518	.38818	.38981	.39152	.38583	.38631
14	6	1.2714	.37384	.37652	.37457	.37563	.37764	.3721	.37451	.37512	.37496	.37738	.37685	.37718
13	7	1.2947	.36203	.36495	.36276	.36330	.36401	.36188	.36437	.36449	.36230	.36462	.36243	.36633

Table 8. Concluded

(c) TS 136.00 to 140.00

Run	Point	M_r	$p_{lo,r}/p_{t,\infty}$ at TS of—										
			136.00	136.25	136.50	136.75	137.50	137.75	138.00	138.50	139.00	139.50	140.00
14	93	0.1000	.99299	.99311	.99313	.99317	.99310	.99319	.99315	.99331	.99345	.99354	.99386
12	43	0.2021	.97200	.97223	.97226	.97228	.97254	.97260	.97263	.97298	.97335	.97391	.97503
12	42	0.3015	.93907	.93950	.93954	.93962	.94019	.94031	.94040	.94115	.94194	.94321	.94559
12	41	0.4044	.89377	.89454	.89455	.89472	.89573	.89595	.89611	.89737	.89880	.90100	.90519
14	87	0.5028	.84183	.84296	.84295	.84322	.84469	.84507	.84528	.84721	.84938	.85268	.85902
14	84	0.6036	.78211	.78365	.78362	.78397	.78596	.78649	.78678	.78944	.79245	.79717	.80609
14	81	0.6535	.75089	.75257	.75258	.75294	.75517	.75580	.75614	.75920	.76269	.76817	.77858
12	38	0.7030	.71908	.72108	.72094	.72131	.72382	.72450	.72491	.72832	.73227	.73860	.75058
14	75	0.7285	.70249	.70449	.70441	.70481	.70748	.70812	.70858	.71223	.71652	.72332	.73621
11	21	0.7538	.68595	.68805	.68796	.68835	.69111	.69192	.69232	.69627	.70086	.70822	.72202
14	69	0.7795	.66896	.67115	.67103	.67138	.67420	.67498	.67548	.67966	.68459	.69248	.70740
16	23	0.8058	.65158	.65376	.65361	.65392	.65688	.65766	.65819	.66261	.66789	.67643	.69255
14	61	0.8284	.63652	.63897	.63861	.63890	.64189	.64267	.64325	.64790	.65359	.66280	.68001
14	57	0.8555	.61877	.62109	.62094	.62120	.62421	.62517	.62581	.63089	.63718	.64734	.66604
14	53	0.8809	.60242	.60489	.60472	.60502	.60826	.60935	.61018	.61585	.62290	.63412	.65435
11	3	0.9038	.58757	.58983	.58965	.58986	.59316	.59445	.59510	.60133	.60897	.62119	.64279
14	44	0.9304	.57074	.57325	.57314	.57335	.57711	.57845	.57968	.58680	.59585	.60981	.63350
12	27	0.9579	.55334	.55590	.55571	.55582	.55973	.56130	.56287	.57122	.58195	.59786	.62373
14	36	0.9816	.53824	.54050	.54026	.53997	.54304	.54479	.54673	.55685	.56984	.58798	.61599
11	20	1.0086	.52168	.52365	.52315	.52237	.52307	.52245	.52107	.53123	.55427	.55747	.60807
14	25	1.0595	.48985	.49228	.49291	.49245	.49294	.49204	.49097	.48932	.48845	.49086	.54955
12	14	1.1106	.45973	.46280	.46341	.46300	.46429	.46507	.46467	.46237	.45972	.45702	.47118
14	23	1.1351	.44497	.44743	.44889	.44677	.44617	.44485	.44343	.44537	.44424	.44473	.46329
10	8	1.1595	.43243	.43721	.43843	.43767	.43313	.43179	.43017	.42888	.42887	.42700	.44432
10	14	1.1796	.42158	.42308	.42313	.42225	.40328	.42123	.42833	.41951	.41695	.41620	.47924
11	44	1.2054	.40706	.40962	.41145	.41053	.41279	.41273	.41196	.41468	.41206	.41401	.41392
13	21	1.2262	.39625	.39683	.39841	.39880	.39964	.39987	.40084	.40047	.40037	.40308	.40945
11	38	1.2483	.38521	.38605	.38617	.38670	.38750	.38570	.38598	.38730	.38662	.38666	.39076
14	6	1.2714	.37431	.37543	.37475	.37265	.37649	.37501	.37489	.37613	.37287	.37452	.37556
13	7	1.2947	.36353	.36254	.36517	.36314	.36377	.36251	.36397	.36351	.36342	.36141	.36204

Table 9. Wind Tunnel Wall Mach Number Distributions

(a) TS 108.0 to 114.5

Run	Point	M_r	$M_{lo,wall}$ at TS of—							
			108.0	108.5	110.0	111.0	111.5	113.0	113.5	114.5
14	93	0.1000	0.0997	0.0995	0.0981	0.0979	0.0983	0.0970	0.1070	0.1012
12	43	0.2021	0.2013	0.2016	0.2009	0.2004	0.1995	0.2003	0.2003	0.2005
12	42	0.3015	0.3004	0.3012	0.3000	0.3000	0.2987	0.3007	0.2995	0.2995
12	41	0.4044	0.4026	0.4034	0.4029	0.4029	0.4011	0.4043	0.4019	0.4021
14	87	0.5028	0.5008	0.5021	0.5012	0.5010	0.4994	0.5035	0.4998	0.5000
14	84	0.6036	0.6005	0.6025	0.6012	0.6009	0.5984	0.6036	0.5992	0.5995
14	81	0.6535	0.6495	0.6516	0.6498	0.6498	0.6472	0.6531	0.6481	0.6484
12	38	0.7030	0.6973	0.6997	0.6985	0.6977	0.6949	0.7014	0.6960	0.6957
14	75	0.7285	0.7227	0.7245	0.7239	0.7231	0.7201	0.7273	0.7217	0.7210
11	21	0.7538	0.7475	0.7496	0.7484	0.7477	0.7446	0.7519	0.7548	0.7455
14	69	0.7795	0.7718	0.7746	0.7734	0.7732	0.7696	0.7772	0.7712	0.7710
16	23	0.8058	0.7981	0.8002	0.7994	0.7985	0.7950	0.8028	0.7965	0.7965
14	61	0.8284	0.8190	0.8217	0.8209	0.8200	0.8165	0.8245	0.8181	0.8181
14	57	0.8555	0.8453	0.8479	0.8476	0.8466	0.8431	0.8517	0.8447	0.8450
14	53	0.8809	0.8705	0.8735	0.8735	0.8725	0.8691	0.8780	0.8711	0.8711
11	3	0.9038	0.8926	0.8959	0.8962	0.8956	0.8923	0.9011	0.8936	0.8936
14	44	0.9304	0.9181	0.9217	0.9236	0.9233	0.9193	0.9289	0.9216	0.9215
12	27	0.9579	0.9433	0.9479	0.9512	0.9510	0.9474	0.9569	0.9491	0.9487
14	36	0.9816	0.9629	0.9680	0.9739	0.9747	0.9705	0.9801	0.9726	0.9721
11	20	1.0086	0.9823	0.9894	1.0014	1.0055	1.0016	1.0055	0.9986	0.9999
14	25	1.0595	0.9976	1.0062	1.0254	1.0351	1.0358	1.0565	1.0488	1.0508
12	14	1.1106	1.0044	1.0141	1.0353	1.0487	1.0511	1.0788	1.0729	1.0767
14	23	1.1351	1.0054	1.0159	1.0387	1.0545	1.0578	1.0891	1.0853	1.0908
10	8	1.1595	1.0088	1.0204	1.0443	1.0628	1.0672	1.1029	1.1006	1.1090
10	14	1.1796	1.0095	1.0212	1.0466	1.0674	1.0727	1.1115	1.1105	1.1226
11	44	1.2054	1.0085	1.0201	1.0439	1.0628	1.0667	1.1019	1.0996	1.1081
13	21	1.2262	1.0096	1.0214	1.0459	1.0652	1.0701	1.1075	1.1055	1.1159
11	38	1.2483	1.0101	1.0219	1.0469	1.0675	1.0720	1.1096	1.1086	1.1200
14	6	1.2714	1.0092	1.0216	1.0476	1.0689	1.0743	1.1149	1.1139	1.1279
13	7	1.2947	1.0125	1.0246	1.0506	1.0734	1.0792	1.1203	1.1197	1.1345

Table 9. Continued

(b) TS 115.0 to 125.5

Run	Point	M_r	$M_{lo,wall}$ at TS of—							
			115.0	116.0	117.0	119.5	121.0	123.5	124.0	125.5
14	93	0.1000	0.1002	0.0995	0.1002	0.1003	0.0995	0.0995	0.1014	0.0993
12	43	0.2021	0.1997	0.2013	0.2001	0.1996	0.2009	0.2011	0.2022	0.2006
12	42	0.3015	0.2991	0.3011	0.2993	0.2989	0.2999	0.3004	0.3016	0.3004
12	41	0.4044	0.4013	0.4030	0.4017	0.4010	0.4025	0.4028	0.4033	0.4031
14	87	0.5028	0.4994	0.5018	0.4993	0.4986	0.5010	0.5009	0.5022	0.5014
14	84	0.6036	0.5987	0.6015	0.5989	0.5981	0.6007	0.6007	0.6019	0.6012
14	81	0.6535	0.6471	0.6508	0.6477	0.6462	0.6495	0.6498	0.6513	0.6505
12	38	0.7030	0.6951	0.6991	0.6951	0.6941	0.6974	0.6987	0.6992	0.6986
14	75	0.7285	0.7201	0.7245	0.7205	0.7195	0.7231	0.7234	0.7250	0.7237
11	21	0.7538	0.7445	0.7495	0.7450	0.7434	0.7474	0.7480	0.7495	0.7489
14	69	0.7795	0.7698	0.7743	0.7702	0.7689	0.7725	0.7729	0.7746	0.7734
16	23	0.8058	0.7954	0.8004	0.7958	0.7939	0.7985	0.7990	0.8010	0.7993
14	61	0.8284	0.8166	0.8216	0.8176	0.8152	0.8199	0.8201	0.8220	0.8211
14	57	0.8555	0.8435	0.8488	0.8438	0.8416	0.8468	0.8468	0.8491	0.8478
14	53	0.8809	0.8693	0.8751	0.8699	0.8682	0.8730	0.8732	0.8752	0.8741
11	3	0.9038	0.8921	0.8977	0.8926	0.8901	0.8958	0.8959	0.8980	0.8966
14	44	0.9304	0.9196	0.9257	0.9204	0.9183	0.9240	0.9242	0.9259	0.9247
12	27	0.9579	0.9472	0.9532	0.9478	0.9455	0.9516	0.9522	0.9543	0.9526
14	36	0.9816	0.9697	0.9763	0.9704	0.9682	0.9745	0.9747	0.9772	0.9762
11	20	1.0086	0.9977	1.0027	0.9980	0.9949	1.0017	1.0028	1.0047	1.0031
14	25	1.0595	1.0496	1.0616	1.0554	1.0461	1.0491	1.0511	1.0534	1.0547
12	14	1.1106	1.0774	1.0933	1.0934	1.0990	1.1070	1.1047	1.1070	1.1030
14	23	1.1351	1.0922	1.1103	1.1121	1.1211	1.1351	1.1364	1.1373	1.1340
10	8	1.1595	1.1100	1.1303	1.1329	1.1489	1.1681	1.1738	1.1758	1.1712
10	14	1.1796	1.1236	1.1450	1.1501	1.1730	1.1908	1.2024	1.2072	1.2008
11	44	1.2054	1.1094	1.1298	1.1330	1.1517	1.1733	1.1886	1.1906	1.1923
13	21	1.2262	1.1170	1.1383	1.1428	1.1649	1.1855	1.2053	1.2028	1.2100
11	38	1.2483	1.1211	1.1428	1.1491	1.1731	1.1935	1.2173	1.2206	1.2243
14	6	1.2714	1.1291	1.1514	1.1587	1.1874	1.2083	1.2342	1.2403	1.2431
13	7	1.2947	1.1358	1.1592	1.1664	1.1956	1.2200	1.2457	1.2444	1.2584

Table 9. Continued

(c) TS 126.0 to 130.0

Run	Point	M_r	$M_{lo,wall}$ at TS of—							
			126.0	126.5	127.0	127.5	128.0	129.0	129.5	130.0
14	93	0.1000	0.1016	0.0986	0.1012	0.0996	0.1002	0.1019	0.1013	0.0994
12	43	0.2021	0.2016	0.2004	0.2002	0.2000	0.2014	0.2012	0.2007	0.1996
12	42	0.3015	0.3007	0.2998	0.2999	0.3001	0.3016	0.3001	0.2993	0.2985
12	41	0.4044	0.4036	0.4020	0.4024	0.4029	0.4035	0.4021	0.4010	0.4005
14	87	0.5028	0.5024	0.5000	0.5006	0.5016	0.5019	0.4999	0.4985	0.4981
14	84	0.6036	0.6025	0.5992	0.6002	0.6014	0.6020	0.5991	0.5976	0.5969
14	81	0.6535	0.6520	0.6486	0.6497	0.6504	0.6511	0.6481	0.6486	0.6458
12	38	0.7030	0.6998	0.6962	0.6972	0.6984	0.6991	0.6959	0.6942	0.6937
14	75	0.7285	0.7257	0.7217	0.7231	0.7241	0.7250	0.7217	0.7198	0.7188
11	21	0.7538	0.7504	0.7495	0.7474	0.7486	0.7496	0.7464	0.7443	0.7434
14	69	0.7795	0.7754	0.7711	0.7724	0.7735	0.7744	0.7709	0.7691	0.7679
16	23	0.8058	0.8013	0.7968	0.7985	0.7997	0.8008	0.7968	0.7950	0.7940
14	61	0.8284	0.8526	0.8477	0.8489	0.8508	0.8517	0.8473	0.8444	0.8154
14	57	0.8555	0.8502	0.8451	0.8468	0.8483	0.8496	0.8450	0.8424	0.8419
14	53	0.8809	0.8761	0.8707	0.8722	0.8738	0.8750	0.8706	0.8683	0.8675
11	3	0.9038	0.8990	0.8931	0.8948	0.8963	0.8973	0.8931	0.8905	0.8896
14	44	0.9304	0.9272	0.9217	0.9230	0.9246	0.9258	0.9211	0.9183	0.9171
12	27	0.9579	0.9551	0.9488	0.9508	0.9520	0.9535	0.9484	0.9452	0.9443
14	36	0.9816	0.9784	0.9727	0.9739	0.9757	0.9771	0.9721	0.9687	0.9674
11	20	1.0086	1.0063	0.996	1.0010	1.0027	1.0039	0.9991	0.9959	0.9945
14	25	1.0595	1.0583	1.0514	1.0507	1.0531	1.0574	1.0525	1.0498	1.0481
12	14	1.1106	1.1069	1.1005	1.1015	1.1032	1.1006	1.0945	1.0904	1.0906
14	23	1.1351	1.1360	1.1292	1.1289	1.1326	1.1341	1.1259	1.1208	1.1205
10	8	1.1595	1.1728	1.1640	1.1639	1.1659	1.1664	1.1589	1.1546	1.0874
10	14	1.1796	1.2035	1.1934	1.1931	1.1933	1.1934	1.1852	1.1788	1.1784
11	44	1.2054	1.1964	1.1880	1.1900	1.1943	1.1982	1.1920	1.1861	1.1878
13	21	1.2262	1.2163	1.2078	1.2100	1.2115	1.2182	1.2105	1.2058	1.2067
11	38	1.2483	1.2300	1.2243	1.2255	1.2287	1.2336	1.2294	1.2220	1.2237
14	6	1.2714	1.2505	1.2443	1.2476	1.2501	1.2535	1.2482	1.2444	1.2448
13	7	1.2947	1.2267	1.2606	1.2644	1.2675	1.2750	1.2666	1.2604	1.2649

Table 9. Continued

(d) TS 130.5 to 138.0

Run	Point	M_r	$M_{lo,wall}$ at TS of—							
			130.5	131.5	133.5	134.0	135.5	137.0	137.5	138.0
14	93	0.1000	0.1000	0.985	0.1001	0.0992	0.1011	0.0994	0.0998	0.10105
12	43	0.2021	0.1997	0.2011	0.1997	0.2009	0.2004	0.2013	0.2017	0.2013
12	42	0.3015	0.2988	0.3005	0.2992	0.2991	0.3001	0.3011	0.3019	0.3030
12	41	0.4044	0.4005	0.4031	0.4007	0.4008	0.4024	0.4039	0.4052	0.4056
14	87	0.5028	0.4983	0.5020	0.4984	0.4987	0.5008	0.5030	0.5039	0.5047
14	84	0.6036	0.5972	0.6018	0.5973	0.5973	0.6009	0.6026	0.6044	0.6052
14	81	0.6535	0.6464	0.6516	0.6464	0.6465	0.6497	0.6527	0.6544	0.6558
12	38	0.7030	0.6942	0.6997	0.6940	0.6940	0.6980	0.7015	0.7033	0.7043
14	75	0.7285	0.7195	0.7253	0.7195	0.7193	0.7234	0.7272	0.7293	0.7307
11	21	0.7538	0.7442	0.7504	0.7445	0.7443	0.7486	0.7526	0.7547	0.7564
14	69	0.7795	0.7688	0.7753	0.7690	0.7689	0.7739	0.7781	0.7807	0.7829
16	23	0.8058	0.7951	0.8017	0.7954	0.7955	0.8003	0.8047	0.8073	0.8102
14	61	0.8284	0.8157	0.8231	0.8164	0.8166	0.8223	0.8269	0.8249	0.8322
14	57	0.8555	0.8426	0.8501	0.8429	0.8432	0.8489	0.8543	0.8565	0.8598
14	53	0.8809	0.8675	0.8754	0.8680	0.8676	0.8763	0.8776	0.8808	0.8841
11	3	0.9038	0.8901	0.8976	0.8898	0.8897	0.8955	0.9000	0.9030	0.9067
14	44	0.9304	0.9175	0.9252	0.9177	0.9177	0.9228	0.9260	0.9288	0.9329
12	27	0.9579	0.9446	0.9522	0.9439	0.9434	0.9490	0.9515	0.9545	0.9578
14	36	0.9816	0.9681	0.9759	0.9676	0.9673	0.9729	0.9750	0.9782	0.9820
11	20	1.0086	0.9949	1.0036	0.9939	0.9936	0.9985	1.0013	1.0050	1.0116
14	25	1.0595	1.0460	1.0540	1.0449	1.0460	1.0498	1.0508	1.0539	1.0612
12	14	1.1106	1.0930	1.1034	1.0924	1.0920	1.0991	1.1028	1.1015	1.1039
14	23	1.1351	1.1167	1.1264	1.1188	1.1200	1.1270	1.1238	1.1210	1.1254
10	8	1.1595	1.1499	1.1590	1.1444	1.1449	1.1507	1.1541	1.1527	1.1520
10	14	1.1796	1.1764	1.1873	1.1689	1.1661	1.1720	1.1719	1.1700	1.1714
11	44	1.2054	1.1887	1.1986	1.1868	1.1869	1.1909	1.1881	1.1861	1.1839
13	21	1.2262	1.2058	1.2220	1.2089	1.2104	1.2117	1.2082	1.2058	1.2031
11	38	1.2483	1.2242	1.2397	1.2295	1.2296	1.2360	1.2317	1.2283	1.2243
14	6	1.2714	1.2432	1.2605	1.2546	1.2541	1.2600	1.2527	1.2519	1.2466
13	7	1.2947	1.2634	1.2788	1.2735	1.2780	1.2834	1.2779	1.2750	1.2710

Table 9. Continued

(e) TS 143.5 to 149.0

Run	Point	M_r	$M_{lo,wall}$ at TS of—							
			143.5	144.0	144.5	145.0	146.0	146.5	148.0	149.0
14	93	0.1000	0.0994	0.0979	0.0996	0.0976	0.0982	0.0985	0.0963	0.0945
12	43	0.2021	0.1974	0.1968	0.1970	0.1961	0.1960	0.1959	0.1916	0.1893
12	42	0.3015	0.2959	0.2941	0.2944	0.2929	0.2928	0.2929	0.2854	0.2817
12	41	0.4044	0.3964	0.3939	0.3937	0.3921	0.3923	0.3933	0.3803	0.3767
14	87	0.5028	0.4923	0.4894	0.4889	0.4873	0.4871	0.4891	0.4705	0.4663
14	84	0.6036	0.5892	0.5859	0.5849	0.5819	0.5818	0.5841	0.5602	0.5540
14	81	0.6535	0.6370	0.6327	0.6321	0.6287	0.6285	0.6309	0.6037	0.5965
12	38	0.7030	0.6844	0.6790	0.6779	0.6741	0.6742	0.6764	0.6452	0.6365
14	75	0.7285	0.7082	0.7034	0.7023	0.6982	0.6976	0.6998	0.6668	0.6576
11	21	0.7538	0.9913	0.9831	0.7249	0.7209	0.7203	0.7226	0.6873	0.6768
14	69	0.7795	0.7563	0.7512	0.7494	0.7451	0.7438	0.7462	0.7086	0.6972
16	23	0.8058	0.7822	0.7761	0.7743	0.7699	0.7688	0.7707	0.7307	0.7182
14	61	0.8284	0.8023	0.7963	0.7942	0.7900	0.7883	0.7906	0.7487	0.7345
14	57	0.8555	0.8252	0.8189	0.8165	0.8119	0.8105	0.8126	0.7677	0.7527
14	53	0.8809	0.8428	0.8360	0.8337	0.8291	0.8281	0.8304	0.7842	0.7683
11	3	0.9038	0.8619	0.8551	0.8528	0.8477	0.8474	0.8505	0.8011	0.7847
14	44	0.9304	0.8737	0.8668	0.8643	0.8595	0.8588	0.8613	0.8140	0.7957
12	27	0.9579	0.8869	0.8796	0.8773	0.8727	0.8725	0.8754	0.8268	0.8086
14	36	0.9816	0.8737	0.8668	0.8878	0.8837	0.8834	0.8862	0.8380	0.8179
11	20	1.0086	0.9137	0.9061	0.9023	0.8978	0.8980	0.9006	0.8516	0.8310
14	25	1.0595	0.9419	0.9301	0.9231	0.9154	0.9112	0.9129	0.8579	0.8357
12	14	1.1106	0.9454	0.9328	0.9246	0.9155	0.9081	0.9075	0.8532	0.8315
14	23	1.1351	0.9261	0.9133	0.9050	0.8970	0.8880	0.8862	0.8403	0.8205
10	8	1.1595	0.9125	0.9006	0.8924	0.8850	0.8767	0.8739	0.8355	0.8174
10	14	1.1796	0.8948	0.8836	0.8764	0.8698	0.8618	0.8591	0.8252	0.8091
11	44	1.2054	0.9204	0.9059	0.8942	0.8842	0.8694	0.8638	0.8212	0.8024
13	21	1.2262	0.9110	0.8962	0.8845	0.8745	0.8593	0.8534	0.8140	0.7963
11	38	1.2483	0.9157	0.9001	0.8883	0.8768	0.8609	0.8544	0.8156	0.7980
14	6	1.2714	0.9525	0.9378	0.9260	0.9150	0.8975	0.8900	0.8490	0.8304
13	7	1.2947	0.9874	0.9741	0.9628	0.9517	0.9346	0.9272	0.8812	0.8605

Table 9. Continued

(f) TS 150.0 to 168.0

Run	Point	M_r	$M_{lo,wall}$ at TS of—							
			150.0	150.5	151.0	152.0	152.5	153.0	153.5	168.0
14	93	0.1000	0.0933	0.0942	0.0936	0.0899	0.0908	0.0890	0.0895	0.0726
12	43	0.2021	0.1879	0.1880	0.1876	0.1835	0.1809	0.1803	0.1800	0.1476
12	42	0.3015	0.2796	0.2785	0.2790	0.2723	0.2693	0.2679	0.2678	0.2193
12	41	0.4044	0.3737	0.3718	0.3725	0.3630	0.3585	0.3564	0.3549	0.2899
14	87	0.5028	0.4616	0.4592	0.4596	0.4474	0.4418	0.4383	0.4368	0.3539
14	84	0.6036	0.5486	0.5450	0.5446	0.5293	0.5218	0.5175	0.5144	0.4136
14	81	0.6535	0.5897	0.5853	0.5847	0.5677	0.5593	0.5547	0.5512	0.4408
12	38	0.7030	0.6287	0.6239	0.6232	0.6036	0.5950	0.5893	0.5851	0.4668
14	75	0.7285	0.6498	0.6438	0.6427	0.6226	0.6130	0.6074	0.6029	0.4800
11	21	0.7538	0.6684	0.6623	0.6609	0.6396	0.6296	0.6233	0.6190	0.4923
14	69	0.7795	0.6886	0.6816	0.6792	0.6573	0.6472	0.6406	0.6354	0.5052
16	23	0.8058	0.7085	0.7013	0.6985	0.6757	0.6648	0.6575	0.6527	0.5178
14	61	0.8284	0.7238	0.7164	0.7135	0.6892	0.6778	0.6709	0.6649	0.5272
14	57	0.8555	0.7421	0.7336	0.7301	0.7057	0.6941	0.6861	0.6802	0.5389
14	53	0.8809	0.7571	0.7481	0.7441	0.7186	0.7073	0.6990	0.6922	0.5493
11	3	0.9038	0.7731	0.7639	0.7591	0.7330	0.7209	0.7128	0.7058	0.5598
14	44	0.9304	0.7838	0.7743	0.7685	0.7426	0.7308	0.7220	0.7149	0.5682
12	27	0.9579	0.7965	0.7863	0.7801	0.7540	0.7416	0.7328	0.7255	0.5768
14	36	0.9816	0.8057	0.7955	0.7885	0.7623	0.7501	0.7415	0.7338	0.5838
11	20	1.0086	0.8181	0.8072	0.8004	0.7735	0.7609	0.7519	0.7443	0.5924
14	25	1.0595	0.8224	0.8114	0.8033	0.7770	0.7652	0.7562	0.7477	0.5946
12	14	1.1106	0.8185	0.8071	0.7999	0.7737	0.7621	0.7532	0.7448	0.5924
14	23	1.1351	0.8086	0.7985	0.7907	0.7675	0.7566	0.7481	0.7406	0.5896
10	8	1.1595	0.8068	0.7974	0.7899	0.7680	0.7578	0.7491	0.7416	0.5868
10	14	1.1796	0.7997	0.7909	0.7841	0.7632	0.7531	0.7450	0.7377	0.5844
11	44	1.2054	0.7924	0.7831	0.7750	0.7540	0.7439	0.7356	0.7274	0.5752
13	21	1.2262	0.7864	0.7774	0.7696	0.7491	0.7392	0.7312	0.7231	0.5711
11	38	1.2483	0.7885	0.7792	0.7715	0.7513	0.7410	0.7330	0.7248	0.5729
14	6	1.2714	0.8200	0.8107	0.8026	0.7816	0.7720	0.7632	0.7549	0.5981
13	7	1.2947	0.8502	0.8399	0.8315	0.8091	0.7993	0.7909	0.7819	0.6213

Table 9. Continued

(g) TS 174.0 to 218.0

Run	Point	M_r	$M_{lo,wall}$ at TS of—							
			174.0	180.0	186.0	192.0	198.0	206.0	216.0	218.0
14	93	0.1000	0.0711	0.0692	0.0644	0.0632	0.0590	0.0548	0.0552	0.0526
12	43	0.2021	0.1407	0.1340	0.1274	0.1221	0.1167	0.1101	0.1081	0.1036
12	42	0.3015	0.2082	0.1978	0.1889	0.1812	0.1736	0.1640	0.1581	0.1535
12	41	0.4044	0.2747	0.2614	0.2486	0.2393	0.2294	0.2176	0.3101	0.2038
14	87	0.5028	0.3345	0.3184	0.3036	0.2911	0.2790	0.2663	0.2562	0.2498
14	84	0.6036	0.3903	0.3708	0.3537	0.3386	0.3249	0.3099	0.2987	0.2911
14	81	0.6535	0.4162	0.3955	0.3770	0.3610	0.3467	0.3299	0.3184	0.3100
12	38	0.7030	0.3899	0.3705	0.3535	0.3388	0.3247	0.3091	0.2979	0.2904
14	75	0.7285	0.4530	0.4296	0.4095	0.3919	0.3765	0.3595	0.3470	0.3382
11	21	0.7538	0.4639	0.4401	0.4199	0.4017	0.3861	0.3684	0.3550	0.3466
14	69	0.7795	0.4760	0.4520	0.4308	0.4124	0.3964	0.3785	0.3653	0.3568
16	23	0.8058	0.4878	0.4630	0.4419	0.4227	0.4074	0.3892	0.3765	0.3670
14	61	0.8284	0.4969	0.4719	0.4496	0.4303	0.4146	0.3956	0.3822	0.3734
14	57	0.8555	0.5077	0.4813	0.4585	0.4393	0.4231	0.4047	0.3914	0.3820
14	53	0.8809	0.5172	0.4900	0.4669	0.4471	0.4306	0.4115	0.3976	0.3893
11	3	0.9038	0.5260	0.4986	0.4757	0.4561	0.4387	0.4201	0.4055	0.3969
14	44	0.9304	0.5337	0.5054	0.4815	0.4616	0.4443	0.4248	0.4108	0.4019
12	27	0.9579	0.5412	0.5133	0.4888	0.4688	0.4509	0.4321	0.4177	0.4087
14	36	0.9816	0.5475	0.5186	0.4944	0.4745	0.4568	0.4374	0.4233	0.4145
11	20	1.0086	0.5556	0.5267	0.5025	0.4817	0.4643	0.4453	0.4304	0.4220
14	25	1.0595	0.5587	0.5309	0.5083	0.4891	0.4721	0.4532	0.4392	0.4301
12	14	1.1106	0.5579	0.5317	0.5098	0.4907	0.4753	0.4572	0.4440	0.4360
14	23	1.1351	0.5529	0.5269	0.5050	0.4867	0.4707	0.4531	0.4403	0.4323
10	8	1.1595	0.5525	0.5266	0.5050	0.4865	0.4709	0.4537	0.4399	0.4324
10	14	1.1796	0.5521	0.5270	0.5068	0.4888	0.4743	0.4570	0.4437	0.4366
11	44	1.2054	0.5426	0.5177	0.4968	0.4800	0.4651	0.4487	0.4363	0.4293
13	21	1.2262	0.5393	0.5148	0.4952	0.4782	0.4640	0.4478	0.4364	0.4295
11	38	1.2483	0.5415	0.5181	0.4971	0.4803	0.4661	0.4505	0.4382	0.4316
14	6	1.2714	0.5665	0.5421	0.5220	0.5053	0.4916	0.4758	0.4641	0.4579
13	7	1.2947	0.5896	0.5645	0.5434	0.5261	0.5115	0.4951	0.4833	0.4767

Table 9. Concluded

(h) TS 224.0 to 320.0

Run	Point	M_r	$M_{lo,wall}$ at TS of—							
			224.0	236.0	248.0	260.0	272.0	284.0	296.0	320.0
14	93	0.1000	0.0527	0.0412	0.0431	0.0415	0.0421	0.0389	0.0383	0.0405
12	43	0.2021	0.1015	0.0937	0.0897	0.0875	0.0870	0.0852	0.0824	0.0802
12	42	0.3015	0.1501	0.1406	0.1355	0.1307	0.1272	0.1256	0.1235	0.1201
12	41	0.4044	0.1982	0.1879	0.1810	0.1750	0.1709	0.1678	0.1651	0.1597
14	87	0.5028	0.2427	0.2307	0.2226	0.2145	0.2101	0.2054	0.2039	0.1962
14	84	0.6036	0.2835	0.2702	0.2604	0.2521	0.2495	0.2420	0.2372	0.2305
14	81	0.6535	0.3027	0.2883	0.2782	0.2699	0.2642	0.2601	0.2560	0.2481
12	38	0.7030	0.3198	0.3057	0.2958	0.2870	0.2802	0.2751	0.2704	0.2630
14	75	0.7285	0.3295	0.3156	0.3053	0.2951	0.2890	0.2838	0.2796	0.2716
11	21	0.7538	0.3373	0.3235	0.3138	0.3054	0.2990	0.2933	0.2890	0.2801
14	69	0.7795	0.3476	0.3332	0.3228	0.3133	0.3073	0.3024	0.2981	0.2896
16	23	0.8058	0.3579	0.3436	0.3327	0.3283	0.3183	0.3127	0.3093	0.3001
14	61	0.8284	0.3642	0.3499	0.3394	0.3290	0.3225	0.3164	0.3136	0.3049
14	57	0.8555	0.3728	0.3580	0.3473	0.3374	0.3317	0.3268	0.3220	0.3120
14	53	0.8809	0.3795	0.3645	0.3539	0.3440	0.3385	0.3333	0.3289	0.3195
11	3	0.9038	0.3878	0.3727	0.3622	0.3523	0.3467	0.3416	0.3370	0.3283
14	44	0.9304	0.3932	0.3778	0.3675	0.3579	0.3515	0.3455	0.3414	0.3323
12	27	0.9579	0.3997	0.3850	0.3747	0.3659	0.3604	0.3555	0.3511	0.3417
14	36	0.9816	0.4050	0.3905	0.3803	0.3722	0.3681	0.3630	0.3575	0.3489
11	20	1.0086	0.4130	0.3990	0.3894	0.3799	0.3754	0.3704	0.3662	0.3574
14	25	1.0595	0.4211	0.4071	0.3975	0.3880	0.3827	0.3771	0.3717	0.3621
12	14	1.1106	0.4273	0.4130	0.4043	0.3942	0.3878	0.3821	0.3769	0.3680
14	23	1.1351	0.4233	0.4099	0.4005	0.3916	0.3869	0.3809	0.3755	0.3659
10	8	1.1595	0.4238	0.4104	0.4008	0.3926	0.3869	0.3819	0.3764	0.3667
10	14	1.1796	0.4288	0.4161	0.4063	0.3992	0.3927	0.3868	0.3821	0.3718
11	44	1.2054	0.4211	0.4087	0.3990	0.3912	0.3856	0.3808	0.3763	0.3671
13	21	1.2262	0.4213	0.4093	0.4004	0.3923	0.3865	0.3809	0.3763	0.3674
11	38	1.2483	0.4243	0.4123	0.4039	0.3957	0.3903	0.3840	0.3792	0.3707
14	6	1.2714	0.4507	0.4390	0.4308	0.4225	0.4157	0.4109	0.4062	0.3972
13	7	1.2947	0.4697	0.4577	0.4507	0.4425	0.4366	0.4312	0.4273	0.4179

Table 10. Mach Number of 6-ft and 8-ft CTSL From Right Side of Centerline Tube

Run	Point	δ_{flat} , min	6-ft CTSL M_r	8-ft CTSL M_r	Run	Point	δ_{flat} , min	6-ft CTSL M_r	8-ft CTSL M_r
14	93	0	0.1000	0.0999	9	3	4	0.9027	0.8953
12	43	0	0.2021	0.2020	9	5	5	0.9053	0.9122
12	42	0	0.3015	0.3014	11	3	4	0.9038	0.9036
5	2	0	0.3992	0.3990	12	30	5	0.9062	0.9059
9	31	0	0.4006	0.4005	14	43	6	0.9298	0.9296
12	41	0	0.4044	0.4043	14	44	7	0.9304	0.9301
9	28	0	0.5014	0.5012	16	21	7.9	0.9463	0.9460
12	40	0	0.5037	0.5035	9	10	8	0.9559	0.9601
14	87	0	0.5028	0.5026	12	27	10	0.9579	0.9577
5	8	0	0.6018	0.6015	14	36	12	0.9816	0.9815
5	9	0	0.6015	0.6012	13	4	14	0.9855	0.9854
11	62	0	0.6047	0.6045	11	20	14	1.0086	1.0087
12	39	0	0.6038	0.6035	11	16	9	1.0284	1.0282
14	84	0	0.6036	0.6033	14	33	10	1.0345	1.0349
16	3	0	0.6033	0.6031	9	22	6	1.0504	1.0501
12	37	0	0.6544	0.6541	14	25	7	1.0595	1.0596
14	81	0	0.6535	0.6532	12	14	5	1.1106	1.1108
12	38	0	0.7030	0.7027	14	22	9	1.1344	1.1344
14	75	0	0.7285	0.7281	14	23	10	1.1351	1.1352
11	21	0	0.7538	0.7534	10	8	18	1.1595	1.1601
14	69	0	0.7795	0.7792	10	13	16	1.1570	1.1575
5	14	0	0.8000	0.8050	14	17	19	1.1585	1.1590
6	8	0	0.8022	0.7991	10	14	26.5	1.1796	1.1720
16	23	0	0.8058	0.8055	11	44	10	1.2054	1.2055
14	61	0	0.8284	0.8282	12	13	12	1.2045	1.2046
14	57	1	0.8555	0.8552	13	21	14	1.2262	1.2263
14	53	3	0.8809	0.8806	11	38	14.5	1.2483	1.2484
					14	6	21	1.2714	1.2715
					13	7	23	1.2947	1.2946

Table 11. Mach Number and Pressure Ratios of Right and Left Sides of Centerline Tube

(a) $M_r = 0.1000$ to 0.8809

Run	Point	$\delta_{\text{flat}}, \text{ min}$	M_r	M_l	M_{ave}	$M_r - M_l$	$p_r/p_{t,\infty}$	$p_l/p_{t,\infty}$	$(p/p_{t,\infty})_{\text{ave}}$
14	93	0	0.1000	0.0994	0.0997	0.0006	0.993033	0.993116	0.993075
12	43	0	0.2021	0.2013	0.2017	0.0008	0.971926	0.972136	0.972031
12	42	0	0.3015	0.3003	0.3009	0.0012	0.938869	0.939367	0.939367
5	2	0	0.3992	0.3974	0.3983	0.0018	0.869002	0.896863	0.896433
9	31	0	0.4006	0.3986	0.3996	0.0020	0.895307	0.896274	0.895791
12	41	0	0.4044	0.4023	0.4034	0.0021	0.893449	0.894471	0.893960
9	28	0	0.5014	0.4987	0.5001	0.0027	0.842205	0.843733	0.842969
12	40	0	0.5037	0.5010	0.5024	0.0027	0.840921	0.842434	0.841678
14	87	0	0.5028	0.5000	0.5014	0.0028	0.841421	0.842995	0.842208
5	8	0	0.6018	0.5984	0.6001	0.0030	0.782878	0.785002	0.783940
5	9	0	0.6015	0.5980	0.5998	0.0035	0.783072	0.785244	0.784158
11	62	0	0.6047	0.6013	0.6030	0.0034	0.781088	0.783184	0.782136
12	39	0	0.6038	0.6004	0.6021	0.0034	0.781657	0.783758	0.782708
14	84	0	0.6036	0.6002	0.6019	0.0034	0.781764	0.783906	0.782835
16	3	0	0.6033	0.6000	0.6017	0.0033	0.781946	0.784035	0.782991
12	37	0	0.6544	0.6505	0.6524	0.0039	0.750045	0.752494	0.751270
14	81	0	0.6535	0.6496	0.6516	0.0039	0.750637	0.753054	0.751846
12	38	0	0.7030	0.6988	0.7009	0.0042	0.718986	0.721703	0.720345
14	75	0	0.7285	0.7241	0.7263	0.0044	0.702546	0.705375	0.703961
11	21	0	0.7538	0.7493	0.7516	0.0045	0.686131	0.689045	0.687588
14	69	0	0.7795	0.7748	0.7771	0.0047	0.669376	0.672466	0.670921
5	14	0	0.8000	0.7951	0.7976	0.0049	0.656002	0.659219	0.657611
6	8	0	0.8022	0.7971	0.7997	0.0051	0.654588	0.657917	0.656253
16	23	0	0.8058	0.8010	0.8034	0.0048	0.652224	0.655390	0.653807
14	61	0	0.8284	0.8234	0.8259	0.0050	0.637504	0.640785	0.639145
14	57	1	0.8555	0.8502	0.8529	0.0053	0.619943	0.623345	0.621644
14	53	3	0.8809	0.8754	0.8782	0.0055	0.603530	0.607064	0.605297

Table 11. Concluded

(b) $M_r = 0.9027$ to 1.2948

Run	Point	$\delta_{\text{flat}}, \text{ min}$	M_r	M_l	M_{ave}	$M_r - M_l$	$p_r / p_{t,\infty}$	$p_l / p_{t,\infty}$	$(p/p_{t,\infty})_{\text{ave}}$
9	3	4	0.9027	0.8971	0.8999	0.0056	0.589501	0.593142	0.591322
9	5	5	0.9053	0.8997	0.9025	0.0057	0.587832	0.591465	0.589649
11	3	4	0.9038	0.8900	0.9009	0.0058	0.588814	0.592543	0.590679
12	30	5	0.9062	0.9004	0.9029	0.0058	0.587296	0.590967	0.589132
14	43	6	0.9298	0.9240	0.9269	0.0058	0.572250	0.575930	0.574090
14	44	7	0.9304	0.9245	0.9275	0.0058	0.571880	0.575581	0.573731
16	21	7.9	0.9463	0.9401	0.9432	0.0062	0.561787	0.565721	0.563754
9	10	8	0.9559	0.9499	0.9530	0.0061	0.555742	0.559541	0.557642
12	27	10	0.9579	0.9519	0.9549	0.0060	0.554488	0.558273	0.556381
14	36	12	0.9816	0.9755	0.9788	0.0061	0.539703	0.543496	0.541600
13	4	14	0.9855	0.9791	0.9823	0.0064	0.537224	0.541235	0.539230
11	20	14	1.0084	1.0027	1.0057	0.0059	0.523009	0.526593	0.524801
11	16	9	1.0284	1.0220	1.0252	0.0064	0.510898	0.514807	0.512853
14	33	10	1.0345	1.0284	1.0315	0.0061	0.507194	0.510907	0.509051
9	22	6	1.0504	1.0430	1.0467	0.0074	0.497662	0.502101	0.499882
14	25	7	1.0595	1.0530	1.0563	0.0065	0.492171	0.496052	0.494112
12	14	5	1.1106	1.1035	1.1071	0.0071	0.462248	0.466339	0.464294
14	22	9	1.1344	1.1279	1.1312	0.0065	0.448626	0.452325	0.450475
14	23	10	1.1351	1.1286	1.1319	0.0065	0.448203	0.451883	0.450043
10	8	18	1.1595	1.1518	1.1556	0.0077	0.434541	0.438820	0.436681
10	13	16	1.1570	1.1498	1.1534	0.0072	0.435897	0.439971	0.437934
14	17	19	1.1585	1.1513	1.1549	0.0072	0.435062	0.439084	0.437073
10	14	26.5	1.1796	1.1732	1.1764	0.0064	0.423422	0.426927	0.425175
11	44	10	1.2054	1.1976	1.2015	0.0078	0.409468	0.413691	0.411580
12	13	12	1.2045	1.1967	1.2006	0.0078	0.409958	0.414143	0.412051
13	21	14	1.2262	1.2178	1.2220	0.0084	0.398449	0.402857	0.400653
11	38	14.5	1.2483	1.2404	1.2444	0.0079	0.386932	0.391000	0.388966
14	6	21	1.2714	1.2631	1.2672	0.0083	0.375142	0.379359	0.377251
13	7	23	1.2948	1.2862	1.2904	0.0086	0.363535	0.367747	0.365641

Table 12. Mach Number Gradients and Standard and Maximum Deviations From Right Side of Centerline Tube for 6-ft and 8-ft CTSL

(a) $M_r = 0.1000$ to 0.8809

Run	Point	$\delta_{\text{flat}}, \text{ min}$	M_r	6-ft CTSL TS 131.0 to 137.0			8-ft CTSL TS 129.0 to 137.0		
				$(dM/dx)_r$	2σ	σ_{max}	$(dM/dx)_r$	2σ	σ_{max}
14	93	0	0.1000	-0.000211	0.000835	0.002572	-0.000114	0.000802	0.002775
12	43	0	0.2021	-0.000294	0.000339	0.000597	-0.000234	0.000395	0.000739
12	42	0	0.3015	-0.000439	0.000464	0.000974	-0.000345	0.000560	0.001088
5	2	0	0.3992	-0.000612	0.001160	0.003411	-0.000504	0.001127	0.003384
9	31	0	0.4006	-0.000590	0.000637	0.001539	-0.000469	0.000754	0.001688
12	41	0	0.4044	-0.000578	0.000623	0.001392	-0.000450	0.000758	0.001547
9	28	0	0.5014	-0.000590	0.000770	0.001962	-0.000547	0.000943	0.002158
12	40	0	0.5037	-0.000672	0.000798	0.001823	-0.000513	0.000967	0.002021
14	87	0	0.5028	-0.000704	0.000789	0.001790	-0.000531	0.000977	0.001992
5	8	0	0.6018	-0.000774	0.000930	0.002144	-0.000574	0.001152	0.002381
9	25	0	0.6026	-0.000765	0.000986	0.002479	-0.000576	0.001182	0.002717
11	62	0	0.6047	-0.000706	0.000949	0.002440	-0.000529	0.001135	0.002666
12	39	0	0.6038	-0.000713	0.000982	0.002301	-0.000527	0.001177	0.002539
14	84	0	0.6036	-0.000732	0.000961	0.002256	-0.000537	0.001176	0.002499
16	3	0	0.6033	-0.000657	0.001195	0.003341	-0.000501	0.001289	0.002895
12	37	0	0.6544	-0.000696	0.001090	0.002576	-0.000497	0.001291	0.002833
14	81	0	0.6535	-0.000701	0.001055	0.002519	-0.000503	0.001270	0.002778
12	38	0	0.7030	-0.000635	0.001185	0.002811	-0.000431	0.001388	0.003085
14	75	0	0.7285	-0.000570	0.001238	0.002998	-0.000380	0.001416	0.003267
11	21	0	0.7537	-0.000520	0.001218	0.003017	-0.000331	0.001415	0.003350
14	69	0	0.7795	-0.000394	0.001308	0.003133	-0.000213	0.001478	0.003413
5	14	0	0.8000	-0.000382	0.001392	0.002913	-0.000092	0.001422	0.003015
6	8	0	0.8022	-0.000341	0.001245	0.003053	-0.000085	0.001323	0.003141
16	23	0	0.8058	-0.000205	0.001452	0.003365	-0.000045	0.001570	0.003640
14	61	0	0.8284	-0.000078	0.001377	0.003296	0.000057	0.001481	0.003552
14	57	1	0.8555	-0.000008	0.001441	0.003385	0.000107	0.001514	0.003632
14	53	3	0.8809	-0.000119	0.001505	0.003501	-0.000008	0.001576	0.003756

Table 12. Concluded

(b) $M_r = 0.9027$ to 1.2948

Run	Point	$\delta_{\text{flat}}, \text{ min}$	M_r	6-ft CTSL TS 131.0 to 137.0			8-ft CTSL TS 129.0 to 137.0		
				$(dM/dx)_r$	2σ	σ_{max}	$(dM/dx)_r$	2σ	σ_{max}
9	3	4	0.9027	-0.000061	0.001396	0.003537	0.000132	0.001394	0.003600
9	5	5	0.9053	-0.000269	0.001441	0.003646	-0.000052	0.001453	0.003781
11	3	4	0.9038	0.000019	0.001489	0.003937	0.000108	0.001428	0.003700
12	30	5	0.9062	-0.000181	0.001481	0.003482	-0.000060	0.001565	0.003741
14	43	6	0.9298	-0.000009	0.001445	0.003379	0.000067	0.001466	0.003584
14	44	7	0.9304	-0.000201	0.001534	0.003509	-0.000109	0.001584	0.003749
16	21	7.9	0.9463	0.000058	0.001712	0.003722	0.000236	0.001785	0.004019
9	10	8	0.9559	0.000064	0.001450	0.003437	0.002419	0.015264	0.074843
12	27	10	0.9579	-0.000246	0.001522	0.003478	-0.000149	0.001539	0.003684
14	36	12	0.9816	-0.000047	0.001517	0.003163	0.000014	0.001422	0.003211
13	4	14	0.9855	-0.000321	0.001483	0.003441	-0.000218	0.001456	0.003576
11	20	14	1.0086	-0.000188	0.001867	0.004258	0.000021	0.001843	0.004116
11	16	9	1.0284	-0.000324	0.002221	0.005299	0.000129	0.002243	0.005371
14	33	10	1.0345	-0.000131	0.002212	0.004490	-0.000180	0.002304	0.005065
9	22	6	1.0504	0.000078	0.001971	0.003164	0.000234	0.001905	0.003640
14	25	7	1.0595	0.000012	0.001905	0.004555	-0.000083	0.001765	0.004641
12	14	5	1.1106	0.001232	0.003411	0.006773	0.000640	0.003363	0.007638
14	22	9	1.1344	-0.000139	0.003028	0.006376	0.000434	0.003104	0.006374
14	23	10	1.1351	-0.000033	0.002796	0.005792	0.000499	0.002910	0.005581
10	8	18	1.1595	-0.000036	0.003602	0.006888	-0.000449	0.003673	0.006443
10	13	16	1.1570	-0.000443	0.003409	0.006409	-0.000539	0.003309	0.006608
14	17	19	1.1585	-0.000203	0.003337	0.005912	-0.000273	0.003268	0.006194
10	14	26.5	1.1796	-0.000109	0.003802	0.008036	-0.001799	0.005503	0.006078
11	44	10	1.2054	-0.000048	0.003015	0.006022	-0.000114	0.002773	0.006171
12	13	12	1.2045	-0.000159	0.003039	0.006082	-0.000224	0.002790	0.006200
13	21	14	1.2262	-0.000182	0.002575	0.005165	-0.000307	0.002444	0.005203
11	38	14.5	1.2483	-0.000242	0.003292	0.008557	-0.000104	0.003044	0.008853
14	6	21	1.2714	-0.000169	0.002614	0.005413	-0.000056	0.002601	0.005055
13	7	23	1.2948	-0.000008	0.002036	0.003732	0.000295	0.002902	0.006489

Table 13. Pressure Ratio Gradients and Standard and Maximum Deviations From Right Side of Centerline Tube for 6-ft and 8-ft CTSL

(a) $M_r = 0.1000$ to 0.8809

Run	Point	$\delta_{\text{flat}}, \text{ min}$	M_r	6-ft CTSL TS 131.0 to 137.0			8-ft CTSL TS 129.0 to 137.0		
				$(dpr/dx)_r$	Pressure ratio standard deviation	Pressure ratio maximum deviation	$(dpr/dx)_r$	Pressure ratio standard deviation	Pressure ratio maximum deviation
14	93	0	0.1000	0.000029	0.000116	0.000362	0.000016	0.000112	0.000390
12	43	0	0.2021	0.000080	0.000092	0.000163	0.000064	0.000107	0.000201
12	42	0	0.3015	0.000171	0.000181	0.000379	0.000134	0.000218	0.000423
5	2	0	0.3992	0.000297	0.000562	0.001649	0.000244	0.000546	0.001637
9	31	0	0.4006	0.000287	0.000310	0.000749	0.000228	0.000366	0.000821
12	41	0	0.4044	0.000283	0.000305	0.000682	0.000220	0.000371	0.000758
9	28	0	0.5014	0.000394	0.000433	0.001105	0.000308	0.000530	0.001215
12	40	0	0.5037	0.000379	0.000450	0.001029	0.000289	0.000545	0.001140
14	87	0	0.5028	0.000397	0.000445	0.001009	0.000299	0.000550	0.001123
5	8	0	0.6018	0.000476	0.000572	0.001319	0.000353	0.000708	0.001465
9	25	0	0.6026	0.000471	0.000606	0.001526	0.000355	0.000727	0.001672
11	62	0	0.6047	0.000435	0.000584	0.001504	0.000326	0.000699	0.001644
12	39	0	0.6038	0.000439	0.000604	0.001417	0.000324	0.000725	0.001564
14	84	0	0.6036	0.000451	0.000591	0.001389	0.000331	0.000724	0.001539
16	3	0	0.6033	0.000405	0.000736	0.002056	0.000308	0.000793	0.001781
12	37	0	0.6544	0.000440	0.000689	0.001631	0.000315	0.000817	0.001794
14	81	0	0.6535	0.000443	0.000668	0.001594	0.000318	0.000803	0.001758
12	38	0	0.7030	0.000409	0.000763	0.001811	0.000278	0.000893	0.001987
14	75	0	0.7285	0.000369	0.000802	0.001942	0.000246	0.000917	0.002117
11	21	0	0.7538	0.000338	0.000792	0.001997	0.000215	0.000920	0.002178
14	69	0	0.7795	0.000257	0.000852	0.002041	0.000139	0.000963	0.002224
5	14	0	0.8000	0.000249	0.000866	0.001898	-0.001717	0.011990	0.058858
6	8	0	0.8022	0.000222	0.000811	0.001988	0.001068	0.006868	0.033556
16	23	0	0.8058	0.000133	0.000945	0.002192	0.000029	0.001022	0.002370
14	61	0	0.8284	0.000051	0.000895	0.002142	-0.000037	0.000963	0.002309
14	57	1	0.8555	0.000005	0.000933	0.002192	-0.000070	0.000981	0.002352
14	53	3	0.8809	0.000076	0.000970	0.002255	0.000005	0.001016	0.002419

Table 13. Concluded

(b) $M_r = 0.9027$ to 1.2948

Run	Point	$\delta_{\text{flat}}, \text{ min}$	M_r	6-ft CTSL TS 131.0 to 137.0			8-ft CTSL TS 129.0 to 137.0		
				$(dpr/dx)_r$	Pressure ratio standard deviation	Pressure ratio maximum deviation	$(dpr/dx)_r$	Pressure ratio standard deviation	Pressure ratio maximum deviation
9	3	4	0.9027	0.000039	0.000894	0.002265	0.002416	0.016851	0.082844
9	5	5	0.9053	0.000172	0.000922	0.002333	-0.002271	0.015532	0.076332
11	3	4	0.9038	-0.000012	0.000884	0.002232	-0.000069	0.000914	0.002368
12	30	5	0.9062	0.000116	0.000947	0.002228	0.000038	0.001002	0.002394
14	43	6	0.9298	0.000006	0.000918	0.002145	-0.000042	0.000931	0.002275
14	44	7	0.9304	0.000128	0.000974	0.002227	0.000069	0.001006	0.002379
16	21	7.9	0.9463	-0.000037	0.001080	0.002348	-0.000149	0.001127	0.002536
9	10	8	0.9559	-0.000040	0.000912	0.002160	-0.001493	0.009406	0.046112
12	27	10	0.9579	0.000155	0.000956	0.002184	0.000094	0.000967	0.002313
14	36	12	0.9816	0.000029	0.000943	0.001966	-0.000009	0.000884	0.001996
13	4	14	0.9855	0.000199	0.000920	0.002134	0.000135	0.000904	0.002218
11	20	14	1.0086	0.000116	0.001146	0.002611	-0.000013	0.001131	0.002524
11	16	9	1.0284	0.000196	0.001348	0.003214	-0.000078	0.001362	0.003257
14	33	10	1.0345	0.000079	0.001339	0.002719	0.000109	0.001394	0.003061
9	22	6	1.0504	-0.000047	0.001182	0.001898	-0.000140	0.001142	0.002181
14	25	7	1.0595	-0.000007	0.001136	0.002719	0.000049	0.001052	0.002770
12	14	5	1.1106	-0.000711	0.001967	0.003898	-0.000369	0.001939	0.004416
14	22	9	1.1344	0.000079	0.001716	0.003619	-0.000246	0.001759	0.003618
14	23	10	1.1351	0.000019	0.001584	0.003275	-0.000283	0.001648	0.003165
10	8	18	1.1595	0.000021	0.002003	0.003834	0.000250	0.002041	0.003589
10	13	16	1.1570	0.000248	0.001900	0.003576	0.000301	0.001843	0.003689
14	17	19	1.1585	0.000114	0.001857	0.003294	0.000152	0.001819	0.003451
10	14	26.5	1.1796	0.000059	0.002079	0.004386	0.003655	0.018258	0.088713
11	44	10	1.2054	0.000026	0.001614	0.003231	0.000061	0.001484	0.003311
12	13	12	1.2045	0.000085	0.001628	0.003265	0.000120	0.001495	0.003328
13	21	14	1.2262	0.000096	0.001354	0.002721	0.000161	0.001285	0.002741
11	38	14.5	1.2483	0.000125	0.001699	0.004427	0.000054	0.001571	0.004580
14	6	21	1.2714	0.000085	0.001319	0.002728	0.000028	0.001313	0.002547
13	7	23	1.2948	0.000129	0.001173	0.002564	-0.000146	0.001434	0.003213

Table 14. Mach Number Gradients of Right and Left Sides of Centerline Tube for 6-ft CTSL

Run	Point	M_r	dM/dx for—			2σ for—			σ_{\max} for—		
			Transducer, left side	Transducer, right side	ESP, right side	Transducer, left side	Transducer, right side	ESP, right side	Transducer, left side	Transducer, right side	ESP, right side
14	93	0.1000	-.000225	-.000211	.000236	.000365	.000835	.001522	.000760	.002572	.002645
12	43	0.2021	-.000289	-.000294	-.001384	.000300	.000339	.007026	.000441	.000597	.020437
12	42	0.3015	-.000487	-.000452	-.000453	.000435	.000436	.0011168	.000657	.001032	.002524
12	41	0.4044	-.000619	-.000761	-.001100	.000643	.000986	.003072	.000976	.002039	.010529
14	87	0.5028	-.000742	-.000704	-.000690	.000836	.000789	.000914	.001204	.001790	.001918
14	84	0.6036	-.000799	-.000732	-.000679	.001074	.000961	.001036	.001541	.002256	.002292
14	81	0.6535	-.000774	-.000701	-.000733	.001187	.001055	.001131	.001713	.002519	.002679
12	38	0.7030	-.000709	-.000635	-.000880	.001312	.001185	.002204	.001946	.002811	.005957
14	75	0.7285	-.000684	-.000570	-.000557	.001346	.001238	.001302	.001917	.002998	.003353
11	21	0.7538	-.000634	-.000520	-.000511	.001357	.001218	.001547	.001973	.003017	.003612
14	69	0.7795	-.000502	-.000394	-.000322	.001402	.001308	.001421	.002015	.003133	.003495
16	23	0.8058	-.000335	-.000205	-.000134	.001426	.001452	.001466	.002149	.003365	.004154
14	61	0.8284	-.000226	-.000078	-.000120	.001417	.001377	.001492	.001765	.003296	.003209
14	57	0.8555	-.000154	-.000008	.000014	.001425	.001441	.001416	.001522	.003385	.002871
14	53	0.8809	-.000222	-.000119	-.000088	.001427	.001505	.001524	.002154	.003501	.003424
11	3	0.9038	-.000025	.000019	.000107	.001381	.001489	.001397	.003487	.003937	.002171
14	44	0.9304	-.000324	-.000201	-.000189	.002823	.001534	.001619	.007625	.003509	.003672
12	27	0.9579	-.000333	-.000246	-.000130	.001439	.001522	.001601	.002324	.003478	.003579
14	36	0.9816	-.000040	-.000047	-.000004	.001310	.001517	.001592	.001975	.003162	.003402
11	20	1.0086	-.000111	-.000188	.000091	.001164	.001867	.002026	.001714	.004258	.005509
14	25	1.0595	.000147	.000012	.000053	.002037	.001905	.001886	.003957	.004555	.004294
12	14	1.1106	.000485	-.000139	-.000032	.003072	.003028	.003065	.006482	.006376	.006340
14	23	1.1351	.000589	-.000033	.000094	.002808	.003028	.003065	.006482	.006376	.006340
10	8	1.1595	.000290	-.000036	.000346	.003534	.003602	.004362	.006233	.006888	.007218

Table 14. Concluded

Run	Point	M_r	dM/dx for—			2σ for—			σ_{\max} for—		
			Transducer, left side	Transducer, right side	ESP, right side	Transducer, left side	Transducer, right side	ESP, right side	Transducer, left side	Transducer, right side	ESP, right side
10	14	1.1796	−.000019	−.000109	.000121	.003735	.003802	.003760	.006415	.008036	.008681
11	44	1.2054	.000296	−.000048	.000093	.002772	.003015	.003173	.005441	.006022	.006103
13	21	1.2262	.000031	−.000182	.000096	.001838	.003575	.002814	.002470	.005165	.005181
11	38	1.2483	.000666	−.000242	−.000090	.003382	.003292	.003327	.006405	.008557	.008101
14	6	1.2714	.000546	−.000169	.000085	.002313	.002614	.002590	.002252	.005413	.005281
13	7	1.2947	.000958	−.000008	.000584	.001994	.002036	.002738	.003202	.003732	.006082

Table 15. Mach Number Gradients and Standard and Maximum Deviations for Alternate CTSL From Left Side of Centerline Tube

(a) 9-ft and 10.5-ft CTSL

Run	Point	$\delta_{\text{flat}}, \text{ min}$	M_r	9-ft CTSL TS 128.00 to 136.75			10.5-ft CTSL TS 126.50 to 136.75		
				$(dM/dx)_l$	2σ	σ_{max}	$(dM/dx)_l$	2σ	σ_{max}
14	93	0	0.1000	-0.000011	0.001209	0.001696	0.000087	0.001252	0.001958
9	37	0	0.2011	-0.000108	0.001063	0.002725	-0.000047	0.001039	0.002531
14	91	0	0.3023	-0.000359	0.000514	0.000870	-0.000225	0.000786	0.001816
14	90	0	0.4017	-0.000425	0.000853	0.002100	-0.000299	0.001080	0.002441
14	87	0	0.5028	-0.000551	0.001157	0.002206	-0.000353	0.001515	0.003477
14	84	0	0.6036	-0.000528	0.001700	0.003948	-0.000362	0.001896	0.003515
14	81	0	0.6535	-0.000614	0.001757	0.003748	-0.000410	0.002028	0.004005
12	38	0	0.7030	-0.000528	0.001894	0.004111	-0.000316	0.002068	0.003830
11	21	0	0.7538	-0.000346	0.002077	0.004070	-0.000166	0.002317	0.004305
16	23	0	0.8058	-0.000377	0.002682	0.005360	-0.000201	0.002924	0.005052
14	61	0	0.8284	-0.000384	0.002354	0.004057	-0.000146	0.002676	0.005177
14	56	0	0.8555	-0.000183	0.002720	0.004808	0.000037	0.002933	0.004988
14	52	2	0.8794	-0.000078	0.002505	0.005063	0.000064	0.002660	0.004630
14	47	4	0.9004	-0.000100	0.002466	0.005105	0.000031	0.002667	0.004953
14	42	5	0.9331	-0.000133	0.002730	0.005222	-0.000002	0.002930	0.005076
14	39	8	0.9555	-0.000002	0.003310	0.006407	0.000060	0.003405	0.006362
14	36	12	0.9816	-0.000185	0.003618	0.006816	-0.000118	0.003699	0.006613

Table 15. Continued

(b) 12-ft and 15-ft CTSL

Run	Point	$\delta_{\text{flat}}, \text{ min}$	12-ft CTSL TS 125.00 to 136.75				15-ft CTSL TS 122.00 to 136.75		
			M_r	$(dM/dx)_l$	2σ	σ_{max}	$(dM/dx)_l$	2σ	σ_{max}
14	93	0	0.1000	0.000143	0.001277	0.002185	0.000152	0.001284	0.002204
9	37	0	0.2011	-0.000060	0.000981	0.002574	-0.000056	0.000952	0.002557
14	91	0	0.3023	-0.000186	0.000775	0.001545	-0.000122	0.000793	0.001534
14	90	0	0.4017	-0.000264	0.001037	0.002197	-0.000190	0.001067	0.001996
14	87	0	0.5028	-0.000316	0.001437	0.003223	-0.000217	0.001427	0.002697
14	84	0	0.6036	-0.000328	0.001798	0.003287	-0.000227	0.001740	0.003034
14	81	0	0.6535	-0.000341	0.001955	0.003537	-0.000221	0.001900	0.003404
12	38	0	0.7030	-0.000285	0.001951	0.003804	-0.000163	0.002039	0.003983
11	21	0	0.7538	-0.000126	0.002205	0.004034	-0.000067	0.002037	0.003824
16	3	0	0.8058	-0.000168	0.002773	0.004831	-0.000097	0.002538	0.004675
14	61	0	0.8284	-0.000092	0.002550	0.004815	0.000002	0.002404	0.004253
14	56	0	0.8555	-0.000008	0.002531	0.004861	0.000034	0.002347	0.004621
14	52	2	0.8794	0.000043	0.002528	0.004656	0.000048	0.002339	0.004677
14	47	4	0.9004	-0.000022	0.002543	0.005007	-0.000020	0.002351	0.005030
14	42	5	0.9331	-0.000031	0.002770	0.005108	-0.000025	0.002539	0.005127
14	39	8	0.9555	-0.000005	0.003234	0.006427	-0.000015	0.002975	0.006456
14	36	12	0.9816	-0.000145	0.002984	0.005457	-0.000105	0.002748	0.005474

Table 15. Concluded

(c) 18-ft and 21-ft CTSL

Run	Point	$\delta_{\text{flat}}, \text{ min}$	M_r	18-ft CTSL TS 119.00 to 136.75			21-ft CTSL TS 116.00 to 136.75		
				$(dM/dx)_l$	2σ	σ_{max}	$(dM/dx)_l$	2σ	σ_{max}
14	93	0	0.1000	0.000101	0.001585	0.003379	0.000109	0.001568	0.003457
9	37	0	0.2011	-0.000011	0.000957	0.002320	0.000037	0.001019	0.002162
14	91	0	0.3023	-0.000063	0.000895	0.001818	-0.000035	0.000880	0.001959
14	90	0	0.4017	-0.000124	0.001095	0.002237	-0.000079	0.001102	0.002357
14	87	0	0.5028	-0.000133	0.001438	0.002883	-0.000084	0.001405	0.002937
14	84	0	0.6036	-0.000136	0.001718	0.003027	-0.000085	0.001658	0.003161
14	81	0	0.6535	-0.000111	0.001893	0.003809	-0.000058	0.001824	0.003947
12	38	0	0.7030	-0.000062	0.002093	0.003881	-0.000024	0.002022	0.003956
11	21	0	0.7538	0.000017	0.001957	0.003915	0.000046	0.001860	0.003987
16	24	1	0.8058	-0.000005	0.002425	0.005011	0.000020	0.002312	0.005078
14	62	1	0.8284	0.000046	0.002317	0.004447	0.000072	0.002170	0.004475
14	58	2	0.8555	-0.000002	0.002343	0.004384	0.000028	0.002201	0.004442
14	53	3	0.8794	0.000001	0.002296	0.004570	0.000032	0.002160	0.004631
14	47	4	0.9004	0.000029	0.002206	0.005064	0.000040	0.002064	0.005087
14	43	6	0.9331	-0.000012	0.002330	0.005061	0.000014	0.002189	0.005111
14	38	7	0.9555	-0.000008	0.002492	0.005568	0.000016	0.002340	0.005615
14	34	10	0.9816	-0.000025	0.002592	0.005539	0.000018	0.002455	0.005620

Table 16. Calibration Data for Langley 16-Foot Transonic Tunnel

(a) $M_{\text{tank}} = 0.1007$ to 0.8820

$p_{\text{tank}}/p_{t,\infty}$	$(p/p_{t,\infty})_{\text{ave}}$	$(p/p_{t,\infty})_{\text{cal}}$	$(p/p_{t,\infty})_{\text{ave}} - (p/p_{t,\infty})_{\text{cal}}$	M_{tank}	M_{ave}	M_{cal}	$M_{\text{ave}} - M_{\text{cal}}$
0.993045	0.993075	0.993256	0.000038	0.1007	0.099686	0.098371	0.001315
0.972007	0.972031	0.972137	-0.000040	0.2032	0.201717	0.201326	0.000390
0.939138	0.939367	0.939362	-0.000131	0.3033	0.300906	0.300279	0.000627
0.896504	0.896433	0.896149	0.000246	0.4021	0.398313	0.398899	-0.000586
0.896022	0.895791	0.895523	-0.000030	0.4031	0.399637	0.400188	-0.000551
0.894175	0.893960	0.893600	0.000080	0.4069	0.403394	0.404128	-0.000734
0.843216	0.842969	0.843063	-0.000044	0.5043	0.500089	0.499922	0.000167
0.841958	0.841678	0.841782	-0.000151	0.5065	0.502383	0.502199	0.000184
0.842373	0.842208	0.842133	0.000106	0.5058	0.501442	0.501576	-0.000134
0.784611	0.783940	0.783951	0.000063	0.6050	0.600104	0.600087	0.000017
0.784880	0.784158	0.784210	0.000046	0.6045	0.599749	0.599664	0.000085
0.783093	0.782136	0.782433	-0.000216	0.6075	0.603038	0.602556	0.000482
0.783609	0.782708	0.782982	-0.000183	0.6066	0.602108	0.601663	0.000445
0.783666	0.782835	0.782951	-0.000155	0.6065	0.601901	0.601712	0.000189
0.783783	0.782991	0.783176	-0.000057	0.6063	0.601748	0.601347	0.000301
0.752304	0.751270	0.751244	0.000080	0.6572	0.652467	0.652509	-0.000042
0.752958	0.751846	0.751953	-0.000017	0.6562	0.651556	0.651387	0.000169
0.721402	0.720345	0.720078	0.000338	0.7055	0.700906	0.701321	-0.000416
0.704938	0.703961	0.703611	0.000429	0.7309	0.726281	0.726821	-0.000540
0.688752	0.687588	0.687454	0.000133	0.7558	0.751515	0.751721	-0.000206
0.671801	0.670921	0.670541	0.000417	0.7817	0.777127	0.777711	-0.000584
0.659020	0.657611	0.657829	-0.000230	0.8013	0.797560	0.797225	0.000335
0.657679	0.656253	0.656512	-0.000268	0.8033	0.799645	0.799247	0.000398
0.655032	0.653807	0.653860	-0.000041	0.8074	0.803400	0.803319	0.000081
0.640469	0.639145	0.639369	-0.000266	0.8297	0.825926	0.825582	0.000344
0.623327	0.621644	0.622205	-0.000572	0.8560	0.852882	0.852017	0.000865
0.606393	0.605297	0.605246	0.000048	0.8820	0.878169	0.878249	-0.000080

Table 16. Continued

(b) $M_{\text{tank}} = 0.9029$ to 1.2927

$p_{\text{tank}}/p_{t,\infty}$	$(p/p_{t,\infty})_{\text{ave}}$	$(p/p_{t,\infty})_{\text{cal}}$	$(p/p_{t,\infty})_{\text{ave}} - (p/p_{t,\infty})_{\text{cal}}$	M_{tank}	M_{ave}	M_{cal}	$M_{\text{ave}} - M_{\text{cal}}$
0.592918	0.591322	0.591585	-0.000308	0.9029	0.899903	0.899494	0.000410
0.592200	0.590679	0.590873	-0.000190	0.9056	0.900906	0.900604	0.000302
0.591152	0.589649	0.589796	-0.000122	0.9040	0.902514	0.902284	0.000230
0.590589	0.589395	0.589224	0.000108	0.9065	0.902910	0.903177	-0.000267
0.575733	0.574090	0.574074	-0.000043	0.9292	0.926891	0.926916	-0.000025
0.575448	0.573731	0.573762	-0.000128	0.9297	0.927455	0.927406	0.000049
0.565339	0.563754	0.563418	0.000308	0.9455	0.943196	0.943728	-0.000532
0.559519	0.557642	0.557404	0.000229	0.9547	0.952886	0.953264	-0.000378
0.557926	0.556381	0.555779	0.000492	0.9568	0.954890	0.955847	-0.000957
0.544089	0.541600	0.541480	0.000017	0.9787	0.978504	0.978697	-0.000193
0.541571	0.539230	0.538870	0.000284	0.9827	0.982313	0.982893	-0.000580
0.527214	0.524801	0.524050	0.000723	1.0061	1.005656	1.006878	-0.001222
0.516450	0.512853	0.512923	-0.000156	1.0273	1.025197	1.025081	0.000116
0.512429	0.509051	0.508777	0.000110	1.0352	1.031458	1.031910	-0.000451
0.503591	0.499882	0.499694	0.000081	1.0524	1.046651	1.046964	-0.000313
0.498959	0.494112	0.494981	-0.000877	1.0613	1.056282	1.054828	0.001454
0.468321	0.464294	0.464289	-0.000188	1.1158	1.107009	1.107016	-0.000008
0.454475	0.450475	0.450875	-0.000423	1.1402	1.131125	1.130421	0.000705
0.454229	0.450043	0.450657	-0.000799	1.1406	1.131886	1.130804	0.001082
0.440480	0.437934	0.437684	0.000181	1.1670	1.153389	1.153836	-0.000447
0.438863	0.436681	0.436176	0.000278	1.1643	1.155634	1.156541	-0.000907
0.439375	0.437073	0.436648	0.000290	1.1661	1.154931	1.155693	-0.000762
0.424896	0.425175	0.423406	0.001619	1.1888	1.176439	1.179669	-0.003230

Table 16. Concluded

(b) Concluded

$p_{\text{tank}}/p_{t,\infty}$	$(p/p_{t,\infty})_{\text{ave}}$	$(p/p_{t,\infty})_{\text{cal}}$	$(p/p_{t,\infty})_{\text{ave}} - (p/p_{t,\infty})_{\text{cal}}$	M_{tank}	M_{ave}	M_{cal}	$M_{\text{ave}} - M_{\text{cal}}$
0.412079	0.411580	0.411945	-0.000515	1.2086	1.201483	1.200804	0.000678
0.412555	0.412051	0.412371	-0.000450	1.2079	1.200605	1.200012	0.000594
0.399596	0.400653	0.400955	-0.000501	1.2279	1.222002	1.221429	0.000573
0.385348	0.388966	0.388420	0.000492	1.2501	1.244365	1.245420	-0.001055
0.372797	0.377251	0.377131	-0.000116	1.2714	1.267246	1.267483	-0.000237
0.360467	0.365641	0.365484	-0.000022	1.2927	1.290416	1.290734	-0.000318

Table 17. Test-Section Wall Divergence Angles for 6-ft and 8-ft CTSL

(a) 1990 calibration

M_∞	δ_{flat} , min
0.10	0
.825	0
.85	1.3
.875	2.8
.90	4.9
.925	6.5
.95	9.3
.975	12.2
.98	13.2
1.00	14.2
1.02	9.6
1.025	9.2
1.03	8.6
1.04	7.3
1.05	6.0
1.10	1.0
1.125	9.5

(b) 1977 calibration with test section air removal

T_{dp} , deg	δ_{flat} in min for M_∞ of—						
	1.15	1.175	1.20	1.225	1.25	1.275	1.30
10	19.3	24.0	8.3	11.8	15.6	18.7	22.2
15	18.9	24.0	8.0	11.4	14.8	18.2	21.6
20	18.6	24.0	7.6	11.0	14.0	17.6	20.9
25	18.2	23.5	7.4	10.4	13.1	16.9	19.6
30	17.8	23.8	7.2	10.2	13.1	16.3	19.4
35	17.9	24.3	7.7	10.9	13.8	17.0	20.2
40	18.3	24.8	8.2	11.4	14.6	17.7	20.8
45	18.7	25.4	8.7	12.0	15.5	18.3	21.5
50	19.1	25.8	9.2	12.5	15.8	19.0	22.3
55	19.5	26.4	9.7	13.0	16.5	19.7	23.0
60	19.9	26.7	10.2	13.6	17.1	20.5	23.7
70	20.7	27.8	11.2	14.8	18.5	22.0	25.1

Table 18. Test-Section Wall Divergence Angles for 9-ft to 21-ft CTSL From 1990 Calibrations

M_∞	δ_{flat} in min for CTSL of—					
	9 ft	10.5 ft	12 ft	15 ft	18 ft	21 ft
0.10	0	0	0	0	0	0
0.80	0	0	0	0	1.0	1.0
0.825	0	0	0	0	1.0	1.0
0.85	0	0	1.0	1.0	2.0	2.0
0.875	2.0	2.0	4.0	2.0	3.0	3.0
0.90	4.0	4.04	4.0	4.0	4.0	4.0
0.925	5.0	5.0	5.0	5.0	6.0	6.0
0.95	8.0	8.0	8.0	8.0	7.0	7.0
0.98	12.0	12.0	10.0	10.0	10.0	10.0

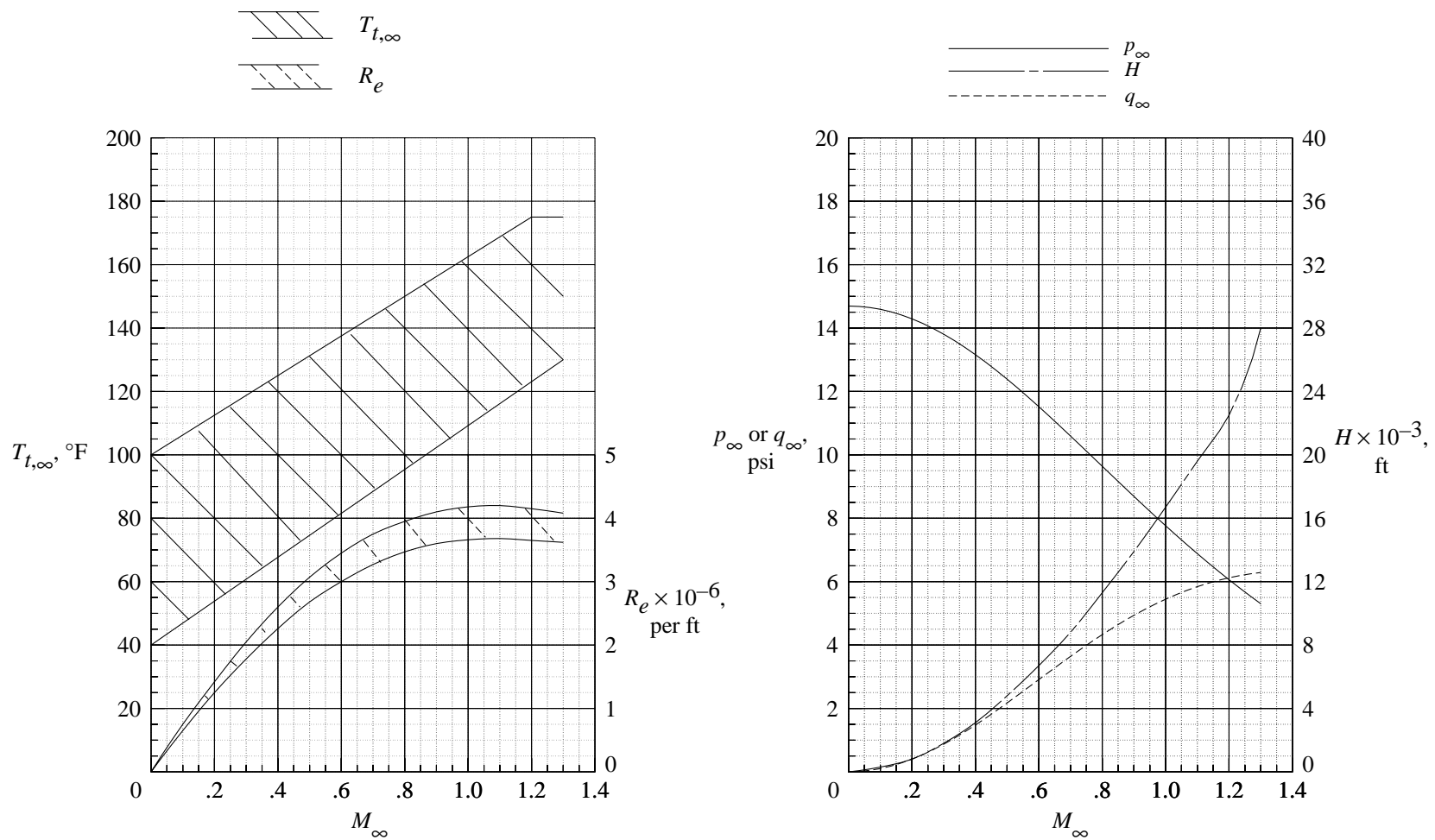
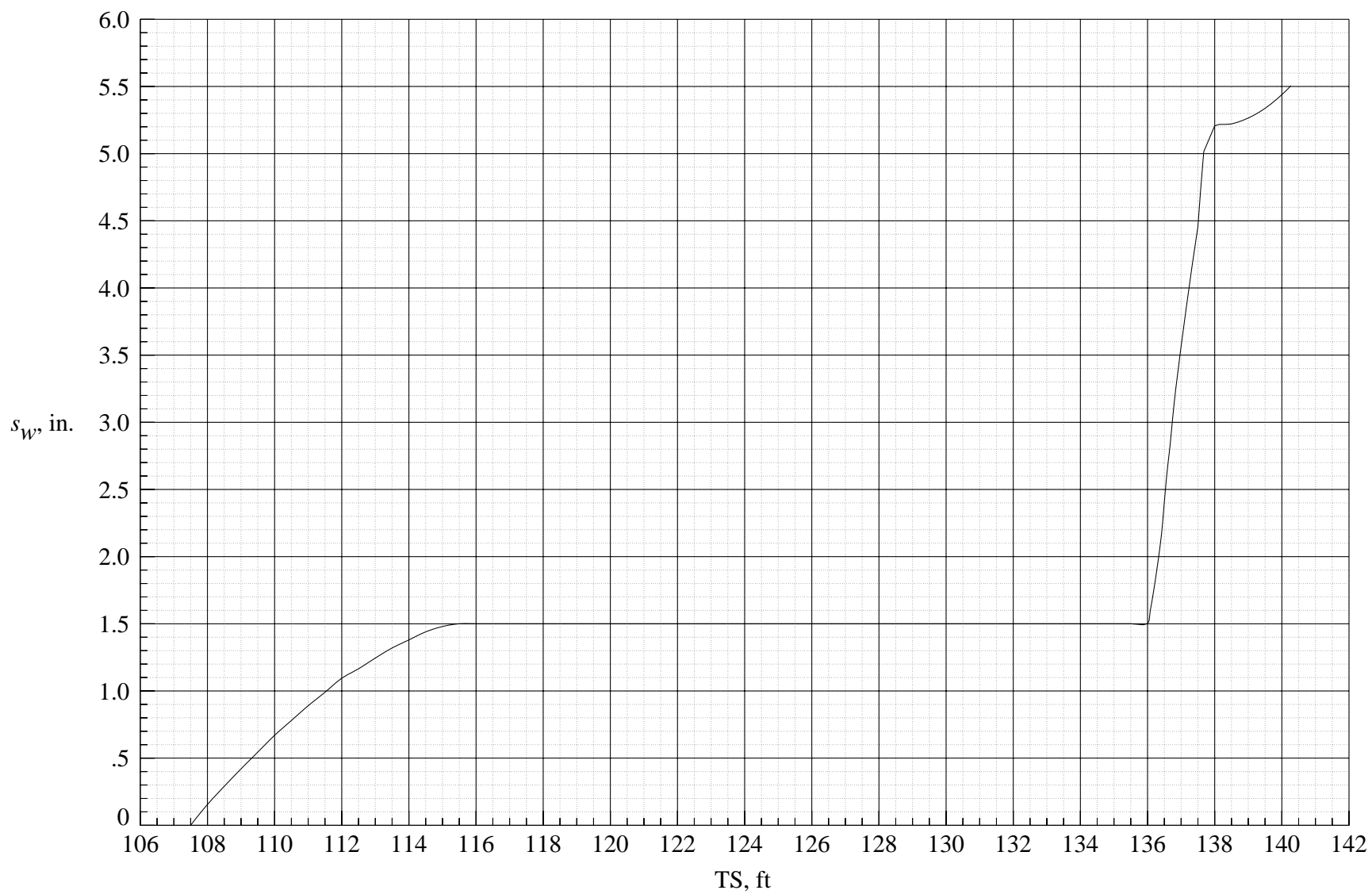
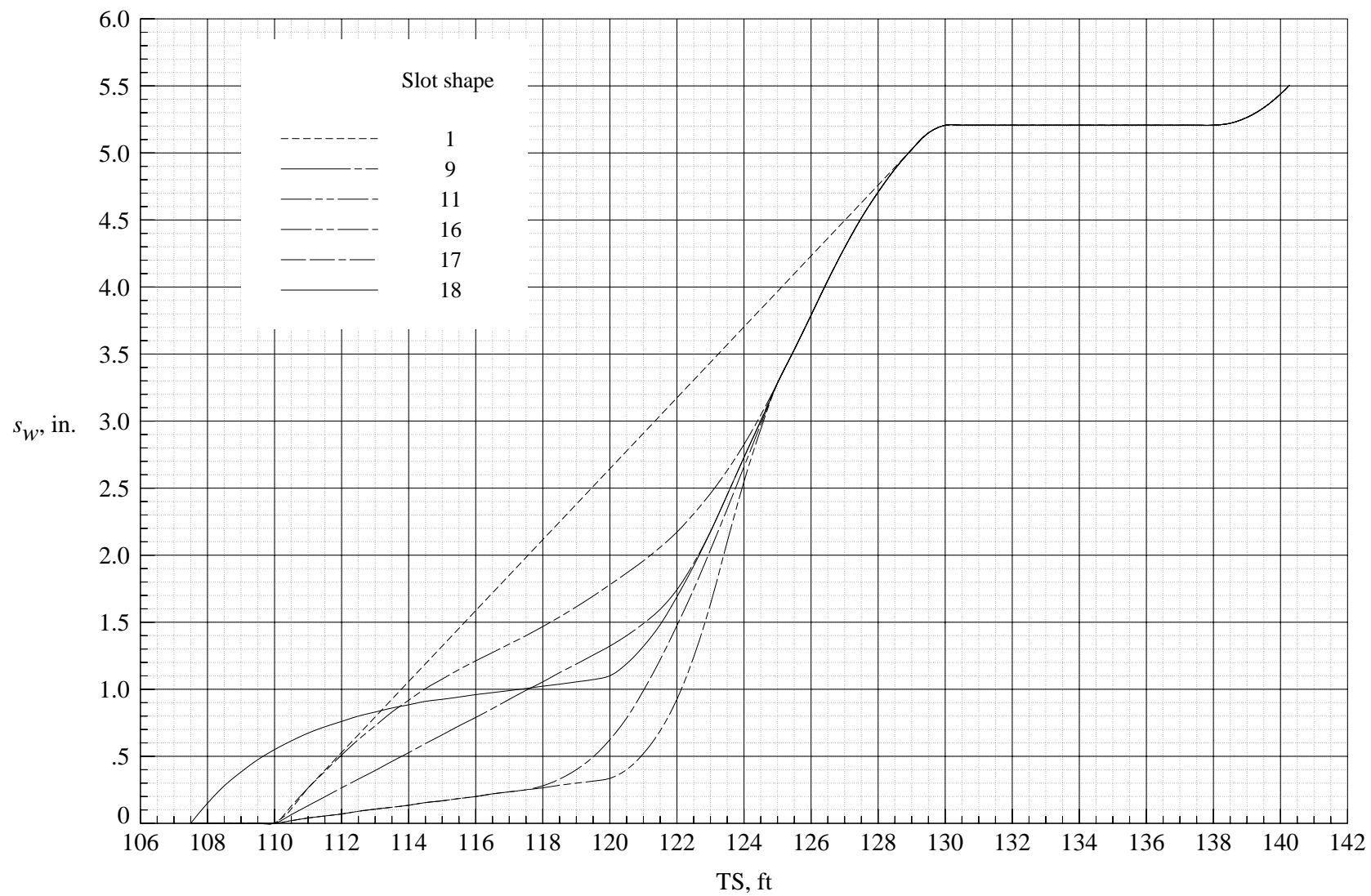


Figure 4. Airstream aerodynamic characteristics of Langley 16-Foot Transonic Tunnel for $p_{t,\infty} = 14.491$ psi.



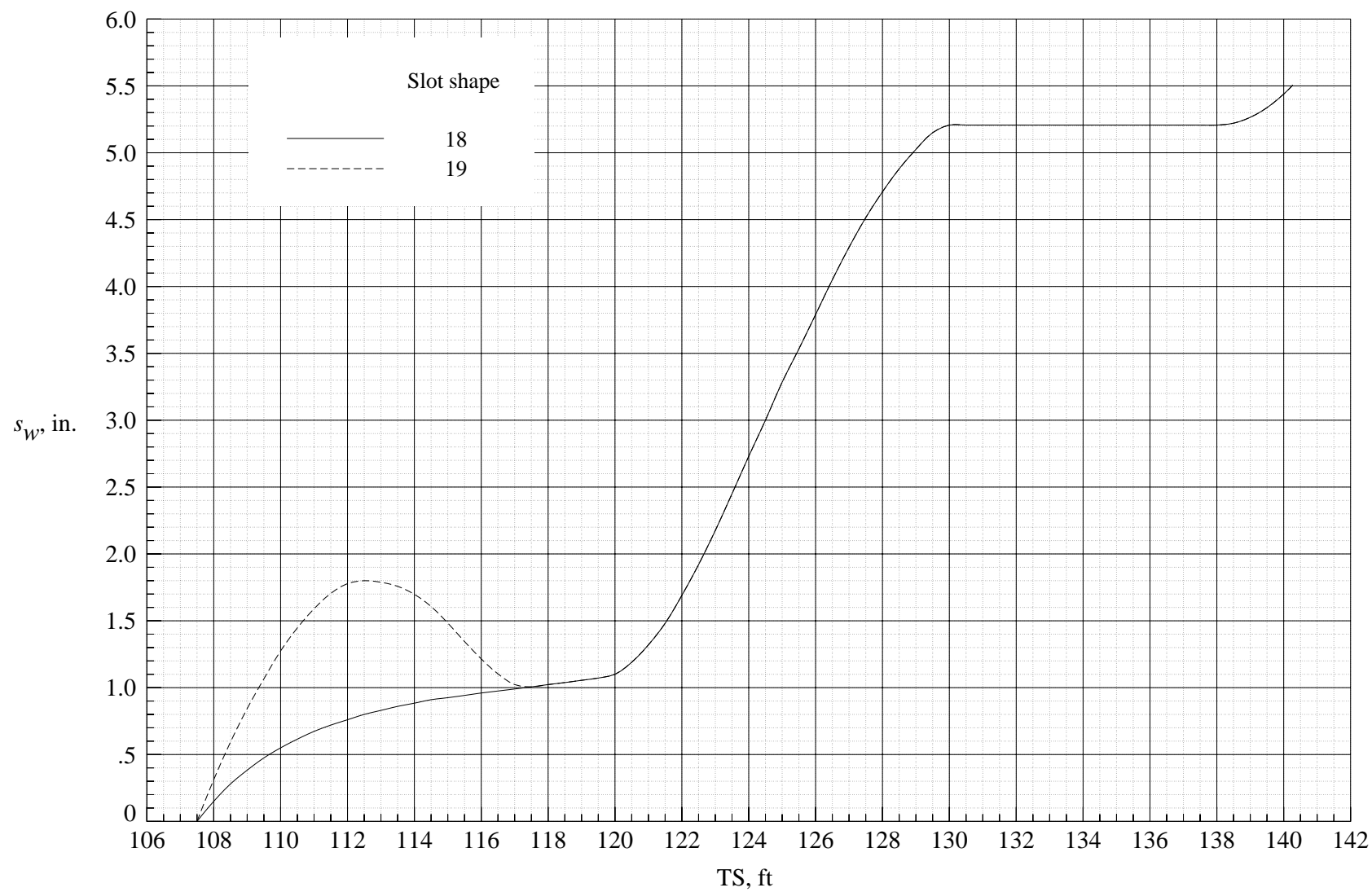
(b) Planform of slot shape 29.

Figure 8. Concluded.



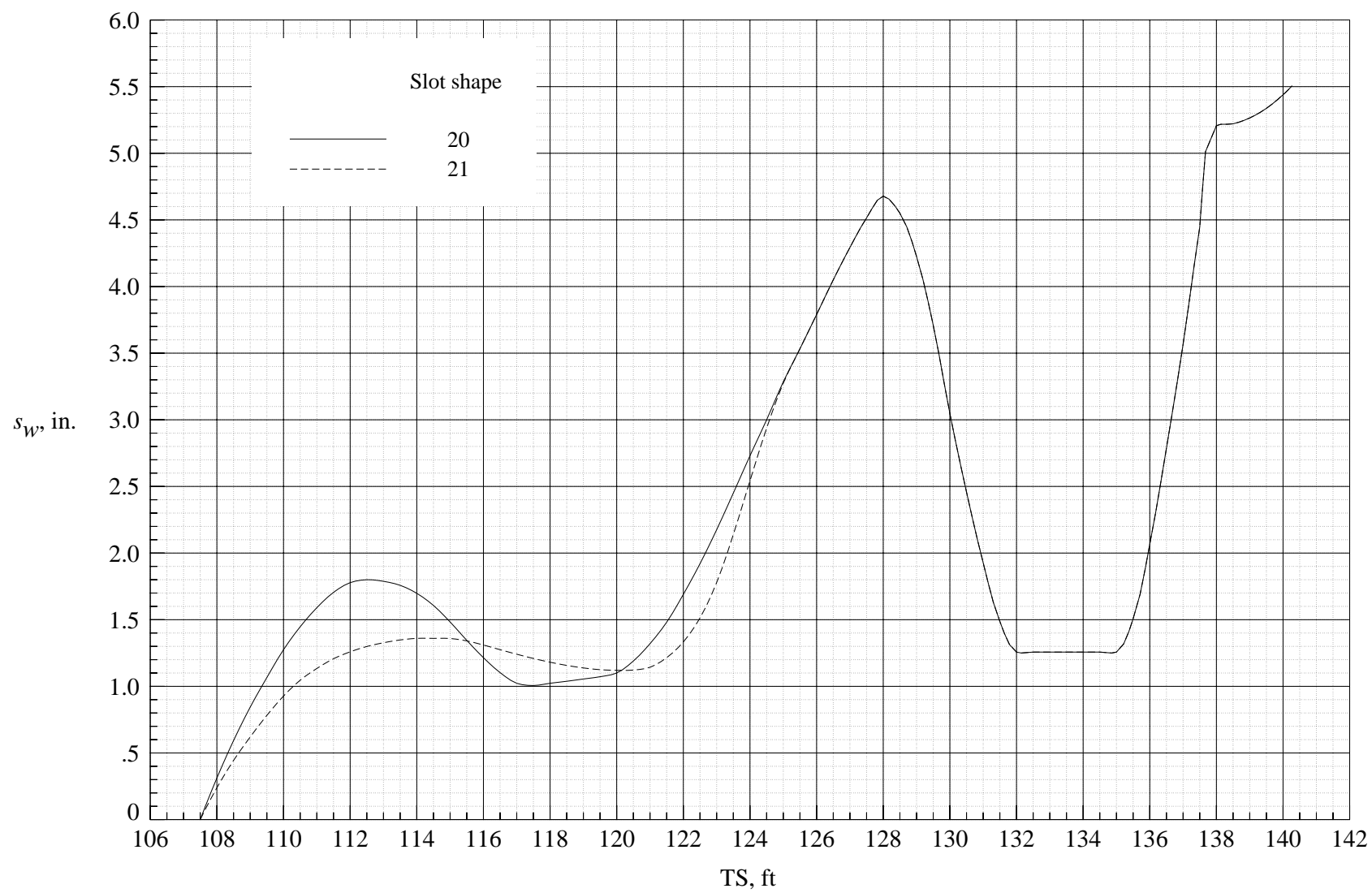
(a) Slot shapes 1 to 18.

Figure 26. Planforms of slot shapes investigated in Langley 16-Foot Transonic Tunnel.



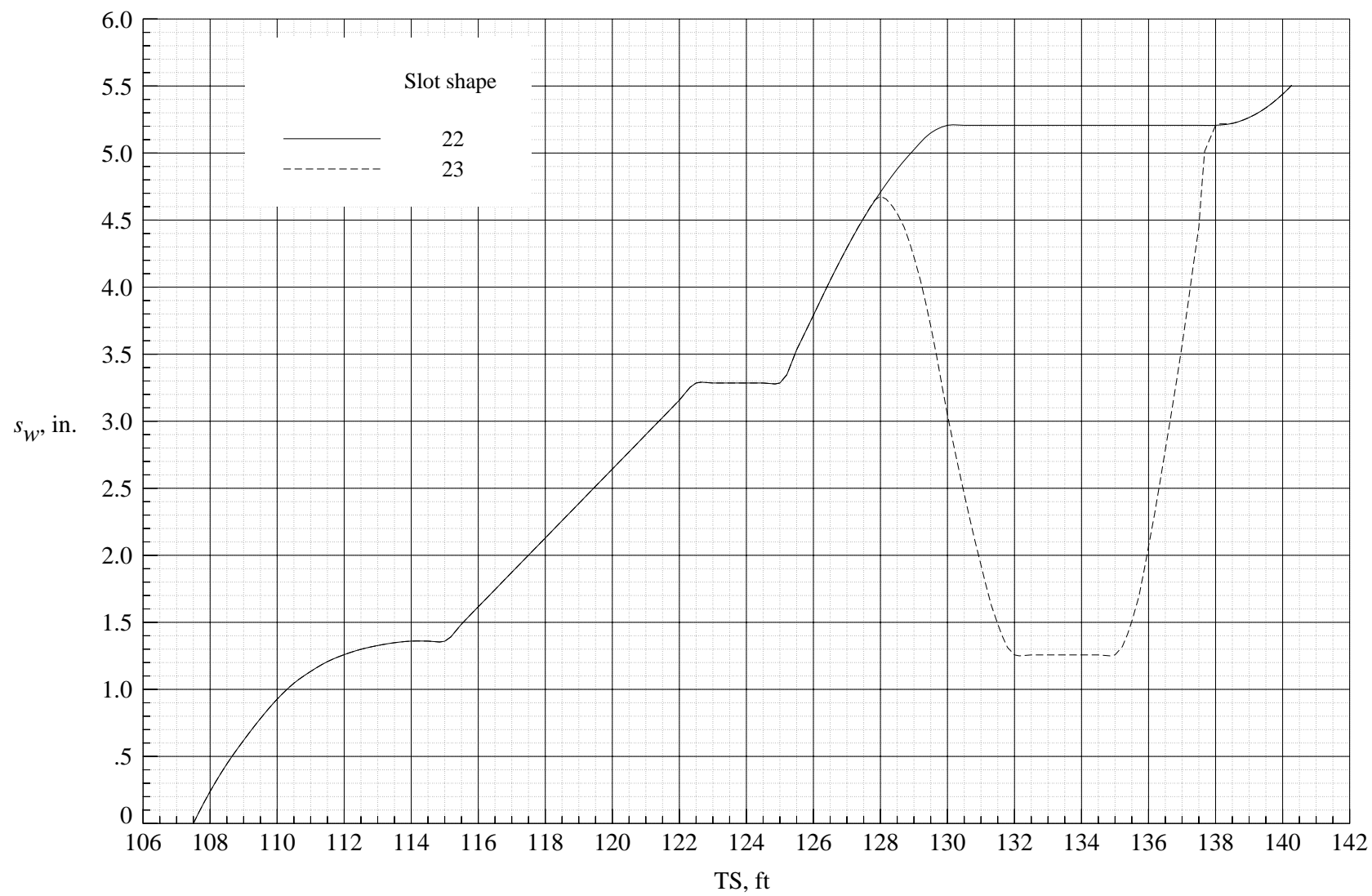
(b) Slot shapes 18 and 19.

Figure 26. Continued.



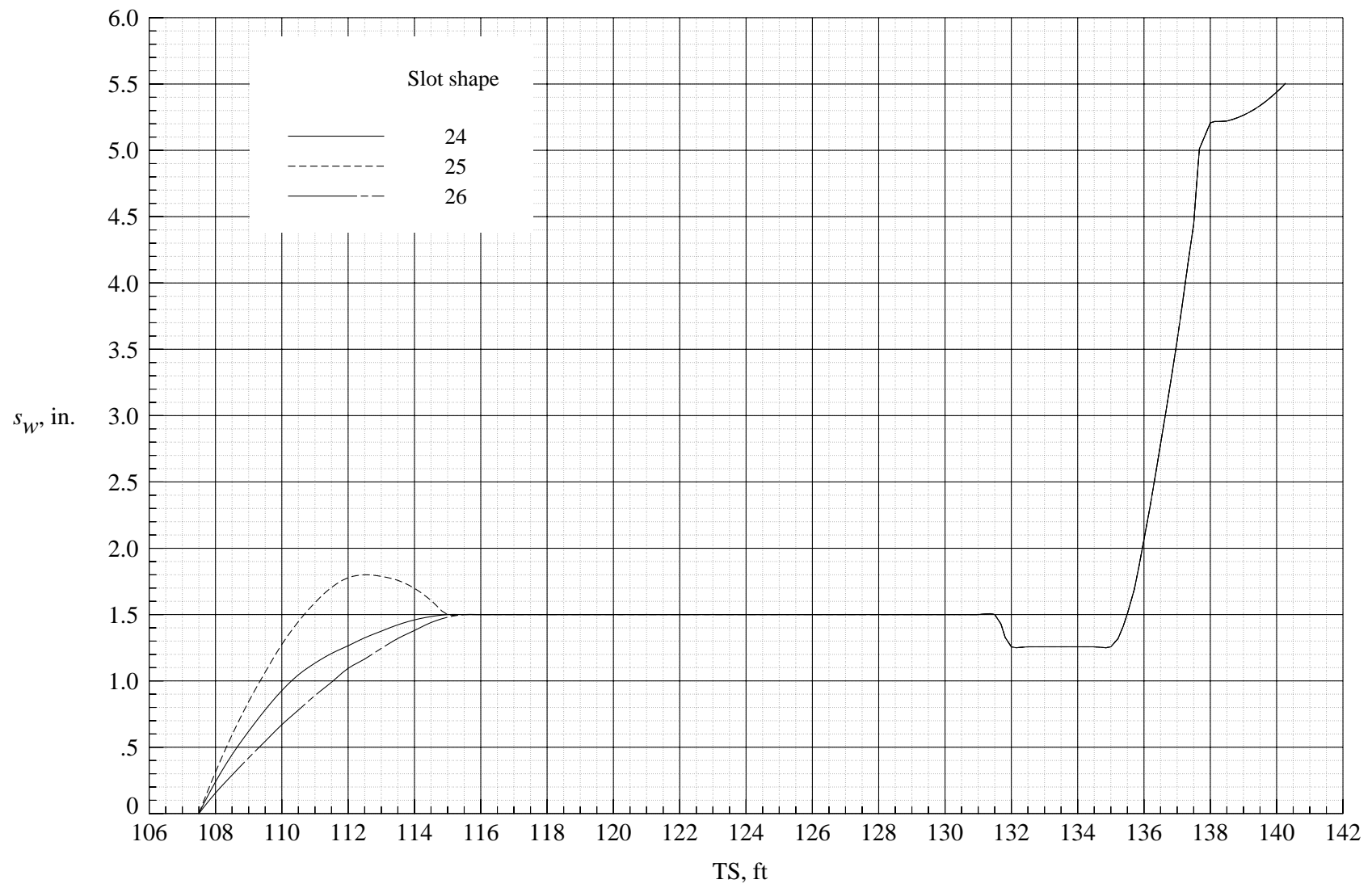
(c) Slot shapes 20 and 21.

Figure 26. Continued.



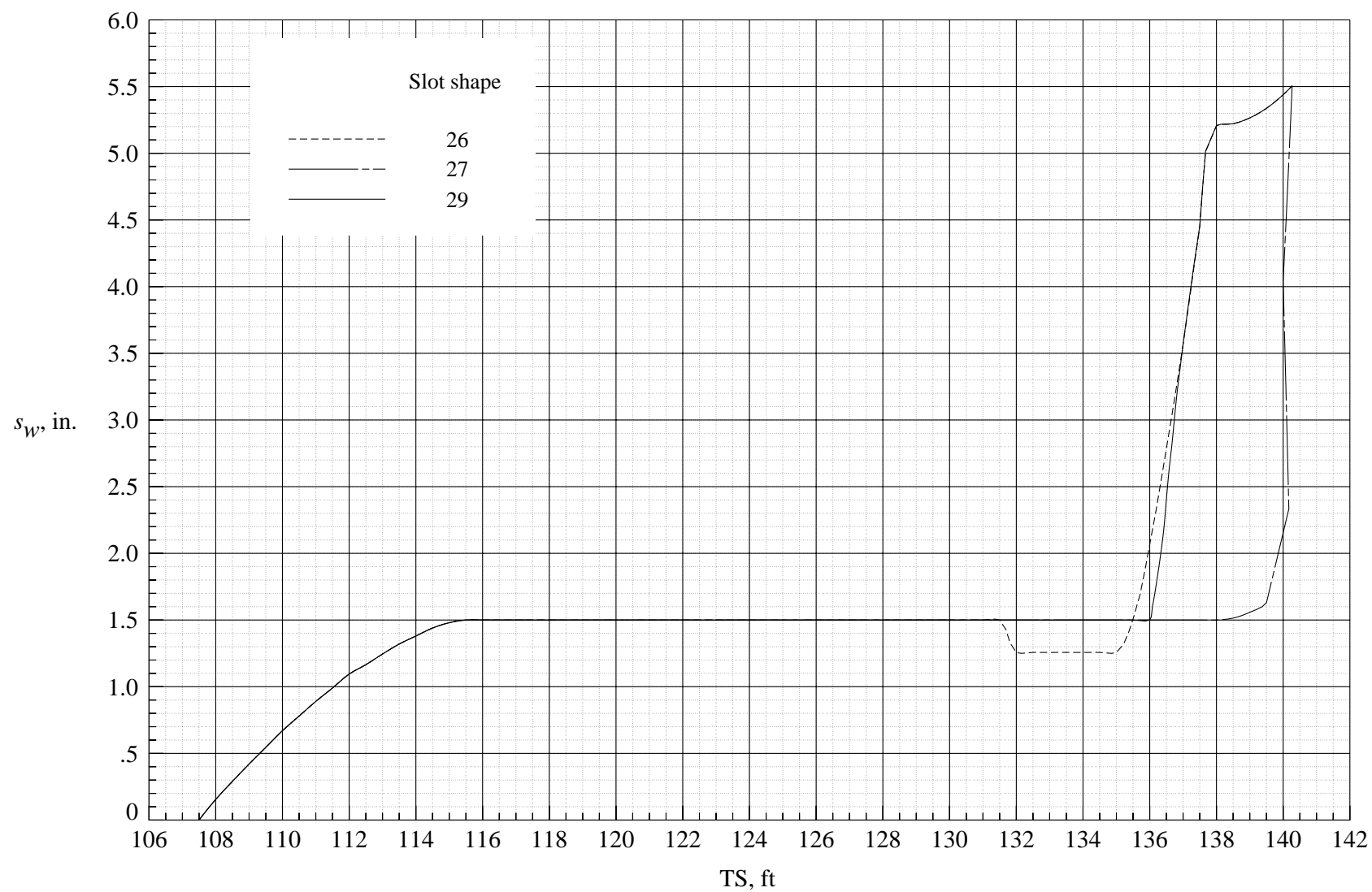
(d) Slot shapes 22 and 23.

Figure 26. Continued.



(e) Slot shapes 24 to 26.

Figure 26. Continued.



(f) Slot shapes 26 to 29.

Figure 26. Concluded.

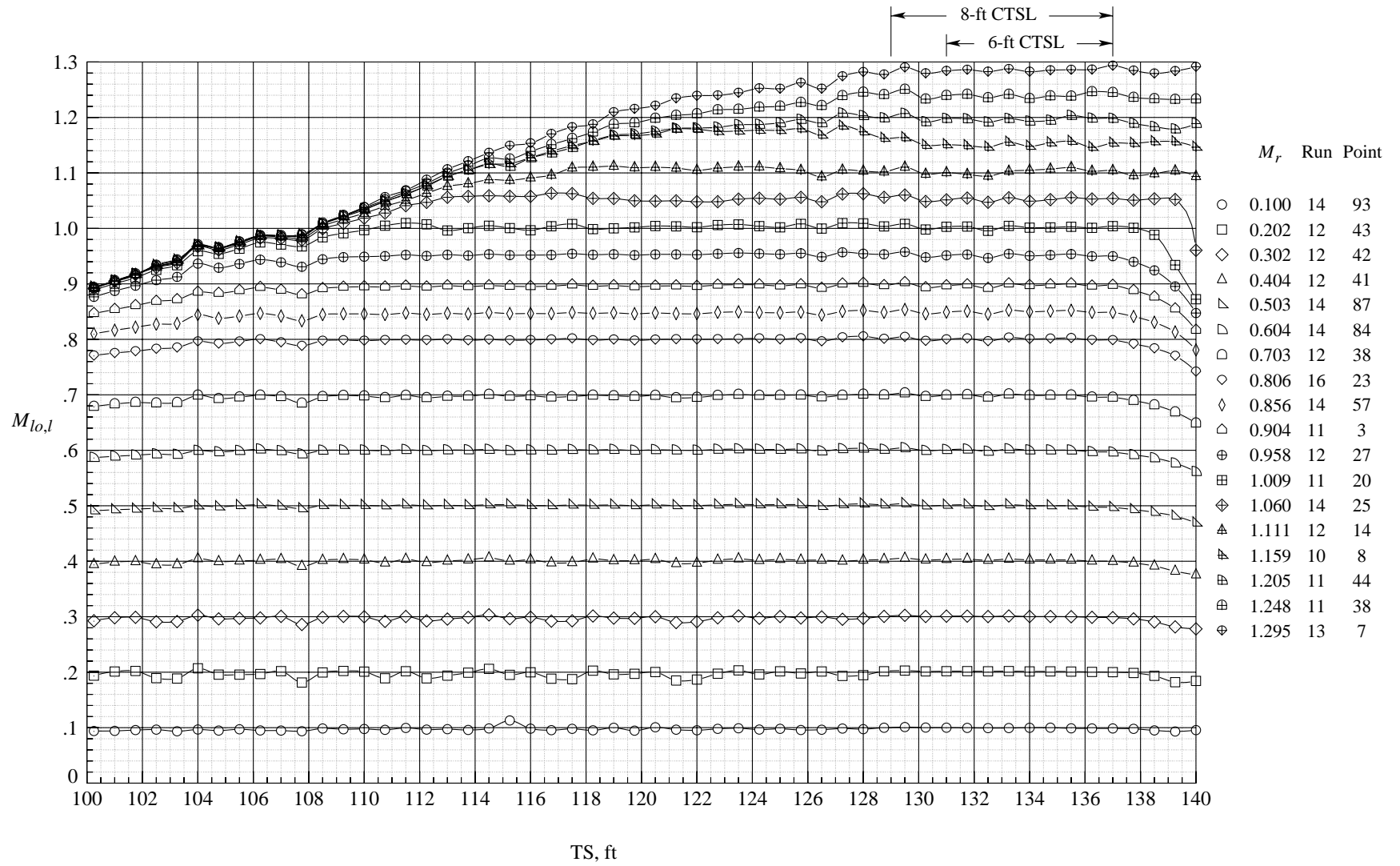


Figure 27. Test-section Mach number distributions from left side of centerline tube.

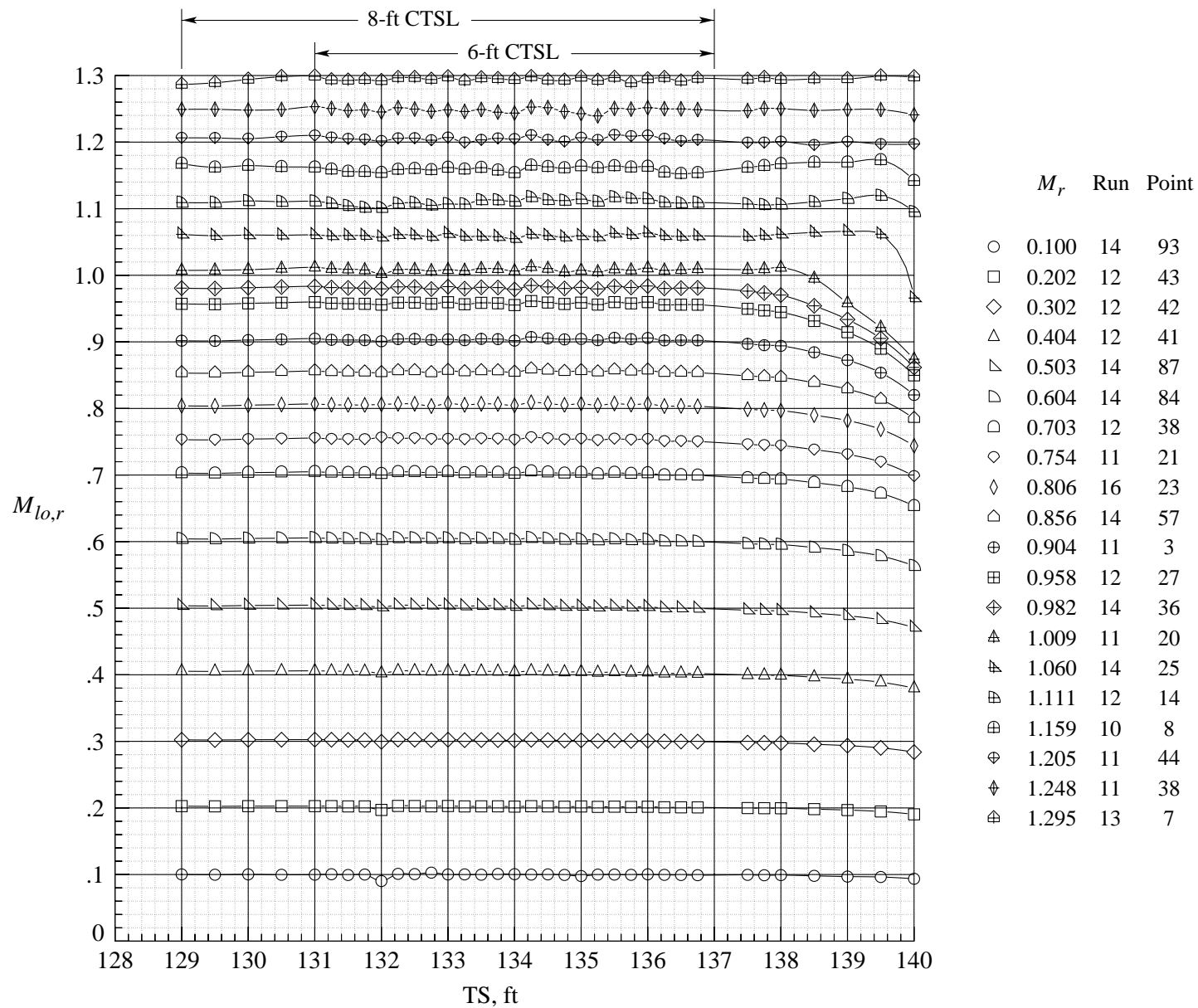


Figure 28. Test-section Mach number distributions from right side of centerline tube.

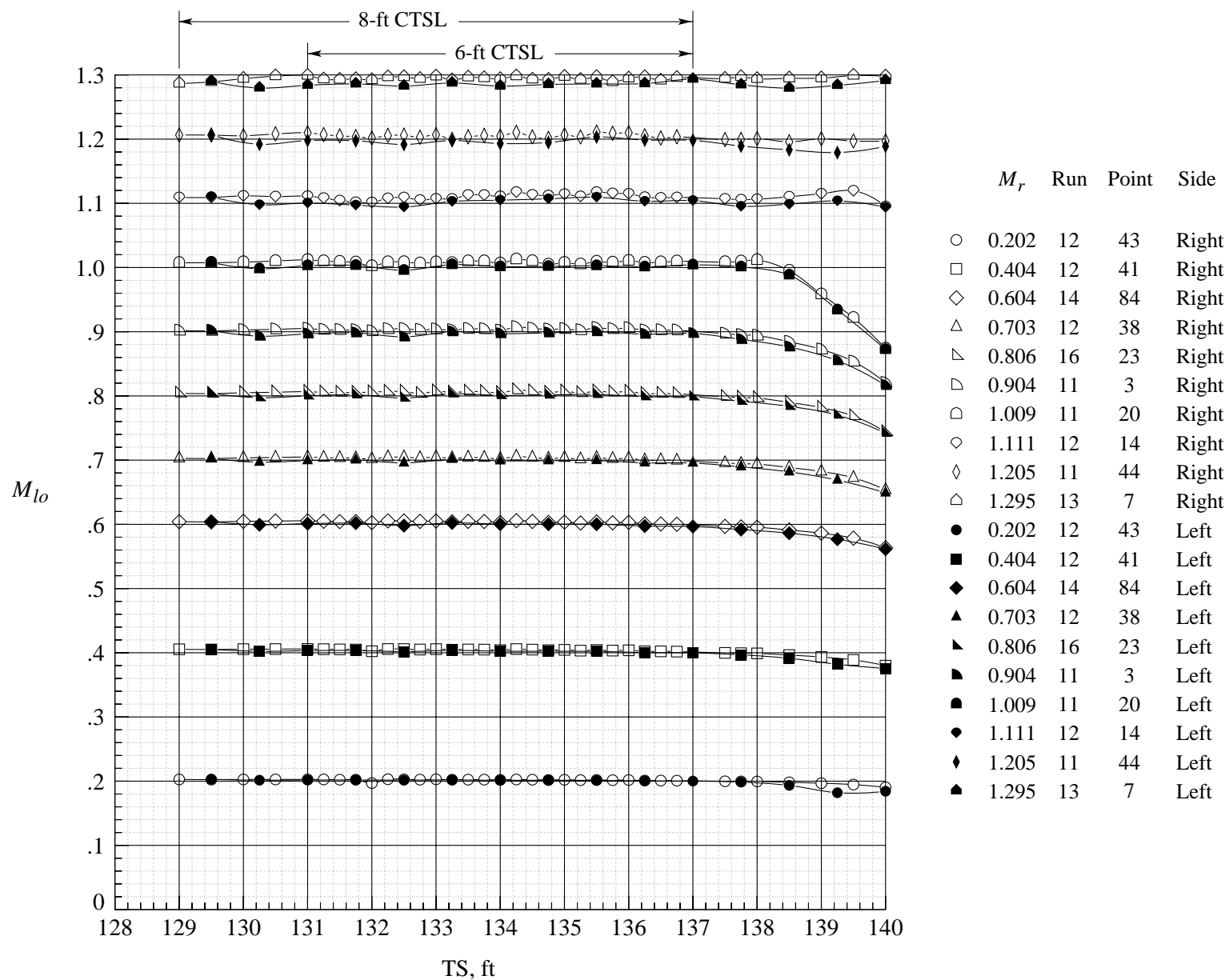


Figure 29. Comparison of Mach number distributions from right and left sides of centerline tube.

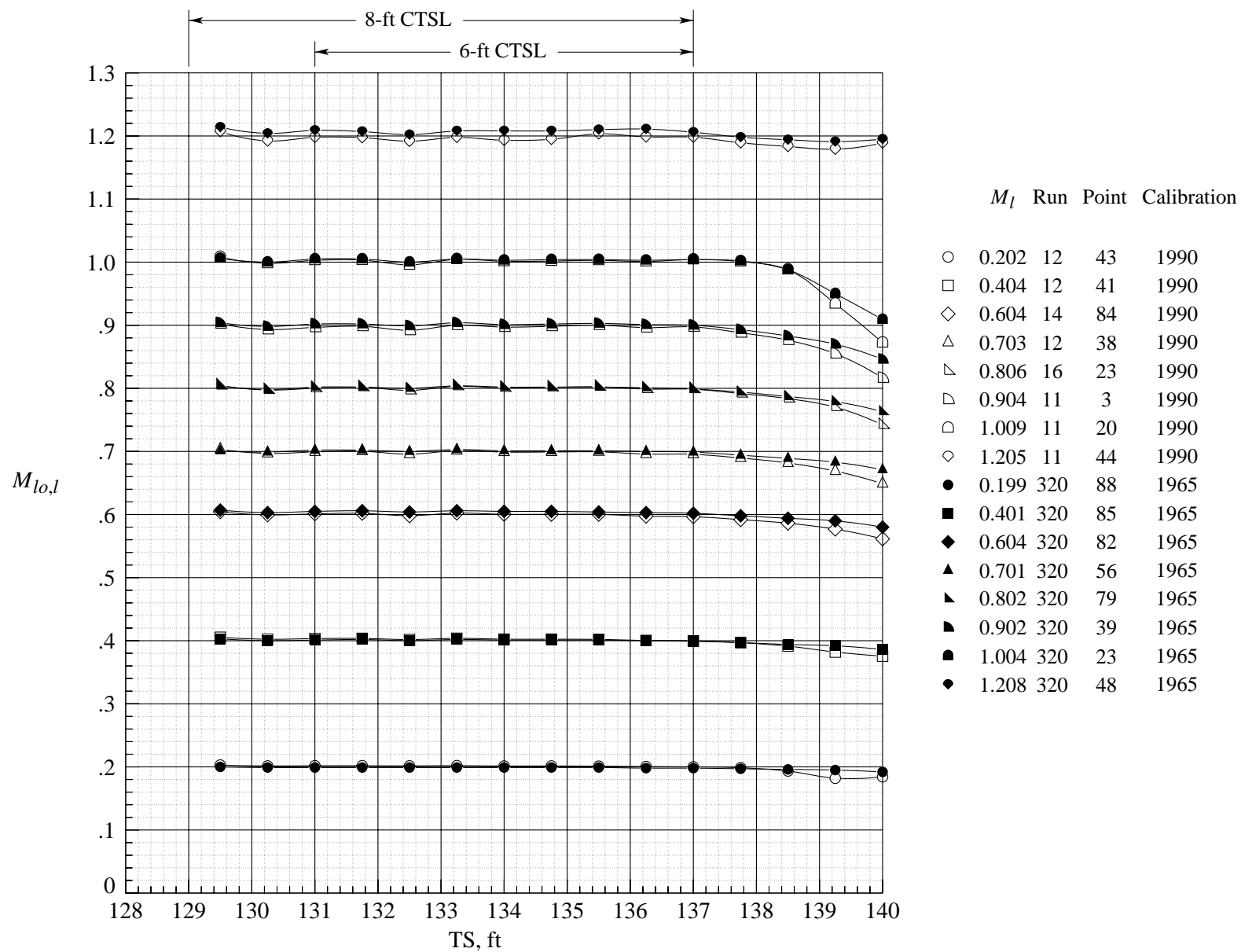


Figure 30. Comparison of Mach number distributions from 1990 and 1965 wind tunnel calibrations from left side of centerline tube.

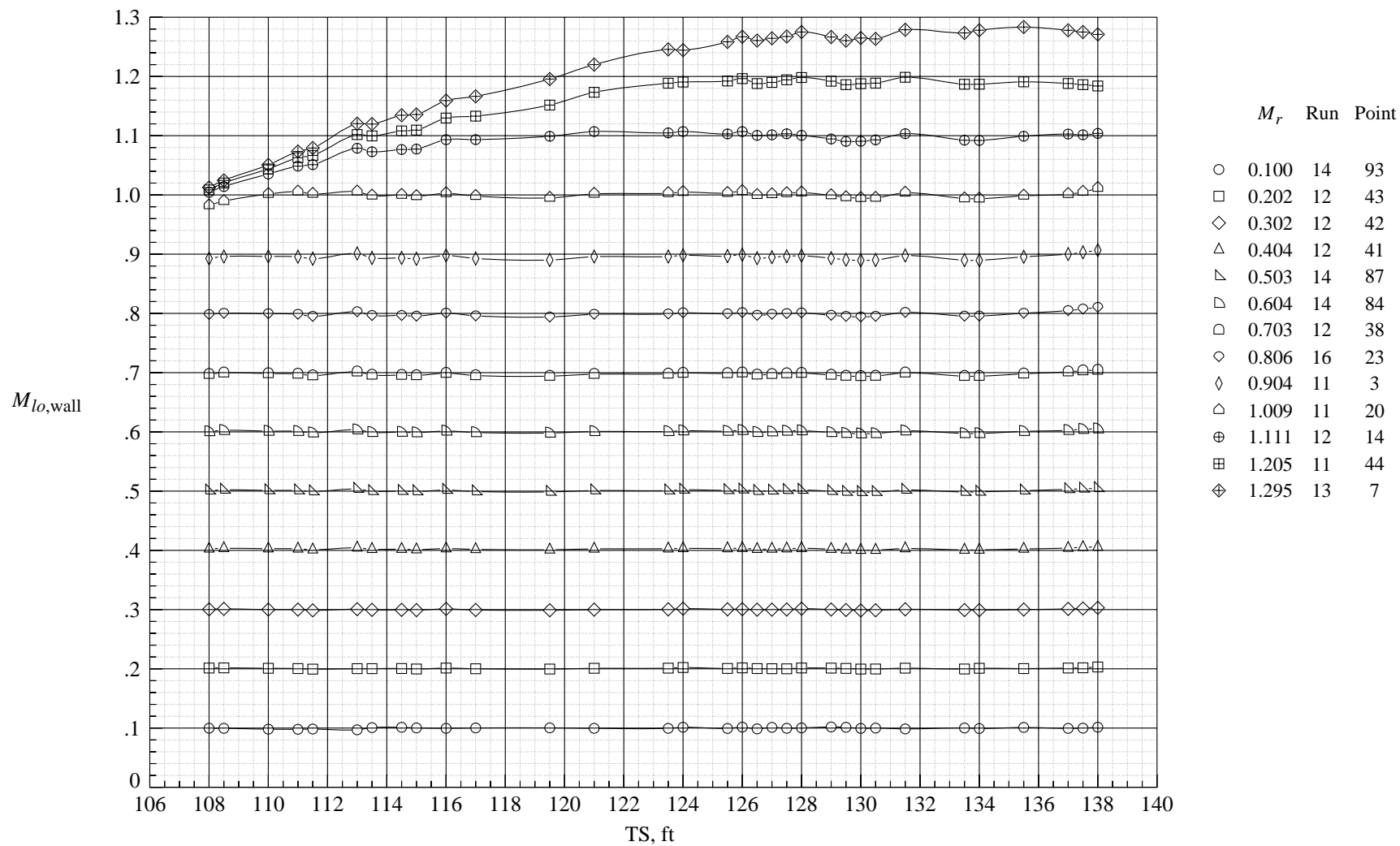


Figure 31. Test-section wall Mach number distributions.

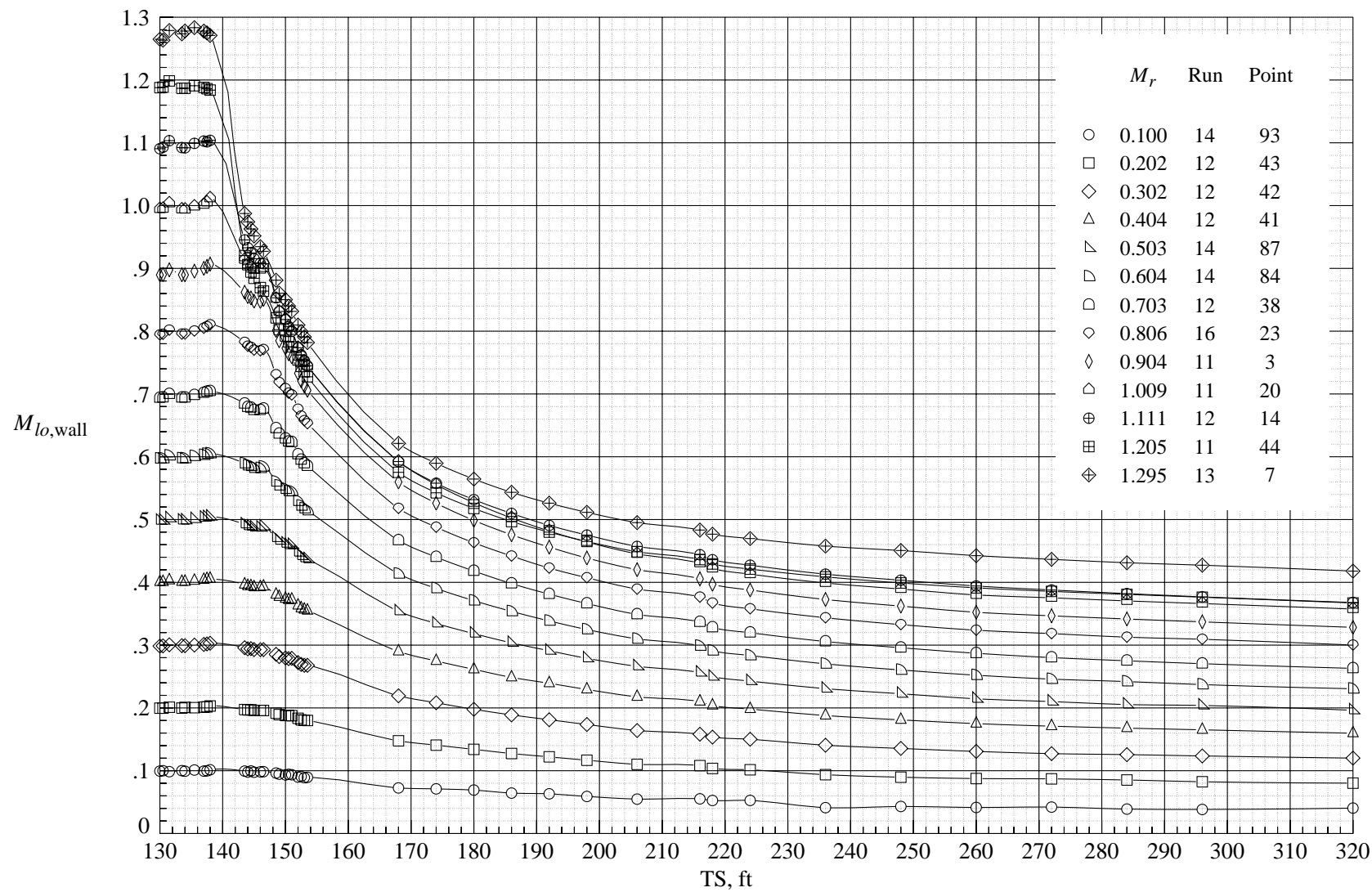
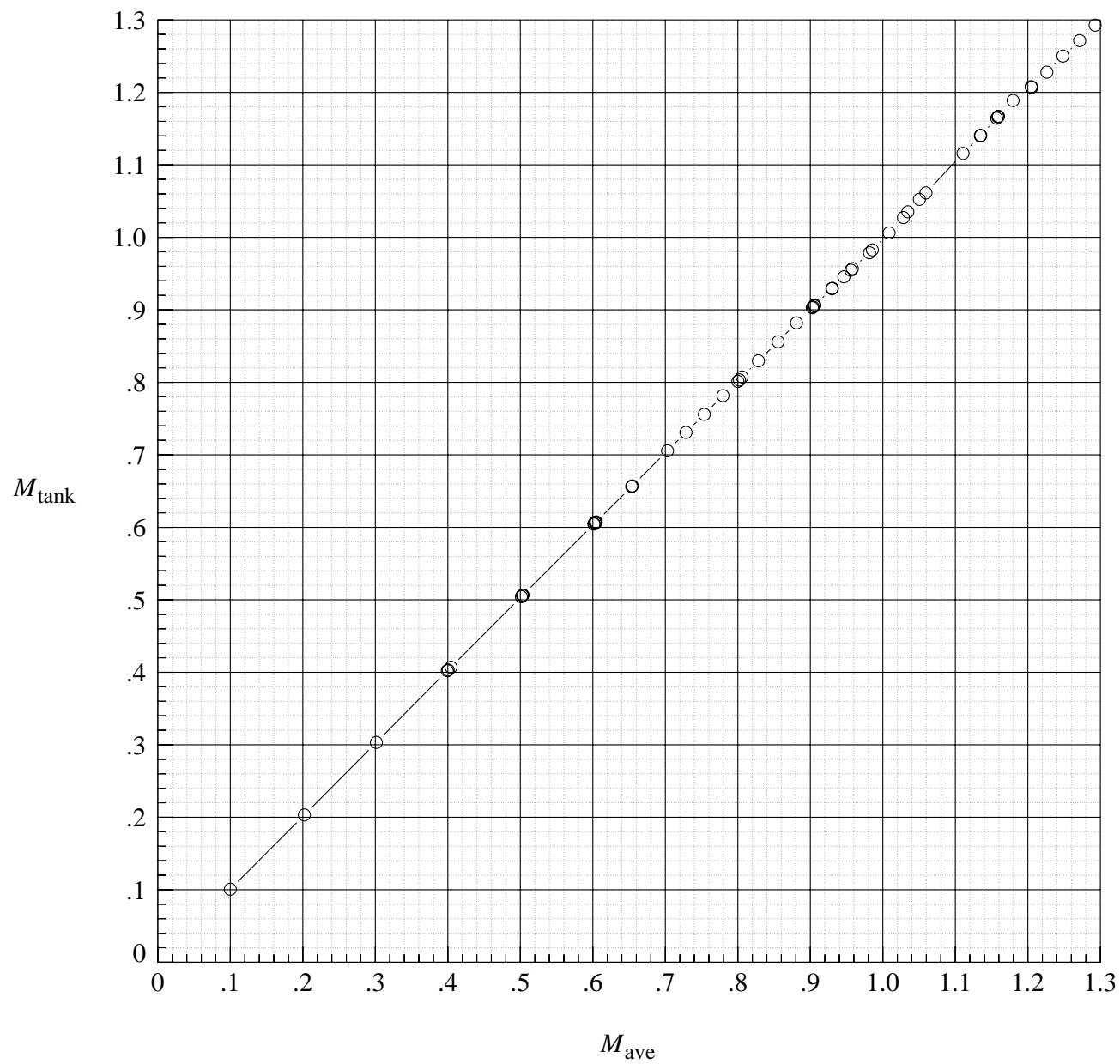
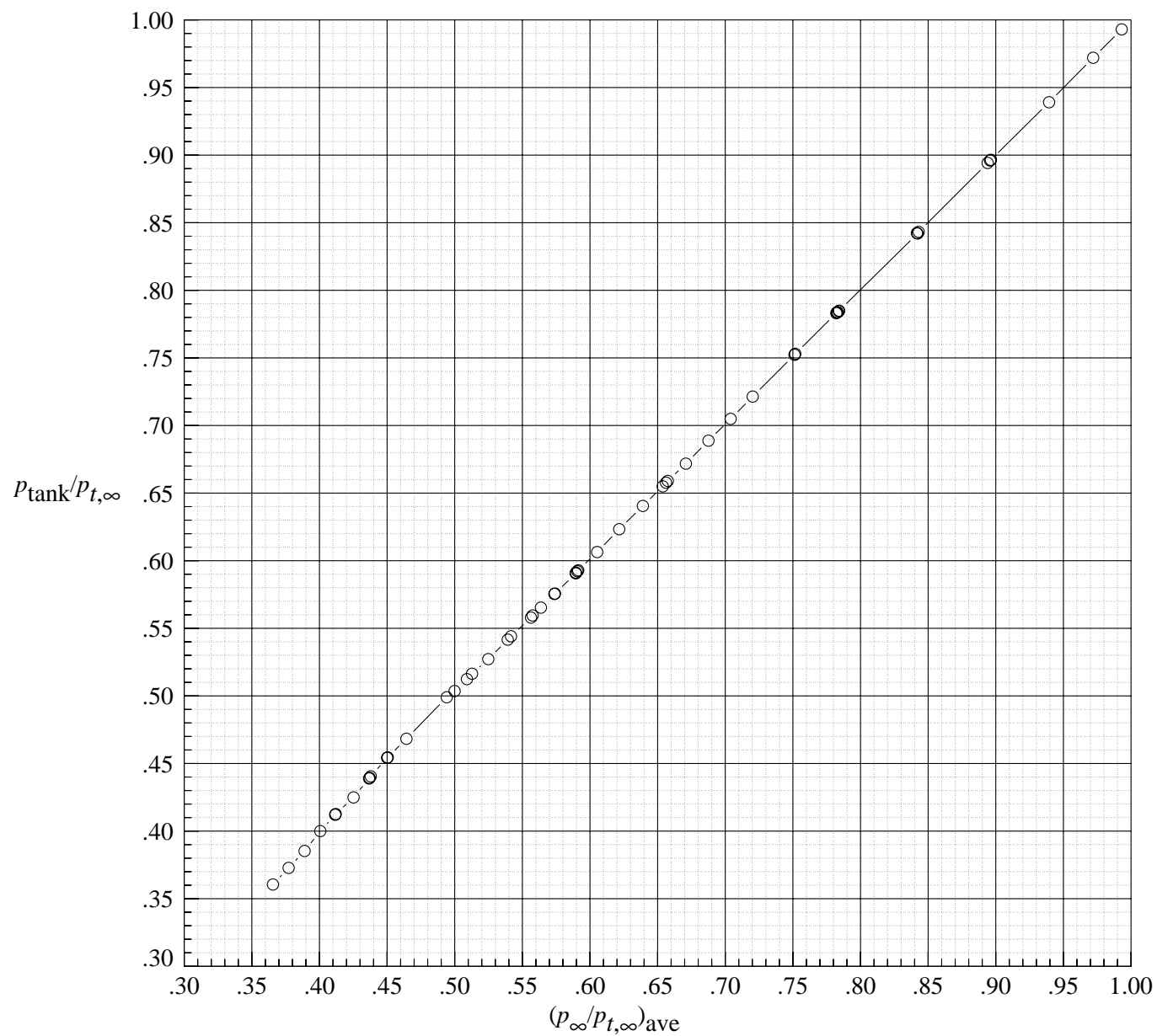


Figure 32. Test-section wall plus diffuser Mach number distributions.



(a) Equivalent tank Mach number and average free-stream Mach number.

Figure 33. Langley 16-Foot Transonic Tunnel calibration of 1990.



(b) Tank pressure and free-stream static pressure.

Figure 33. Concluded.

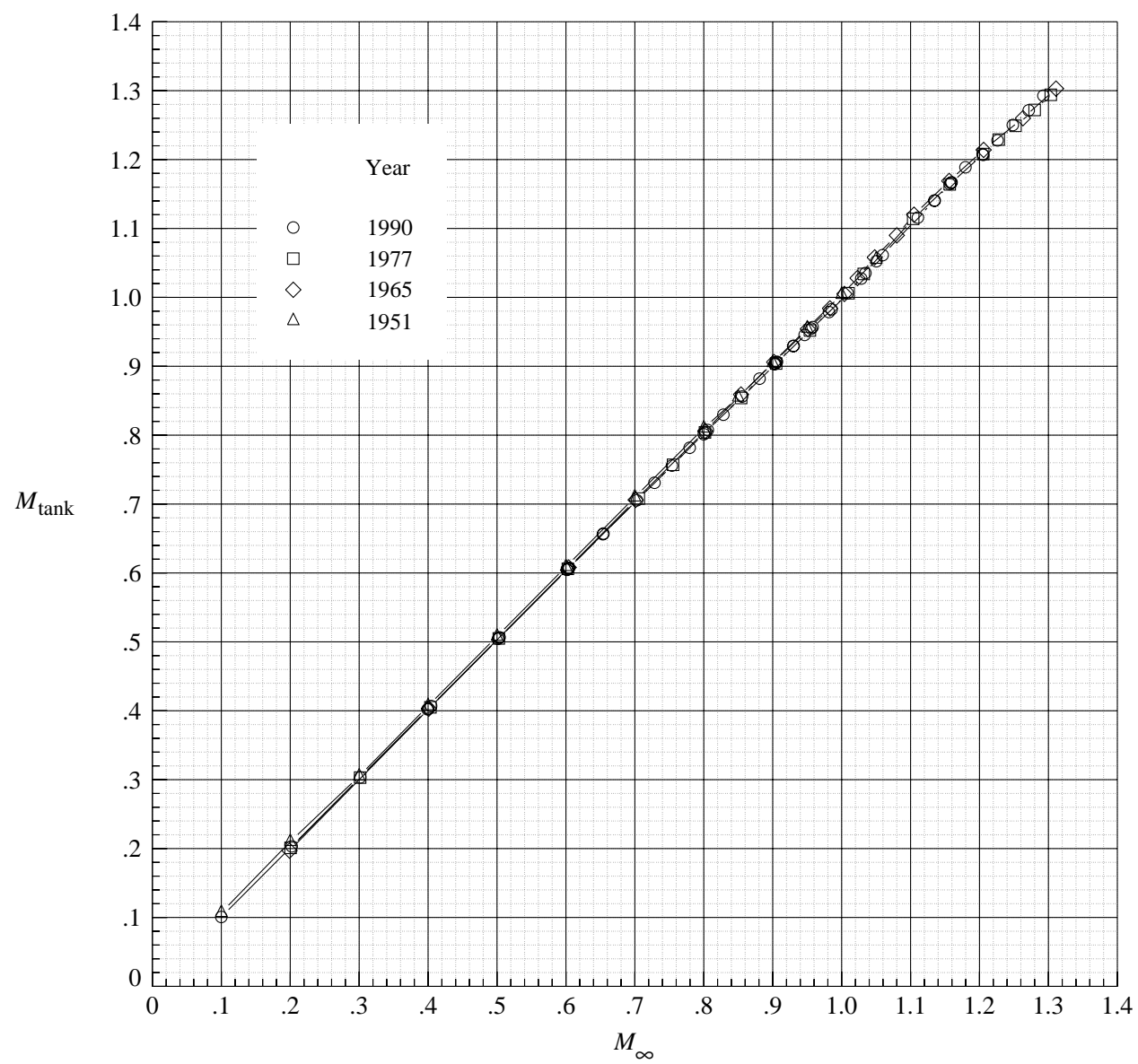


Figure 34. Wind tunnel calibrations from 1951 to 1990.

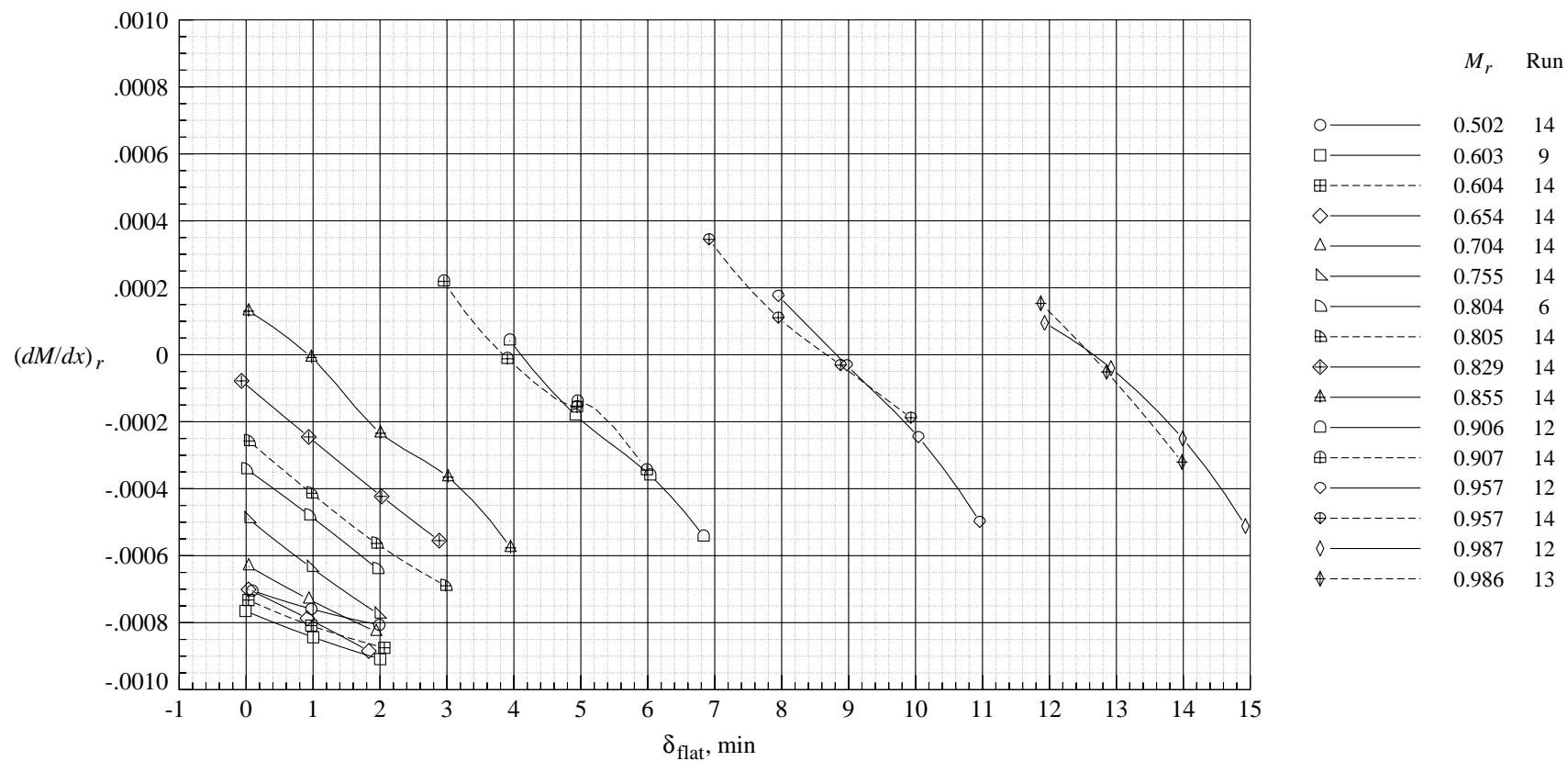
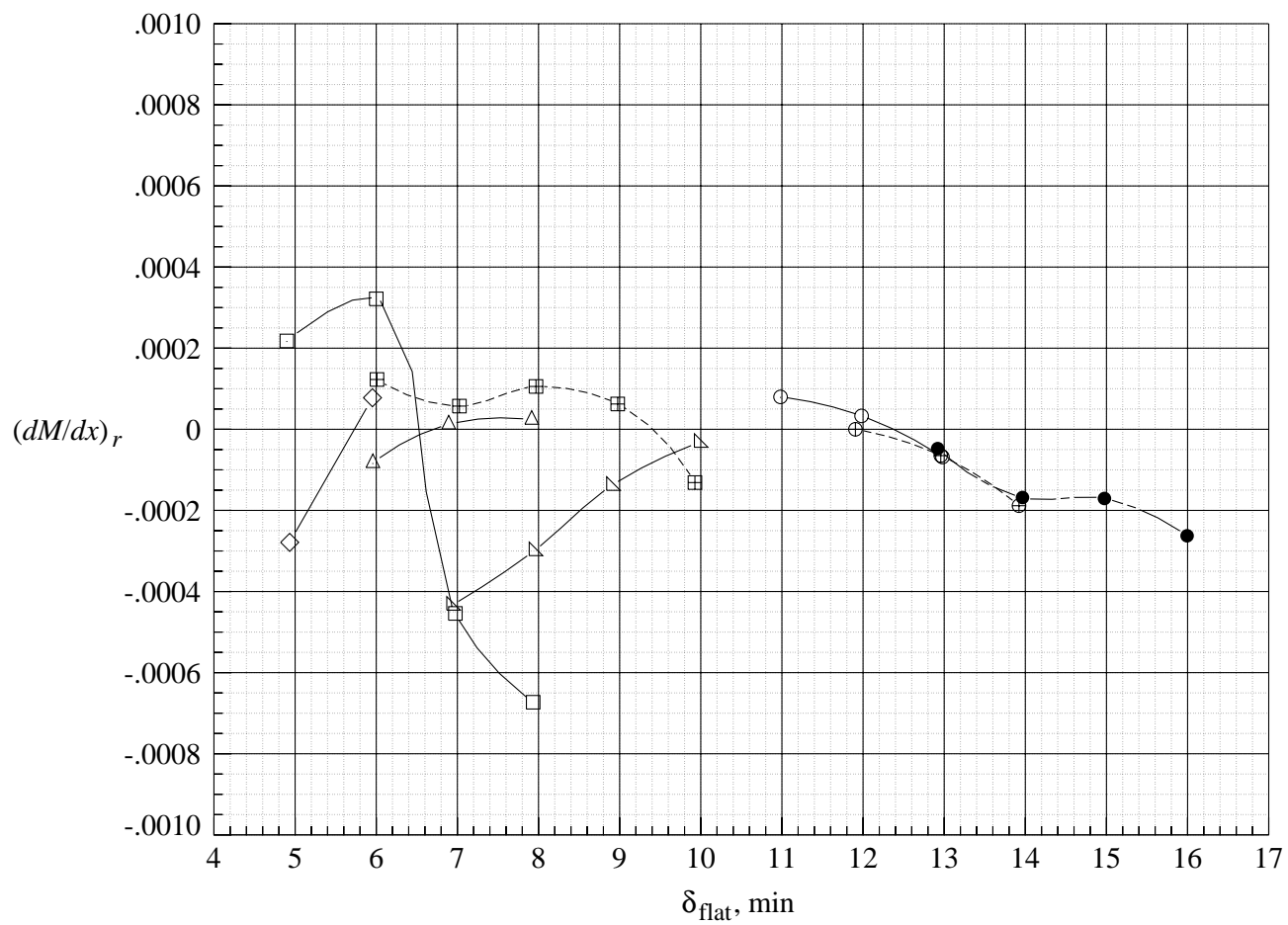
(a) $M = 0.50$ to 0.99 .

Figure 35. Variation of Mach number gradient with flat divergence for 6-ft test section from 1990 wind tunnel calibration.



(b) $M = 1.00$ to 1.13 .

Figure 35. Concluded.

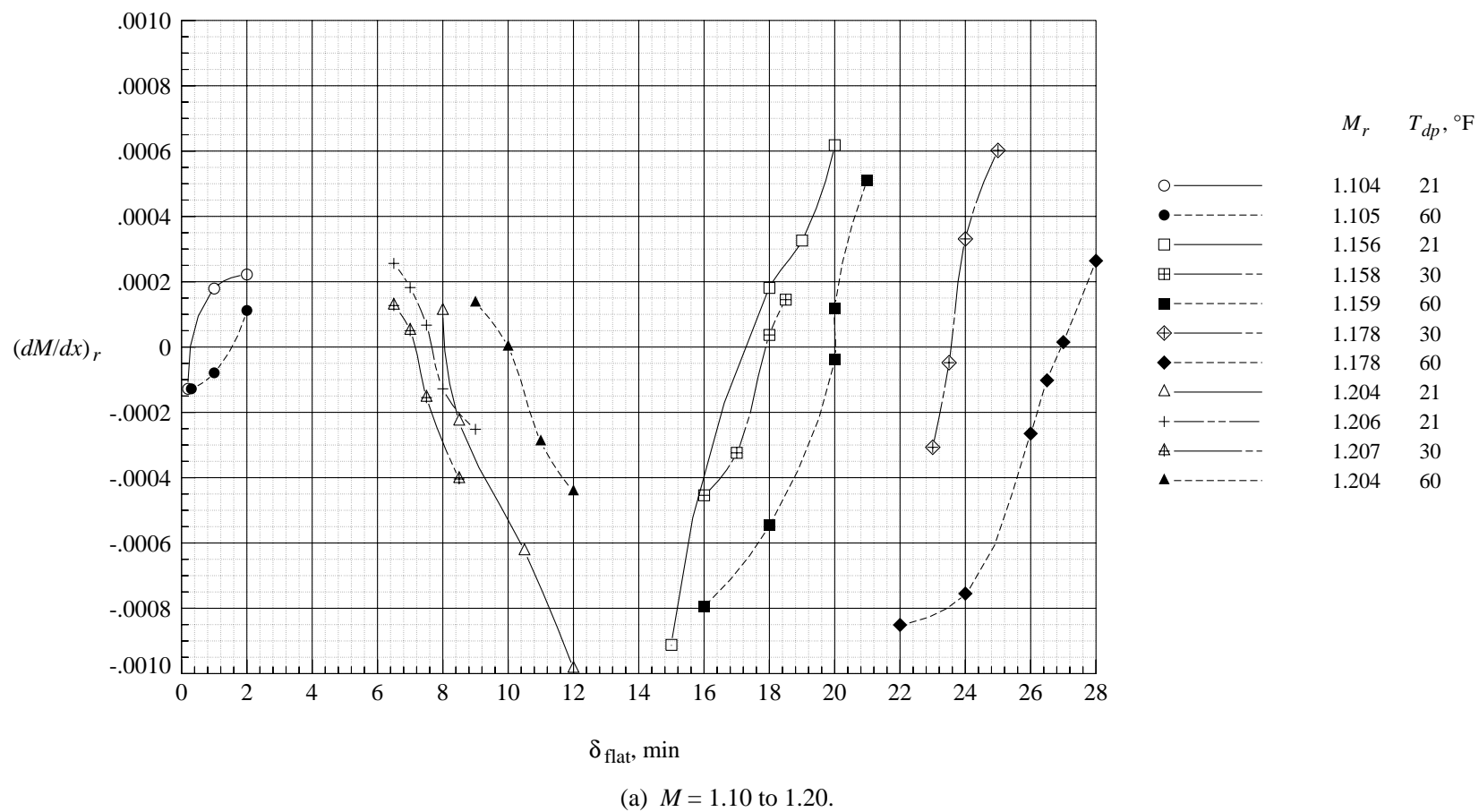
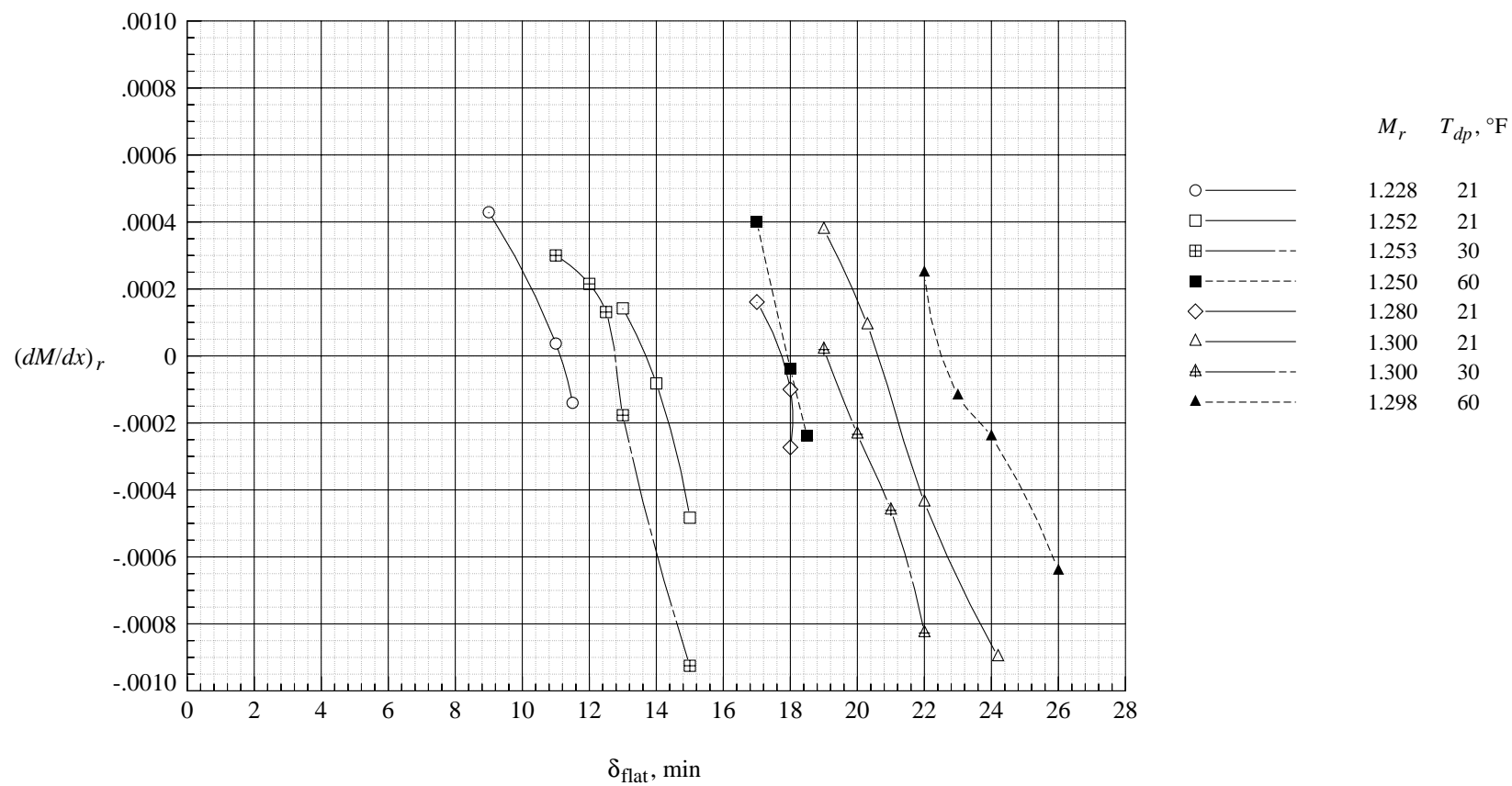


Figure 36. Variation of Mach number gradient with flat divergence for 6-ft test section from 1977 wind tunnel calibration.



(b) $M = 1.225$ to 1.30 .

Figure 36. Concluded.

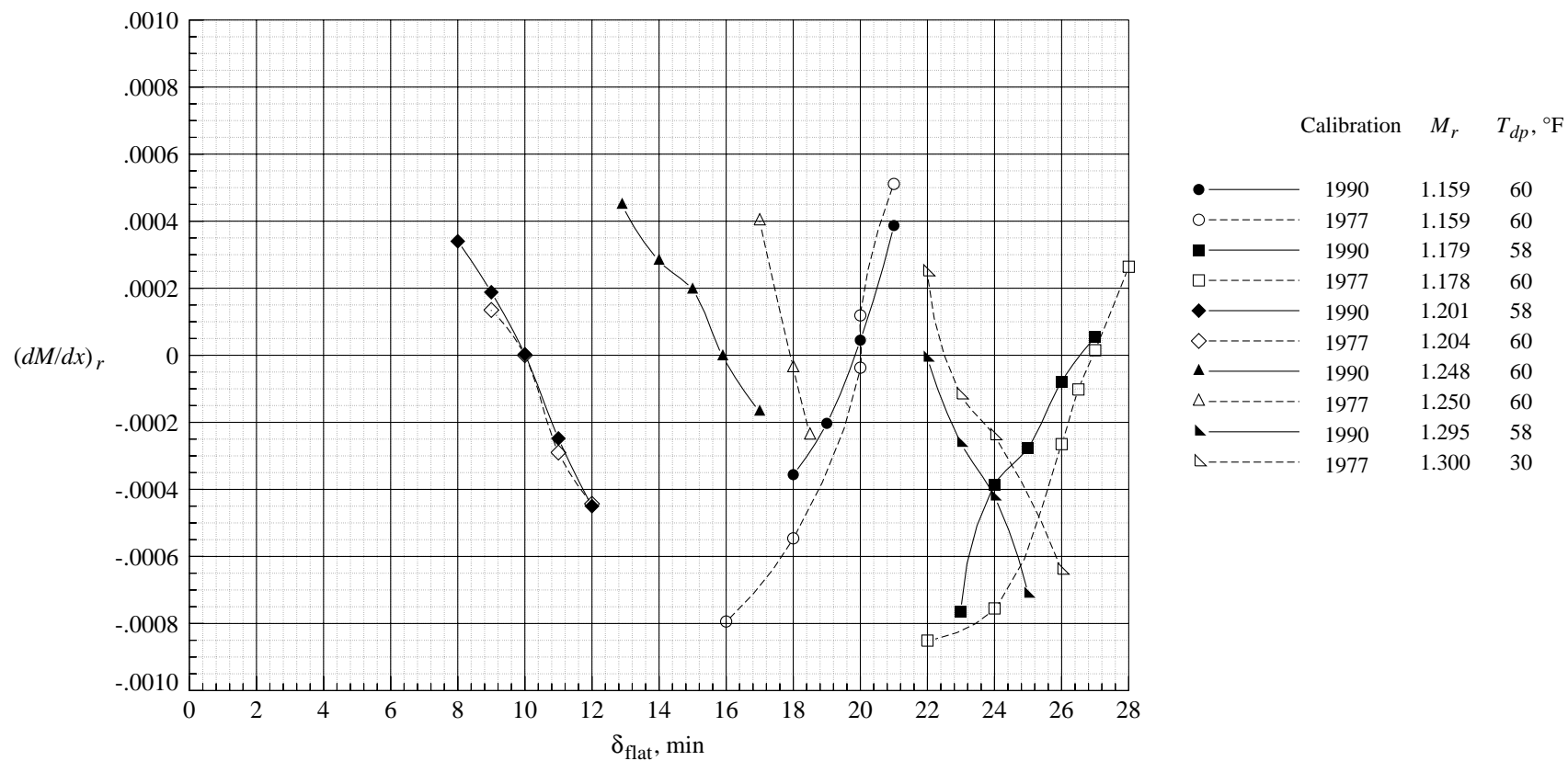


Figure 37. Mach number gradients for 1990 and 1977 wind tunnel calibrations.

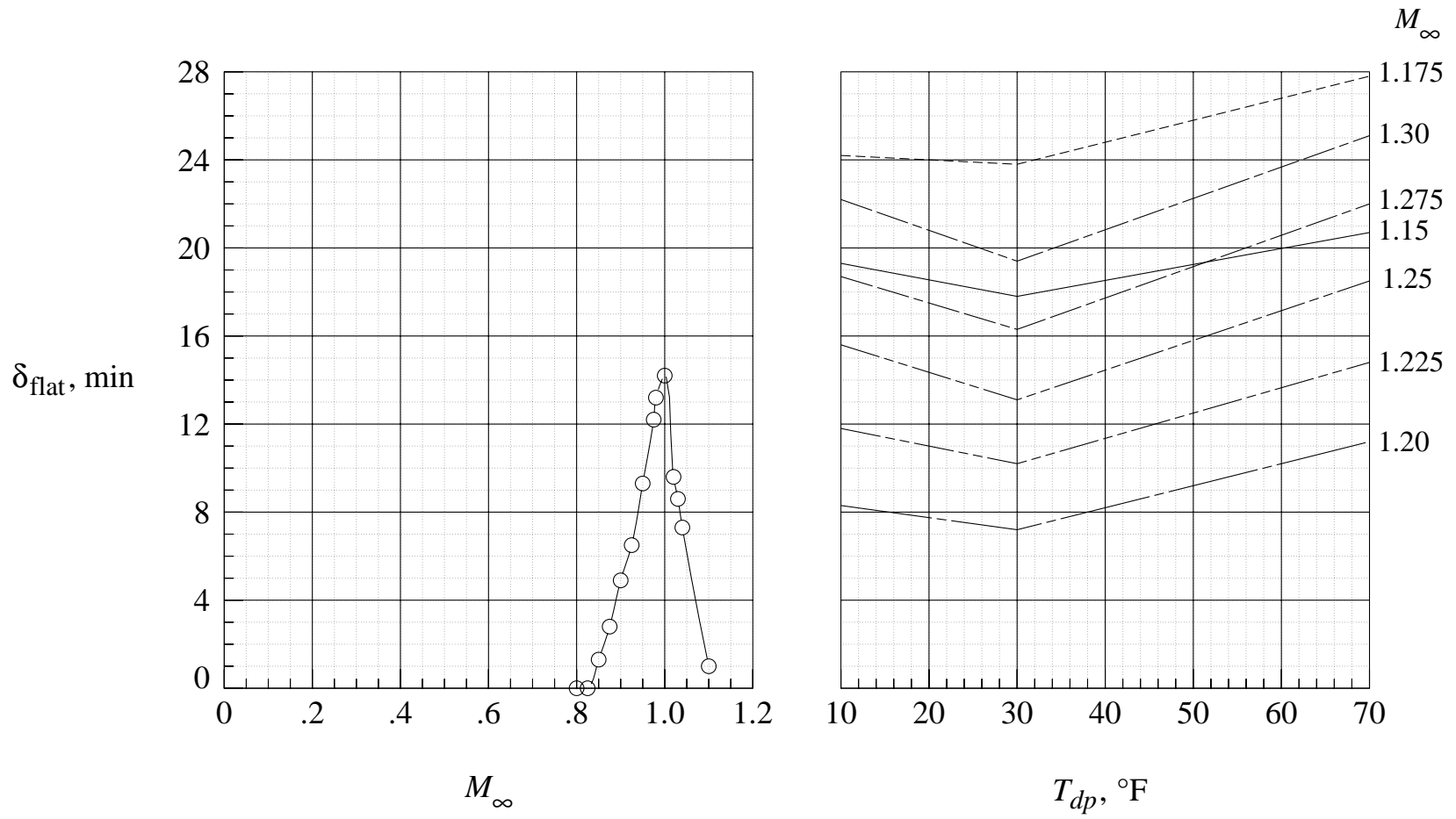


Figure 38. Schedule of wall divergence for 16-Foot Transonic Tunnel.

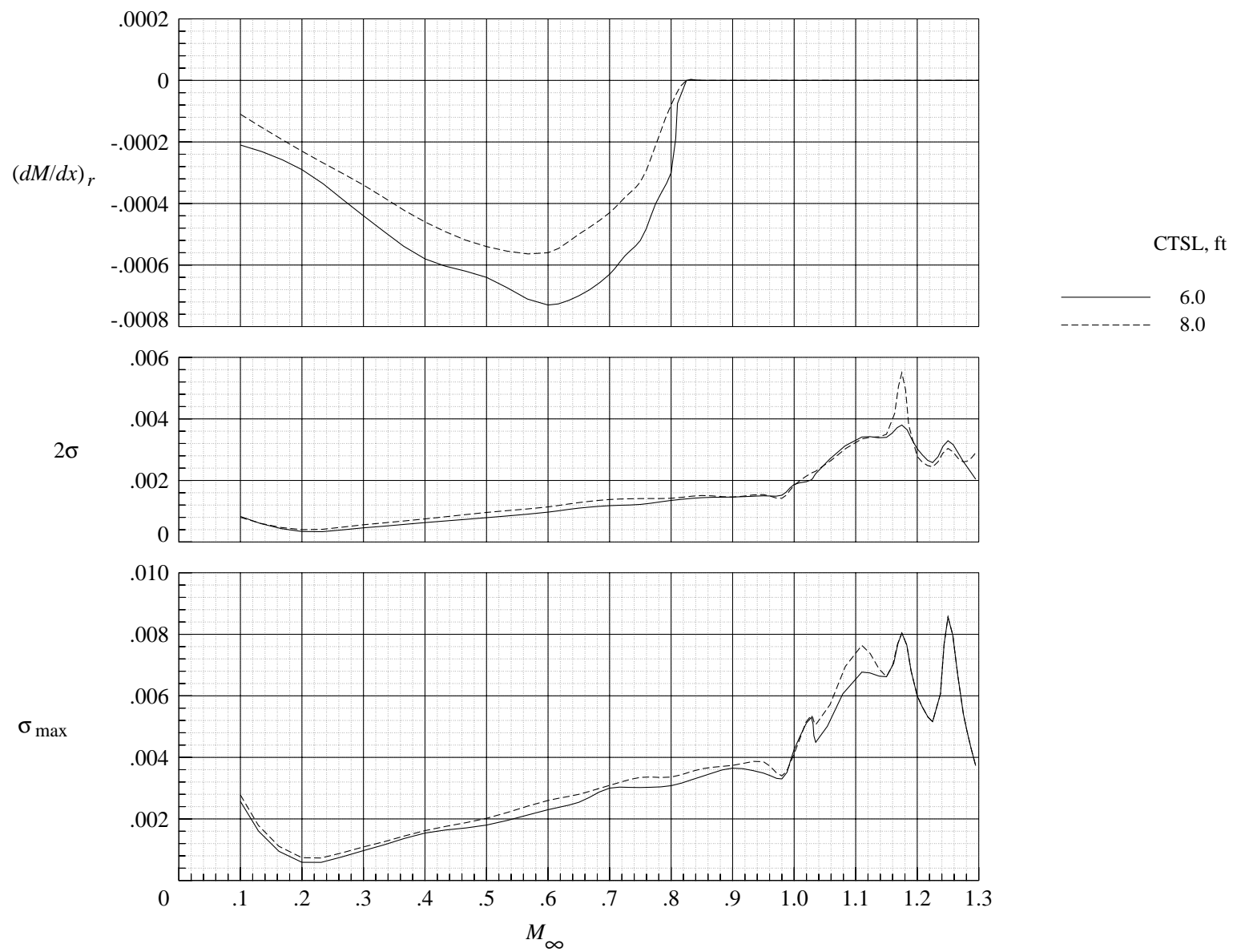


Figure 39. Average Mach number gradient and standard and maximum deviations for two CTSL from 1990 wind tunnel calibration.

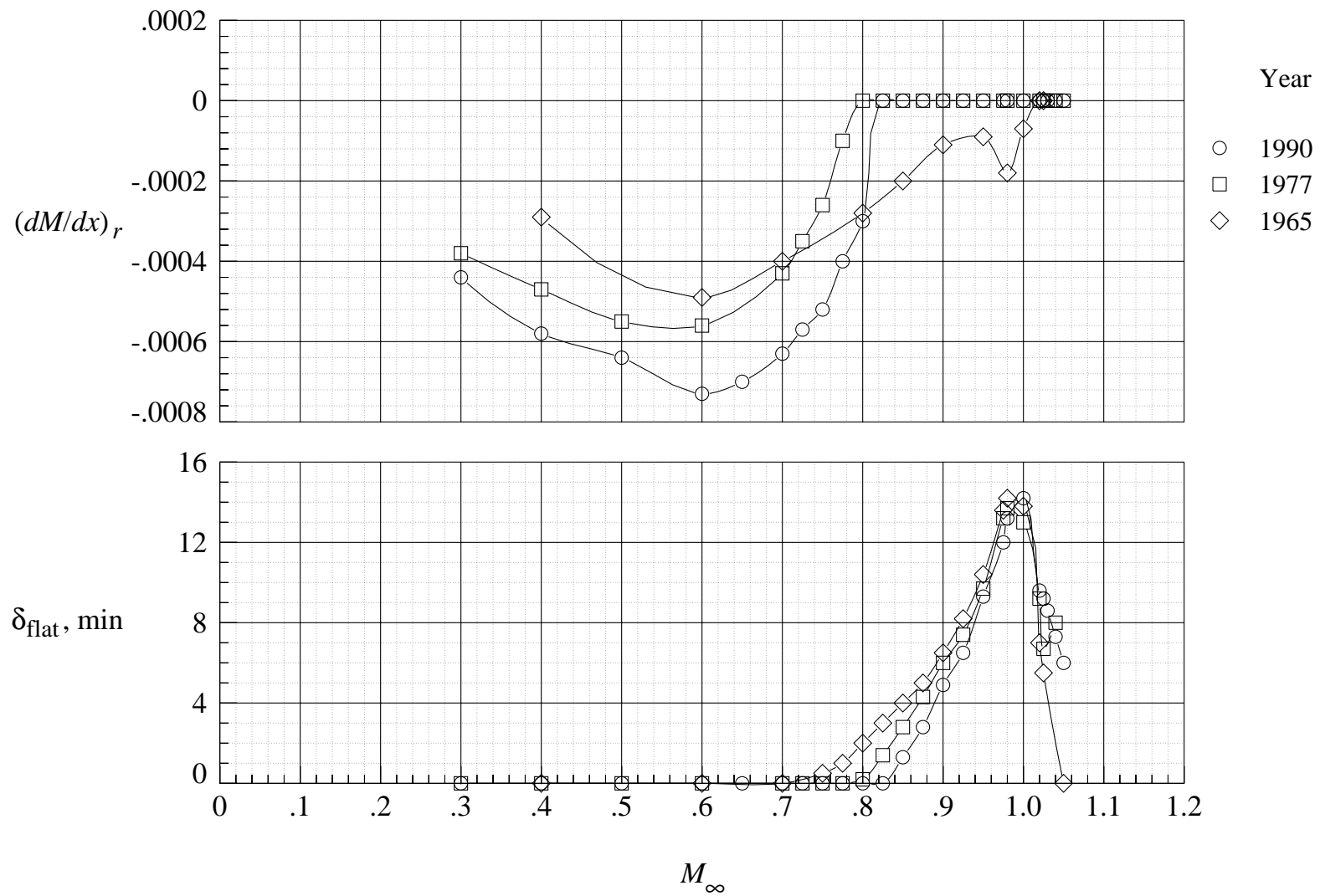


Figure 40. Comparison of Mach number gradients and flat divergence angles from 1990, 1977, and 1965 wind tunnel calibrations.

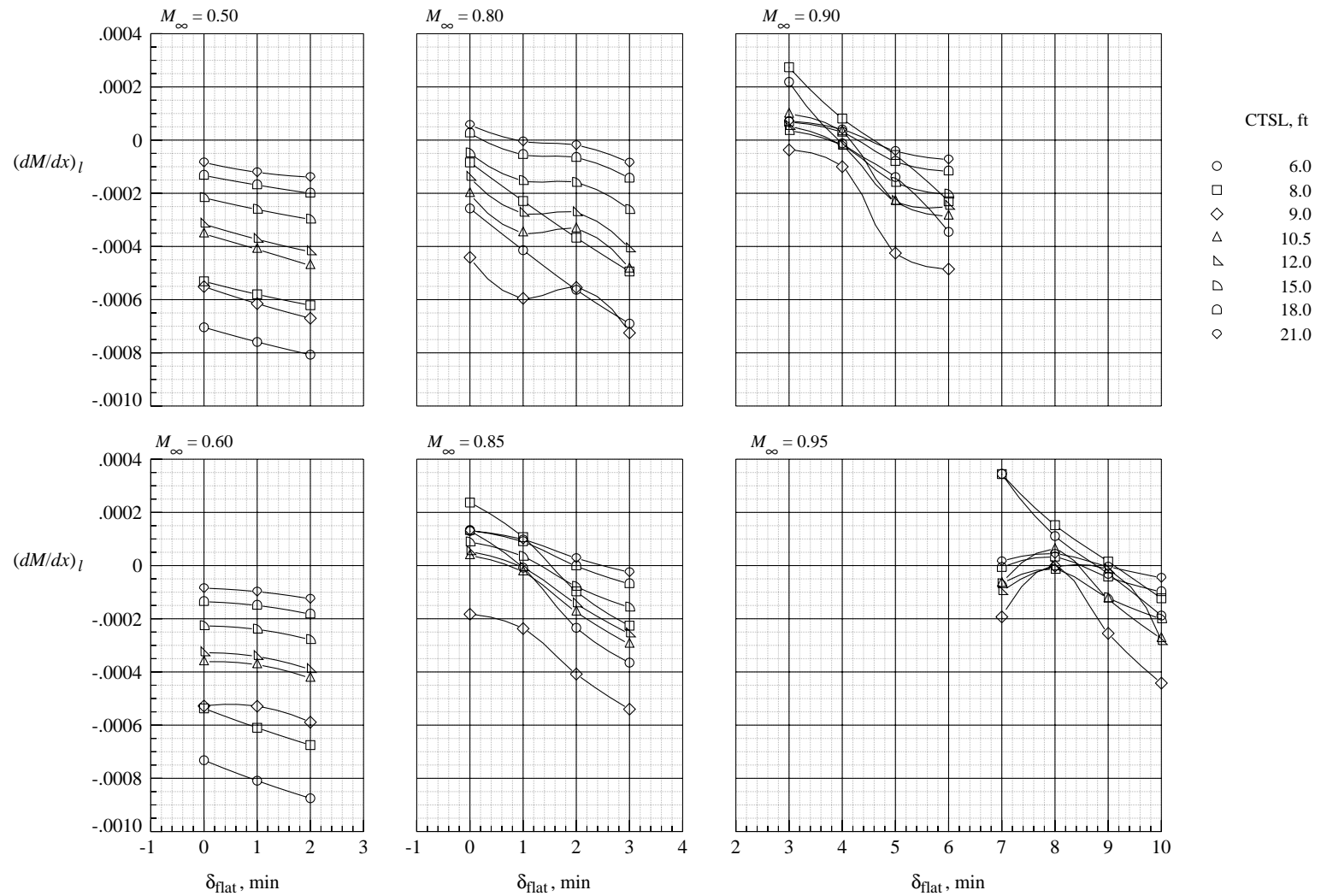


Figure 41. Variation of Mach number gradient with flat divergence for all CTSL for selected Mach numbers.

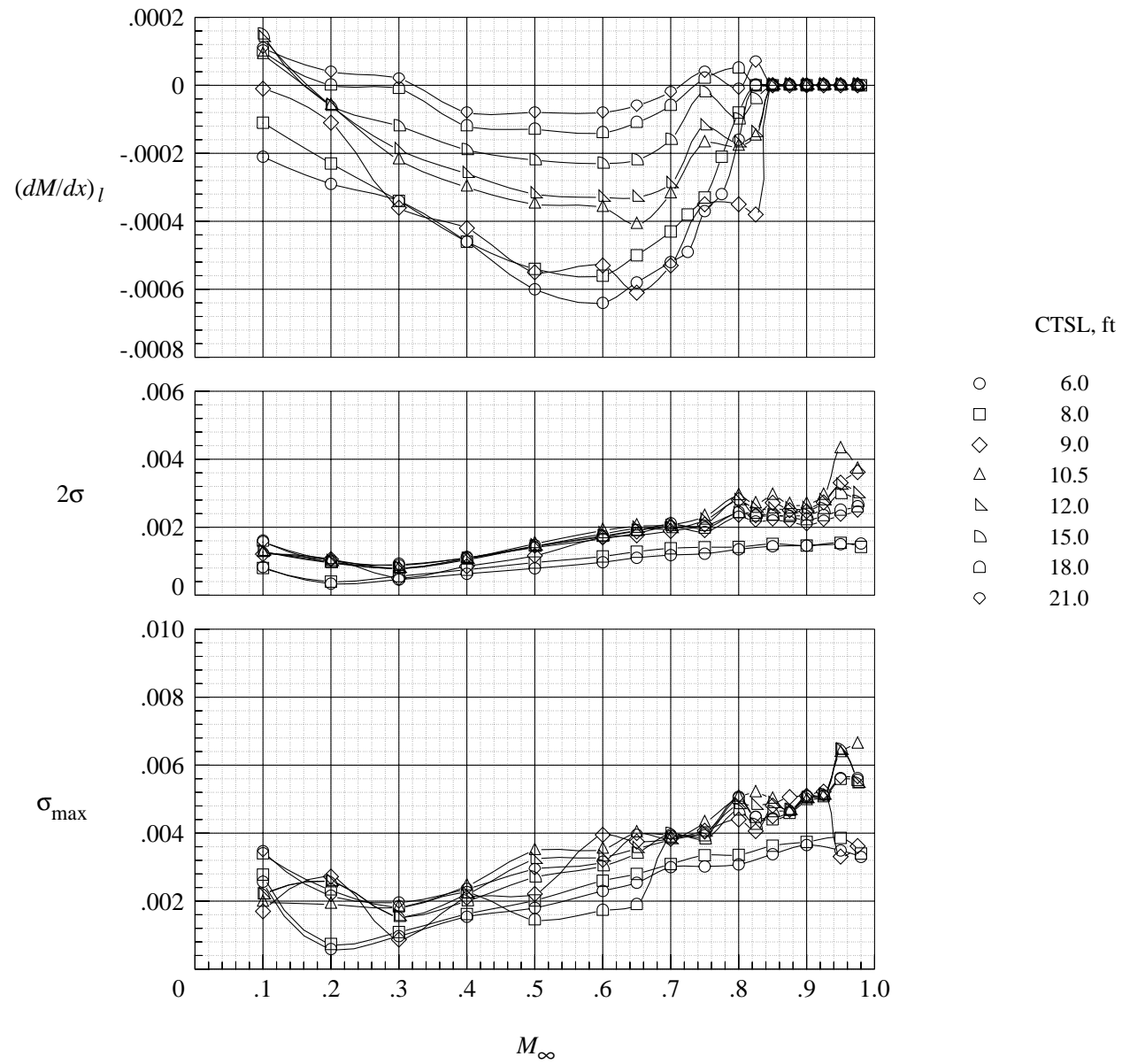


Figure 42. Average Mach number gradient and standard and deviations for CTSL from the 1990 wind tunnel calibration.

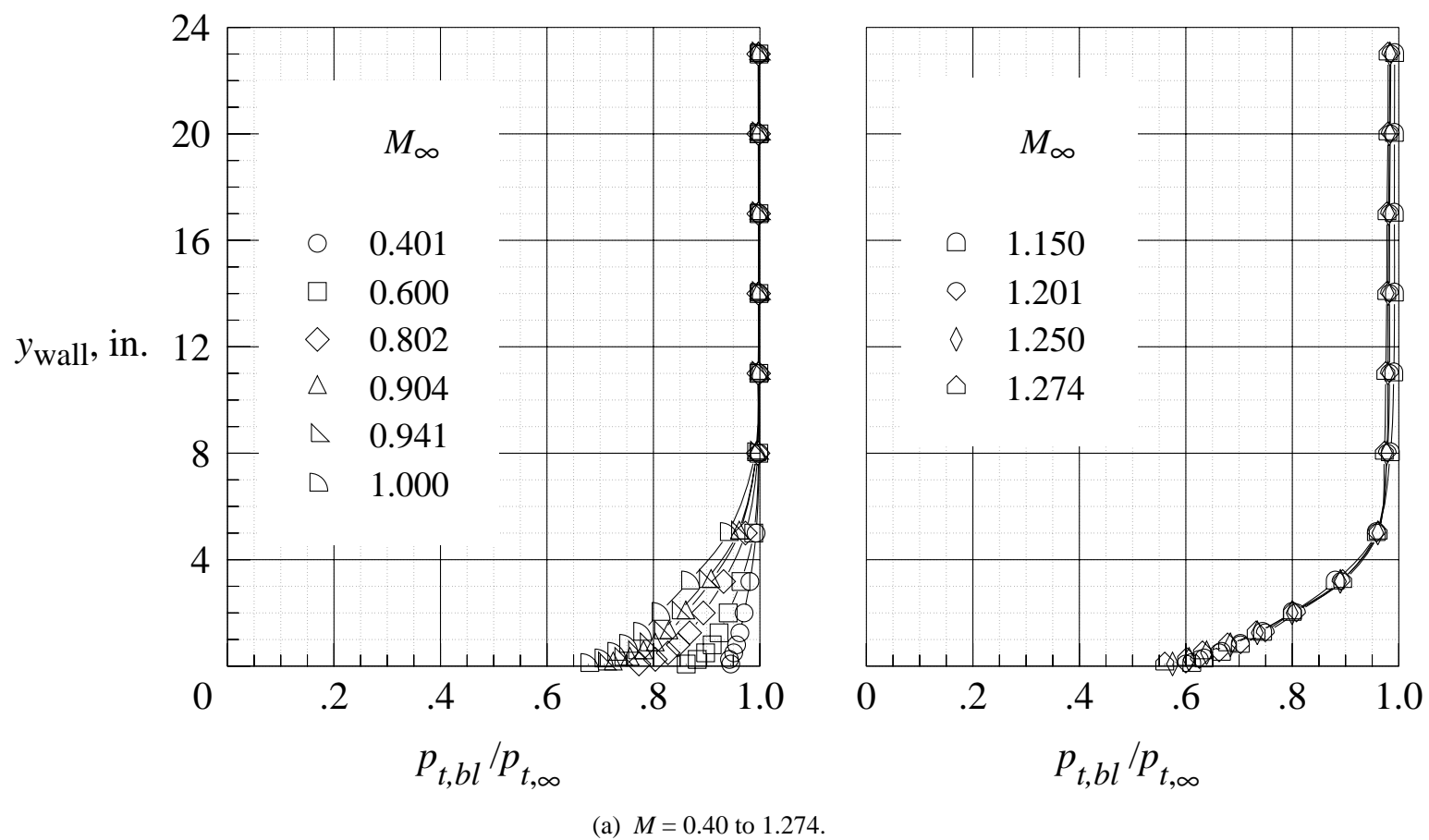
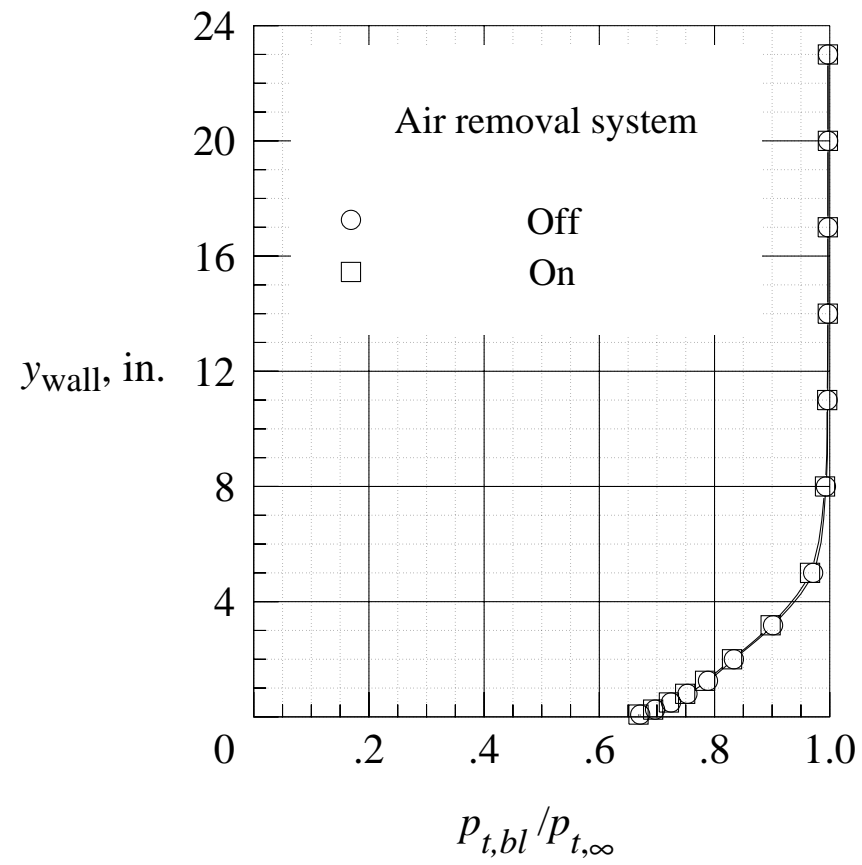


Figure 43. Test section boundary-layer distributions at TS 133.00.



(b) $M = 1.05$.

Figure 43. Concluded.

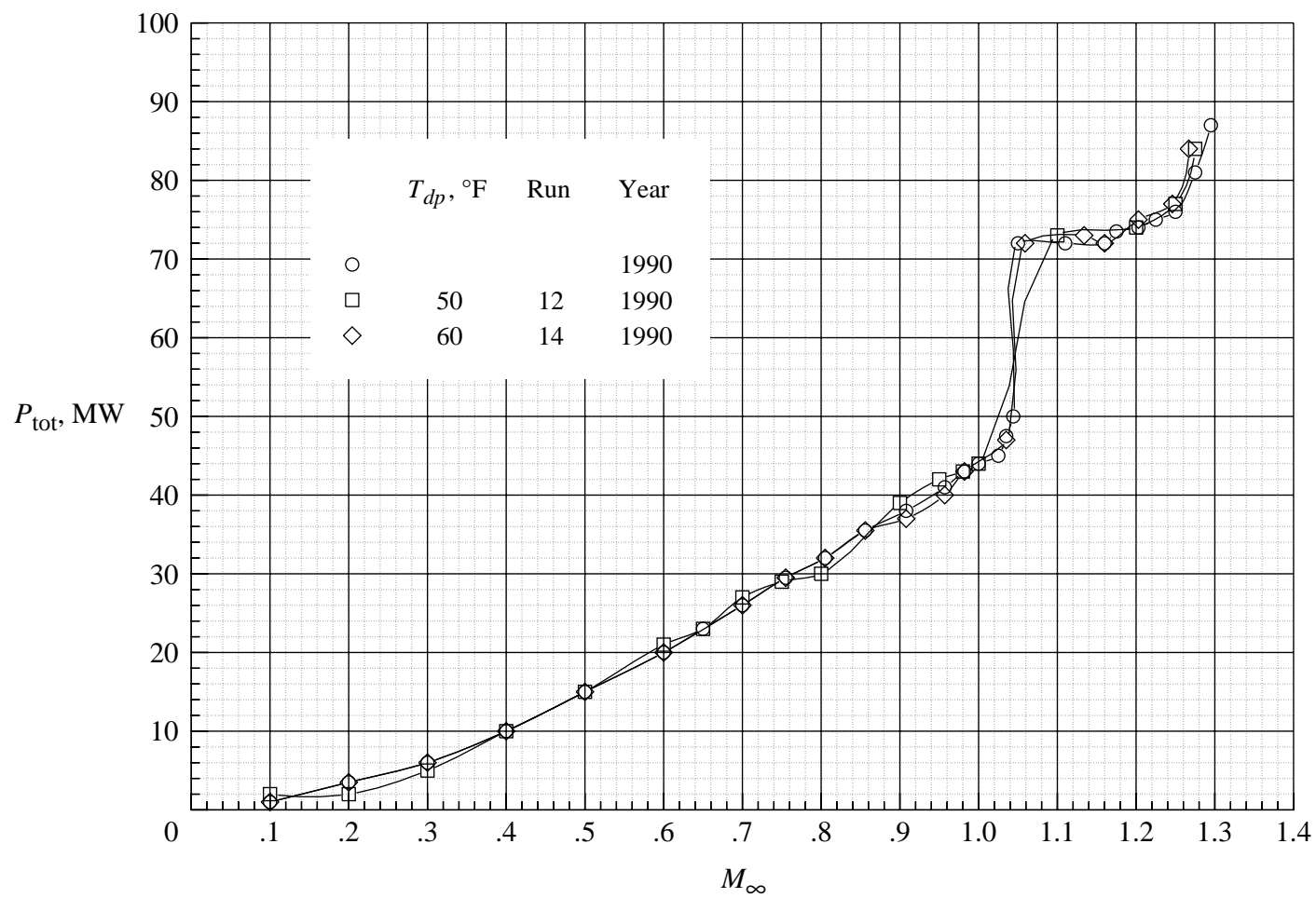


Figure 44. Total power for Langley 16-Foot Transonic Tunnel from 1990 wind tunnel calibration.

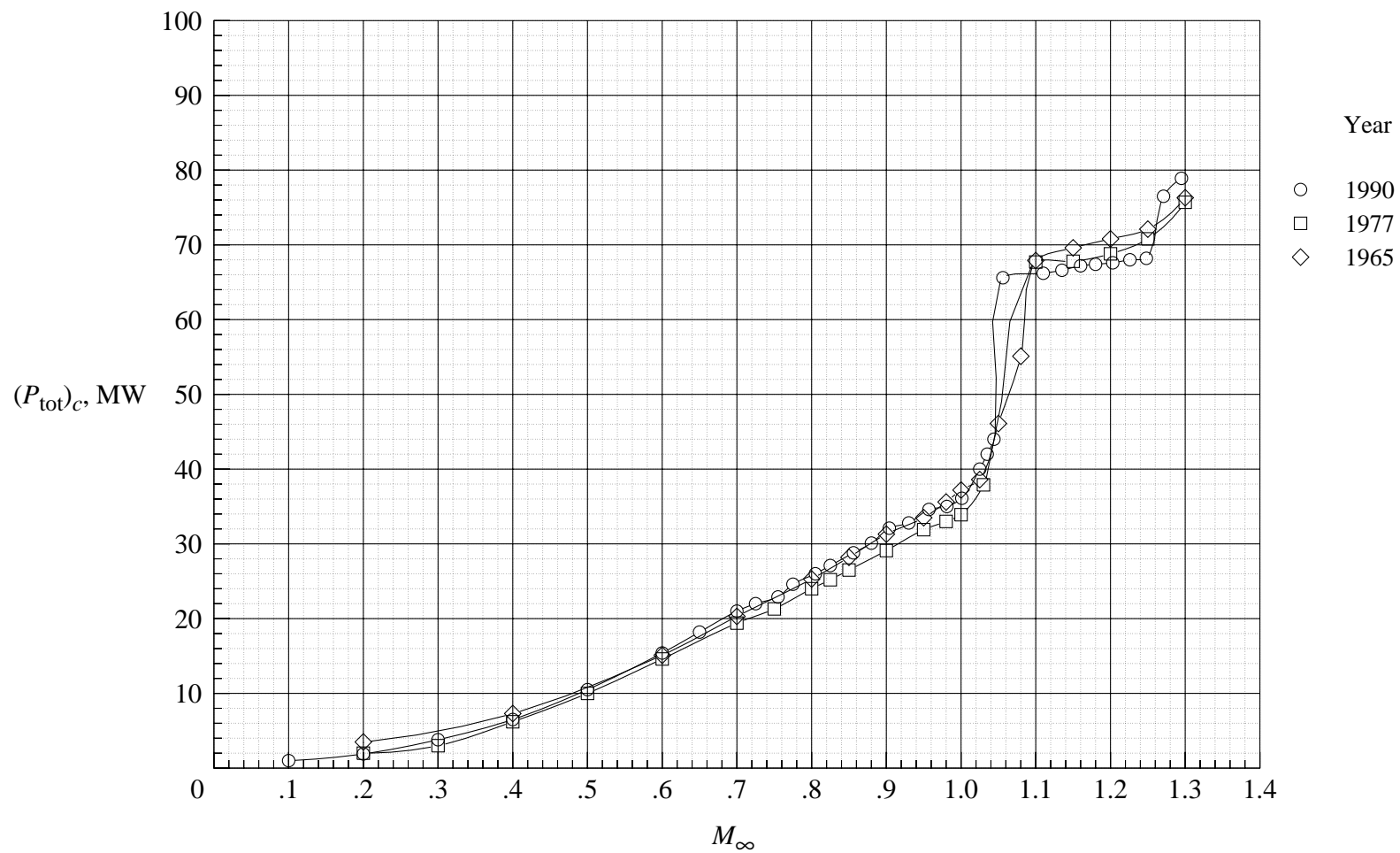


Figure 45. Comparison of corrected total power for Langley 16-Foot Transonic Tunnel from 1990, 1977, and 1965 wind tunnel calibrations.

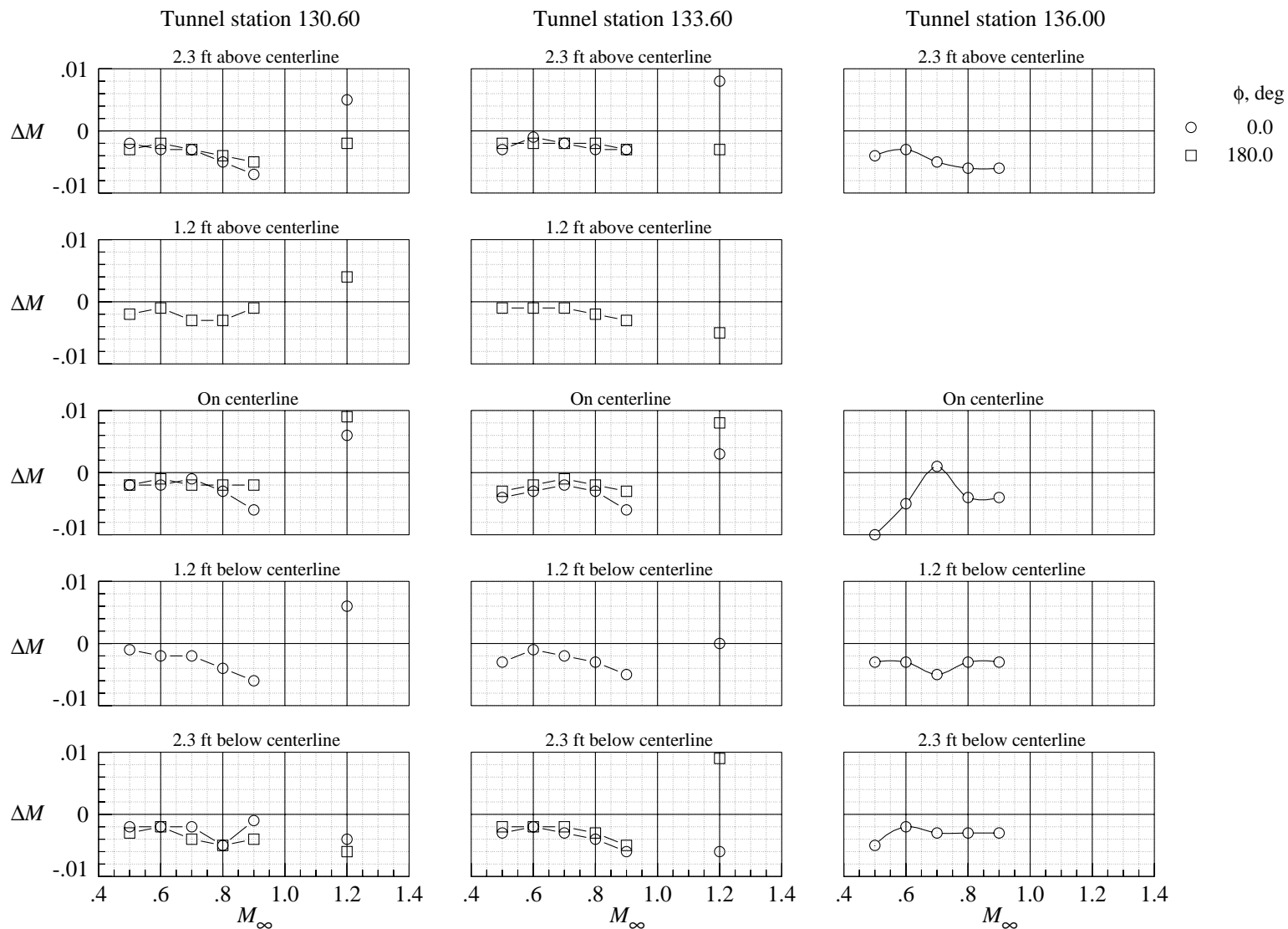


Figure 46. Vertical distribution of test-section incremental Mach number at three tunnel stations. $\Delta M = M_{\text{probe}} - M_\infty$.

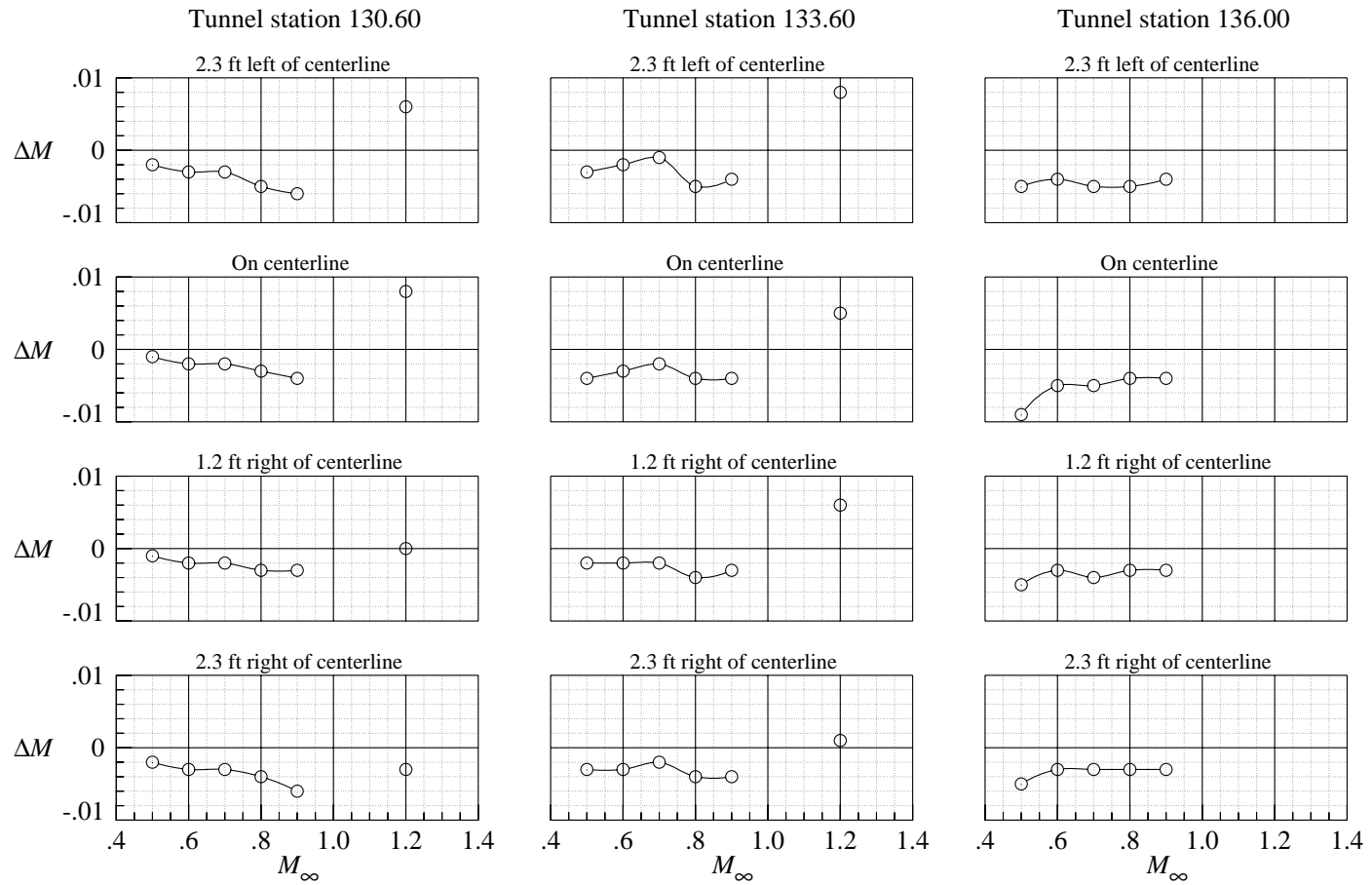


Figure 47. Lateral distribution of test-section incremental Mach number at three tunnel stations. $\Delta M = M_{\text{probe}} - M_\infty$.

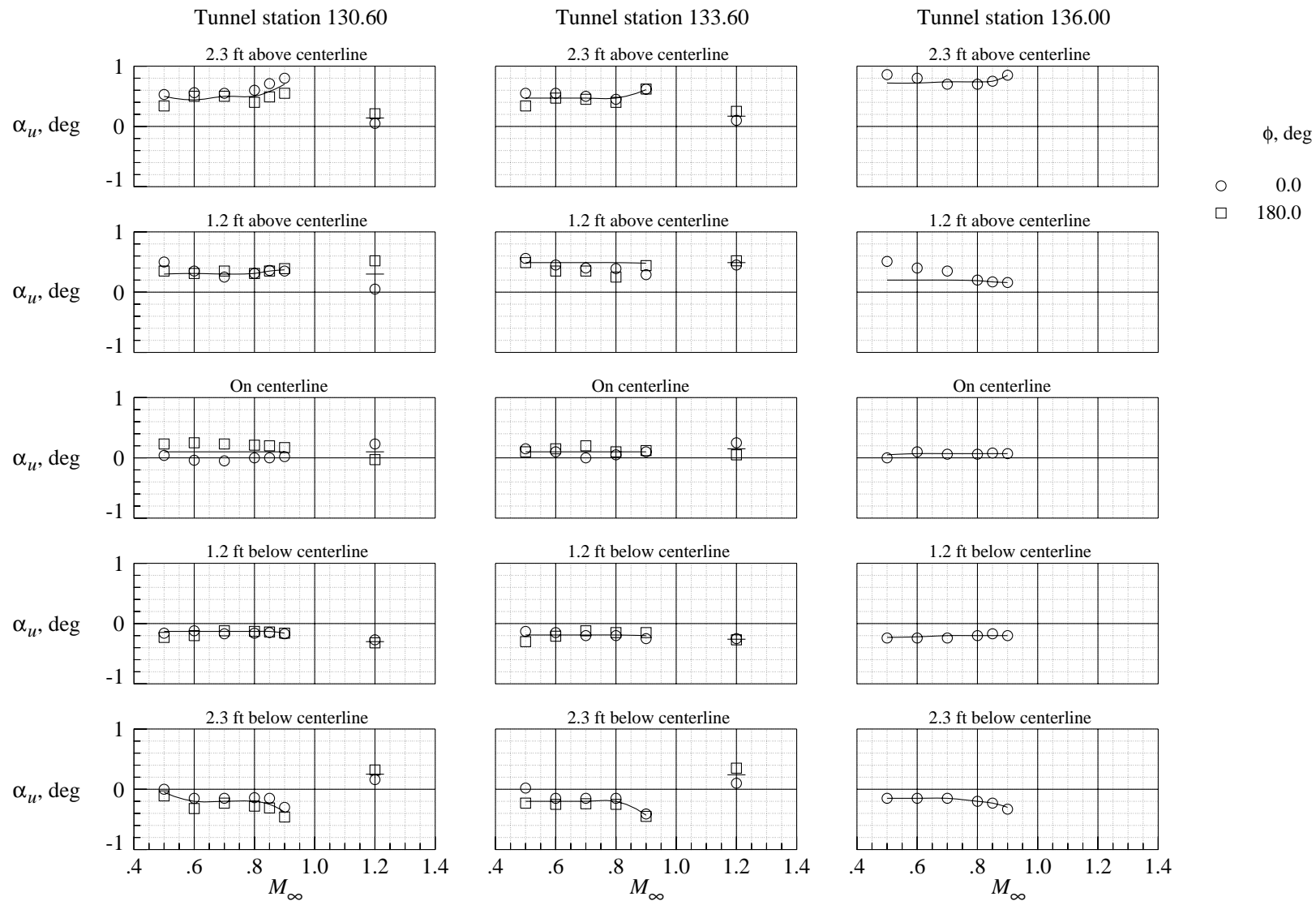


Figure 48. Test-section upflow characteristics at three tunnel stations.

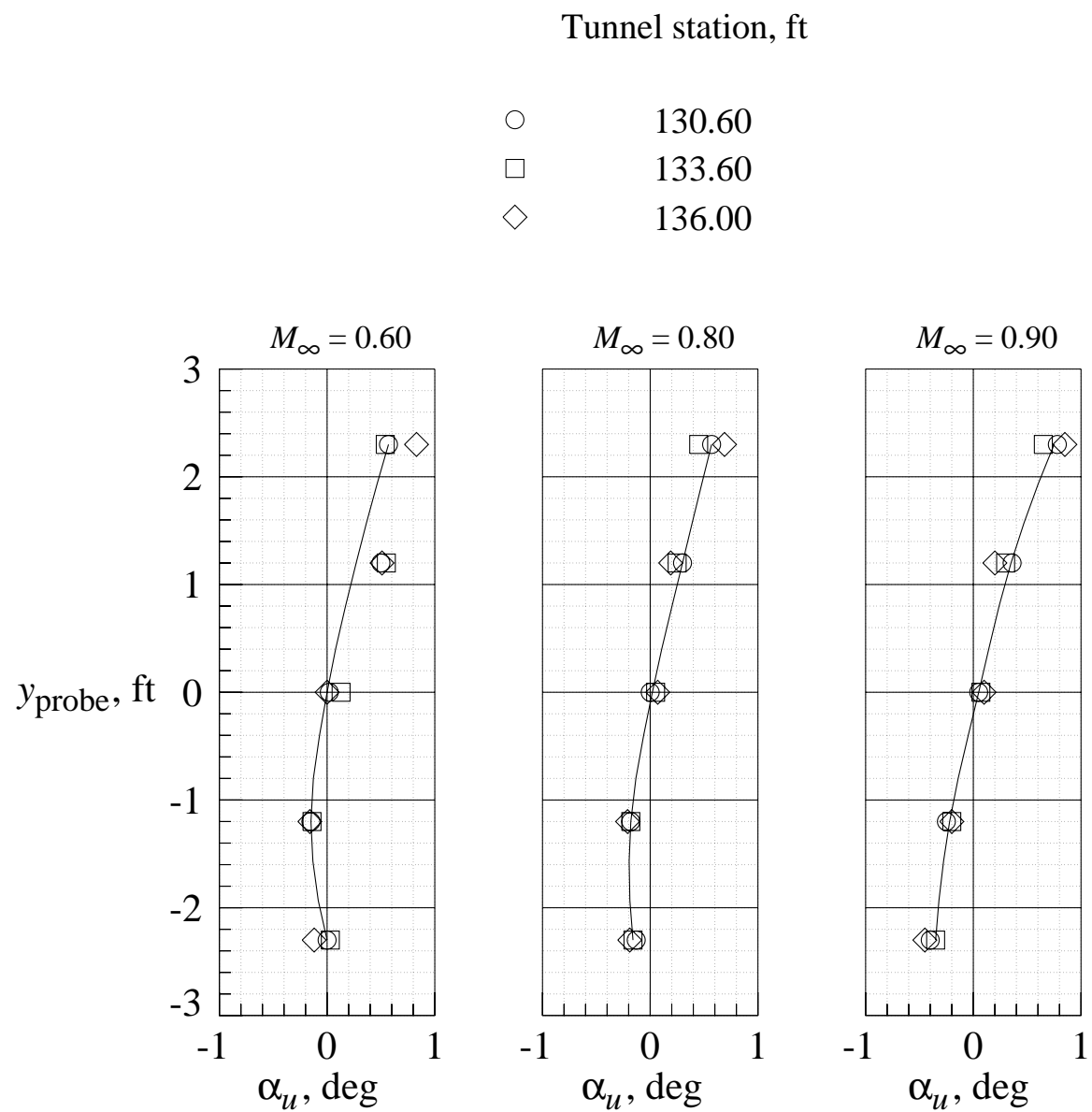


Figure 49. Test-section upflow characteristics for flow angle probe at $\phi = 0^\circ$.

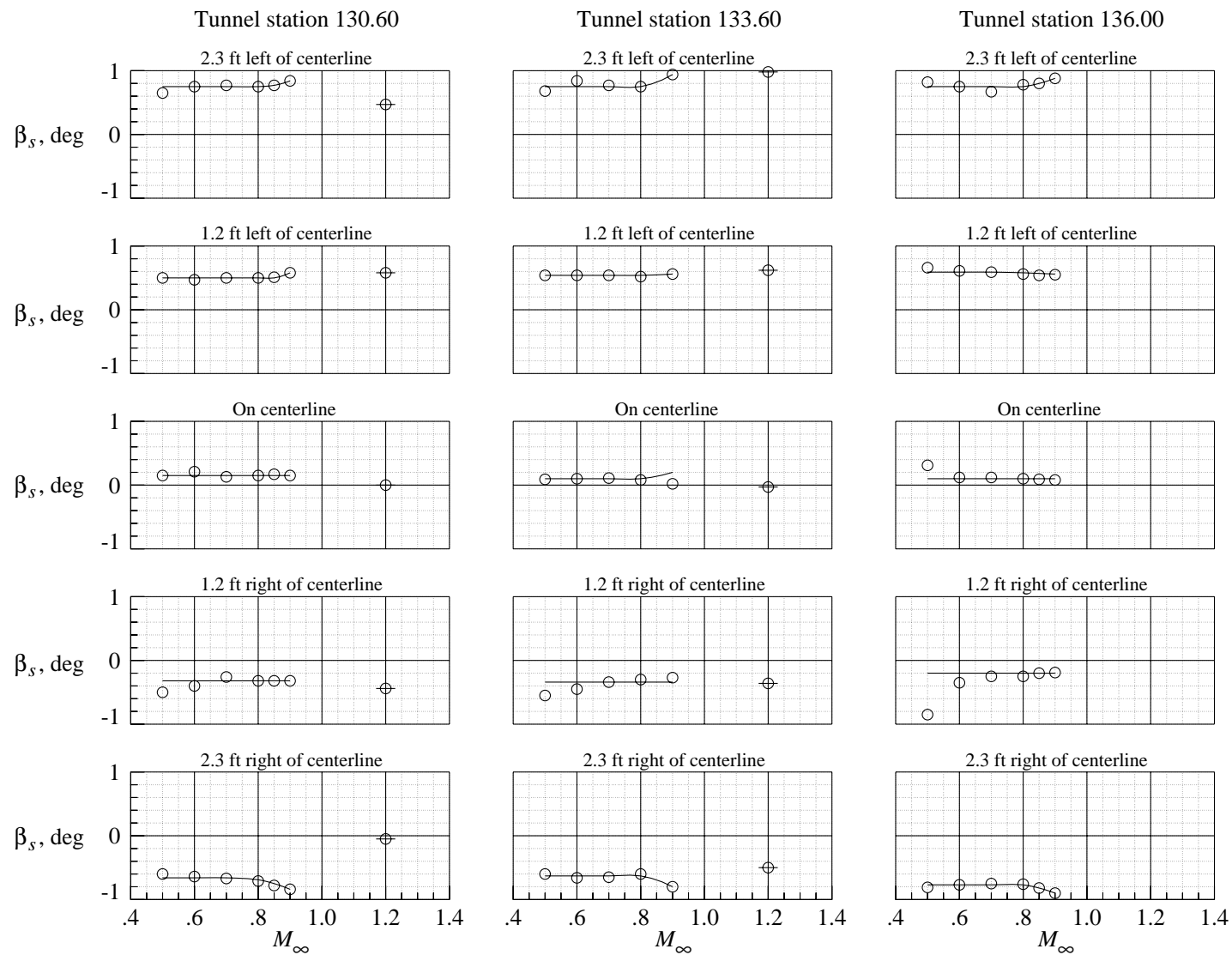


Figure 50. Test-section sideflow characteristics at three tunnel stations.

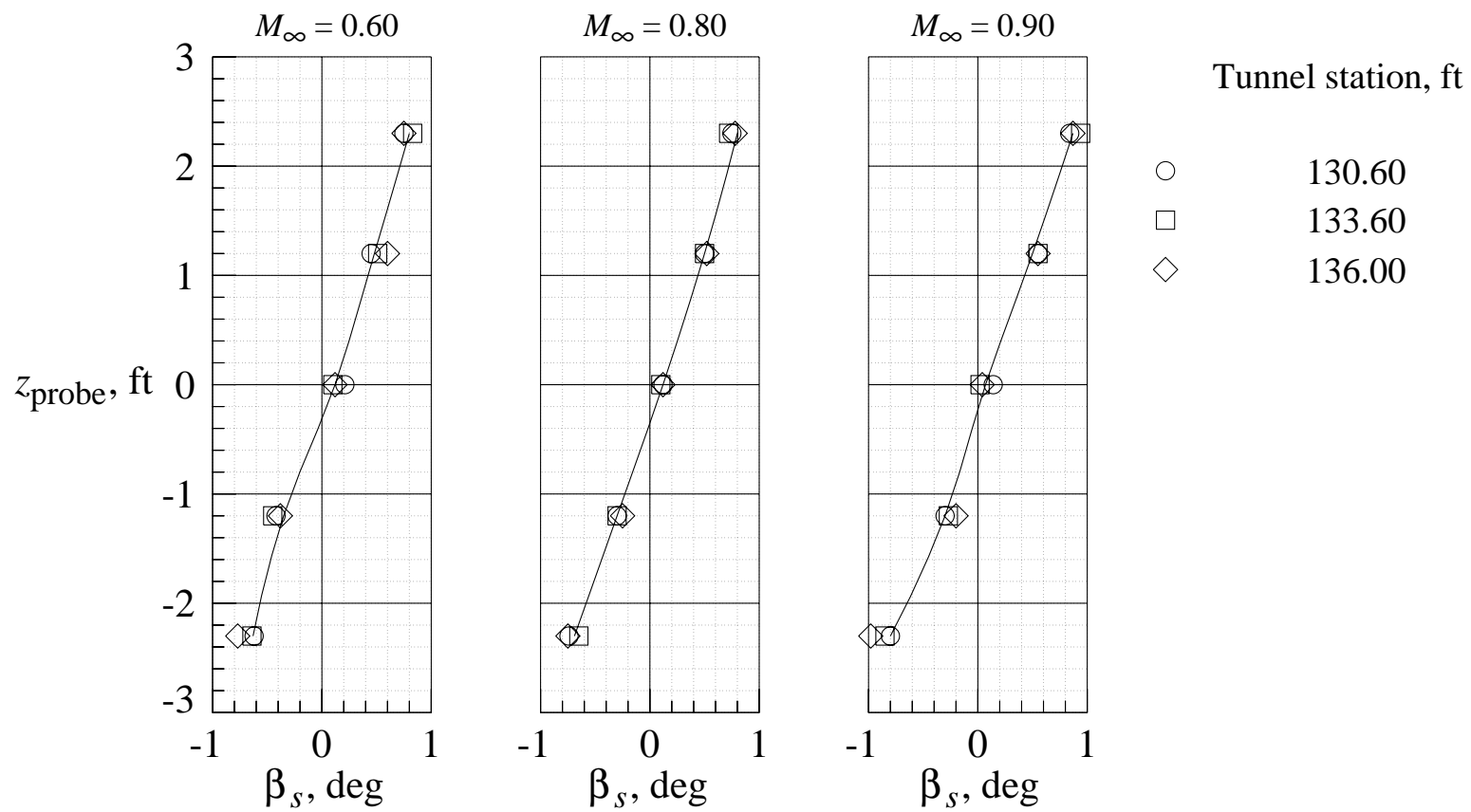


Figure 51. Test-section sideflow characteristics for flow angle probe at $\phi = 90^\circ$.

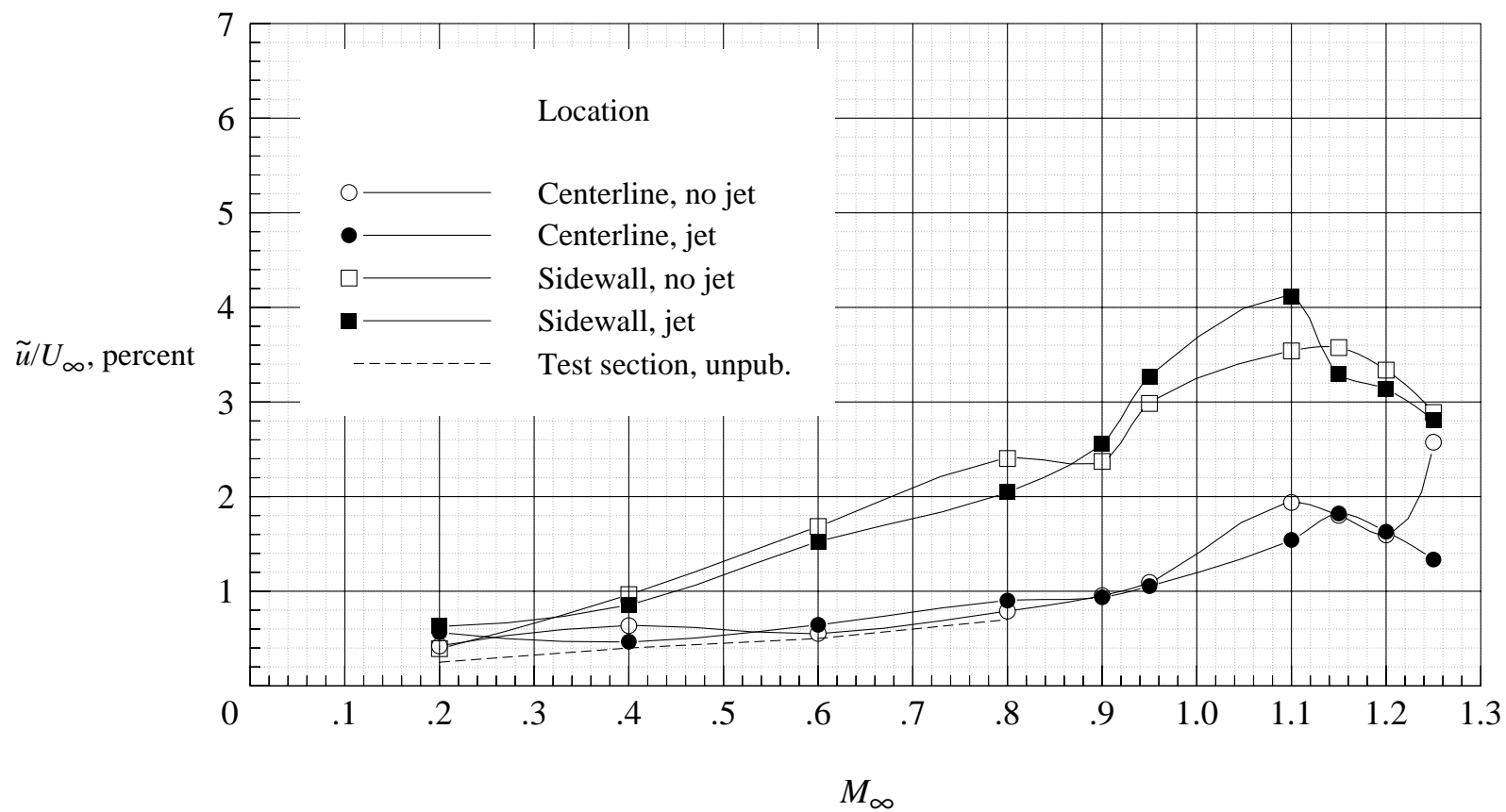
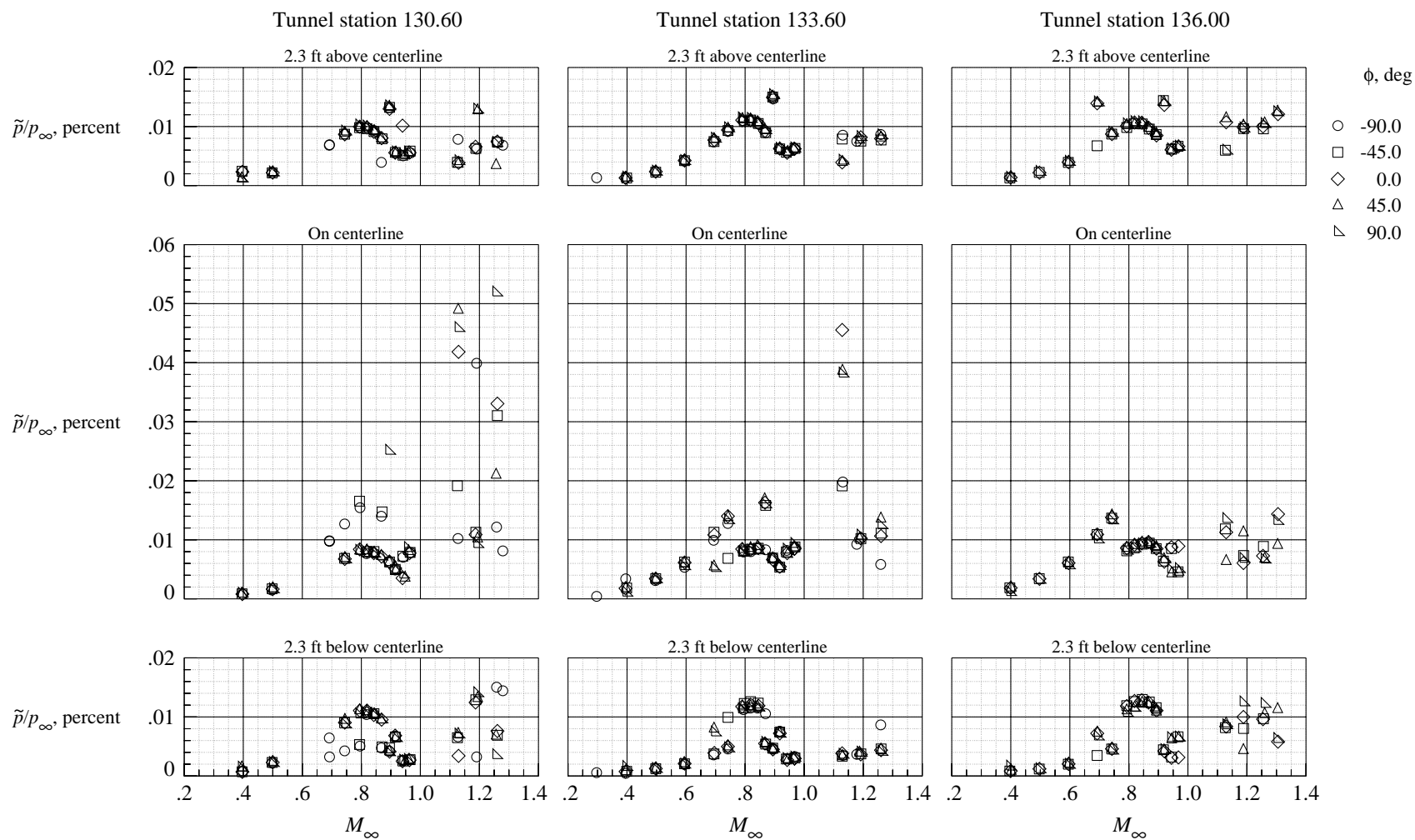
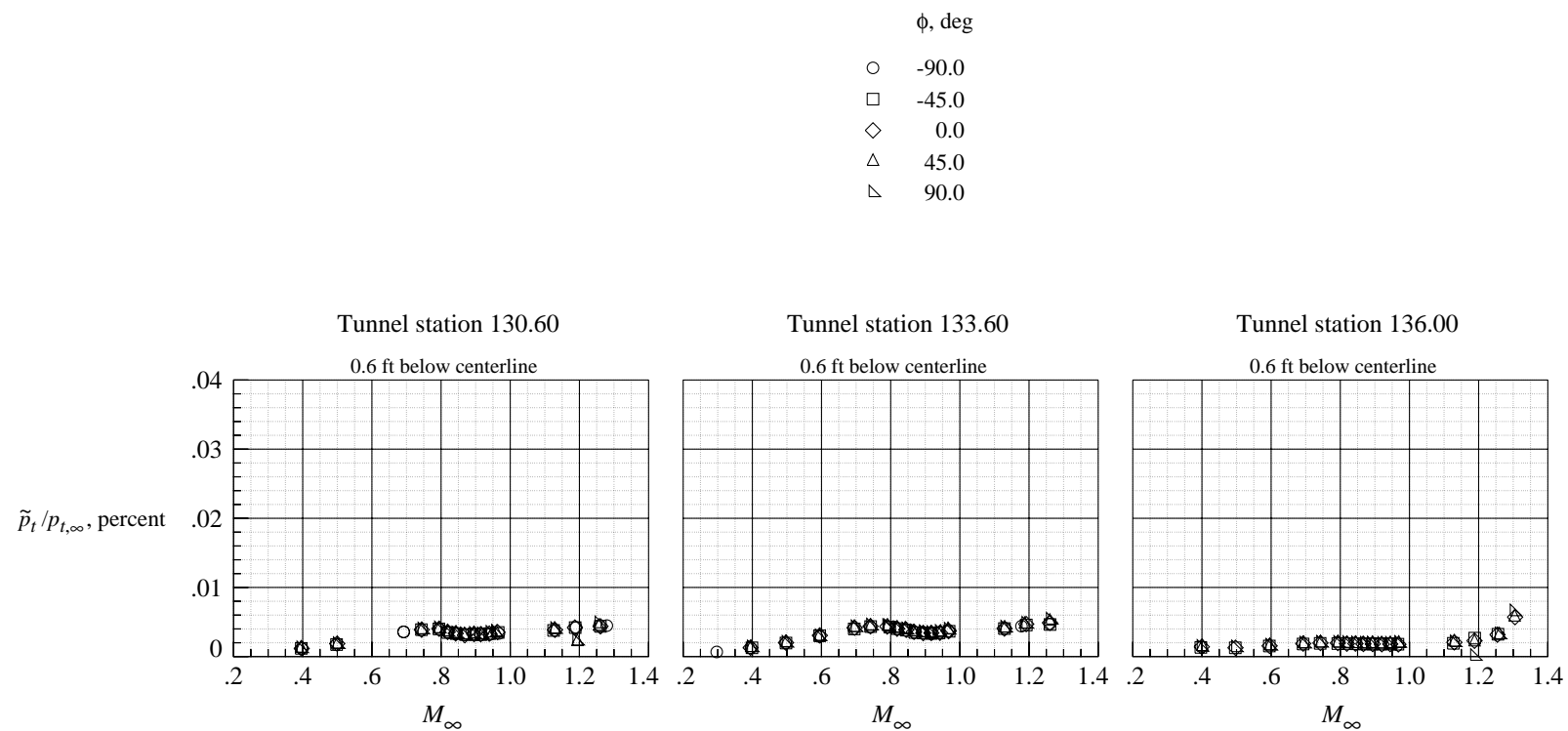


Figure 52. Wind tunnel turbulence characteristics in quiescent chamber.



(a) Static-pressure fluctuations.

Figure 53. Test-section pressure fluctuation characteristics at three tunnel stations.



(b) Total-pressure fluctuations.

Figure 53. Concluded.

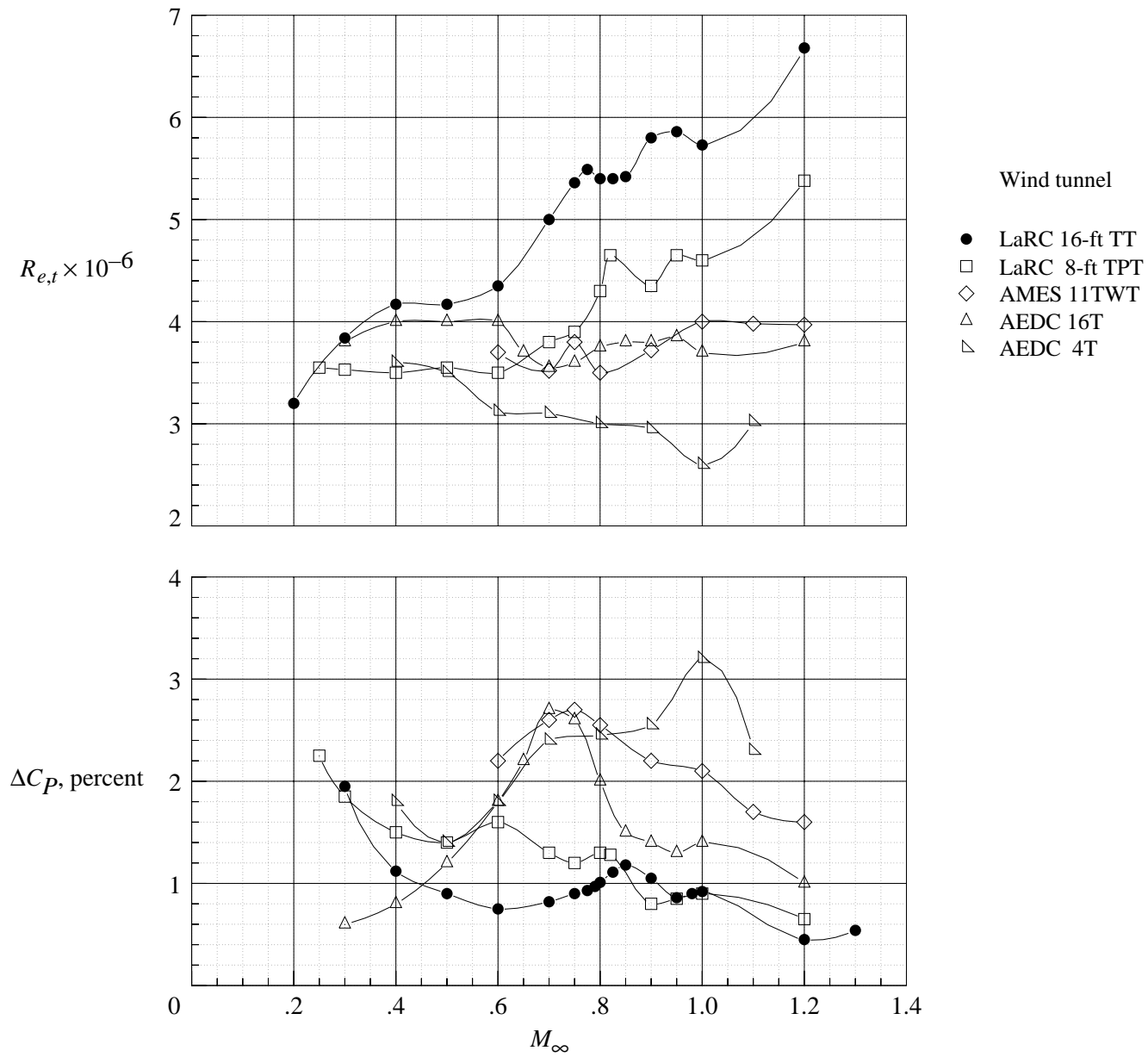


Figure 54. Transition Reynolds number and noise characteristics for Langley 16-Foot Transonic Tunnel and other facilities. (From ref. 19.)

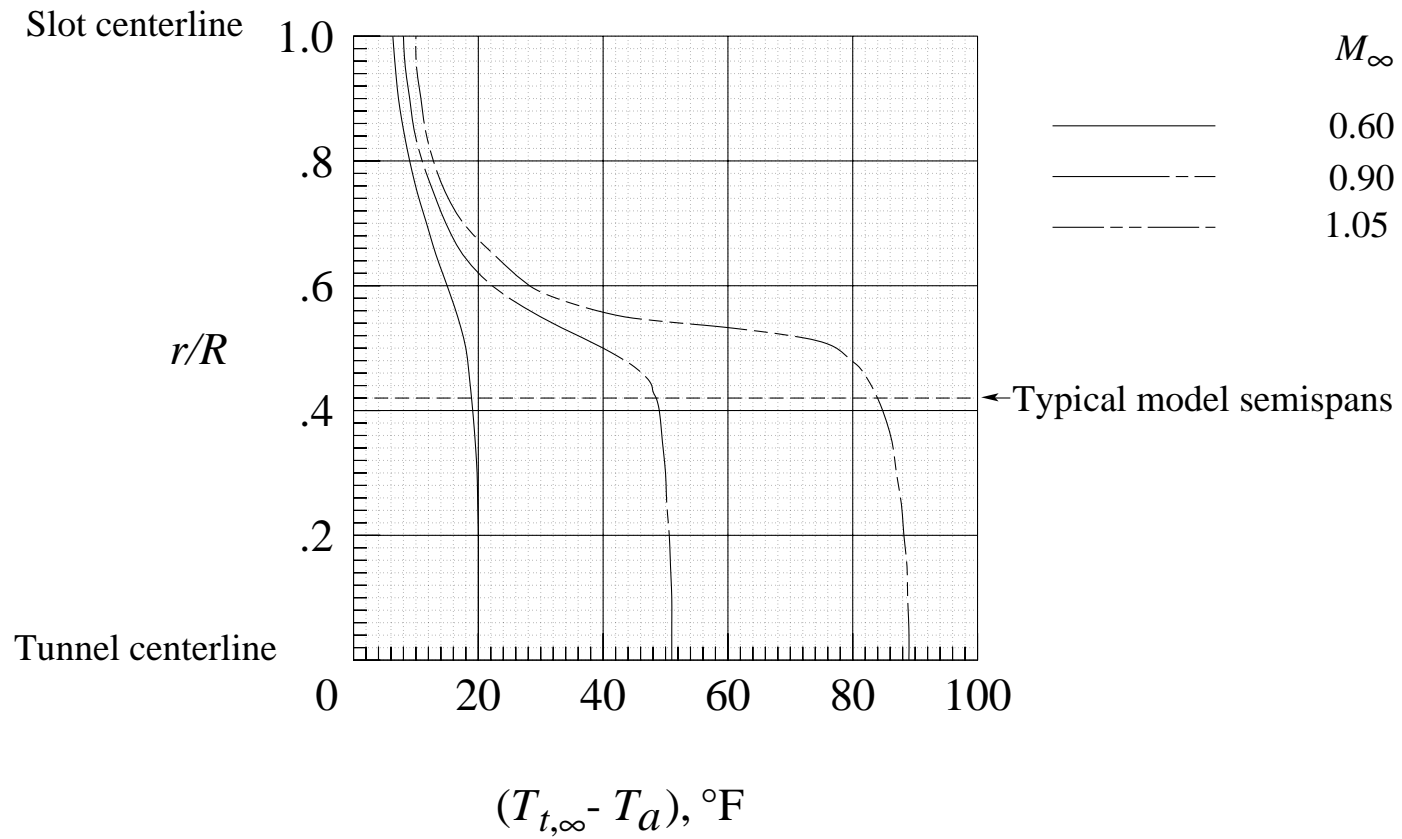


Figure 55. Stagnation temperature rise above outside air at TS 127.00.

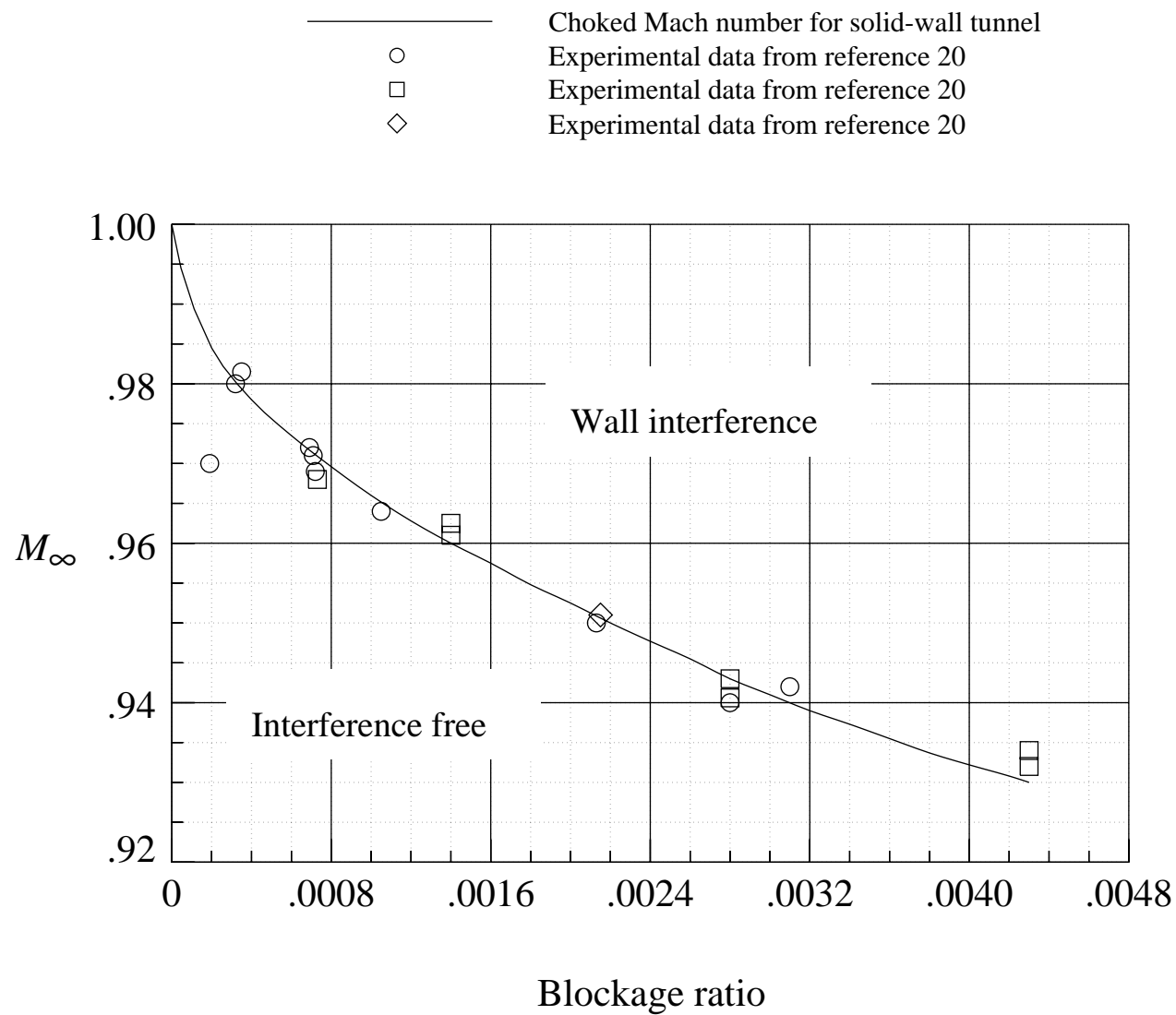
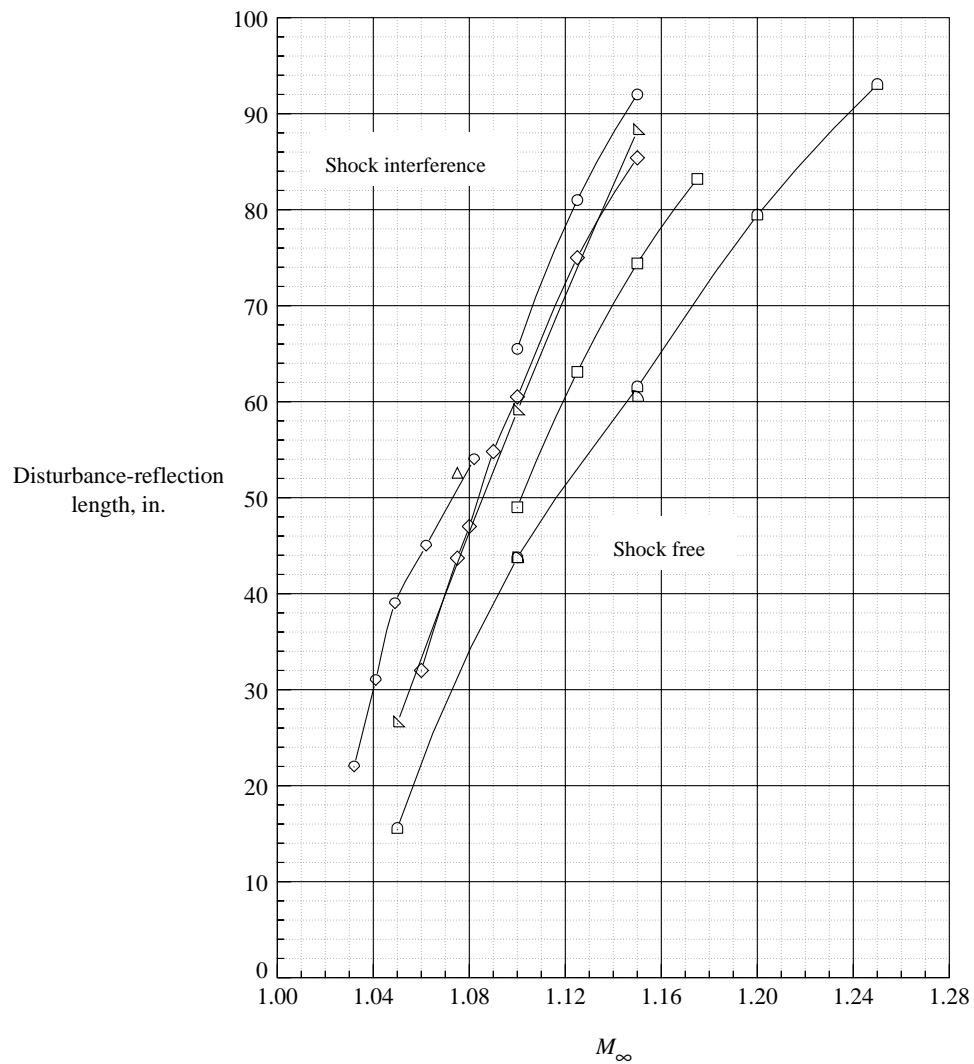


Figure 57. Variation of Mach number with blockage ratio for interference free data.



	Model	Length, in.	Nose half angle, deg	Location	Reference
○	1	96.0	20	Centerline	21
□	2	96.0	40	Centerline	21
◇	3	96.0	Ogive	Centerline	21
△	5	60.0	20	Centerline	21
▴	9	100.3	28	Centerline	21
▷	21	72.0	28	±22 in. off centerline	Unpublished
◻	22	96.0	28	±22 in. off centerline	Unpublished
◊	SRB	64.0	10	Centerline	Unpublished

Figure 58. Boundary-reflected-disturbance lengths measured in Langley 16-Foot Transonic Tunnel.

<u>Bypass ratio</u>	<u>Full size fan dia., in.</u>	<u>Scale, percent</u>	<u>Model fan dia., in.</u>	<u>Transport aircraft</u>
6DD	69.0	9.68	6.6	Medium twin
12GD	93.8	9.68	9.05	Medium twin
6DD	123.5	5.89	7.26	Large twin
12GD	167.9	5.89	9.88	Large twin

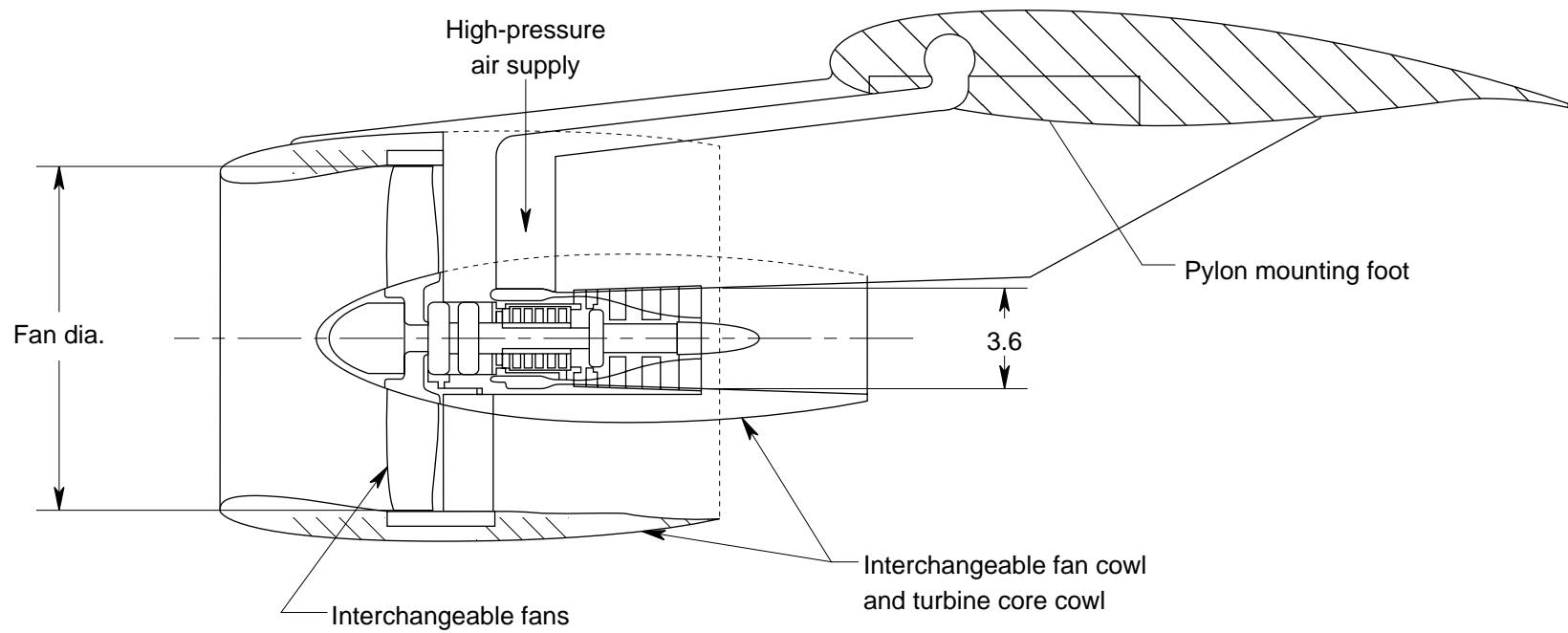


Figure 73. Variable bypass ratio turbofan simulator. Dimensions are in inches.

REPORT DOCUMENTATION PAGE			Form Approved OMB No. 0704-0188	
Public reporting burden for this collection of information is estimated to average 1 hour per response, including the time for reviewing instructions, searching existing data sources, gathering and maintaining the data needed, and completing and reviewing the collection of information. Send comments regarding this burden estimate or any other aspect of this collection of information, including suggestions for reducing this burden, to Washington Headquarters Services, Directorate for Information Operations and Reports, 1215 Jefferson Davis Highway, Suite 1204, Arlington, VA 22202-4302, and to the Office of Management and Budget, Paperwork Reduction Project (0704-0188), Washington, DC 20503.				
1. AGENCY USE ONLY (Leave blank)		2. REPORT DATE September 1995		3. REPORT TYPE AND DATES COVERED Technical Paper
4. TITLE AND SUBTITLE The NASA Langley 16-Foot Transonic Tunnel <i>Historical Overview, Facility Description, Calibration, Flow Characteristics, and Test Capabilities</i>			5. FUNDING NUMBERS WU 505-59-30-04	
6. AUTHOR(S) Francis J. Capone, Linda S. Bangert, Scott C. Asbury, Charles T. L. Mills, and E. Ann Bare				
7. PERFORMING ORGANIZATION NAME(S) AND ADDRESS(ES) NASA Langley Research Center Hampton, VA 23681-0001			8. PERFORMING ORGANIZATION REPORT NUMBER L-17445	
9. SPONSORING/MONITORING AGENCY NAME(S) AND ADDRESS(ES) National Aeronautics and Space Administration Washington, DC 20546-0001			10. SPONSORING/MONITORING AGENCY REPORT NUMBER NASA TP-3521	
11. SUPPLEMENTARY NOTES				
12a. DISTRIBUTION/AVAILABILITY STATEMENT Unclassified-Unlimited Subject Category 09 Availability: NASA CASI (301) 621-0390			12b. DISTRIBUTION CODE	
13. ABSTRACT (Maximum 200 words) The Langley 16-Foot Transonic Tunnel is a closed-circuit single-return atmospheric wind tunnel that has a slotted octagonal test section with continuous air exchange. The wind tunnel speed can be varied continuously over a Mach number range from 0.1 to 1.3. Test-section plenum suction is used for speeds above a Mach number of 1.05. Over a period of some 40 years, the wind tunnel has undergone many modifications. During the modifications completed in 1990, a new model support system that increased blockage, new fan blades, a catcher screen for the first set of turning vanes, and process controllers for tunnel speed, model attitude, and jet flow for powered models were installed. This report presents a complete description of the Langley 16-Foot Transonic Tunnel and auxiliary equipment, the calibration procedures, and the results of the 1977 and the 1990 wind tunnel calibration with test-section air removal. Comparisons with previous calibrations showed that the modifications made to the wind tunnel had little or no effect on the aerodynamic characteristics of the tunnel. Information required for planning experimental investigations and the use of test hardware and model support systems is also provided.				
14. SUBJECT TERMS Wind tunnel; Calibration			15. NUMBER OF PAGES 202	
			16. PRICE CODE A10	
17. SECURITY CLASSIFICATION OF REPORT Unclassified	18. SECURITY CLASSIFICATION OF THIS PAGE Unclassified	19. SECURITY CLASSIFICATION OF ABSTRACT Unclassified	20. LIMITATION OF ABSTRACT	